UNIVERSIDADE DE BRASÍLIA
INSTITUTO DE CIÊNCIAS BIOLÓGICAS
PÓS-GRADUAÇÃO EM NANOCIÊNCIA E NANOBIOTECNOLOGIA

DISSERTAÇÃO DE MESTRADO

ESTUDO DA PENETRAÇÃO CUTÂNEA *IN VITRO* DE NANOCARREADORES DE ÓXIDOS DE FERRO COM DIFERENTES COBERTURAS

DÉBORA PIRES PORTO BARBOSA

BRASÍLIA – DF
2023

UNIVERSIDADE DE BRASÍLIA
INSTITUTO DE CIÊNCIAS BIOLÓGICAS
PÓS-GRADUAÇÃO EM NANOCIÊNCIA E NANOBIOTECNOLOGIA

Débora Pires Porto Barbosa

ESTUDO DA PENETRAÇÃO CUTÂNEA *IN VITRO* DE NANOCARREADORES DE ÓXIDOS DE FERRO COM DIFERENTES COBERTURAS

Orientadora:

Professora Maria Aparecida Godoy Soler

Dissertação apresentada ao Instituto ao curso de Pós-Graduação em Nanociência e Nanobiotecnologia da Universidade de Brasília como requisito parcial para a obtenção do título de Mestre em Nanociência e Nanobiotecnologia.

BRASÍLIA – DF

2023

AGRADECIMENTOS

Agradeço aos meus pais, Eliana e Otávio, por todo o carinho, apoio e amor incondicional durante a minha vida, especialmente durante a faculdade. Amo vocês!

Á minha irmã Cris, minha companheira de leitura e fofocas. Te amo meu bem, obrigada por deixar esse mestrado mais leve.

Á minha dinda maravilhosa, Luciana, que me inspira cada dia mais. Te amo!

À minha irmã postiça Ana Carolina, muito obrigada pelo apoio e carinho durante esses anos.

Aos meus chuchus, minhas amigas de infância, muito obrigada por fazer parte da minha vida, por todos esses anos de amizade, por serem o meu porto seguro em várias etapas da minha vida. Em especial, a Gabi de Paiva, por sempre me perguntar como estão as sobrinhas dela, vulgo minhas nanopartículas.

Aos amigos que fiz durante a graduação e a pós, obrigada por toda a ajuda, companhia e amizade. Em especial, a Gabriela Sousa, por todo apoio durante os períodos difíceis nesses 7 anos.

À minha orientadora, Professora Maria Aparecida, por ter me orientado durante a iniciação científica, TCC e na realização deste trabalho. Obrigada pela confiança e contribuição para minha formação acadêmica e cientifica.

Aos meus colegas nanoworkers, integrantes do grupo de pesquisa da Professora Maria Aparecida, em especial a Aline, Luana, Deizilene, Antônia e Deyse. Obrigada tanto pela amizade quanto pelo treinamento nas técnicas de caracterização e na síntese das nanopartículas.

Ao professor Paulo Souza, do Instituto de Física, pelos experimentos de ressonância ferromagnética, cujos resultados permitiram a quantificação das partículas na pele.

À Luana Afiune pela amizade e auxílio durante a realização desse trabalho. Muito obrigada por compartilhar seu conhecimento comigo e sempre me fornecer concelhos que facilitaram a realização desse trabalho.

Ao professor Sebastião William e os alunos Alexandre, Emanoel e João, do Laboratório Espectroscopia Ótica (CNANO) do Instituto de Física, pelo apoio nas medidas de espectroscopia de infravermelho e Raman.

Ao professor Leonardo Paterno por fornecer o padrão de ferro para a análise de absorção atômica (AAS) e aos técnicos Cleber e Lennine, da Central Analítica do IQ, pela realização das medidas de AAS.

À Ingrid, do Laboratório de Microscopia e Microanálise (Instituto de Ciências Biológicas - UNB), pelas micrografias de Microscopia Eletrônica de Transmissão.

À Luma, do Laboratório de Tecnologia de Medicamentos, Alimentos e Cosméticos (LTMAC) pelo treinamento na técnica de tape stripping e tratamento das orelhas de suínos para realização da permeação. A Rayssa e Geisa, do LTMAC, pelo auxílio na análise estatística dos dados obtidos.

À professora Taís Gratieri, da Faculdade de Farmácia, pelas discussões sobre os resultados do estudo de penetração cutânea das nanoformulações.

À Universidade de Brasília por me acolher durante a graduação e a pós. Obrigada pela oportunidade!

À CAPES pela bolsa de mestrado.

A menos que modifiquemos a nossa maneira de pensar, não seremos capazes de resolver os problemas causados pela forma como nos acostumamos a ver o mundo.

Albert Einstein

RESUMO

Este trabalho tem como objetivo o estudo da penetração cutânea de diferentes nanocarreadores de oxido de ferro e para aplicação na administração tópica de fármacos. As nanopartículas (NPs) foram sintetizadas via coprecipitação em meio básico e funcionalizadas com 3 surfactantes diferentes, o ácido láurico (aniônico), a dodecilamina (catiônico) e o Pluronic F127 (não iônico), formando dispersões coloidais estáveis em meio aquoso. Os nanocarreadores sintetizados foram caracterizados por meio das técnicas de espalhamento dinâmico de luz, microscopia eletrônica de transmissão, espectroscopia no infravermelho e Raman. As NPs apresentaram diâmetro médio na faixa de 6,50 nm, enquanto o tamanho hidrodinâmico variou de 130 a 230 nm, dependendo do tipo de cobertura. A partir dos espectros Raman obtidos, observou-se que a oxidação das partículas de magnetita para maguemita foi efetiva, enquanto a análise dos espectros no infravermelho indica a presença da cobertura nos 3 nanocarreadores, sendo um funcionalizado com a bicamada de ácido láurico, outro com bicamada de ácido láurico e dodecilamina e o terceiro com bicamada de ácido láurico e Pluronic F127. Estudos de penetração cutânea *in vitro* dos 3 nanosistemas utilizando pele da orelha de suínos, como modelo para a pele humana, e empregando o método Saarbrüecken modificado, foram realizados por 12, 24 e 36 horas. A concentração de ferro em 2 camadas de pele (estrato córneo e o folículo piloso) foi obtida por ressonância ferromagnética, não tendo sido observada a presença de ferro na pele remanescente. Os resultados obtidos indicam que os 3 nanocarreadores sintetizados apresentam potencial para a aplicação tópica de fármacos, possibilitando um tratamento local e sem atingir a corrente sanguínea.

Palavras-chave: nanocarreadores, nanopartículas, óxido de ferro, penetração cutânea, administração tópica, ácido láurico, dodecilamina, Pluronic F127, alopecia.

ABSTRACT

This study aims the investigation of the cutaneous penetration with three different iron oxide nanocarriers and evaluate its applications in topical administration of drugs. The nanoparticles (NPs) were synthesized via coprecipitation in basic aqueous medium method and functionalized with 3 different surfactants, lauric acid (anionic), dodecylamine (cationic) and Pluronic F127 (non-ionic), forming stable aqueous colloidal dispersions. The synthesized nanocarriers were characterized by dynamic light scattering, transmission electron microscopy, infrared and Raman spectroscopy. The NPs presented mean diameterof 6.5 nm, while the hydrodynamic diameter ranged from 130 to 230 nm, depending on the type of coating. Raman spectra indicated that the oxidation process from magnetite to maghemite nanoparticles was effective, while the analysis of the infrared spectra indicated the presence of the respective coatings on the 3 nanocarriers, one functionalized with a bilayer of lauric acid, other with a bilayer of lauric acid and dodecylamine and the third with a bilayer of lauric acid and Pluronic F127. *In vitro* skin penetation studies of the 3 nanosystems, using pig ear skin as a model for human skin through modified Saarbrüecken method, were performed for 12, 24 and 36 hours. Using ferromagnetic resonance, it was possible to quantify the concentration of iron in 2 layers of skin, the stratum corneum and the hair follicle. It was not observed the presence of iron in the remaining skin. These findings indicate that the 3 synthesized nanocarriers are promising for topical application of drugs, allowing a local treatment,and without reaching the bloodstream.

Keywords: nanocarriers, nanoparticles, iron oxide, cutaneous penetration, topical administation, lauric acid, dodecylamine, Pluronic F127, alopecia.

LISTA DE FIGURAS

LISTA DE TABELAS

LISTA DE ABREVIAÇÕES E SIGLAS

AL: Ácido Láurico

D_H: Tamanho Hidrodinâmico

$D_{\text{méd}}$: Diâmetro Médio

DDA: Dodecilamina

EDL: Espalhamento Dinâmico de Luz

EC: Estrato Córneo

Fe: Ferro

FM: Fluido Magnético

FP: Folículo Piloso

FTIR: Espectroscopia no Infravermelho por Transformada de Fourier

IONs: Iron oxide nanoparticles

NPs: Nanopartículas

PLU: Pluronic F127

MET: Microscopia Eletrônica de Transmissão

MNT: Magnetita

MGM: Maguemita

MGM-AL/DDA: Nanopartículas de óxido de ferro funcionalizadas com bicamada de ácido láurico/dodecilamina

MGM-AL/PLU: Nanopartículas de óxido de ferro funcionalizadas com bicamada de ácido láurico/Pluronic F127

MGM-BL: Nanopartículas de óxido de ferro funcionalizadas com bicamada de ácido láurico

MGM-ML: Nanopartículas de óxido de ferro funcionalizadas com monocamada de ácido láurico

PBS: Phosphate-buffered saline

PdI: Índice de Polidispersão

pH: potencial hidrogeniônico

PR: Pele Remanescente

PEO: Poli(óxido de etileno)

PEO-PPO-PEO: copolímero tribloco anfifílico

PPO: Poli(óxido de propileno)

RFM: Ressonância Ferromagnética

ζ: Potencial Zeta

SUMÁRIO

CAPÍTULO 1

INTRODUÇÃO E OBJETIVOS

1.1. Introdução

As nanopartículas de óxidos de ferro, do inglês iron oxide nanoparticles (IONs) são muito estudados para aplicação em meio biológico por apresentarem superparamagnetismo, biocompatibilidade e baixa toxicidade. Em adição, podem ser funcionalizadas com moléculas diversas que, além de promover sua estabilidade em meio hidrofílico, podem conter sítios disponíveis para ancoragem de fármacos, anticorpos, marcadores, entre outros (M. A. G. Soler *et al.*, 2011; Maria A. G. Soler *et al.*, 2011; Soler; Paterno, 2017; Rivera, 2018). Devido às suas propriedades, apresentam grande potencial para aplicações em nanomedicina, como melhora do contraste de imagens de ressonância magnética, terapia gênica, magneto-hipertermia e veículos carreadores de fármacos (drug delivery system) (Berry *et al.*, 2019; Rivera *et al.*, 2019).

As IONs funcionalizadas constituem uma plataforma para ancoragem de fármacos, formando nanocarreadores eficientes para a sua liberação no organismo em um local específico. Estes nanocarreadores apresentam grande estabilidade, maior taxa de absorção pelos tecidos e liberação modificada, diminuindo a dosagem necessária bem como os efeitos colaterais, quando comparados com as formulações tradicionais. Em adição, por serem superparamagnéticas, podem ser direcionadas a um órgão ou tecido específico, por meio da aplicação de um gradiente de campo magnético ou ancoragem de um marcador específico (El-Hammadi; Arias, 2015; Rivera *et al.*, 2019).

A administração de fármacos via aplicação tópica tem sido utilizada visando a diminuição dos efeitos colaterais e melhorar a adesão do paciente ao tratamento. Entretanto, o desenvolvimento de formulações tópicas eficientes que consigam permear a barreira natural da pele, o estrato córneo, tem sido um desafio. Devido ao seu tamanho reduzido e formato, os nanosistemas têm se mostrado promissores para ultrapassar esta barreira, promover uma liberação modificada do fármaco na região de interesse e aumentar a atividade terapêutica empregando doses menores (Musazzi *et al.*, 2017; Pereira *et al.*, 2018; Afiune *et al.*, 2020). Entre os nanosistemas explorados, os nanocarreadores de óxido de ferro com diâmetro menor que 20 nm apresentaram resultados promissores na permeação do estrato córneo, sendo observada a permeação de diferentes fármacos, utilizando-se nanoformulações em estado semissólido (Musazzi *et al.*, 2017) e líquido (fluido magnético), com e sem aplicação de um campo magnético externo (Rao *et al.*, 2015; Afiune *et al.*, 2020). Além disso, as IONs podem ser sintetizadas por métodos simples, de baixo custo e em escala industrial, que permitem a modulação de suas propriedades físicas e magnéticas em função da aplicação desejada (El-Hammadi; Arias, 2015).

Além do diâmetro das partículas, as propriedades físico-químicas da cobertura superficial também influenciam na capacidade de permeação do nanosistema, podendo facilitar a penetração do fármaco nas camadas da pele (Musazzi *et al.*, 2017). Por exemplo, o ácido láurico (AL) e a dodecilamina (DDA) podem agir como potencializadores da permeação em administração de fármacos via tópica ou transdérmica. Verificou-se que DDA potencializa a permeação transdérmica de moléculas como vitamina D3 (Alsaqr; Rasoully; Musteata, 2015) e testosterona (Zhao *et al.*, 2002, 2009). No caso do AL, observou-se também um aumento da permeação de moléculas com ou sem carga, como salicilato de sódio, cafeína, naloxona e ondansetrona (Green; Guy; Hadgraft, 1988; Babu; Chen; Kanikkannan, 2015), enquanto que IONs funcionalizadas com bicamada de AL constituem um promissor nanocarreador para aplicação tópica dos fármacos finasterida e dutasterida, possibilitando sua liberação controlada e direcionamento para o folículo piloso, região de interesse (Afiune *et al.*, 2020).

Neste contexto, este trabalho tem como objetivo investigar o efeito do tratamento superficial das nanopartículas com coberturas de diferentes cargas superficiais, considerando a influência de cada um deles na estabilidade e biodistribuição de cada nanocarreador nas 3 camadas da pele: estrato córneo, folículo piloso e pele remanescente. Neste estudo, nanopartículas de óxido de ferro, sintetizadas via coprecipitação em meio aquoso, foram funcionalizados com três diferentes surfactantes: ácido láurico, dodecilamina e Pluronic F127, dispersos em meio aquoso, para os estudos de penetração cutânea em pele suína, empregando o método Saarbrüecken modificado (Afiune *et al.*, 2020).

1.2. Objetivos

1.2.1. Objetivo geral

Sintetizar e caracterizar diferentes nanosistemas formados por nanopartículas de óxido de ferro funcionalizadas com bicamadas de ácido láurico, ácido láurico/dodecilamina e ácido láurico/Pluronic F127 e verificar a influência da cobertura de cada nanocarreador na penetração cutânea *in vitro* em pele suína.

1.2.2. Objetivos específicos

- Sintetizar e caracterizar as nanopartículas de óxidos de ferro que serão empregadas para obter os três diferentes tipos de nanocarreadores;
- Funcionalizar as nanopartículas sintetizadas com uma monocamada de ácido láurico;
- Funcionalizar as nanopartículas sintetizadas com uma bicamada de laurato;
- Desenvolver um protocolo para funcionalizar as nanopartículas sintetizadas com uma monocamada de laurato com a segunda camada de dodecilamina;
- Funcionalizar as nanopartículas sintetizadas com uma bicamada laurato/Pluronic F127;
- Caracterizar e comparar os nanocarreadores sintetizados;
- Estudar a estabilidade dos nanocarreadores sintetizados em função do tempo decorrido após a síntese;
- Avaliar a penetração *in vitro*, retenção cutânea e folicular das nanopartículas em função do tratamento superficial das partículas em pele de suíno;

CAPÍTULO 2

ADMINISTRAÇÃO CUTÂNEA DE FÁRMACOS

2.1. Anatomia da pele

A pele é o maior órgão do corpo humano, representando cerca de 16% do peso corporal e com uma área superficial entre 1,5 e 2 m². Ela funciona como uma barreira de proteção, separando os órgãos do corpo e a rede de circulação sanguínea do ambiente externo, controlando a perda de fluidos essenciais e a entrada de corpos estranhos no organismo (Gratieri; Gefuso; Lopez, 2008; Ushirobira, 2019).

A pele é constituída por 2 camadas principais interligadas entre si, a epiderme e a derme (Figura 1). A epiderme é a camada mais externa, formada por tecido epitelial especializado, cuja espessura pode variar de acordo com a região do corpo. Por ser uma área não vascularizada, os fármacos precisam permear essa camada para atingir a corrente sanguínea, na derme. Pode ser dividida em duas partes, a epiderme viável e o estrato córneo, principal barreira limitante à difusão percutânea de fármacos (Vieira, 2013).

O estrato córneo (EC) é a região mais superficial da pele, composto por células escamosas mortas, os corneócitos, dispersos em uma matriz rica em lipídios não polares, como ceramidas (18%), ácidos graxos livres (19%), esteroides (14%) e triglicerídeos (25%), além de possuir uma baixa umidade, cerca de 7 a 20% da quantidade total de água presente na pele (Gratieri; Gefuso; Lopez, 2008; Vieira, 2013).

A derme é formada por duas camadas, a papilar e a reticular. É uma camada vascularizada, que contem terminações nervosas e os apêndices cutâneos: folículo piloso, glândulas sebáceas e sudoríparas. A camada mais externa, a papilar, é formada por papilas que se projetam em direção a epiderme, proporcionando uma maior área de contato entre essas duas regiões (Kolimi; Nyavanandi; Dudhipala, 2022; Teles, 2023).

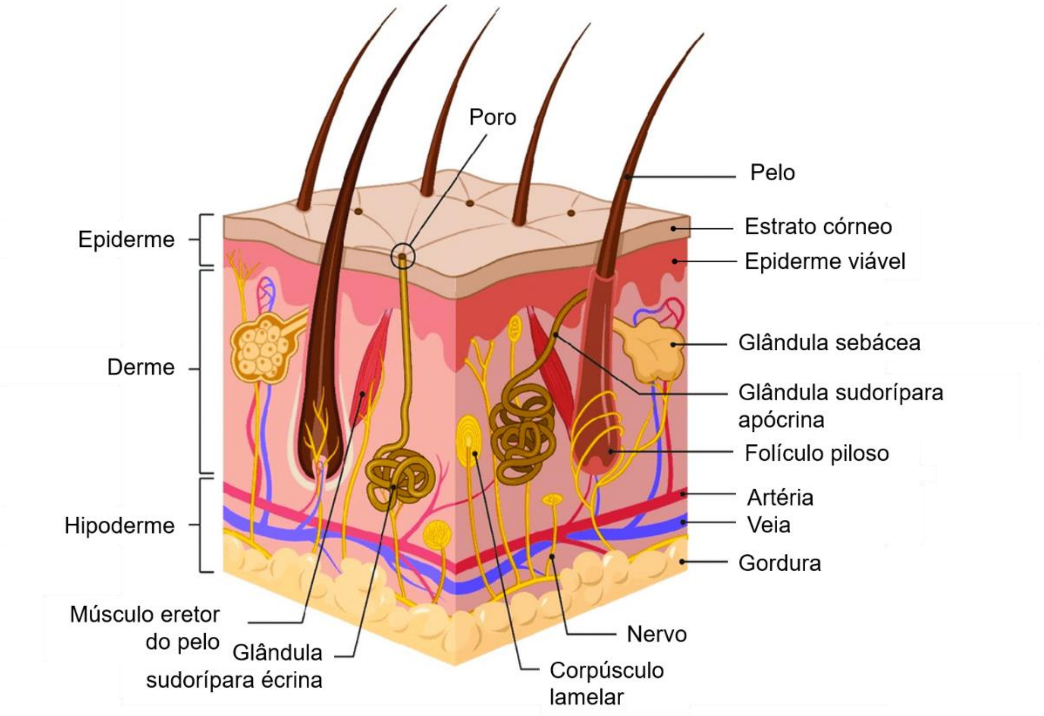

Figura 1. Ilustração da anatomia da pele. Adaptado de Kolimi; Nyavanandi; Dudhipala, 2022.

2.2. Administração cutânea

A administração de fármacos através da pele apresenta diversas vantagens em relação às vias tradicionais (oral e injetável), como por exemplo: é um método não invasivo, não provoca perturbações gastrointestinais, impede o efeito de primeira passagem, melhora o controle da concentração do fármaco no organismo, minimizando o risco de efeitos secundários ou níveis subterapêuticos, além de facilitar a suspenção do tratamento ao identificar algum efeito colateral. Todas essas vantagens tendem a aumentar a adesão do paciente ao tratamento (Bettoni, 2009; Pereira *et al.*, 2018; Afiune *et al.*, 2020).

Existem 2 tipos de aplicação cutânea, com finalidades distintas: administração tópica, utilizada para tratamento de doenças dermatológicas, com ação na periferia, sem atingir a corrente sanguínea; e a administração transdérmica, que é um tratamento sistêmico, onde o fármaco deve permear as camadas da pele e atingir a corrente sanguínea em um nível terapêutico (Vieira, 2013).

Apesar de suas vantagens, a administração cutânea de fármacos ainda é pouco utilizada, devido à dificuldade dos medicamentos ultrapassarem a barreira da pele e atingirem o local de ação em concentrações desejáveis. Os nanosistemas apresentam um grande potencial para o carreamento de fármacos através da pele devido à sua capacidade de penetrar o EC (Pereira *et al.*, 2018).

2.2.1. Vias de absorção cutânea

As principais rotas de penetração de fármacos estão ilustradas na Figura 2 (Razavi; Darvishi, 2018), onde se observa: (i) a via intracelular, pela qual os fármacos se difundem ao redor dos corneócitos, através da matriz lipídica, sendo a preferível para moléculas lipofílicas pequenas; (ii) a via transcelular, pela qual os fármacos se difundem pelo EC intacto, passando através dos corneócitos e da matriz lipídica, é mais utilizada por moléculas hidrofílicas ou moderadamente lipofílicas e (iii) a via apêndices cutâneos, na qual as moléculas penetram na pele através dos apêndices cutâneos (folículo piloso, glândula sebácea e sudorípara), possibilitando a permeação de íons e moléculas hidrofílicas maiores, que dificilmente conseguiriam atravessar por meio das rotas i e ii. Juntas, as rotas intracelular e transcelular formam a via traspidérmica, que é a dominante e envolve necessariamente a passagem das partículas pelo EC (Carazo *et al.*, 2018; Zoabi; Touitou; Margulis, 2021).

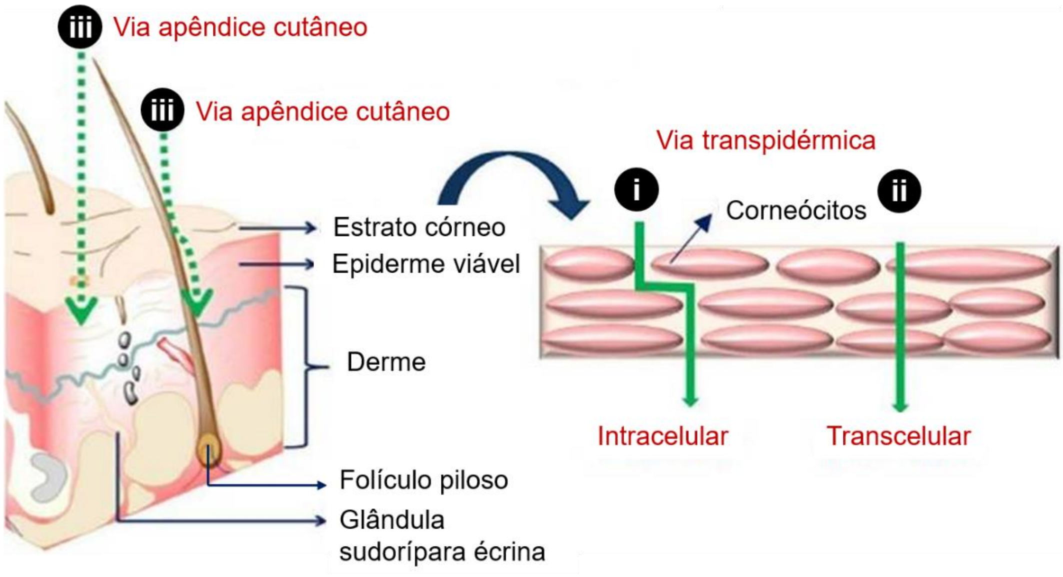

Figura 2. Ilustração das principais vias de permeação de fármacos. Adaptado de Razavi; Darvishi, 2018.

A escolha de uma via de permeação depende das propriedades físico-químicas dos fármacos e do veículo. A penetração via apêndices cutâneos é mais rápida inicialmente, porém a quantidade de fármaco que penetra através da via transdérmica é maior, visto que os apêndices cutâneos constituem apenas aproximadamente 0,1% da superfície da pele, com exceção ao couro cabeludo (Rao *et al.*, 2015; Carazo *et al.*, 2018; Teles, 2023). Para diversas moléculas, a penetração pelo estrato córneo é lenta, de forma que o fármaco não consegue se acumular na região de interesse e atingir níveis terapêuticos antes de ser metabolizado pela pele. Portanto, é necessário o desenvolvimento de novos sistemas que consigam permear o EC e aumentar o tempo de vida do medicamento no organismo (Razavi; Darvishi, 2018; Ushirobira, 2019).

2.3. Nanosistemas aplicados a tratamentos cutâneos

Atualmente, os nanosistemas, como nanopartículas lipídicas (Lin *et al.*, 2018), poliméricas (Ushirobira *et al.*, 2020) e metálicas (Rao *et al.*, 2015; Raviraj *et al.*, 2021), têm sido explorados como potenciais carreadores de fármacos por apresentarem diversas vantagens como: tamanho reduzido, alta estabilidade, biocompatibilidade, podem encapsular moléculas em sua estrutura, retardando a sua degradação em meio biológico, promovem uma liberação modificada do medicamento no sítio de ação, diminuindo a dose necessária e, consequentemente, os efeitos colaterais (Razavi; Darvishi, 2018). Em adição, as NPs apresentam um grande potencial para o tratamento de doenças que atingem o folículo piloso, devida à sua tendência natural de se acumular nessa região. A profundidade na qual esses carreadores se acumulam depende do seu tamanho, conforme se observa na Figura 3. Partículas maiores, com cerca de 2 a 3 µm tentem a atingir apenas a porção superior do folículo. Partículas com tamanho entre 200 e 300 nm conseguem chegar até o istmo, possibilitando a liberação do fármaco nas glândulas sebáceas. Enquanto as partículas menores, com menos de 40nm, conseguem atingir a região mais profunda do folículo, o bulbo capilar (Pereira *et al.*, 2018; Ushirobira, 2019).

As nanopartículas de óxido de ferro (IONs), têm despertado interesse para este último tipo de administração de fármaco, pois geralmente são menores do que 40 nm e conseguem penetrar camadas mais internas da pele (Afiune, 2019).

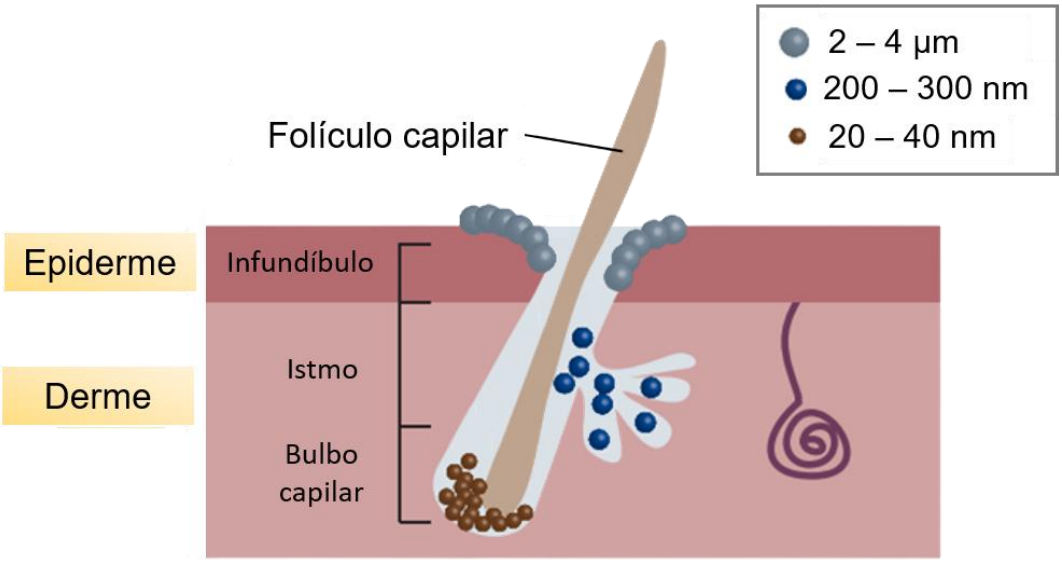

Figura 3. Distribuição de nanosistemas no folículo piloso em função do tamanho da partícula, adaptado de Pereira et al., 2018.

2.3.1 Nanosistemas formados por partículas de óxido de ferro

Estudos recentes mostram que os nanosistemas formados por NPs de óxidos de ferro são capazes de promover a permeação de agentes quimioterápicos com (Rao *et al.*, 2015; Zhang *et al.*, 2019; Viratchaiboott *et al.*, 2022) ou sem a aplicação de um campo magnético (Raviraj *et al.*, 2021) para o tratamento de tumores mais superficiais, como o câncer de mama, listados na Tabela 1. Além disso, também podem ser utilizados para administração tópica de fármacos, evitando a ação sistêmica e potencias efeitos colaterais. Afiune *et al.* (2020) desenvolveu um nanocarreador formado por NPs de óxidos de ferro capaz de potencializar a penetração dos fármacos dutasterida e finasterida e direcioná-los para o seu sítio de ação, o folículo piloso. Gonçalves *et al.* (2017) obteve um hidrogel de Pluronic 127 com IONs capaz de liberar o óxido nítico, um potencializador da regeneração cutânea.

Tabela 1. Nanocarreadores de óxido de ferro desenvolvidos para administração cutânea de fármacos.

Nanosistema	Fármaco	Diâmetro	Teste	Vantagens
IONs funcionalizadas com copolímero não iônico	5-fluorouracil e doxorrubicina	25 nm	*In vivo*	Aumento da penetração transdermal dos fármacos avaliados, sem a necessidade de incorporá-los em sua estrutura (Raviraj *et al.*, 2021).
IONs funcionalizadas com surfactante aniônico	Dutasterida e finasterida	8 nm	*In vitro*	Aumento da penetração cutânea dos fármacos, direcionando-os para o folículo piloso, sitio de ação dos medicamentos, sem atingir a corrente sanguínea, ideal para aplicação tópica (Afiune *et al.*, 2020).
IONs funcionalizadas com pectina	5-fluorouracil	27 nm	*In vitro*	Aumento do coeficiente de difusão e da liberação do fármaco ao aplicar campo magnético e elétrico, além de reduzir o tempo de liberação (Viratchaiboott *et al.*, 2022).
Microagulhas carregadas com IONs funcionalizadas com polímeros não iônicos	Cloridrato de lidocaína	9 a 11 nm	*In vivo* e *in vitro*	Ao aplicar uma radiação de infravermelho próximo, é possível modular a liberação do anestésico, sem atingir o sistema nervoso, possibilitando a anestesia local (Li; Liao; Zheng, 2022).

IONs com ácido oleico, encapsuladas em uma matriz de celulose bacteriana	Doxorrubicina e hematoporfirina	–	*In vivo* e *in vitro*	O nanocarreador sintetizado pode ser utilizado para o tratamento de tumores superficiais por terapia fotodinâmica e quimioterapia, sendo observada a permeação cutânea dos fármacos ao aplicar um campo magnético (Zhang *et al.*, 2019).
IONs funcionalizadas com surfactante aniônico	Epirrubicina	10 nm	*In vitro*	Ao aplicar um campo magnético, observou-se a absorção transcutânea do fármaco. Além disso, a ancoragem do fármaco no nanocarreador é modulada por meio do pH, ao entrar em contato com uma região mais ácida, como células tumorais, o quimioterápico é liberado (Rao *et al.*, 2015).
IONs com ácido tiomálico, dispersar em um hidrogel de Pluronic F127	Óxido nítrico	11 nm	*In vitro*	As IONS com ácido tiomálico são capazes de prolongar a meia-vida do óxido nítrico, que acelera o processo de cicatrização cutânea, e promover uma liberação controlada na pele, sem atingir a corrente sanguínea. O hidrogel de Pluronic aumenta a estabilidade do sistema (Gonçalves *et al.*, 2017).

CAPÍTULO 3

NANOPARTÍCULAS DE ÓXIDO DE FERRO

3.1. Magnetismo

Os materiais encontrados na natureza possuem momento de dipolo magnético ($\vec{m}$), que tem origem no movimento angular orbital (L) e de spin dos elétrons (S), de forma que as propriedades magnéticas dependem da sua estrutura atômica. Pode-se classificar os materiais como: os que possuem $\vec{m} \neq 0$, considerados materiais magnéticos como os ferrimagnéticos e ferromagnéticos, e os que possuem $\vec{m} = 0$, chamados de diamagnéticos, e também de materiais não magnéticos (Francisquini; Schoenmaker; Souza, 2012).

Ao submeter um sólido a um campo magnético externo ($\vec{H}$), surge um campo magnético ($\vec{B}$) induzido no material (equação 1), que depende tanto da magnitude de $\vec{H}$ quanto da magnetização do material ($\vec{M}$), definida como momento magnético por unidade de volume (V).

$$\vec{B} = \mu(\vec{H} + \vec{M}) \qquad (1)$$

$$\vec{M} = \frac{\vec{m}}{V} \qquad (2)$$

onde µ é a permeabilidade magnética do meio. A magnitude de M também depende do campo magnético aplicado e pode ser dada por:

$$\vec{M} = \chi\vec{H} \qquad (3)$$

sendo χ a susceptibilidade magnética do material. Ela indica a resposta do material ao campo aplicado. Quando a susceptibilidade é negativa, os momentos magnéticos se alinham em direção oposta ao campo aplicado e o material é chamado de diamagnético. Os materiais paramagnéticos possuem momentos magnéticos individuais desordenados (magnetização nula na ausência de um campo) que se aliam em uma única direção ao se aplicar um campo externo. Sua susceptibilidade é positiva, porém pequena em relação aos materiais ordenados.

Os materiais ordenados são classificados em ferromagnéticos, ferrimagnéticos e antiferromanéticos. Os materiais ferromagnéticos possuem seus momentos magnéticos individuais ordenados em uma única direção. Os materiais ferrimagnéticos são compostos por momentos antiparalelos de magnitude diferentes. Dessa forma, ambos possuem magnetização espontânea abaixo da temperatura de Curie. Enquanto os materiais antiferromagnéticos são formados por momentos antiparalelos de mesma magnitude, resultando em uma magnetização nula na ausência de um campo externo.

A Temperatura de Curie (T_C) é a temperatura em que ocorre a desordenação dos momentos devido à energia térmica. Acima desta temperatura, os materiais ordenados se tornam paramagnéticos. A Figura 4 apresenta uma ilustração dos momentos magnéticos na ausência e na presença de um campo externo para os materiais diamagnéticos, paramagnéticos, ferromagnéticos, ferrimagnéticos e antiferromagnéticos.

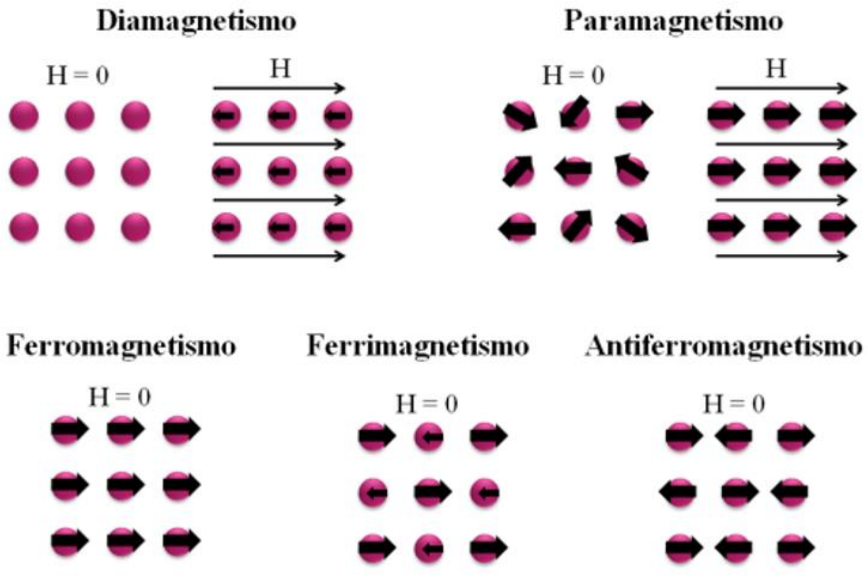

Figura 4. Ilustração dos momentos de dipolo magnético nos materiais diamagnéticos, paramagnéticos, ferromagnéticos, ferrimagnéticos e antiferromagnéticos, conforme o indicado (Letti, 2013).

No estudo desses materiais, avalia-se o comportamento da magnetização ($\vec{M}$) ou do campo induzido ($\vec{B}$) em função da variação do campo externo ($\vec{H}$), originando a curva de magnetização, ou histerese. Em uma curva típica para materiais ferromagnéticos e ferrimagnéticos, conforme a ilustração apresentada na Figura 5, o módulo de $\vec{M}$ aumenta com o aumento do campo aplicado, até que seja atingida a magnetização de saturação (M_s), que é a magnetização máxima que o material pode atingir. Quando o campo ($\vec{H}$) é removido, a magnetização resultante não é nula, chamada de magnetização remanescente (M_r). Para que a magnetização seja zerada, é necessário aplicar um campo de sentido oposto, chamado de campo coercitivo (H_c). Caso o campo coercitivo tenha valor elevado, o material magnético é considerado duro e, caso seja H_c baixo, o material é considerado macio.

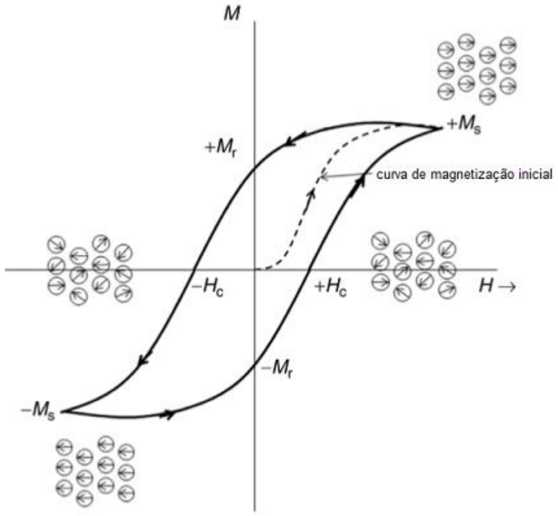

Figura 5. Curva de Histerese típica de materiais ferromagnéticos e ferrimagnéticos mostrando a magnetização de saturação (M_s), a magnetização remanescente (M_r) e o campo coercitivo (H_c). Adaptado de Soler; Paterno, 2016.

Superparamagnetismo

O superparamagnetismo só ocorre em materiais de baixa dimensão (escala nanométrica) e é um fenômeno magnético semelhante ao paramagnetismo, porém com uma magnetização de saturação superior. Materiais com dimensão abaixo do diâmetro crítico (D_c) se organizam em monodomínios magnéticos, em que os momentos magnéticos individuais estão alinhados na direção do eixo de fácil magnetização, de forma que, ao se aplicar um campo externo, há a formação de um grande momento magnético (Durán et al., 2006).

No limite da mudança de multidomínios para monodomínios, há um aumento do campo coercitivo até que atinja o seu valor máximo no D_c. Para valores menores que D_c, a coercitividade tende a diminuir até que ela se torne nula, ao atingir o limite do superparamagnetismo (Rivera, 2013). A partir desse valor de diâmetro, a partícula se encontra desmagnetizada na ausência de um campo externo ($M_r = H_c = 0$), sendo considerada então superparamagnética. Neste regime, a relaxação magnética ocorre com reversão do momento magnético efetivo, devido à agitação ocasionada pela energia térmica das partículas. Por isso, existe uma temperatura crítica para que a energia térmica seja o suficiente para promover a relaxação, chamada temperatura de bloqueio (T_B), que separa dois estados magnéticos. Acima dessa temperatura, as NPs apresentam comportamento superparamagnético e, abaixo dessa temperatura, as partículas apresentam magnetização remanente (Francisquini; Schoenmaker; Souza, 2012; Rivera, 2013).

3.2. Estrutura

As ferritas cúbicas, MFe_2O_3 (M = Fe^{2+}, Co^{2+}, Ni^{2+}, Mg^{2+}, Cu^{2+} e Zn^{2+}), possuem estrutura do tipo espinélio, composta por 32 átomos de O^{2-}, que ocupam os vértices, formando uma rede cúbica de face centrada. Os íons de ferro (III) e os cátions divalentes possuem 2 tipos de coordenação, tetraédrica (sítio A) e octaédrica (sítio B).

A estrutura espinélio pode ser do tipo normal, onde os cátions trivalentes ocupam apenas os sítios octaédricos e os cátions divalentes ocupam apenas o sítio octaédrico; ou inverso, onde tem-se os sítios A são ocupados, na mesma proporção tanto pelos íons M^{2+} quanto pelos M^{3+} e o sítios B são ocupados exclusivamente pelos íons M^{3+} (Soler *et al.*, 2005; Francisquini; Schoenmaker; Souza, 2012; Soler; Paterno, 2017).

A magnetita (Fe_3O_4) e a maguemita (Fe_2O_3) são óxidos de ferro puros e possuem estrutura espinélio inversa (Figura 6). A maguemita é obtida a partir da oxidação da magnetita, naturalmente ou por exemplo, sob aquecimento e borbulhamento de gás oxigênio (Alcantara, 2007), e é composta apenas por íons Fe^{3+}.

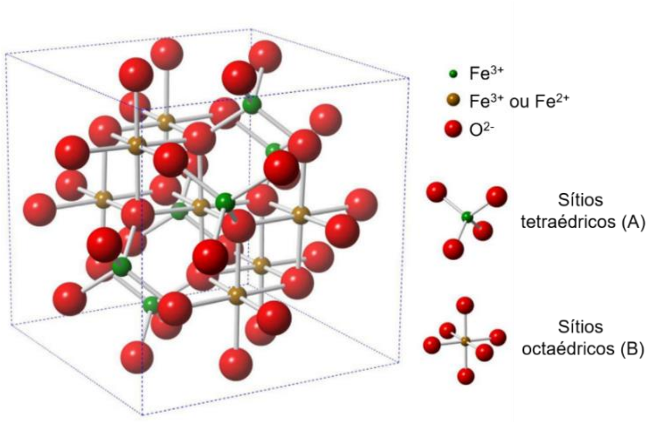

Figura 6. Representação de uma estrutura do tipo espinélio inverso. Adaptado de Galvão *et al*., 2016.

3.3. Métodos de síntese

Entre os métodos químicos de síntese, os mais utilizados para obtenção das IONs são a coprecipitação de sais de ferro em meio aquoso e a decomposição térmica de organometálicos ou complexos metálicos (Soler; Paterno, 2017).

Síntese via coprecipitação em meio aquoso

Esse método consiste na adição de uma solução saturada de sais de ferro (II) e ferro (III), em proporção 1:2, de forma controlada em uma solução alcalina aquosa, de acordo com a reação abaixo (equação 4):

$$2Fe^{3+}{}_{(aq)} + Fe^{2+}{}_{(aq)} + 8OH^{-}{}_{(aq)} \rightarrow Fe_3O_{4_{(s)}} + 4H_2O_{(l)} \qquad (4)$$

A formação de NPs via coprecipitação ocorre em 2 etapas: nucleação, onde são formados vários cristais de magnetita devido à supersaturação da solução, seguida pelo crescimento, em que os núcleos formados se aglomeram por difusão. Consequentemente, obtém-se uma amostra polidispersa, cuja dispersão pode ser superior a 20% (Souza, 2011; Soler; Paterno, 2017).

Para obter-se NPs com uma baixa distribuição de tamanho é necessário que a etapa de nucleação seja rápida e a de crescimento lenta. Pode-se realizar o controle da nucleação e do crescimento das NPs a partir do grau de saturação da solução de sais de ferro, velocidade de agitação, pH e força iônica do meio (Souza, 2011; Soler;

Paterno, 2017). Para interromper a aglomeração das NPs, é necessário funcionalizar sua superfície, criando uma repulsão entre as partículas.

O método de coprecipitação é de baixo custo, simples e acessível, apresenta facilidade de produção em larga escala, além de produzir IONs de diâmetro inferior a 10 nm, geometria aproximadamente esférica e dispersos em meio aquoso. Devido às suas características, foi o método utilizado neste trabalho.

Síntese via decomposição térmica

Este método consiste na decomposição térmica de complexos metálicos, como o tris(acetilacetonato)ferro(III), ($Fe[acac]_3$) (Sun; Zeng, 2002), pentacarbonil de ferro ($FeCO_5$) e o oleato de ferro ($Fe[olea]_3$) (Hufschmid *et al.*, 2015), na presença de um solvente orgânico de alto ponto de ebulição. Esses complexos metálicos são mais estáveis que os sais de ferro, o que permite uma separação entre as etapas de nucleação e crescimento das NPs. A nucleação ocorre quando o primeiro ligante é eliminado, o crescimento ocorre apenas com a eliminação dos outros dois ligantes, em temperaturas mais altas. Dessa forma, é possível produzir NPs com baixa dispersão de tamanho e, consequentemente, com propriedades uniformes (Hufschmid *et al.*, 2015; Soler; Paterno, 2017). Contudo, esse método apresenta desvantagens em relação ao de coprecipitação. A decomposição térmica não é completa, de forma que um dos ligantes é mantido como surfactante, promovendo a estabilização das NPs em meio orgânico apolar. Para aplicações biológicas, é necessário que as IONs estejam dispersas em meio aquoso, sendo necessário realizar uma etapa de troca de ligantes. O método é realizado em altas temperaturas, o que torna o processo de síntese em larga escala mais complexo (Soler; Paterno, 2017).

3.4. Funcionalização

Devido às forças atrativas (interações dipolo magnético e interações de Van der Walls), as NPs tendem a se aglomerar espontaneamente, reduzindo a energia livre de Gibbs. Para ambas aplicações, biológicas e tecnológicas, é necessário que as partículas estejam dispersas em um meio, polar ou apolar. Para atingir a estabilização coloidal, é necessário funcionalizar a superfície das NPs, para introduzir forças repulsivas entre elas para evitar a aglomeração.

A estabilização das IONs pode ser realizada por dois mecanismos: repulsão eletrostática e repulsão estérica. É possível combinar ambos os mecanismos, utilizando um surfactante com terminais com carga, resultando em uma repulsão eletroestérica.

A repulsão eletrostática ocorre quando a superfície das NPs está carregada (negativa ou positivamente) com cargas de mesmo sinal. A superfície das IONs apresenta grupos hidroxilas (-OH), que são suscetíveis ao pH do meio em que estão dispersas. Dessa forma, é possível estabilizá-las a partir da alteração do pH do meio. A partir de uma titulação potenciométrica, é possível determinar o pH em que a superfície das NPs está carregada e seu ponto de carga zero (*point of zero charge* - PZC). Para os óxidos de ferro, tem-se que PZC está entre 6 – 8 e nessa faixa de pH as NPs floculam rapidamente. Abaixo dessa faixa, ocorre a protonação dos grupos hidroxilas, resultando em IONs com carga superficial positiva. Acima do pH_{pzc}, o grupo -OH está desprotonado e as IONs adquirem carga negativa. Em ambos os casos, o fluido magnético obtido, denominado fluido magnético iônico, é estável. Contudo, para aplicação biológica, é necessário que o meio de dispersão tenha pH próximo ao pH fisiológico, em torno de 7,4. Nessa faixa, as NPs floculam, de forma que a estabilização eletrostática não pode ser utilizada para aplicação *in vivo* (M. A. G. Soler *et al.*, 2011; Begin-Colin; Felder-Flesch, 2012; Nunes *et al.*, 2014).

O outro método de estabilização consiste na ancoragem de moléculas ou polímeros, chamados de surfactantes, na superfície das IONs que preservem suas propriedades, evitem sua oxidação e a aproximação das partículas por impedimento estérico. Os surfactantes geralmente possuem um grupo terminal capaz de se ligar à superfície da NP e uma cauda que interage com o dispersante, evitando aproximação das IONs. Os fluidos obtidos nesse processo são denominados fluidos magnéticos surfactados (Viali, 2009; Viali *et al.*, 2010). No caso da aplicação biológica *in vivo*, além de garantir a estabilização do coloide em meio fisiológico, o surfactante escolhido deve também ser biocompatível; apresentar sítios disponíveis para ancoragem de ativos, como, por exemplo, fármacos, anticorpos e marcadores; retardar a absorção e posterior eliminação das IONs pelo sistema reticuloendotelial e favorecer a biodistribuição, ou seja, aumentar o tempo de retenção das IONs no organismo. Além disso, os surfactantes podem ser específicos para um determinado tecido ou célula, de forma que o nanocarreador seja direcionado ao seu local de ação.

3.5. Ácido láurico

O ácido láurico (AL) ou dodecanóico ($CH_3(CH_2)_{10}COOH$), é um ácido graxo de cadeia média, saturado, anfifílico, composto por 12 carbonos (Figura 7). É um surfactante aniônico, utilizado em indústrias farmacêuticas, alimentícia (principal ácido graxo do óleo de coco) e cosmética, não sendo tóxico em baixas concentrações (Mamani *et al.*, 2013). Além de ser biocompatível, possui capacidade antifúngica e antimicrobiana (Nakatsuji *et al.*, 2009). Devido às suas características, tem sido utilizado como cobertura de NPs na forma de bicamada para promover a estabilização e dispersão em meio aquoso (Chaves, 2008; Herrera *et al.*, 2015), e incorporação de fármacos hidrofóbicos (Saldanha, 2012; Santos, 2012; Afiune, 2019).

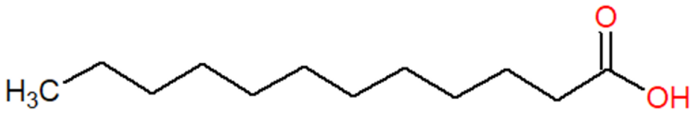

Figura 7. Fórmula estrutural do ácido láurico. Ilustração da autora.

Para obter um FM aquoso, a funcionalização da ION com AL deve ser realizada com uma bicamada e ocorre em duas etapas. Inicialmente, as IONs são cobertas com uma monocamada do ácido por meio da quimissorção, onde o grupo carboxilato se liga aos átomos de ferro, adquirindo um caráter hidrofóbico. Em seguida, ocorre a fisissorção do surfactante na monocamada, por Força de London (interação dipolo induzido-dipolo induzido) adicionando mais uma camada de AL, formando a bicamada, com o grupo carboxilato em contato com o meio. Dessa forma, o nanocarreador formado possui uma região hidrofóbica, onde é possível incorporar moléculas de mesmo caráter, e uma região hidrofílica, possibilitando a suspensão em meio aquoso (Silva, 2017; Afiune, 2019).

3.6. Dodecilamina

A dodecilamina ($CH_3(CH_2)_{11}NH_2$) é uma amina de cadeia média, saturada e anfifílica, composta por 12 carbonos, conforme a ilustração apresentada na Figura 8. É um surfactante catiônico, possui atividade bactericida e não é toxico em baixas concentrações e pode ser utilizado como sítio para ancoragem de fármacos hidrofóbicos (Mokashi *et al.*, 2020; Han *et al.*, 2022).

Figura 8. Fórmula estrutural da dodecilamina. Ilustração da autora.

Devido às suas propriedades, a DDA tem sido utilizado na funcionalização de nanocompósitos de carbono e óxido de grafeno, na forma de monocamada, aumentando sua estabilidade e dispersão em solventes orgânicos e matrizes poliméricas (Ferreira *et al.*, 2017; Alkhouzaam; Qiblawey, 2021). Enquanto que, a funcionalização com uma bicamada do surfactante permite a dispersão dos nanosistema em meio aquoso, além servir como um sítio para ancoragem de moléculas hidrofóbicas, como fármacos (Aslam *et al.*, 2007; Qurrat-ul-Ain; *et al.*, 2020).

3.7. Pluronic F127

O Pluronic® é um copolímero em blocos, anfifílico e não iônico, com estrutura do tipo PEO-PPO-PEO, sendo o poli(óxido de etileno) (PEO) a porção hidrofílica e o poli(oxido de proprileno) (PPO) a porção hidrofóbica (Py-Daniel *et al.*, 2016).

O Pluronic F127 (PLU) faz parte desse grupo de copolímeros e é formado por 100 unidades repetidas em sequência de PEO nas extremidades e 65 unidades de PPO (Figura 3). Além de promover a estabilização das IONs em meio aquosos sem alterar as propriedades magnéticas, possibilita a ancoragem de moléculas hidrofóbicas nos nanocarreadores (Jain *et al.*, 2005; Morales *et al.*, 2005). O PLU é um copolímero não toxico, biocompatível, biodegradável e foi aprovado pela FDA

(Food and Drug Administration – Estados Unidos) (Diniz *et al.*, 2015; Gomes *et al.*, 2018). Essas características fazem com que o copolímero seja ideal para a cobertura das NPs para aplicações em meio fisiológico.

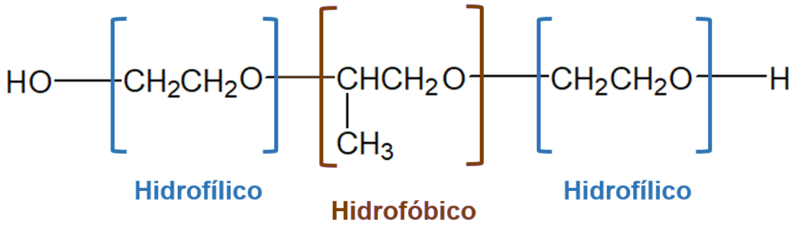

$$\mathrm{HO}-\left[\mathrm{CH_2CH_2O}\right]-\left[\underset{\mathrm{CH_3}}{\mathrm{CH}}\mathrm{CH_2O}\right]-\left[\mathrm{CH_2CH_2O}\right]-\mathrm{H}$$

Figura 9. Fórmula estrutural do Pluronic F127. Ilustração da autora.

Para a funcionalização das IONs com o copolímero, é necessário primeiramente inserir uma monocamada de um surfactante em sua superfície, como o ácido oleico por exemplo, de forma que elas adquiram um caráter hidrofóbico. Depois, adiciona-se o PLU, que se liga à monocamada por forças de London pela bloco PPO e os blocos PEO ficam em contato com o meio, tornando possível a sua dispersão em meio aquoso, conforme apresentado na ilustração da Figura 10 *(Jain et al.*, 2005; Jain, *et al.*, 2009). Neste estudo a primeira monocamada será de ácido láurico.

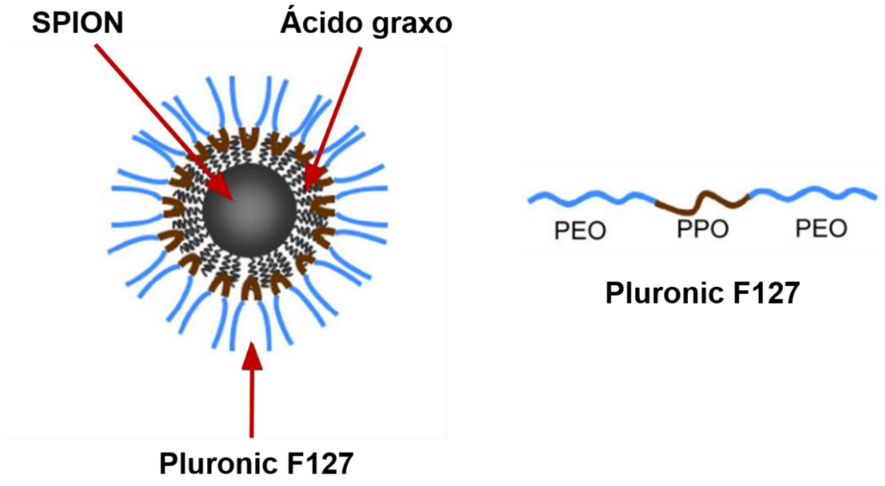

Figura 10. Ilustração de uma SPION funcionalizada com bicamada de ácido oleico e Pluronic. Adaptada de Jain *et al*., 2009.

CAPÍTULO 4

NANOCARREADORES: SÍNTESE E CARACTERIZAÇÃO

Os nanocarreadores foram sintetizados pelo método de coprecipitação em meio aquoso. O sólido formado por NPs de magnetita foi submetido à oxidação obtendo-se as NPs de maguemita que foram funcionalizadas com bicamadas de ácido láurico, ácido láurico/dodecilamina e ácido láurico/Pluronic F127.

4.1. Materiais

Para a síntese e funcionalização das nanopartículas de óxido de ferro foram utilizados: cloreto de ferro (II) tetrahidratado ($FeCl_2.4H_2O$), cloreto de ferro (III) hexahidratado ($FeCl_3.6H_2O$), hidróxido de sódio (NaOH), ácido clorídrico (HCl), ácido láurico ($C_{12}H_{24}O_2$), dodecilaminda ($C_{12}H_{27}N$) e Pluronic F127. Todos os reagentes foram adquiridos da Sigma-Aldrich e utilizados sem tratamento prévio. Toda a água utilizada neste trabalho foi ultrapura.

4.2. Síntese das nanopartículas de óxido de ferro

Os nanocarreadores foram obtidos utilizando as seguintes etapas: (i) síntese da magnetita; (ii) oxidação para obtenção das NPs de maguemita; (iii) funcionalização com monocamada de ácido láurico e (iv) funcionalização com a bicamada, obtendo-se 3 suspensões coloidais em meio aquoso, conforme ilustrado na Figura 11, e descrição a seguir.

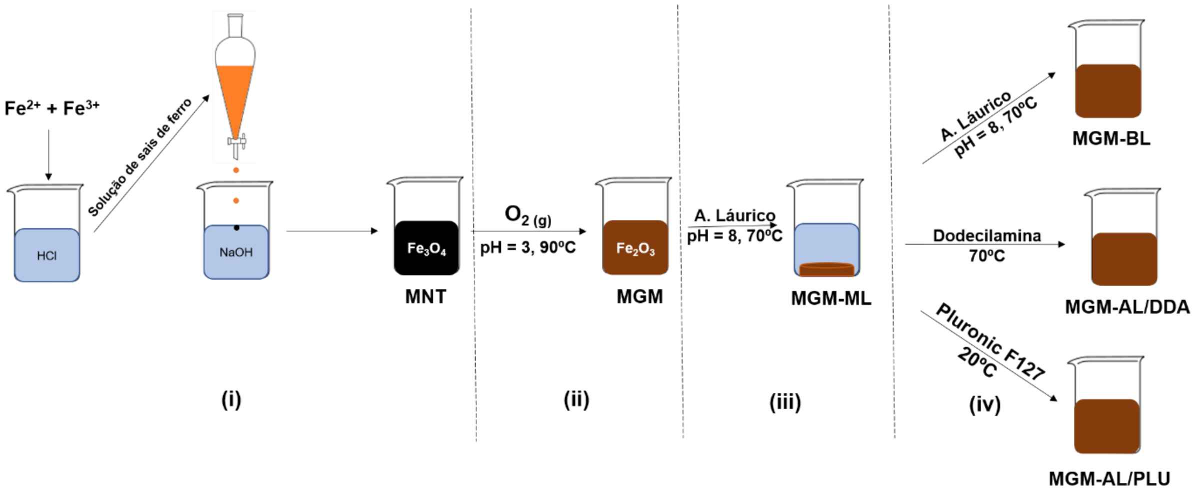

Figura 11. Representação esquemática do processo de síntese e funcionalização das IONs. Ilustração da autora.

4.2.1. Síntese da magnetita

As NPs de magnetita, Fe_3O_4, foram obtidas por meio da coprecipitação em meio aquoso alcalino dos íons Fe^{2+} e Fe^{3+}, em proporções estequiométricas 1:2. Inicialmente, 0,0225 mol de $FeCl_2.4H_2O$ e 0,045 mol $FeCl_3.6H_2O$ foram dissolvidos em 150mL de uma solução 0,08 mol.L^{-1} de ácido clorídrico (HCl). Essa mistura foi adicionada, gota a gota, em 150 mL de uma solução de hidróxido de sódio (1,5 mol.L^{-1}), à velocidade constante, sob agitação mecânica (700 rpm) e à temperatura ambiente. Observou-se imediatamente a formação de um precipitado preto, evidenciando os processos de nucleação e crescimento das nanopartículas de magnetita (Letti, 2017; Letti *et al.*, 2017). Após adição total da solução de sais de ferro, a amostra ficou sob agitação por 30 minutos, à temperatura ambiente. Em seguida, sólido preto e magnético formado foi isolado do sobrenadante por decantação magnética, lavado com água ultrapura 5 vezes para remoção de impurezas, ressuspenso em água, e o pH foi ajustado para 3 com uma solução de HCl (2,0 mols.L^{-1}). Em seguida, o fluido obtido foi sonicado por 10 minutos para quebra de aglomerados (amplitude de 40% e pulso de 5 segundos on e 5 segundos off). Uma alíquota desse material, denominado MNT, foi seca no SpeedVac Concentrator para caracterização e a outra parte foi submetida ao processo de oxidação por borbulhamento de oxigênio para obtenção das nanopartículas de maguemita, $\gamma\text{-}Fe_2O_3$ (Viali *et al.*, 2010).

4.2.2. Síntese da maguemita

As nanopartículas de maguemita foram obtidas a partir da oxidação da magnetita por borbulhamento de oxigênio (Alcantara, 2007; Viali, 2009; Afiune, 2019). O precursor, suspenso em água deionizada (pH = 3), foi submetido a aquecimento a 90ºC com borbulhamento de oxigênio (fluxo de 1 $L.min^{-1}$), sob agitação magnética por 3 horas, resultando na oxidação do Fe^{2+} para Fe^{3+}, e obtenção da suspensão de nanopartículas de maguemita. Após o resfriamento, a suspensão foi centrifugada (4.000 rpm, 10 minutos, temperatura ambiente). Uma alíquota, denominada MGM, foi seca no SpeedVac Concentrator para caracterização e o restante da amostra foi funcionalizada.

Figura 12. Nanopartículas de maguemita, suspensas em água deionizada.

4.3. Funcionalização das nanopartículas de maguemita

4.3.1. Funcionalização com monocamada de laurato

As NPs de maguemita recém obtidas foram aquecidas até 75 ºC e o pH foi ajustado para 8 sob agitação magnética. Em seguida, adicionou-se lentamente 5,1 mmols de AL, mantendo-se o pH sempre em torno de 8 em agitação por 30 minutos, resultando em NPs funcionalizadas com uma monocamada de laurato. A formação da primeira camada foi evidenciada pela dispersão de uma alíquota das IONs em n-hexano (Figura 13).

As IONs funcionalizadas foram separadas com o auxílio de um imã e foram lavadas 5 vezes com água deionizada quente para remoção de excesso de AL. Uma alíquota desse material, nomeado MGM-AL, foi seca no SpeedVac Concentrator para caracterização e o restante foi dividido em 3 partes para funcionalização com ácido láurico, dodecilamina ou Pluronic F127.

Figura 13. Nanopartículas funcionalizadas com monocamada de AL, suspensas em hexano (fase a); fase (b) meio aquoso.

4.3.2. Funcionalização com a bicamada de laurato/laurato

Nesta etapa, NPs funcionalizadas com uma monocamada de AL foram suspensas em 100 mL de água. A suspensão foi aquecida a cerca de 75 ºC e o pH foi ajustado para aproximadamente 8. Adicionou-se lentamente AL (2,7 mmols), observando-se a suspensão das IONs na fase aquosa, para a formação da segunda camada, hidrofílica. A suspensão foi mantida sob agitação por 1 hora à 75 ºC. O fluido obtido foi dialisado em membrana semipermeável por 48 horas para remoção do excesso de ácido láurico e centrifugado para remoção de aglomerados. O sobrenadante coletado foi nomeado MGM-BL e o pH foi ajustado para 7,4.

Figura 14. Nanopartículas funcionalizadas com bicamada de AL em meio aquoso (fase b). Fase (a) hexano.

4.3.3. Funcionalização com a bicamada de laurato/dodecilamina

O procedimento adotado foi semelhante à associação da segunda camada de ácido láurico (AL). NPs funcionalizadas com uma monocamada de AL foram suspensas em 100 mL de água. Após aquecimento a 75 ºC, adicionou-se lentamente dodecilamina (2,3 mmols) observando-se a precipitação das NPs. Após 10 minutos de agitação, observou-se a dispersão das nanopartículas no meio aquoso, evidenciando a formação da bicamada. A suspensão foi mantida sob agitação por 1 hora a 75 ºC e. O fluido foi dialisado por 24 horas para remoção do excesso de DDA e, após ajuste do pH para 4,80, centrifugado para remoção de aglomerados. O sobrenadante coletado foi nomeado MGM-AL/DDA.

4.3.4. Funcionalização com a bicamada de laurato/Pluronic F127

Neste caso, as NPs funcionalizadas com uma monocamada de AL foram suspensas em 100 mL de água e adicionou-se lentamente PLU (3,3 10^{-5} mol), observando-se a suspensão das IONs na fase aquosa até que a formação da segunda camada seja evidenciada. A suspensão ficou sob agitação por 48 horas à temperatura ambiente e o pH foi ajustado para 7,4. O fluido foi centrifugado para remoção de aglomerados e nomeado MNT-AL/PLU.

4.4. Técnicas de caracterização

A técnica de microscopia eletrônica de transmissão (MET) foi utilizada para analisar a morfologia, o diâmetro médio e a dispersão de tamanho das NPs. As análises foram realizadas no microscópio eletrônico de transmissão Jeol Jim-1011 com voltagem de 80kV, no Laboratório de Microscopia Eletrônica – Instituto de Ciências Biológicas.

As micrografias foram utilizadas para medir os diâmetros das partículas utilizando o software ImageJ. Com um número grande de dados obteve-se os histogramas de distribuição de tamanho. Considerando que as nanopartículas possuem formato aproximadamente esférico, pode-se utilizar um ajuste do tipo log-normal, Equação 5, para obter o diâmetro médio ($D_{méd}$) e o desvio padrão do diâmetro (dispersão - σ).

$$\mathrm{P(D)} = \frac{1}{D\sigma\sqrt{2\pi}} e^{-\frac{\ln(\frac{D}{D_{méd}})^2}{2\sigma^2}} \qquad (5)$$

O espalhamento dinâmico de luz (EDL) foi utilizado para obter o tamanho hidrodinâmico (D_H) e o índice de polidispersão (PdI) dos nanosistemas, que depende do meio de dispersão e do surfactante utilizado na cobertura (Rivera, 2018). Além disso, essa técnica também pode ser utilizada para observar a estabilidade de uma suspensão, comparando as distribuições de tamanho obtidas em função do tempo. Já o PdI indica o grau de dispersão da amostra, de forma que, quanto menor o seu valor, mais homogênea é a distribuição de tamanho dos aglomerados.

O potencial Zeta (ζ) se refere à carga elétrica efetiva na superfície das NPs em contato com o líquido. Quanto maior for o módulo dessa carga, mais afastadas estarão as partículas, reduzindo as forças atrativas de Van der Waals, impedindo ou diminuindo a agregação das NPs. Dessa forma, o potencial Zeta pode ser relacionado com a estabilidade da suspensão (Matos, 2016).

As medidas do tamanho hidrodinâmico e do potencial zeta foram realizadas no equipamento Zetasizer (Nano ZS90, Malvern), empregando-se uma diluição 1:20 para as amostras MGM-BL e MGM-AL/PLU e uma diluição 1:100 para a amostra MGM-AL/DDA, no Laboratório de Nanobiotecnologia, no Instituto de Ciências Biológicas.

O espectro Raman está intimamente relacionado às características do material analisado, como o arranjo atômico, interações entre as moléculas, simetria cristalina e pode ser utilizado para identificação de um material específico (Soler; Qu, 2012). É uma técnica não destrutiva e geralmente não requer preparação prévia da amostra (Letti, 2013). Essa técnica pode ser utilizada para estudar as fases das NPs sintetizadas antes e depois do processo de oxidação, bem como para investigar os efeitos da interação da partícula com o meio, e com a cobertura (Morais *et al.*, 2000, 2001; Melo *et al.*, 2006; Soler *et al.*, 2007; Soler e Qu, 2012; Letti, 2017; Letti *et al.*, 2017).

Os espectros Raman foram adquiridos na configuração micro-Raman (lente objetiva com magnificação de 50x) utilizando-se o espectrômetro LabRAM HR Evolution (Horiba Scientific, Quioto, Japão), equipado com uma CCD. A excitação das amostras foi realizada com um laser de diodo com $\lambda = 532$ nm com potência de 0,3 W para evitar a degradação da amostra, na faixa de comprimento de onda de 200 a 800 cm^{-1}. As medidas foram realizadas no Laboratório Espectroscopia Ótica do Instituto de Física (UnB).

A espectroscopia no infravermelho baseia-se na absorção de radiação no infravermelho pela molécula. A molécula absorve radiação infravermelha quando a vibração de seus grupos funcionais produz um campo elétrico oscilante, provocando uma mudança em seu momento dipolo. Caso a frequência do feixe incidente seja igual à frequência de vibração de um determinado grupo, ocorrerá a absorção. Dessa forma, cada substância tem um espectro próprio e essa técnica pode ser utilizada para a identificação de moléculas (Pavia *et al.*, 2010).

Os espectros no infravermelho foram utilizados para verificar a funcionalização das IONs e a análise da interação entre a superfície da partícula e a cobertura (Herrera *et al.*, 2015). As medidas foram realizadas utilizando-se pastilhas de KBr e as leituras foram realizadas na faixa de números de onda de 400 a 4000 cm^{-1}, com resolução de 4 cm^{-1}, usando-se o equipamento FTIR Varian 640IR, no Laboratório Espectroscopia Ótica do Instituto de Física (UnB).

A concentração de ferro total de cada amostra foi obtida por espectrometria de absorção atômica (AAS), utilizando o equipamento Varian, modelo AA240FS, na Central Analítica II do Instituto de Química (UnB), após digestão ácida**.** Uma alíquota (13 µL) de cada amostra foi digerida com 2 gotas de ácido clorídrico P.A (36,46% v/v) e depois foi feita a diluição para 10 mL utilizando-se uma solução de ácido nítrico 2%. Para determinação da concentração de ferro, foi utilizada uma curva de calibração, preparada com o padrão de ferro 1000 mg/L (Sigma-Aldrich).

4.5. Resultados e discussão

A morfologia e tamanhos das IONs foram obtidas por meio de micrografias de MET. As Figuras 15(a), 15(b) e 15(c) apresentam imagens típicas obtidas das amostras MGM-BL, MGM-AL/DDA e MGM-AL/PLU, respectivamente. Observa-se que as IONs possuem formato aproximadamente esférico, conforme relatado na literatura para NPs sintetizadas pelo método de coprecipitação (Soler; Paterno, 2017). Os histogramas de tamanhos obtido das imagens de MET são mostrados nas Figuras 15(d), 15(e) e 15(f) (M. A. G. Soler *et al.*, 2011). A partir do ajuste dos dados, empregando-se uma distribuição log-normal, obteve-se o diâmetro médio das partículas ($D_{méd}$) igual a 6,59 (± 0,05) nm e dispersão de tamanhos (σ) igual a 0,171 (± 0,009) nm para o fluido MGM-BL, $D_{méd}$ = 6,51 (± 0,04) nm e σ = 0,187 (± 0,009) nm para MGM-AL/DDA e $D_{méd}$ = 6,44 (± 0,08) nm e σ = 0,19 (± 0,02) nm para MGM-AL/PLU.

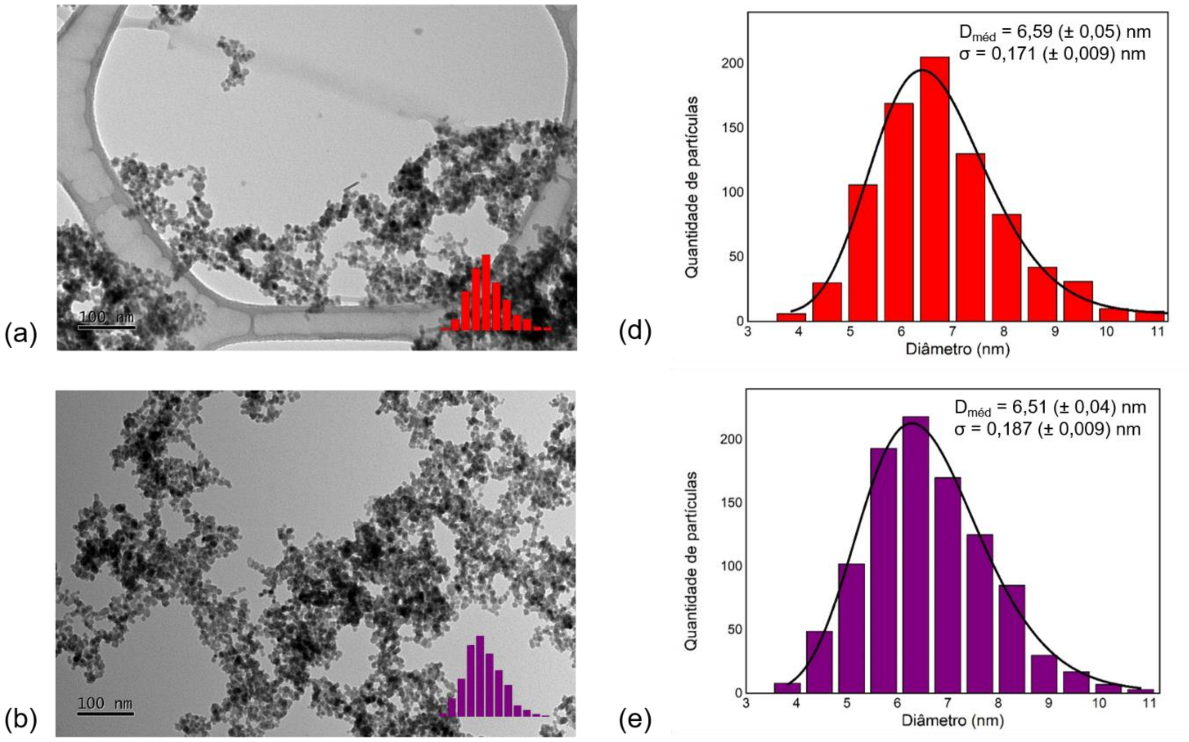

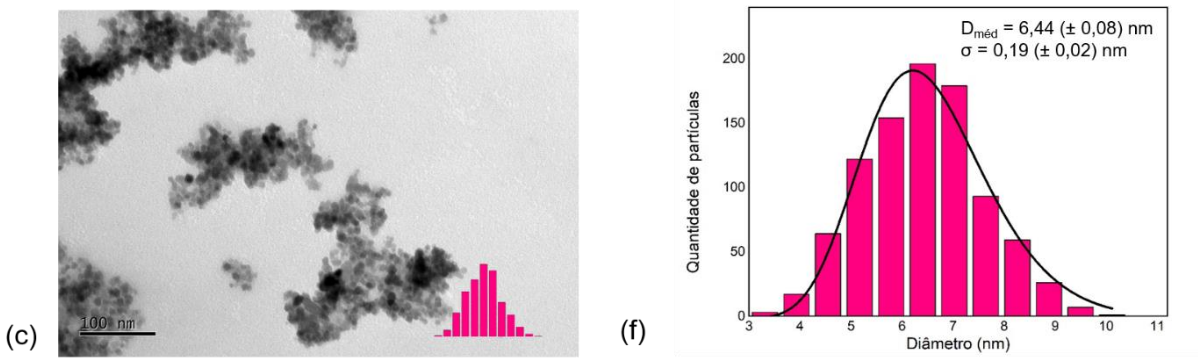

Figura 15. Micrografias típicas obtidas por MET das amostras (a) MGM-BL, (b) MGM- AL/DDA e (c) MGM- AL/PLU e histogramas de distribuição de diâmetro das amostras (d) MGM-BL, (e) MGM-AL/DDA e (f) MGM- AL/PLU.

Para a determinação do teor de ferro nas amostras por AAS, foi feita uma curva de calibração com a faixa de concentração entre 1 e 10 mg/L (Figura 16).

A análise da regressão linear na faixa de concentração analisada confirmou a linearidade da curva, cujo coeficiente de correlação linear (r) foi igual a 0,9999. Dessa forma, essa curva pode ser utilizada para determinar o teor de ferro nas amostras sintetizadas.

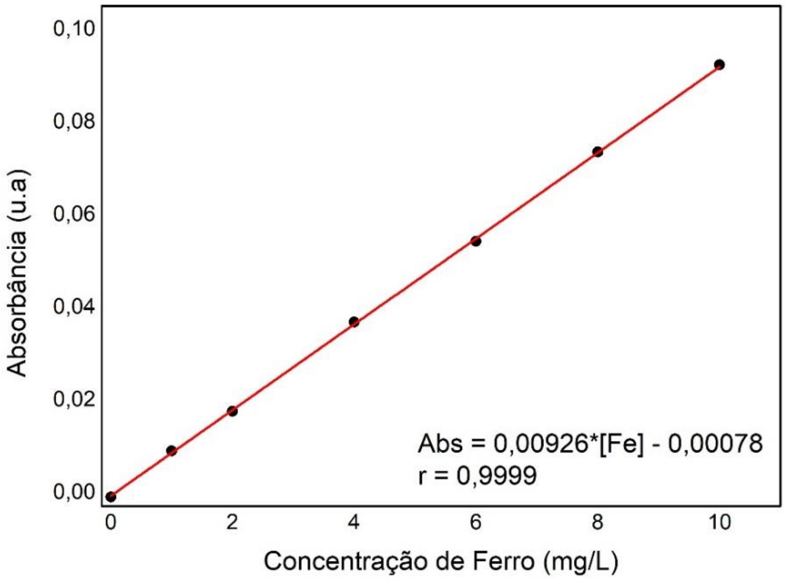

Figura 16. Curva de calibração da absorção por AAS em função da concentração de ferro. Equação da reta: y=0,00926*x - 0,00078; r = 0,9999.

A partir da absorção atômica de cada amostra e da curva de calibração, foi determinada a concentração de ferro para cada amostra. Os resultados obtidos estão na listados na Tabela 2

Tabela 2. Concentração total de ferro das amostras, obtidas por AAS.

Amostra	Concentração de Ferro (g/L)
MGM-BL	1,92 ± 0,02
MGM-AL/DDA	2,91 ± 0,01
MGM-AL/PLU	1,80 ± 0,02

Os coloides sintetizados foram monitorados por um período de 60 dias, a temperatura ambiente (25 ºC) a partir da data da síntese, visando estudar a sua estabilidade por meio de dados do tamanho hidrodinâmico (D_H), do potencial zeta (ζ) e potencial hidrogeniônico (pH). Os tamanhos hidrodinâmicos médios obtidos neste período e seus respectivos índices de polidispersão (PdI), os potenciais zeta e pH estão listados na Tabela 3.

Tabela 3. Potencial hidrogeniônico (pH), tamanho hidrodinâmico (D_H) médio, índice de polidispersão (PdI) e potencial Zeta (ζ) dos nanocarreadores sintetizados em função do tempo.

		MGM-BL		
Tempo (dias)	pH	D_H (nm)	PdI	ζ (mV)
0	7,48 ± 0,01	158,0 ± 0,9	0,18 ± 0,05	-32,5 ± 0,3
60	7,20 ± 0,01	150,6 ± 0,8	0,19 ± 0,01	- 32,8 ± 0,7
		MGM-AL/PLU		
Tempo (dias)	pH	D_H (nm)	PdI	ζ (mV)
0	7,48 ± 0,01	231 ± 1	0,14 ± 0,02	-16,4 ± 0,3
60	6,70 ± 0,01	196 ± 1	0,09 ± 0,02	- 17,9 ± 0,3
		MGM-AL/DDA		
Tempo (dias)	pH	D_H (nm)	PdI	ζ (mV)
0	4,75 ± 0,01	135 ± 1	0,17 ± 0,01	42,6 ± 0,9
60	4,72 ± 0,01	110,7 ± 0,6	0,182 ± 0,005	42 ± 1

Dados apresentados: média ± desvio padrão, n=3. ANOVA, $p<0,05$

Observa-se na Tabela 3 que o pH e índice de polidispersão das três amostras se manteve praticamente constante durante o período de análise, não apresentando diferença significativa entre os valores registrados nos 60 dias ($p>0,05$). Os PdIs obtidos estão dentro do esperado para amostras sintetizadas por coprecipitação e indicam uma amostra com baixa polidispersividade. Já o tamanho hidrodinâmico apresentou uma leve redução no valor ($p < 0,005$), indicando que houve a precipitação das nanopartículas maiores, porém a maior parte da amostra se manteve estável.

Durante o período de análise, o potencial zeta do coloide MGM-BL se manteve abaixo de - 30 mV, de forma que a amostra pode ser considerada estável por repulsão eletrostática (Matos, 2016). A carga superficial negativa indica que o grupo carboxila do ácido láurico está desprotonado no pH de análise (7,5). Os resultados obtidos de D_H, PdI e potencial zeta para a amostra MGM-BL no período avaliado reafirmam a alta estabilidade das IONs cobertas com BL, havendo relato da sua estabilidade por 90 dias, à temperatura ambiente e a 10 ºC (geladeira), não apresentando diferenças significativas desses parâmetros (Afiune *et al.*, 2020).

O Pluronic F127 é um copolímero não iônico, ou seja, não apresenta carga, de forma que a estabilidade da amostra MGM-AL/PLU é promovida majoritariamente por repulsão estérica e deve ser analisada a partir do D_H. Apesar disso, obteve-se um potencial zeta negativo para a amostra MGM-AL/PLU. Isso pode ter ocorrido por causa da funcionalização das NPs previamente com uma monocamada de ácido láurico. Devida a formação da primeira e segunda camada de AL serem sequencial e nas mesmas condições de reação, muitas vezes não é possível separá-las. O potencial negativo indica que houve uma funcionalização parcial com uma bicamada de AL.

Já o coloide MGM-AL/DDA apresentou potencial superior a 30 mV durante o período analisado, de forma que ele também pode ser considerável estável por repulsão elétrica. A carga positiva indica que o grupo amina da dodecilamina está protonado no pH analisado, 4,8.

Para analisar a fase das IONs após síntese e oxidação, utilizou-se a espectroscopia Raman. O espectro Raman obtido da amostra MGM é mostrado na Figura 17. A linha em vermelho corresponde ao ajuste gerado por funções lorentzianas, as linhas em verde correspondem aos modos vibracionais Raman previstos para a fase maguemita (MGM).

A partir dos valores obtidos do ajuste e daqueles previstos pela teoria para o material bulk cristalino e nanoparticulados disponíveis na literatura, pode-se associar os picos observados na Figura 17 aos seguintes modos vibracionais característicos da fase MGM 363 (T_{2g}), 504 (E_g) e 706 (A_{1g}) cm^{-1}, indicando que síntese e a oxidação foram efetivas (Viali, 2009; Letti, 2013; Afiune, 2019).

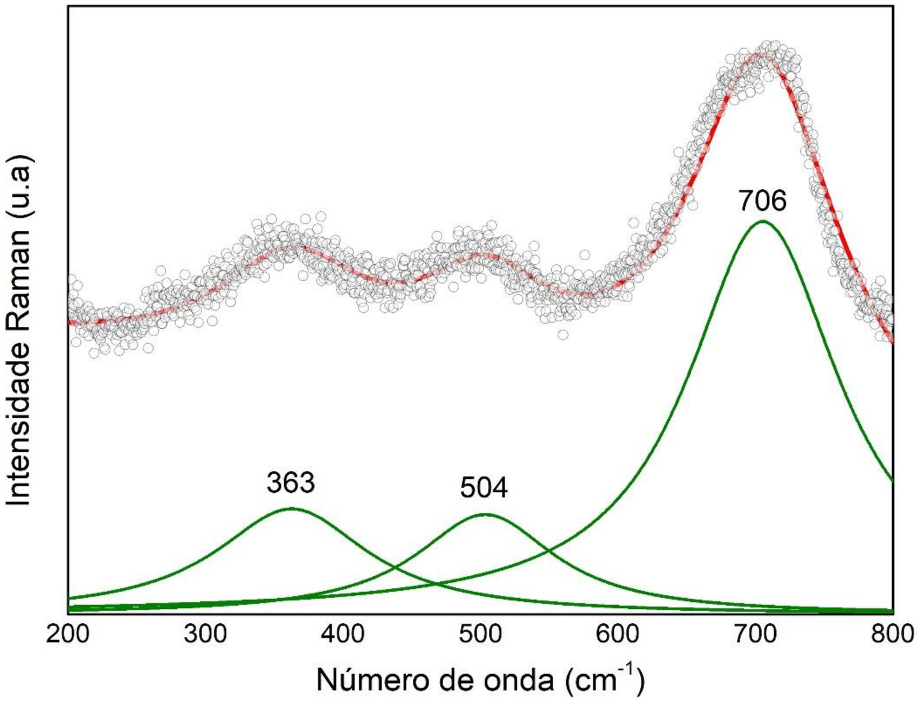

Figura 17. Espectro Raman obtido da amostra maguemita sintetizada.

Para avaliar a funcionalização das IONs e determinar a interação entre as camadas dos surfactantes e a nanopartícula, foram realizadas as análises dos espectros de infravermelho dos três nanocarreadores obtidos, além dos surfactantes puros.

Os espectros IV do AL puro, das amostras MGM-ML e MGM-BL estão apresentados na Figura 18. Observa-se que o espectro do AL apresenta as bandas características de um ácido carboxílico, como a absorção O-H, uma banda larga que ocorre na região 3600 a 3200 cm^{-1}, as bandas de estiramento assimétrico $\nu_a CH_3$ em 2960 cm^{-1} e $\nu_a CH_2$ em 2920 cm^{-1}, os estiramentos simétricos $\nu_s CH_3$ em 2870 cm^{-1} e $\nu_s CH_2$ em 2850 cm^{-1}, a vibração de dobramento da rotação do $\delta(CH_2)$ no plano em 719 cm^{-1}, que está associado com a presença de pelo menos quatro CH_2 em uma cadeia aberta, denominada banda de cadeia longa, e o estiramento C=O em 1701 cm^{-1} (Pavia *et al.*, 2010; Herrera *et al.*, 2015).

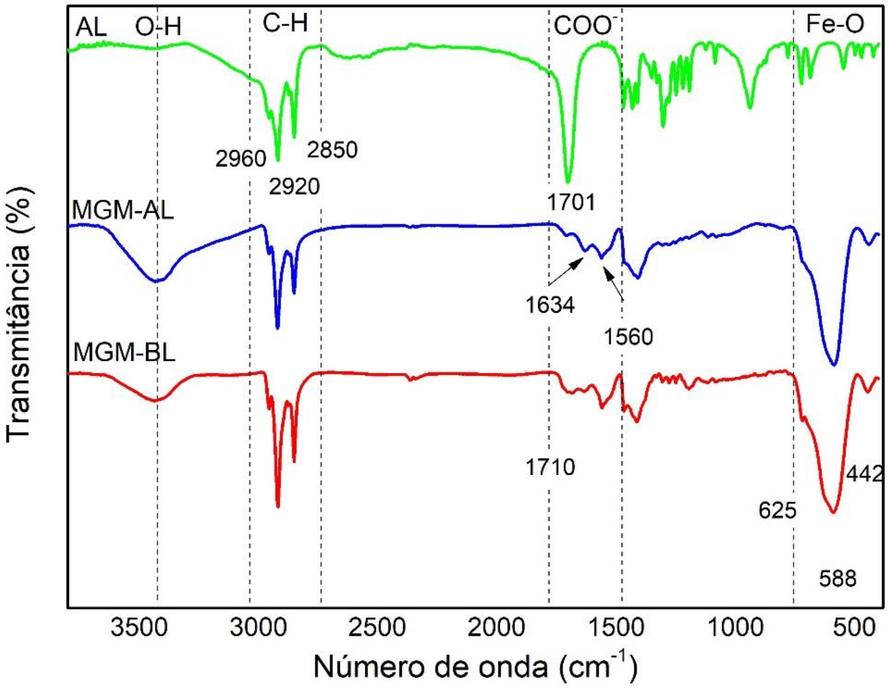

Figura 18. Espectro infravermelho obtido das amostras AL (em verde), MGM-AL (em azul) e MGM-BL (em vermelho).

No espectro das amostras MGM-BL e MGM-AL (Figura 18), observa-se os picos atribuídos aos estiramentos da ligação Fe-O de óxidos de ferro em 442, 588 e 625 cm^{-1}. Como ambas as amostras foram funcionalizadas apenas com ácido láurico, não há diferença considerável entre os espectros.

A funcionalização com laurato da superfície das NPs nas amostras MGM-AL e MGM-BL é sugerida devido à presença das vibrações associadas aos estiramentos de CH_2 e CH_3, observadas em ambos os espectros sofrendo pequenas alterações em relação ao AL puro, como a ausência do modo vibracional correspondente à carbonila (C=O) e o surgimento de duas novas estruturas em 1634 e 1560 cm^{-1}, que correspondem aos modos de vibração do carboxilato assimétrico $\nu_a(COO^-)$ e simétrico $\nu_s(COO^-)$, respectivamente. A diferença de comprimento de onda entre as vibrações $\nu_a(COO^-)$ e $\nu_s(COO^-)$ pode ser utilizada para determinar o tipo de interação que ocorre entre os carboxilatos e os metais (Deacon; Phillips, 1980; Herrera *et al.*, 2015; Afiune, 2019). No caso desta amostra obteve-se uma diferença de 74 cm^{-1}, o que indica uma ligação entre o ferro e o carboxilato do tipo bidentada quelante (Figura 19).

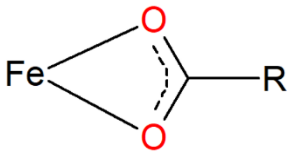

Figura 19. Representação de uma coordenação bidentada quelante. Ilustração da autora.

Os espectros de infravermelho do DDA puro e das amostras MGM-AL e MGM-AL/DDA estão apresentados na Figura 20. No espectro da amostra DDA observa-se as bandas características da cadeia de hidrocarbonetos da dodecilamina entre 2920 e 2852 cm^{-1}. O pico em torno de 3300 cm^{-1} deve-se ao estiramento da ligação N-H. Os picos em 1570 a 1650 cm^{-1} são devido aos modos de dobramento do N-H, enquanto o pico em 1320 cm^{-1} deve-se ao estiramento C-N (Pavia *et al.*, 2010). No espectro da amostra MGM-AL/DDA é possível observar o surgimento de uma banda larga na faixa de 1580 cm^{-1}, que pode estar relacionada com a deformação da ligação N-H. O pico referente ao estiramento da ligação N-H foi encoberto pela banda do estiramento da ligação O-H, uma vez que estas regiões se sobrepõem (Pavia, 2013). A amostra também apresenta os picos característicos da ligação Fe-O entre 628 e 443 cm^{-1}.

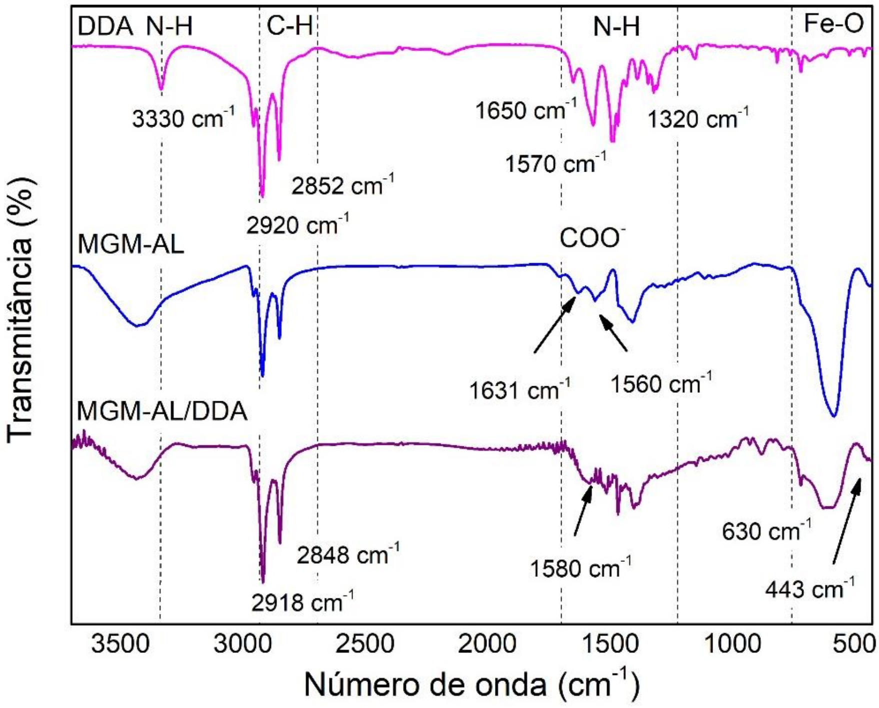

Figura 20. Espectro infravermelho obtido das amostras DDA (em rosa), MGM-AL (em azul) e MGM-AL/DDA (em roxo).

Na Figura 21 é possível observar um deslocamento dos picos referentes aos estiramentos simétrico e assimétrico do grupo CH_2 no espectro da amostra MGM-AL/DDA, em comparação com as amostras DDA e MGM-AL. Esse deslocamento pode estar relacionado com a interação (do tipo dipolo induzido) entre as cadeias de hidrocarbonetos do ácido láurico e da dodecilamina, que ocorrem para a formação da bicamada, conforme se observa na Figura 22 (Kale *et al*., 2011).

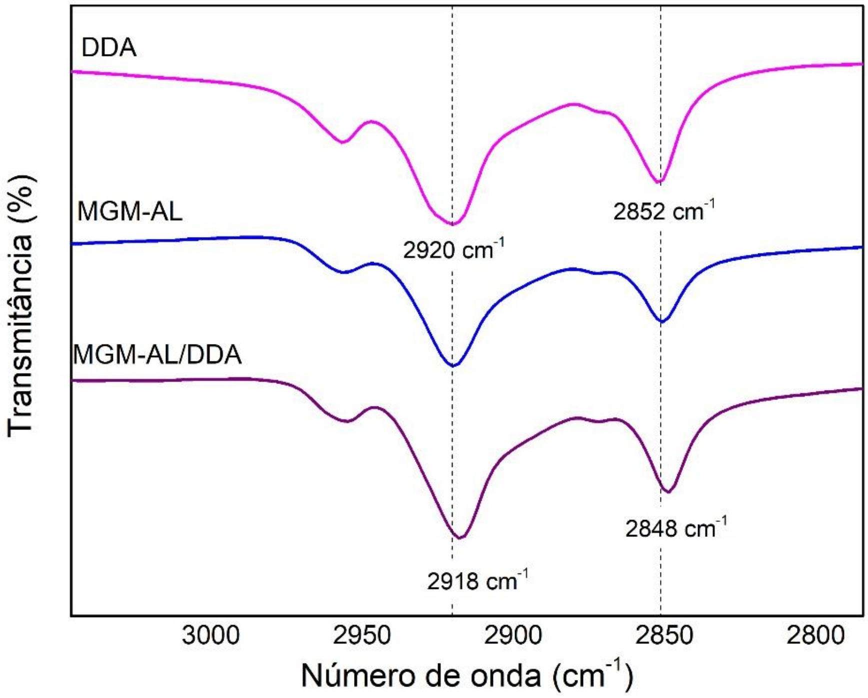

Figura 21. Ampliação dos espectros DDA, MGM-AL e MGM-AL/DDA na faixa de 3040 e 2780 cm^{-1}.

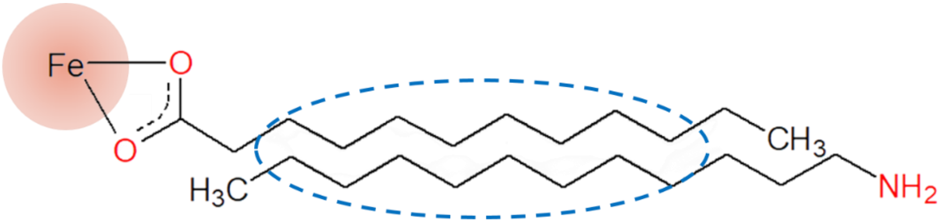

Figura 22. Interação do tipo dipolo induzido entre as cadeias de hidrocarbonetos do ácido láurico e da dodecilamina, destacado em azul, responsável pelo deslocamento das bandas de vibração do CH_2 nos espectros de FTIR. Ilustração da autora.

Os espectros de infravermelho do PLU puro e das amostras MGM-AL e MGM-AL/PLU estão apresentados na Figura 23. O espectro do fluido MGM-AL/PLU apresenta picos correspondentes a primeira camada de AL em 1634 e 1560 cm^{-1}, que correspondentes aos modos de vibracionais $\boldsymbol{\nu}_a(\mathrm{COO^-})$ e $\boldsymbol{\nu}_s(\mathrm{COO^-})$, respectivamente, e bandas correspondentes a cadeia carbônica, tanto do PLU quanto do AL entre 2960 e 2850 cm^{-1}, que correspondem às frequências de estiramentos simétricos e assimétricos de CH_2 e CH_3. O principal indicativo da funcionalização com a segunda camada composta por PLU é o aparecimento do pico em 1110 cm^{-1}, equivalente ao estiramento do grupo éter ($\boldsymbol{\nu}$C-O-C), presente na estrutura do copolímero (Yan-lei Su *et al.*, 2002; Pavia *et al.*, 2010; Gomes *et al.*, 2018).

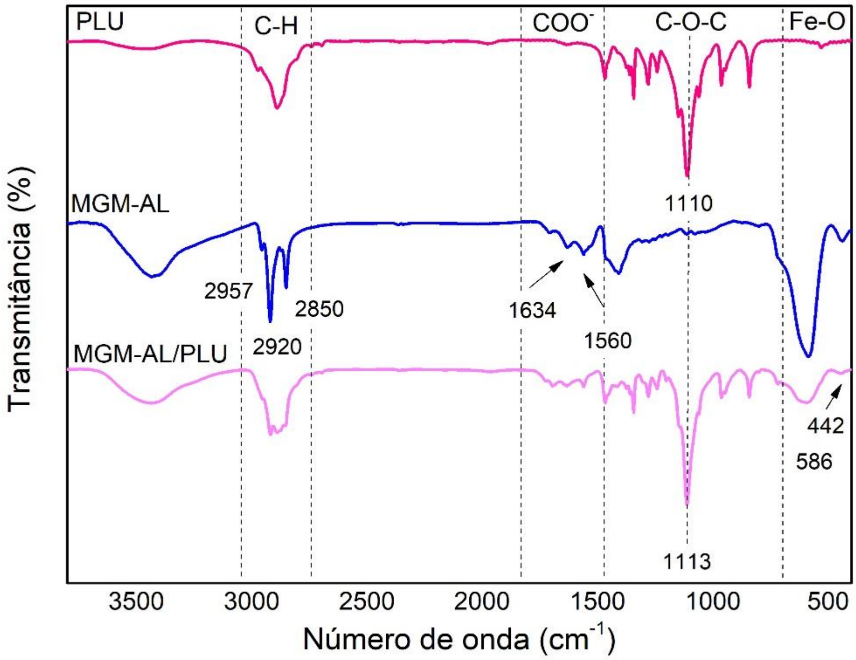

Figura 23. Espectro infravermelho obtido das amostras PLU (em pink), MGM-AL (em azul) e MGM-AL/PLU (em rosa claro).

Os modos vibracionais mais relevantes em cada amostra e seus respectivos números de onda estão identificados na Tabela 4.

Tabela 4. Modos vibracionais identificados nas amostras AL, MGM-AL, MGM-BL, PLU, MGM-AL/PLU, DDA e MGM-AL/DDA e seus respectivos números de onda.

Modo vibracional	**Número de onda (cm^{-1})**						
	AL	MGM-AL	MGM-BL	PLU	MGM-AL/PLU	DDA	MGM-AL/DDA
$\boldsymbol{\nu}$(O-H)	3445	3421	3430	3454	3440	-	3430
$\boldsymbol{\nu}$(N-H)	-	-	-	-	-	3330	-
$\boldsymbol{\nu}_a(CH_3)$	2960	2957	2957	2970	2960	2957	2957

$\nu_a(\mathrm{CH_2})$	2920	2920	2918	2890	2920	2920	2918
$\nu_s(\mathrm{CH_3})$	2872	2872	2872	-	-	2872	2872
$\nu_s(\mathrm{CH_2})$	2850	2850	2850	2856	2850	2852	2848
$\nu(\mathrm{C{=}O})$	1701	1705	1710	-	1701	-	-
$\nu_a(\mathrm{COO^-})$	-	1634	1633	-	1634	-	-
$\nu_s(\mathrm{COO^-})$	-	1560	1559	-	1560	-	-
$\delta(\mathrm{N\text{-}H})$	-	-	-	-	-	1650, 1570	1580
$\nu(\mathrm{C\text{-}O\text{-}C})$	-	-	-	1110	1113	-	-
$\nu(\mathrm{Fe\text{-}O})$	-	625, 588, 440	626, 588, 442	-	625, 588, 442	-	628, 588, 443

CAPÍTULO 5

PENETRAÇÃO CUTÂNEA

A penetração e retenção cutânea de cada nanocarreador foi analisada através do método Saarbrüecken modificado, em pele de orelha de suínos. A quantificação do ferro em cada camada da pele foi obtida através de medidas de ressonância ferromagnética.

5.1. Métodos

5.1.1. Estudo da penetração cutânea *in vitro* dos fluidos sintetizados

A penetração *in vitro* foi realizada em peles de orelha de suínos, utilizando-se o método Saarbrüecken modificado (Angelo *et al.*, 2016; Afiune, 2019). As orelhas foram adquiridas de um frigorífico local, logo após o abate e sangria, antes da escalda. Assim que chegaram ao laboratório, as orelhas foram limpas com água destilada, a pele externa foi extraída, separada do tecido subcutâneo e cortadas em círculos de aproximadamente 3 cm de diâmetro, conforme ilustrado na Figura 24. Os discos foram armazenados no congelador (-18ºC) até a realização dos experimentos (por um período de no máximo 30 dias).

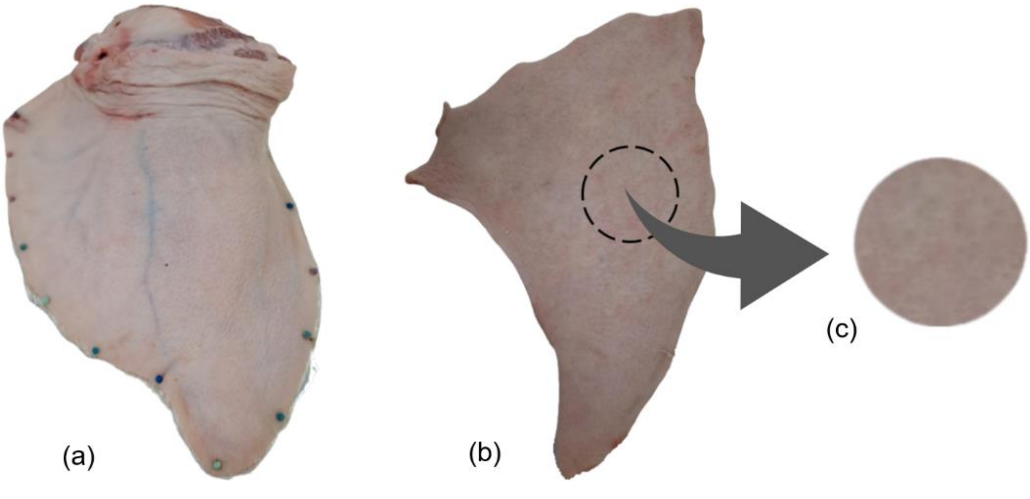

Figura 24. Imagens típicas da (a) orelha de suíno inteira, (b) pele extraída da orelha e (c) disco de pele utilizada nos experimentos de permeação *in vitro*. Ilustração da Autora.

Para os experimentos de penetração *in vitro*, as peles foram colocadas sobre um suporte, com uma cavidade preenchida com papel filtro e 600 µL de tampão fosfato-salino (PBS – do inglês phosphate-buffered saline), de pH aproximadamente 7,4, para manter a hidratação da pele, e fixadas nos compartimentos doadores de células de Franz com área de difusão igual a 2,27 cm². Esses compartimentos foram preenchidos com 1 mL do coloide, conforme ilustração apresentada na Figura 25, e mantidos por períodos de 12, 24 e 36 horas de penetração em três experimentos. Após esse período, as peles foram retiradas do suporte e o excesso de fluido magnético foi removido com água ultrapura e papel absorvente.

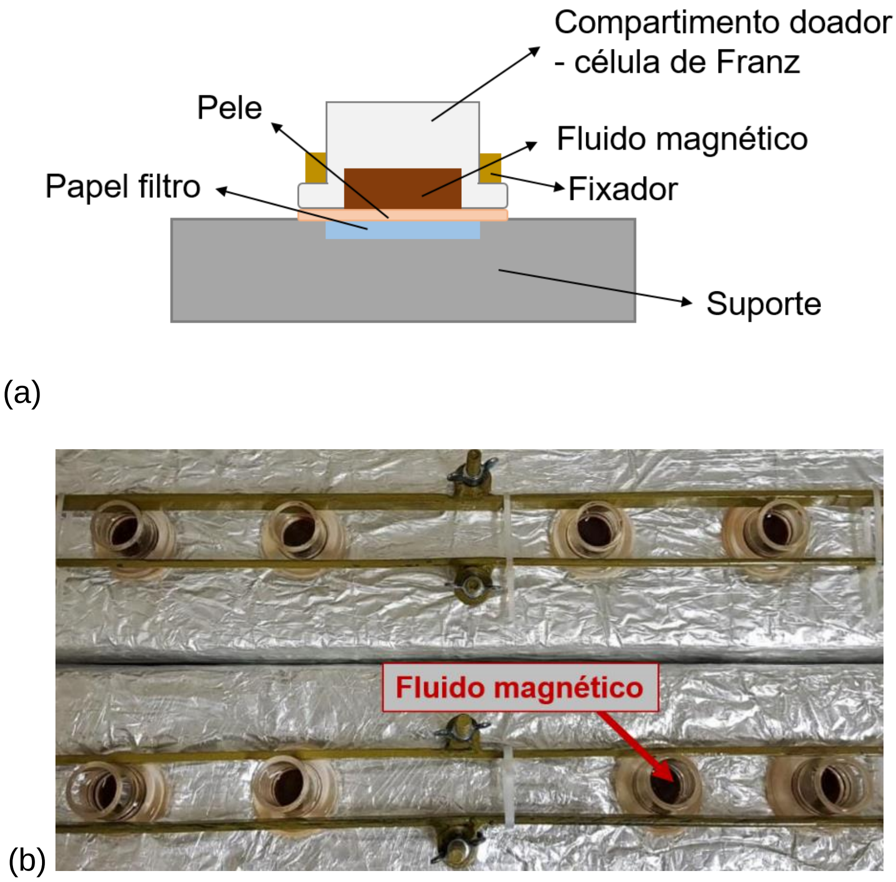

Figura 25. Ilustrações (a) da visão lateral e (b) da visão superior das amostras dispostas nos suportes para a realização do experimento de penetração cutânea. Ilustração da autora.

A Figura 26 mostra como os discos de pele ficaram após a penetração de 24h. É possível visualizar a olho nu a diferença entre a retenção de cada nanosistema.

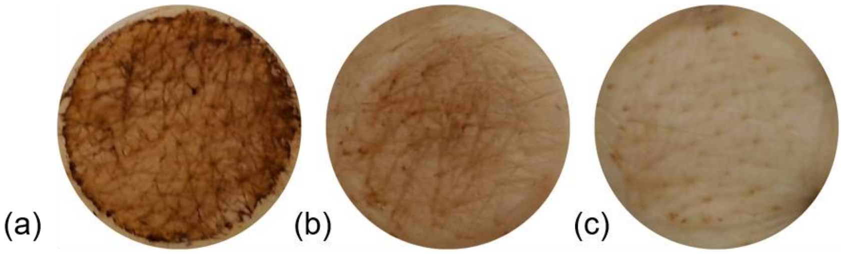

Figura 26. Discos de pele após a penetração de 24h para os fluidos (a) MGM-BL (b) MGM-AL/DDA e (c) MGM-AL/PLU. Ilustração da autora.

5.1.2. Técnica do tape stripping diferencial

As 3 camadas da pele foram extraídas por meio da técnica do tape stripping diferencial (Teichmann *et al.*, 2005; Afiune, 2019) com o auxílio de fitas adesivas (Figura 27). O estrato córneo (EC) foi removido utilizando-se 10 fitas, em movimentos a favor do crescimento do pelo. Em seguida, o folículo piloso (FP) foi removido empregando-se 2 fitas. Nessa etapa, colocou-se 1 gota de cola de cianoacrilato sobre a pele e, em seguida, a fita adesiva foi pressionada por 1 minuto sobre a gota até a cola estar completamente seca e removida em um único movimento, contrário ao crescimento do pelo. A camada de pele restante foi nomeada pele remanescente (PR).

Figura 27. Etapas da extração das camadas da pele. Ilustração da autora.

5.1.3. Preparação das amostras para a quantificação de ferro

Três seções retangulares, de aproximadamente 0,51 cm² cada, foram cortadas da área central de cada disco de camada da pele (EC, FP e PR) obtido por tape stripping, conforme a ilustração da Figura 28, e inseridas em uma seringa de 1mL. Em seguida, adicionou-se 500 µL de PBS em cada amostra e elas foram congeladas e armazenadas em nitrogênio líquido para a leitura (Afiune, 2019).

Figura 28. Preparação da amostra para as medidas de ressonância ferromagnética. A seção da pele utilizada está destacada em vermelho. Ilustração da autora.

5.1.4. Quantificação de ferro nas camadas da pele por ressonância ferromagnética.

A biodistribuição das NPs nas camadas da pele após a permeação foi obtida por meio da técnica de ressonância ferromagnética (RFM), utilizando-se o protocolo desenvolvido por Afiune *et al.* (2020). Os espectros de RFM foram obtidos no equipamento Bruker, modelo EMX Plus (Bruker, Alemanha), com frequência de micro-ondas na banda X, cavidade ressonante modelo ER4102ST, campo de modulação de 100 kHz, potência de microondas de 2 mW e campo e tempo varredura iguais a 10

Gauss e 60s, respectivamente. Utilizou-se o suporte Finger Dewar de quartzo – Noxygen (Alemanha) para análise das amostras. As medidas foram realizadas no Núcleo de Física Aplicada, Instituto de Física – UnB.

Para obter uma curva de calibração da intensidade do sinal de RFM em função da concentração e massa total de ferro, foram preparadas 6 diluições de cada um dos fluidos MGM-AL/DDA, MGM-AL/PLU e MGM-BL. Para análise no RFM, as amostras foram preparadas em 3 etapas sucessivas (i a iii), com o congelamento em nitrogênio líquido entre cada etapa: (i) preencheu-se uma seringa, de 1 mL, com 150 µL de PBS; (ii) transferiu-se 200 µL da diluição e (iii) adicionou-se mais 150 µL de PBS, completando os 500 µL, mesmo volume utilizado para preparar as seringas contendo as camadas da pele. Esse procedimento foi adotado para garantir que a porção da amostra contendo a diluição tivesse a mesma área que as amostras das camadas da pele. As curvas de calibração foram obtidas relacionando as amplitudes do sinal RFM obtidas pelo equipamento e a concentração total de ferro, obtida por AAS, ou massa total de ferro contida em cada nanosistema.

5.1.5. Análise estatística

Todos os resultados apresentados neste capítulo são expressos em média ± desvio padrão (DP) e foram analisados utilizando-se o software GraphPad Prism®. Diferenças significativas entre os dados foram obtidas por análise de variância (two-way ANOVA), e pelo teste de comparações múltiplas de Tukey. O nível de significância foi definido como $p < 0,05$ e os valores de p foram expressos conforme os diferentes níveis de significância: $p < 0,05$ (*), $p < 0,01$(**) e $p < 0,001$ (***) e $p < 0,0001$ (****).

5.2. Resultados e discussão

A Figura 29 apresenta a curva de calibração obtida para a amostra MGM-BL, correlacionando a amplitude do sinal RFM com a massa total de ferro, em µg. Esse fluido foi escolhido para fazer a curva por apresentar maior estabilidade em diluições maiores.

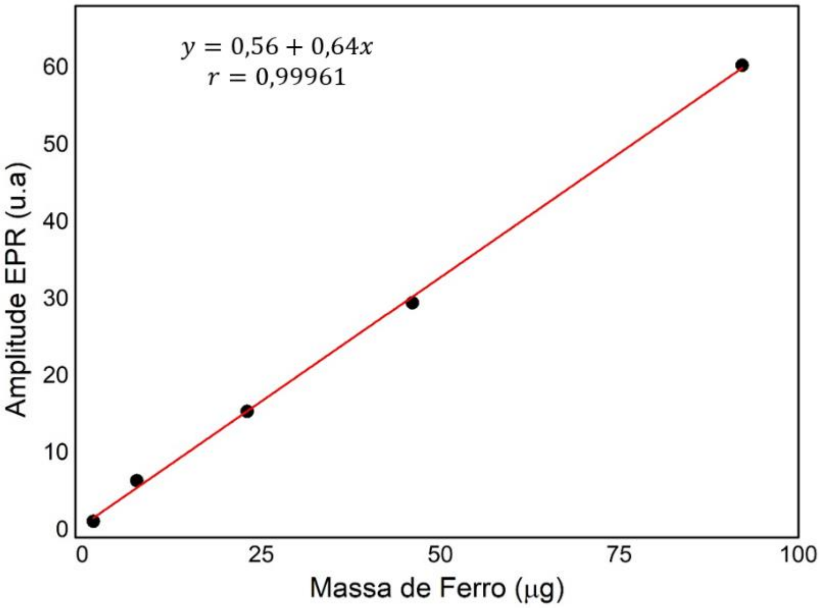

Figura 29. Curva de calibração da amplitude do sinal RFM em função da massa de ferro, em µg.

A curva apresenta um coeficiente de correlação linear, r, superior a 0,99, confirmando a linearidade da curva na faixa de concentração avaliada. A partir da equação de reta obtida, pode-se quantificar a biodistribuição das NPs nas camadas 3 da pele, estrato córneo (EC), folículo piloso (FP) e pele remanescente (PR) apresentada nas Figuras 30 e 31.

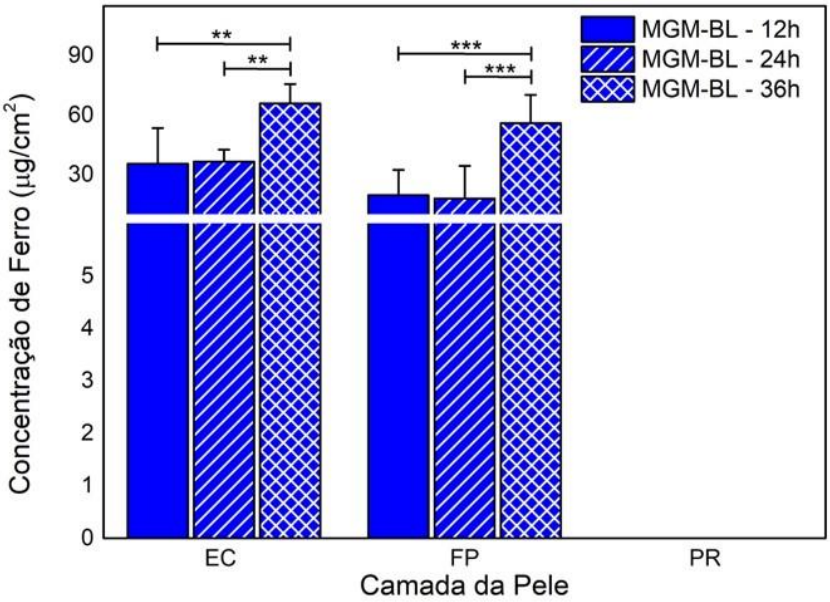

(a)

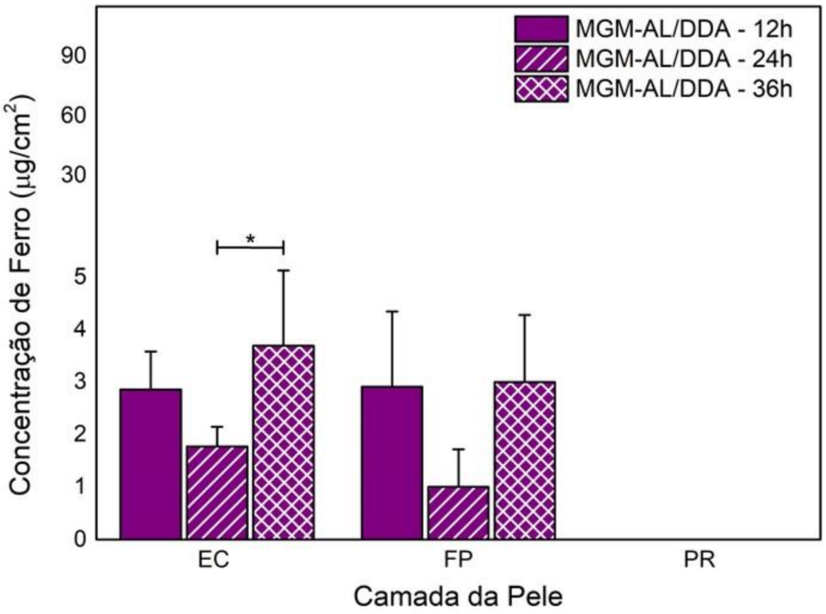

(b)

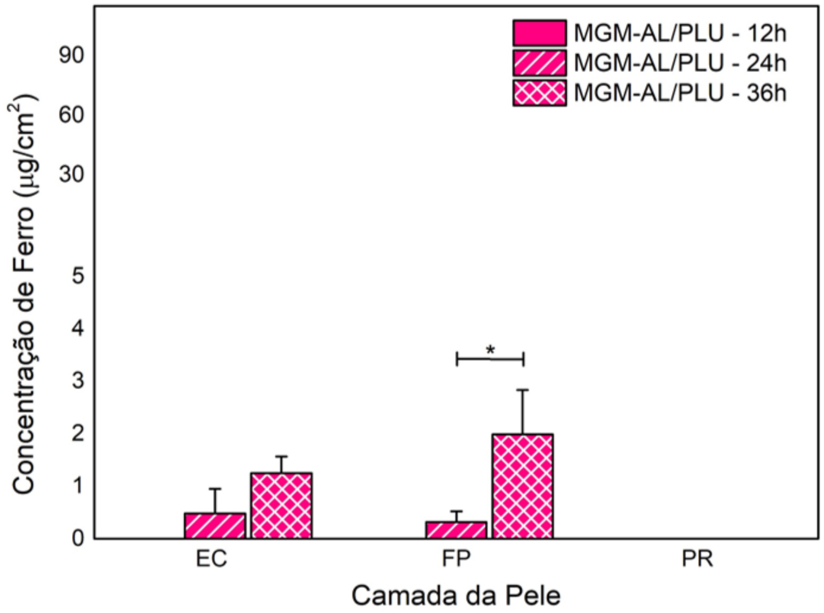

(c)

Figura 30. Quantificação da concentração de ferro, em µg/cm², retida em cada camada da pele após 12, 24 e 36h de penetração dos nanocarreadores (a) MGM-BL, (b) MGM-AL/DDA e (c) MGM-AL/PLU. Dados apresentados como média ± desvio padrão, n=6. ANOVA $p < 0,05$.

Considerando-se os dados obtidos da concentração de ferro para os 3 nanocarreadores, não foi possível determinar a concentração de ferro retida na pele remanescente, pois a razão amplitude/ruído foi elevada, de forma que o sinal não pode ser utilizado para quantificar a retenção de ferro nessa camada da pele.

No caso da amostra MGM-BL (Figura 30a), ao comparar os períodos de 12 e 24 horas de penetração cutânea, não observou-se diferença entre a quantidade de ferro retida em cada camada da pele. No entanto, comparando-se os períodos 12 e 24 horas com o de 36 horas, foi possível observar um aumento no acúmulo das NPs no EC e no FP. Em adição, não se observou diferença significativa entre a quantidade de ferro presente no EC e FP nos 3 períodos analisados.

Para o coloide MGM-AL/DDA, Figura 30b, observou-se apenas uma pequena diferença entre a concentração de ferro no EC nos períodos de 24 e 36 horas. Assim como na amostra MGM-BL, não se observou diferença entre o acúmulo de NPs no EC e no FP nos 3 intervalos de tempo analisados.

Os dados do experimento para o fluido MGM-AL/PLU, Figura 30c, mostram que não foi possível quantificar o ferro no período de 12 horas de penetração, devido à baixa amplitude do sinal, indicando que 12 horas de penetração não é o suficiente para acumular uma quantidade detectável de NPs na pele. Com 24 e 36 horas, foi possível observar a presença do nanocarreador no EC e no FP, observando-se uma diferença entre a presença no FP para os períodos de 24 e 36 horas.

Para verificar se há diferença na penetração em função da cobertura de cada nanocarreador, foram construídos 3 gráficos comparando a biodistribuição das NPs de cada fluido para cada um dos tempos estudados (Figura 31).

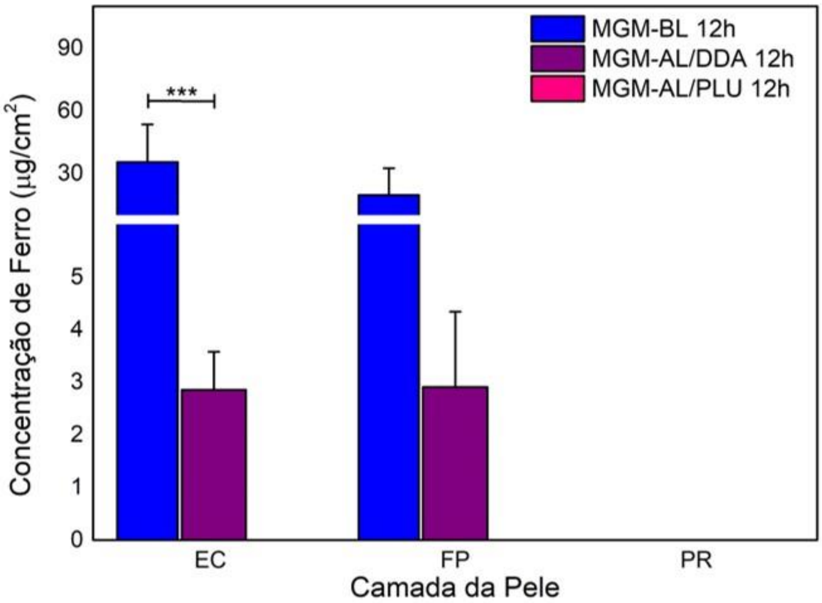

(a)

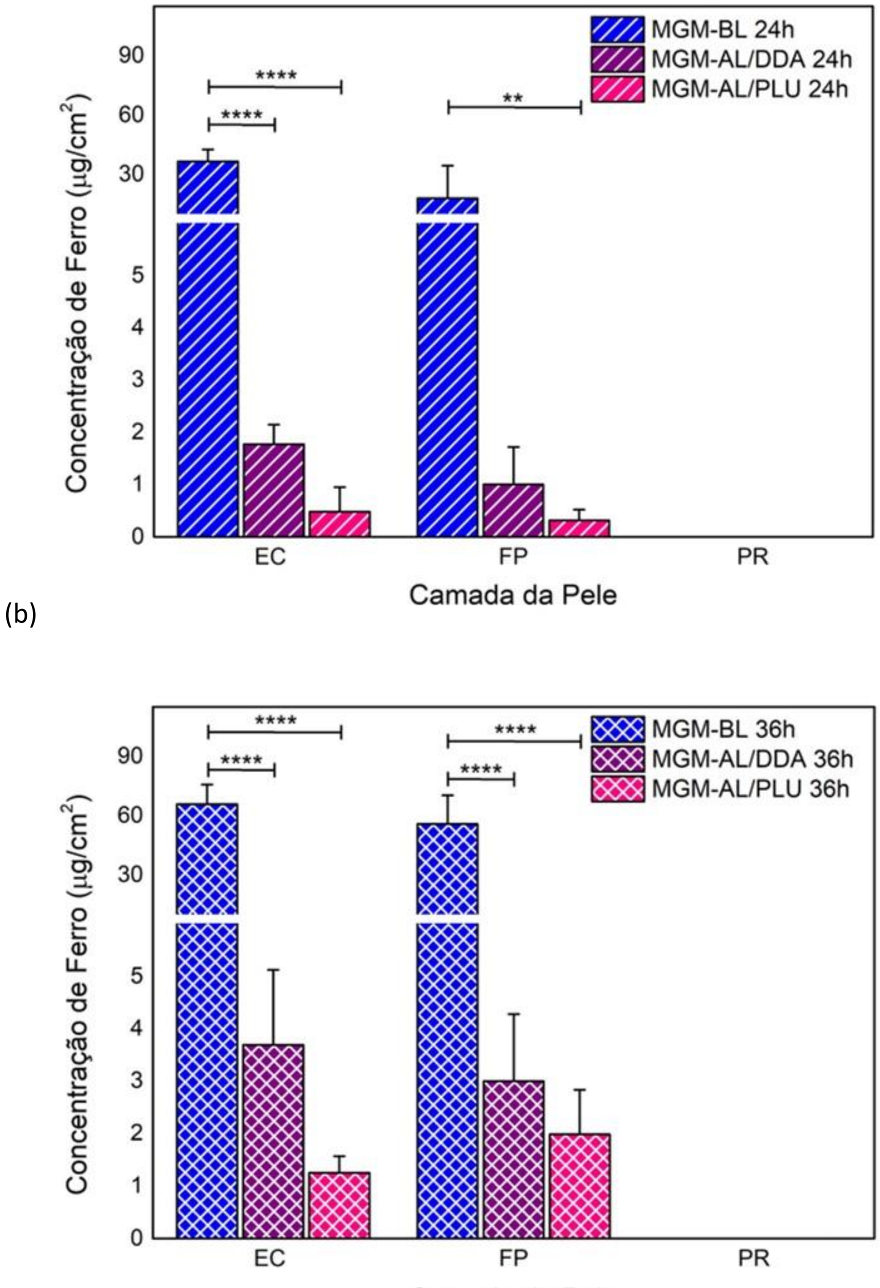

Figura 31. Quantificação da concentração de ferro, em µg/cm², retida em cada camada da pele após (a) 12h, (b) 24h e (c) 36h de penetração dos nanocarreadores MGM-BL, MGM-AL/DDA e MGM-AL/PLU. Dados apresentados como média ± desvio padrão, n=6. ANOVA p < 0,05.

Para o estudo de penetração em 12h, Figura 31 (a), identificou-se uma diferença entre o acúmulo de ferro no EC entre os fluidos MGM-BL e MGM-AL/DDA. Para a penetração de 24h, Figura 31 (b), observou-se uma diferença significativa entre a distribuição do MGM-BL no EC e no FP, comparando-se com os outros dois nanosistemas. Após 36h de penetração, observou-se um aumento significativo na diferença do acúmulo de Fe nas 2 camadas da pele entre os fluidos MGM-BL em comparação as amostras MGM-AL/DDA e MGM-AL/PLU. Comparando os 3 períodos analisados, observa-se que a quantidade de ferro acumulada em cada camada da pele é maior para o fluido MGM-BL, indicando que o ácido láurico foi o melhor potencializador da permeação para as nanopartículas sintetizadas nos parâmetros de penetração utilizados.

O fluido MGM-AL/DDA possui carga positiva e pH 4,7, na faixa do pH fisiológico da pele. A pele possui um ponto isoelétrico, ou seja, o ponto em que ela possui carga neutra, entre 4 e 4,5. Acima disso, possui um residual de carga negativo, devido à ionização dos grupos carboxílicos dos aminoácidos presentes em sua superfície (Gratieri; Gefuso; Lopez, 2008). A atração entre a carga positiva das partículas e a carga da pele pode ter gerado uma interação forte, fazendo com que as NPs estabelecessem uma barreira na superfície do EC, impedindo aproximação de outras partículas e, consequentemente, a sua penetração nas demais camadas da pele, conforme a ilustração da Figura 32.

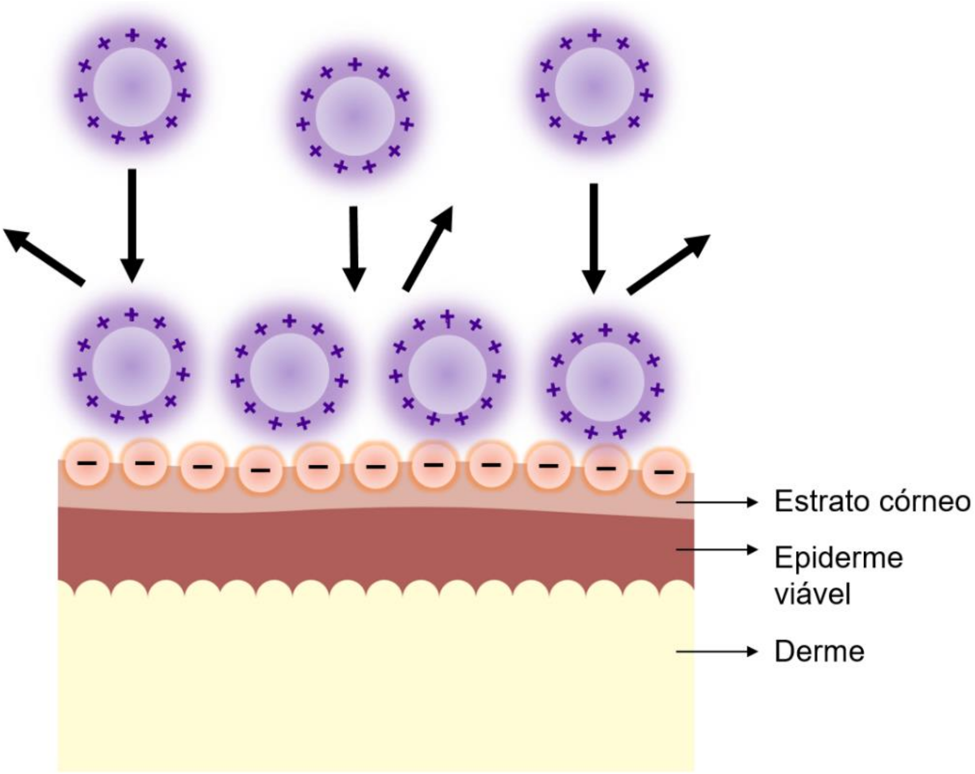

Figura 32. Ilustração da barreira gerada pela interação entre as NPs MGM-AL/DDA e as cargas residuais da pele. Ilustração da autora.

Para complementar os dados obtidos, o ensaio da penetração cutânea das amostras MGM-BL e MGM-AL/DDA foi realizado analisando-se a retenção de ferro em cada fita removida do estrato córneo. A distribuição das nanopartículas pode ser observada a olho nu, conforme as imagens inseridas nos gráficos das Figuras 33 e 34, nas áreas circuladas em vermelho

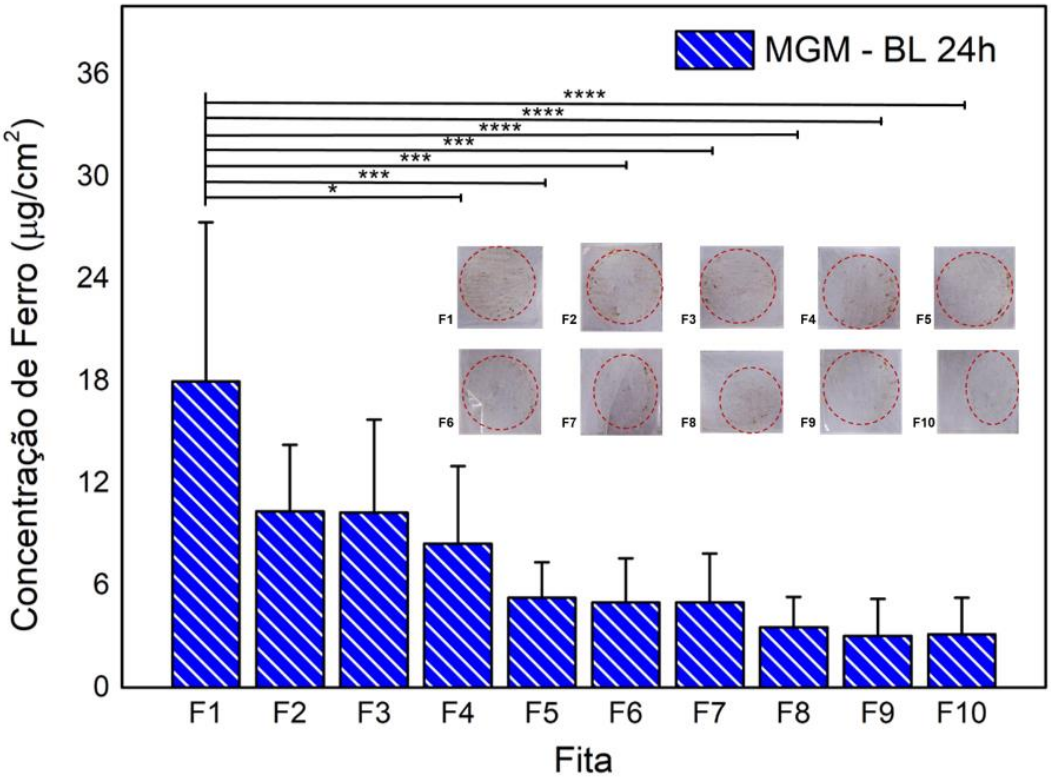

Figura 33. Quantificação da concentração de ferro, em µg/cm^2, retida em cada fita extraída do EC (F1 a F10) após 24h de penetração cutânea para o fluido MGM-BL. As respectivas imagens são apresentadas no interior da figura, sendo observada a presença de nanopartículas na região circulada em vermelho. Dados apresentados como média ± desvio padrão, n=6. ANOVA $p < 0,05$.

Para a amostra MGM-BL, é possível perceber a presença de NPs em todas as 10 camadas do EC, conforme as imagens inseridas na Figura 33. A quantidade do nanocarreador diminuiu para as camadas mais internas do EC, conforme o esperado, porém ainda é possível observar a presença de NPs em uma quantidade significativa.

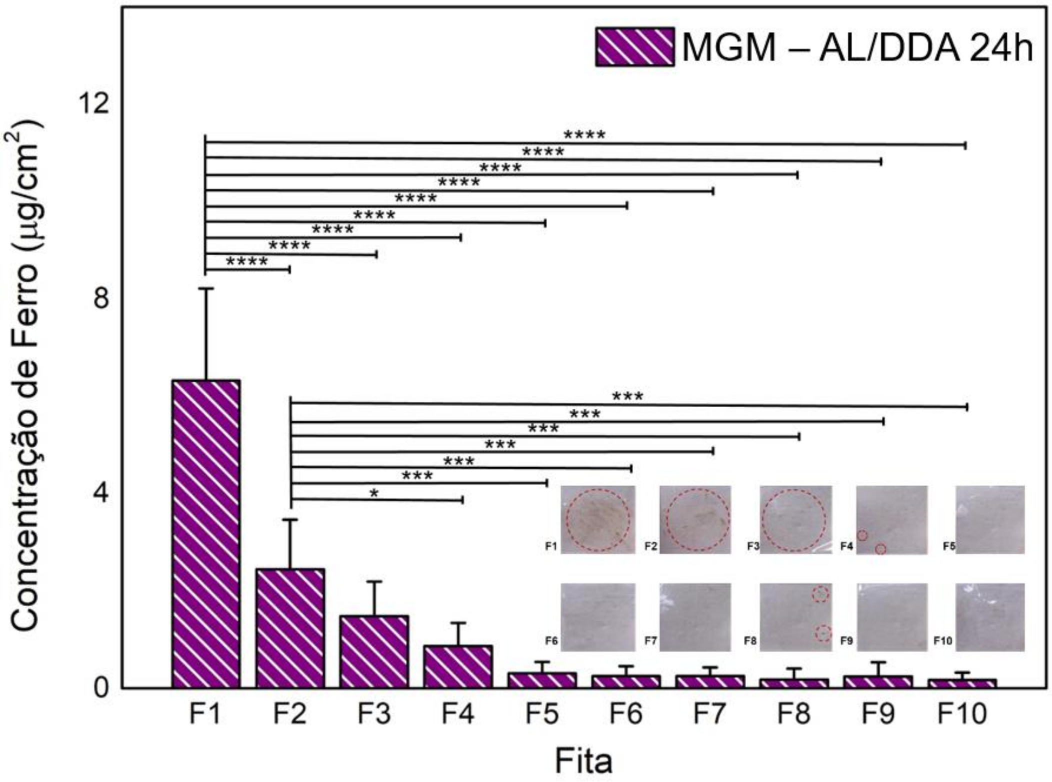

Figura 34. Quantificação da concentração de ferro, em µg/cm², retida em cada fita extraída do EC (F1 a F10) após 24h de penetração cutânea para o fluido MGM-AL/DDA. As respectivas imagens são apresentadas no interior da figura, sendo observada a presença de nanopartículas na região circulada em vermelho. Dados apresentados como média ± desvio padrão, n=6. ANOVA p < 0,05.

No caso da amostra MGM-AL/DDA, Figura 34, é possível observar, a olho nu, a presença de NPs somente até a quarta fita, com exceção a oitava fita. A partir do gráfico da distribuição das partículas, percebe-se uma redução drástica entre a concentração de ferro presente na primeira fita em comparação com as demais. Para a amostra MGM-BL, essa redução só foi observada a partir da fita 5. A retenção da amostra MGM-AL/DDA apenas nas camadas superiores corrobora a hipótese de que o nanocarreador positivo interage com a carga residual negativa da pele, formando uma barreira, impedindo a penetração de mais partículas.

Devido seu tamanho, menor que 40nm, os nanosistemas sintetizados podem ser indicados para o tratamento tópico de doenças que atingem o folículo piloso (Pereira *et al.*, 2018). Para verificar se os carreadores podem ser utilizados para essa finalidade, primeiro é necessário determinar o fator de direcionamento folicular, que é a quantidade de NPs retidas no FP dividida pela quantidade total de Fe retida em todas as camadas da pele (Figura 34).

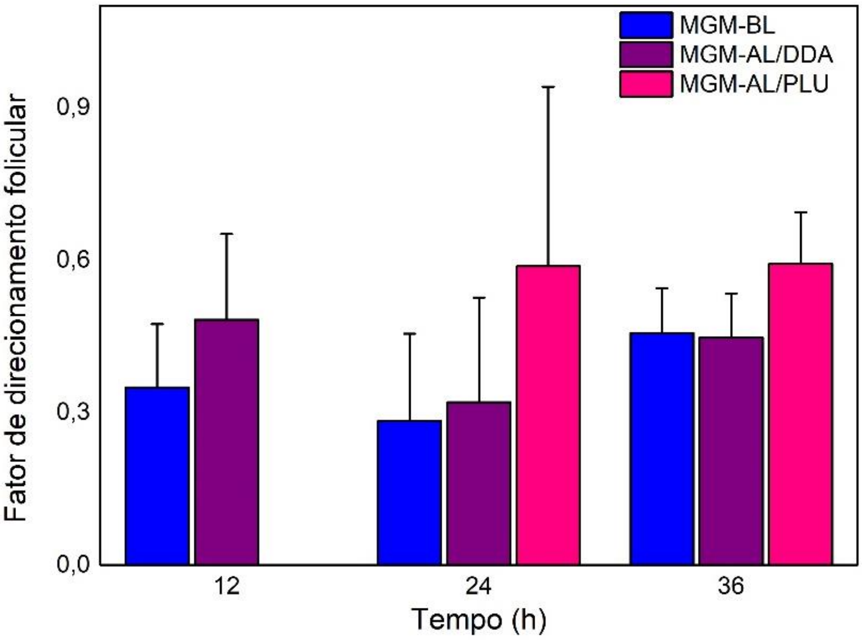

Figura 35. Fator de direcionamento folicular em 12, 24 e 36 horas de permeação para os 3 nanosistemas MGM-BL, MGM-AL/DDA e MGM-AL/PLU, conforme indicação. Dados apresentados como média ± desvio padrão, n=6. ANOVA $p < 0,05$.

A análise estatística dos dados apresentados na Figura 35 indicou que não há diferença entre os fatores de direcionamento dos 3 nanosistemas em nenhum dos períodos analisados ($p > 0,05$) e que todos direcionam as NPs para o folículo piloso. A partir disso, pode-se considerar que os 3 nanocarreadores podem ser utilizados para atingir o FP. Para as amostras MGM-AL/DDA e MGM/AL/PLU, pode ser necessário adicionar algum método para potencializar a permeação dos carreadores, como a aplicação de um campo magnético (Rao *et al.*, 2015; Zhang *et al.*, 2019) ou elétrico (Viratchaiboott *et al.*, 2022).

Esse resultado indica que, apesar da quantidade de partículas que consegue ultrapassar o EC ser modulada pelo surfactante que reveste as NPs, a sua biodistribuição nas camadas da pele, após a penetração do EC, depende mais das características do núcleo do nanocarreador. Como os 3 sistemas foram obtidos a partir do mesmo precursor, MGM-AL, os fatores de direcionamento são semelhantes.

CONCLUSÃO

Nesse trabalho foram produzidos três nanocarreadores de óxido de ferro funcionalizados com bicamada de ácido láurico, laurato/dodecilamina e laurato/Pluronic F127, dispersos em meio aquoso, para a obtenção de novos sistemas carreadores de fármacos visando a administração tópica de medicamentos hidrofóbicos. As partículas e os coloides obtidos foram caracterizados por meio das técnicas de espectroscopia Raman e no infravermelho, espalhamento dinâmico de luz, potencial zeta, e microscopia eletrônica de transmissão (MET).

As micrografias MET mostram partículas esféricas, com diâmetro médio de 6,5 nm, e dispersão de tamanho de acordo com os dados da literatura para NPs sintetizadas pelo método de coprecipitação em meio aquoso. Os dados de espectroscopia Raman indicaram que o processo de oxidação foi efetivo e as NPs foi efetiva de óxido de ferro apresentam a fase maguemita.

Os resultados obtidos por FT-IR indicam que houve uma coordenação entre o grupo carboxilato do ácido láurico e o ferro da NP por uma ligação bidentada quelante, formando a monocamada da cobertura. No caso do fluido MGM-AL/DDA houve uma interação entre as cadeias de hidrocarbonetos do AL e da DDA, enquanto que, para a amostra MGM-AL/PLU, observou-se uma interação entre as cadeias de AL e do PPO do Pluronic. O monitoramento da estabilidade dos fluidos ao longo do tempo após a preparação, por meio do tamanho hidrodinâmico, do potencial zeta e do pH, mostrou que os surfactantes escolhidos promovem a estabilização das nanopartículas em meio aquoso, a partir de repulsão predominantemente estérica (bicamada AL/PLU) e eletroestérica (bicamada AL e AL/DDA), formando suspensões coloidais estáveis por pelo menos 60 dias.

Os nanocarreadores desenvolvidos foram empregados em ensaios *in vitro* de penetração cutânea durante 12, 24 e 36 horas, utilizando pele da orelha de suínos como modelo para a pele humana. As diferentes camadas da pele, como o estrato córneo, folículo piloso e pele remanescente, foram extraídas por meio da técnica de tape stripping diferencial e a concentração de ferro presente em cada camada foi obtida por espectroscopia de ressonância ferromagnética. Os resultados obtidos indicam que, após 24 horas, todos os 3 nanosistemas conseguem ultrapassar a barreira de proteção da pele, o estrato córneo, e se acumular no folículo piloso, sem atingir a pele remanescente. Desta forma, possuem grande potencial para administração tópica de fármacos que tenham ação no folículo piloso.

Considerando a quantidade de ferro que conseguiu permear o EC, o fluido MGM-BL foi o que apresentou a maior concentração de Fe nas 2 camadas da pele, indicando que o ácido láurico é o melhor potencializador da penetração cutânea passiva, ou seja, sem nenhum mecanismo para aumentar a penetração, para as nanopartículas sintetizadas e nos parâmetros de penetração utilizados. Em adição, não foi observada diferença entre os fatores de direcionamento folicular ao comparar-se os três nanosistemas.

PERSPECTIVA

Para a continuidade da pesquisa, sugere-se o estudo da penetração cutânea dos fluidos MGM-AL/DDA e MGM-AL/PLU em diferentes pH ou com a aplicação de um campo elétrico para verificar se há um aumento da quantidade de ferro retido nas camadas da pele. Sugere-se também, a incorporação de fármacos que tenham como região de ação o folículo piloso, como a dutasterida por exemplo, para verificar sua liberação no local de ação.

REFERÊNCIAS

AFIUNE, Luana A.F. *et al*. Novel iron oxide nanocarriers loading finasteride or dutasteride: Enhanced skin penetration for topical treatment of alopecia. **International Journal of Pharmaceutics**, [*s. l.*], v. 587, 2020.

AFIUNE, Luana Alves de Freitas. **Síntese e caracterização de complexos nanoestruturados para aplicação tópica**. 2019. 1–89 f. Tese (Doutorado em Nanociência e Nanobiotecnologia) - Universidade de Brasília, Brasília, 2019.

ALCÂNTARA, Gustavo Braga. **Nanopartículas de maguemita complexadas com ácido oleico**. 2007. 140 f. Dissertação (Mestrado em Física) - Universidade de Brasília, Brasília, 2007.

ALKHOUZAAM, Abedalkader; QIBLAWEY, Hazim. Synergetic effects of dodecylamine-functionalized graphene oxide nanoparticles on antifouling and antibacterial properties of polysulfone ultrafiltration membranes. **Journal of Water Process Engineering**, [*s. l.*], v. 42, p. 102120, 2021.

ALSAQR, Ahmed; RASOULLY, Mohammed; MUSTEATA, Florin Marcel. Investigating Transdermal Delivery of Vitamin D3. **AAPS PharmSciTech**, [*s. l.*], v. 16, n. 4, p. 963–972, 2015.

ANGELO, T. *et al.* Minoxidil topical treatment may be more efficient if applied on damp scalp in comparison with dry scalp. **Dermatologic Therapy**, [*s. l.*], v. 29, n. 5, p. 330–333, 2016.

ASLAM, M *et al.* Synthesis of Amine-Stabilized Aqueous Colloidal Iron Oxide Nanoparticles. **Crystal Growth & Design**, [*s. l.*], v. 7, n. 3, p. 471–475, 2007.

BABU, R. Jayachandra; CHEN, Li; KANIKKANNAN, Narayan. Percutaneous penetration enhancers chemical methods in penetration enhancement: Modification of the stratum corneum. *In*: DRAGICEVIC, Nina; MAIBACH, Howard I. (org.). **Percutaneous Penetration Enhancers Chemical Methods in Penetration Enhancement: Modification of the Stratum Corneum**. [*S. l.*]: Springer-Verlag Berlin Heidelberg, 2015. p. 133–150.

BEGIN-COLIN, Sylvie; FELDER-FLESCH, Delphine. Functionalisation of Magnetic Iron Oxide Nanoparticles. In: THANH, Nguyen TK (Org.). **Magn. Nanoparticles from Fabr. to Clin. Appl.** CRC Press, 2012. p. 151–192.

BERRY, Sarah L. *et al.* Nanoparticle-mediated magnetic hyperthermia is an effective method for killing the human-infective protozoan parasite Leishmania mexicana *in vitro*. **Scientific Reports**, [*s. l.*], v. 9, n. 1, p. 1–9, 2019.

BETTONI, Clarissa Cassani. **Avaliação da penetração cutânea de nanocápsulas de isotretinoína por tape stripping *in vitro* em pele humana e suína**. 2009. Dissertação (Mestrado em Ciências Farmacêuticas) - Universidade Federal do Rio Grande do Sul, Porto Alegre, 2009.

CARAZO, E.; BORREGO-SÁNCHEZ, A.; GARCÍA-VILLÉN, F.; SÁNCHEZ-ESPEJO, R.; CEREZO, P.; AGUZZI, C.; VISERAS, C. Advanced Inorganic Nanosystems for Skin Drug Delivery. **The Chemical Record**, v. 18, n. 7–8, p. 891–899, 2018.

CHAVES, Sacha Braun. **Efeitos biológicos de nanopartículas magnéticas recobertas por bicamada de ácido láurico: estudos *in vitro* e *in vivo***. 2008. 112 f. Tese (Doutorado em Biologia Animal) - Universidade de Brasília, Brasília, 2008.

DEACON, G.B.; PHILLIPS, R.J. Relationships between the carbon-oxygen stretching frequencies of carboxylato complexes and the type of carboxylate coordination. **Coordination Chemistry Reviews**, [*s. l.*], v. 33, n. 3, p. 227–250, 1980.

DINIZ, Ivana M. A. *et al.* Pluronic F-127 hydrogel as a promising scaffold for encapsulation of dental-derived mesenchymal stem cells. **Journal of Materials Science: Materials in Medicine**, [*s. l.*], v. 26, n. 3, p. 153, 2015.

DURÁN, Nelson; MATTOSO, Luiz Henrique Capparelli; MORAIS, Paulo Cezar de. **Nanotecnologia: Introdução, Preparação e Caracterização de Nanomateriais e Exemplos de Aplicação**. São Paulo: Artliber Editora, 2006. *E-book*.

EL-HAMMADI, Mazen M.; ARIAS, José L. Iron oxide-based multifunctional nanoparticulate systems for biomedical applications: A patent review (2008-present). **Expert Opinion on Therapeutic Patents**, [*s. l.*], v. 25, n. 6, p. 691–709, 2015.

FERREIRA, F V *et al.* Applied Surface Science Dodecylamine functionalization of carbon nanotubes to improve dispersion , thermal and mechanical properties of polyethylene based nanocomposites. **Applied Surface Science**, [*s. l.*], v. 410, p. 267–277, 2017.

FRANCISQUINI, Elton; SCHOENMAKER, Jeroen; SOUZA, José Antonio. Nanopartículas Magnéticas e suas Aplicações. **Química Supramol. e Nanotecnologia**. 1ª ed. [S.l.]: Atheneu, 2012. p. 269–289.

GALVÃO, Wesley S. *et al.* Super-paramagnetic nanoparticles with spinel structure: A review of synthesis and biomedical applications. **Solid State Phenomena**, [*s. l.*], v. 241, p. 139–176, 2016.

GOMES, Deizilene S.B. *et al.* New insights on the formation of gold nanoparticles and Pluronic nanocomposites: Kinetics and thermodynamics parameters. **Journal of Molecular Liquids**, [*s. l.*], v. 268, p. 181–189, 2018.

GONÇALVES, Isadora Concenção. **Síntese e Caracterização de Nanopartículas de Ferrita de Cobanto Dopada com Cério**. 2020. 59 f. Tese (Doutorado em Ciências de Materiais) - Instituto Militar de Engenharia, Rio de Janeiro, 2020.

GONÇALVES, L. C. *et al.* Superparamagnetic Iron Oxide Nanoparticles Dispersed in Pluronic F127 Hydrogel: Potential Uses in Topical Applications. **RSC advances**, [*s. l.*], v. 7, n. 24, p. 14496–14503, 2017.

GRATIERI, TAÍS; GELFUSO, GUILHERME MARTINS; LOPEZ, Renata Fonseca Vianna. Princípios básicos e aplicação da iontoforese na penetração cutânea de fármacos. **Química Nova**, [*s. l.*], v. 31, n. 6, p. 1490–1498, 2008.

GREEN, Philip G.; GUY, Richard H.; HADGRAFT, Jonathan. *In vitro* and *in vivo* enhancement of skin permeation with oleic and lauric acids. **International Journal of Pharmaceutics**, [*s. l.*], v. 48, n. 1–3, p. 103–111, 1988.

HAN, Sang Myung; *et al.* Development of a pH-Responsive Polymer Based on Hyaluronic Acid Conjugated with Imidazole and Dodecylamine for Nanomedicine. **Macromolecular Research**, [*s. l.*], v. 30, n. 8, p. 547–556, 2022.

HERRERA, W.T. *et al.* Structural and vibrational studies of fatty acids-functionalized iron oxide nanoparticles via alkaline co-precipitation route. **NANOCON 2015 - 7th International Conference on Nanomaterials - Research and Application, Conference Proceedings**, [*s. l.*], n. June 2017, p. 1–10, 2015.

HUFSCHMID, Ryan *et al.* Synthesis of phase-pure and monodisperse iron oxide nanoparticles by thermal decomposition Graphical abstract HHS Public Access. **Nanoscale**, [*s. l.*], v. 7, n. 25, p. 11142–11154, 2015.

JAIN, Tapan K. et al. Iron Oxide Nanoparticles for Sustained Delivery of Anticancer Agents. **Molecular Pharmaceutics**, v. 2, n. 3, p. 194–205, 2005.

JAIN, Tapan K. et al.. Magnetic resonance imaging of multifunctional pluronic stabilized iron-oxide nanoparticles in tumor-bearing mice. **Biomaterials**, v. 30, n. 35, p. 6748–6756, 2009.

KALE, Anup *et al.* Magnetite/CdTe magnetic-fluorescent composite nanosystem for magnetic separation and bio-imaging. **Nanotechnology**, [*s. l.*], v. 22, n. 22, 2011.

KOLIMI, Praveen; NYAVANANDI, Dinesh; DUDHIPALA, Narendar. Innovative Treatment Strategies to Accelerate Wound Healing : Trajectory and Recent Advancements. **Cells**, [*s. l.*], v. 11, n. August, 2022.

LETTI, Camila Jéssica. **Estudo das propriedades de filmes automontados formados por nanopartículas de óxido de ferro e polímeros**. 2017. 130 f., il. Tese (Doutorado em Física) - Universidade de Brasília, Brasília, 2017.

LETTI, Camila Jéssica. **Estudo de nanocompósitos formados por partículas de óxidos de ferro e polímeros por meio da espectroscopia Raman**. 2013. xxiii, 111 f., il, Dissertação (Mestrado em Física) - Universidade de Brasília, Brasília, 2013.

LETTI, C. J. *et al.* The role of polymer films on the oxidation of magnetite nanoparticles. **Journal of Solid State Chemistry**, [*s. l.*], v. 246, p. 57–64, 2017.

LI, Yafeng; LIAO, Xiaoxiang; ZHENG, Bin. Studies on local anesthetic lidocaine hydrochloride delivery via photo-triggered implantable polymeric microneedles as a patient-controlled transdermal analgesia system. **Journal of biomaterials science, Polymer Edition**, [*s. l.*], v. 33, n. 2, p. 155–173, 2022.

LIN, Hongwei *et al.* Increased skin permeation efficiency of imperatorin via charged ultradeformable lipid vesicles for transdermal delivery. **International Journal of Nanomedicine**, [*s. l.*], v. 13, p. 831–842, 2018.

MAMANI, J.B. *et al.* Synthesis and characterization of magnetite nanoparticles coated with lauric acid. **Materials Characterization**, [*s. l.*], v. 81, p. 28–36, 2013.

MATOS, Hannah Larissa Siqueira. **Síntese de nanopartículas de óxido de ferro funcionalizadas para remoção de Pb2+**. 2016. 87 f. Universidade Federal de Goiás, Goiânia, 2016.

MELO, T.F.O. *et al.* Investigation of surface passivation process on magnetic nanoparticles by Raman spectroscopy. **Surface Science**, [*s. l.*], v. 600, n. 18, p. 3642–3645, 2006.

MOKASHI, S *et al.* Killing of bacterial spores by dodecylamine and its effects on spore inner membrane properties. **Journal of applied microbiology**, [*s. l.*], v. 129, n. 6, p. 1511–1522, 2020.

MORAIS, Paulo Cesar *et al.* Raman investigation of uncoated and coated magnetic fluids. **Journal of Physical Chemistry A**, [*s. l.*], v. 104, n. 13, p. 2894–2896, 2000.

MORAIS, Paulo Cesar *et al.* Raman spectroscopy in magnetic fluids. **Biomolecular Engineering**, [*s. l.*], v. 17, n. 2, p. 41–49, 2001.

MORALES, M. A. *et al.* Magnetic studies of iron oxide nanoparticles coated with oleic acid and Pluronic® block copolymer. **Journal of Applied Physics**, [*s. l.*], v. 97, n. 10, p. 203–205, 2005.

MUSAZZI, Umberto M. *et al.* Impact of semi-solid formulations on skin penetration of iron oxide nanoparticles. **Journal of Nanobiotechnology**, [*s. l.*], v. 15, n. 1, p. 1–10, 2017.

NAKATSUJI, Teruaki *et al.* Antimicrobial Property of Lauric Acid Against Propionibacterium Acnes: Its Therapeutic Potential for Inflammatory Acne Vulgaris. **Journal of Investigative Dermatology**, [*s. l.*], v. 129, n. 10, p. 2480–2488, 2009.

NUNES, Eloiza S *et al.* Evidence of iron (III) reduction in γ-Fe_2O_3 nanoparticles due to meso-2,3-dimercaptosuccinic acid functionalization. **Materials Research Express**, [*s. l.*], v. 1, n. 1, p. 016107, 2014.

PAVIA, Donald L. et al. **Introdução à espectroscopia**. 2010.

PEREIRA, Maira N. *et al.* Nanotechnology advances for hair loss. **Therapeutic Delivery**, [*s. l.*], v. 9, n. 8, p. 593–604, 2018.

PY-DANIEL, Karen R. *et al.* Highly efficient photodynamic therapy colloidal system based on chloroaluminum phthalocyanine/pluronic micelles. **European Journal of Pharmaceutics and Biopharmaceutics**, [*s. l.*], v. 103, p. 23–31, 2016.

QURRAT-UL-AIN; *et al.* Anionic azo dyes removal from water using amine-functionalized cobalt-iron oxide nanoparticles: a comparative time-dependent study and structural optimization towards the removal mechanism optimization towards the removal mechanism. **RSC advances**, [*s. l.*], v. 10, p. 1021–1041, 2020.

RAO, Yue Feng *et al.* Epirubicin-loaded superparamagnetic iron-oxide nanoparticles for transdermal delivery: Cancer therapy by circumventing the skin barrier. **Small**, [*s. l.*], v. 11, n. 2, p. 239–247, 2015.

RAVIRAJ, Vanisri *et al.* Non-invasive transdermal delivery of chemotherapeutic molecules *in vivo* using superparamagnetic iron oxide nanoparticles. **Cancer Nanotechnology**, [*s. l.*], v. 12, n. 1, p. 1–15, 2021.

RAZAVI, Hanieh; DARVISHI, Mohammad Hassan. Silver Sulfadiazine Encapsulated in Lipid-Based Nanocarriers for Burn Treatment. **Journal of Burn Care & Research**, [*s. l.*], v. 39, n. 3, p. 319–325, 2018.

RIVERA, Luis M.R. et al. Biocompatible superparamagnetic carriers of chondroitin sulfate. **Materials Research Express**, v. 6, n. 6, 2019.

RIVERA, Luis M. R. **Síntese de complexos nanoestruturados formados por óxidos de ferro e sulfato de condroitina**. 2013. 96 f., il. Dissertação (Mestrado em Nanociência e Nanobiotecnologia) - Universidade de Brasília, Brasília, 2013.

RIVERA, Luis M.R. **Síntese e caracterização de nanoestruturas superparamagneticas baseadas em óxidos de ferro e glicosaminoglicanos**. 2018. Tese (Doutorado em Nanociência e Nanobiotecnologia) - Universidade de Brasília, Brasília, 2018.

SALDANHA, Camila de Arruda. **Avaliação da atividade antifúngica da anfotericina b conjugada com nanopartículas magnéticas estabilizadas com bicamada de ácido láurico no tratamento da paracoccidioidomicose**. 2012. xiv, 86 f., il. Tese (Doutorado em Biologia Animal) - Universidade de Brasília, Brasília, 2012.

SANTOS, Michelly Christine dos; LIMA, Emília Celma de Oliveira. **Estudo do efeito**

do potencial de superfície na internalização de nanopartículas de magnetita em células cultivadas. Goiânia-GO, Brasil.

SILVA, Matheus Oliveira da. **Nanopartículas de ɣ-Fe2O3 revestidas com bicamada de ácido láurico: funcionalização com acetato, propionato, butirato e succinato de ródio(II) e com albumina de soro bovino**. 2017. xiii, 101 f., il. Tese (Doutorado em Nanociência e Nanobiotecnologia) - Universidade de Brasília, Brasília, 2017.

SOLER, Maria A. G. *et al.* Spectroscopic Study of Maghemite Nanoparticles Surface-Grafted with DMSA. **The Journal of Physical Chemistry A**, [*s. l.*], v. 115, n. 6, p. 1003–1008, 2011.

SOLER, M.A.G. *et al.* Study of molecular surface coating on the stability of maghemite nanoparticles. **Surface Science**, [*s. l.*], v. 601, n. 18, p. 3921–3925, 2007. Disponível em: https://linkinghub.elsevier.com/retrieve/pii/S0039602807003081. Acesso em: 16 maio 2019.

SOLER, M. A. G. *et al.* **Superparamagnetic iron oxides**. *In*: ENCYCLOPEDIA OF NANOSCIENCE AND NANOTECHNOLOGY. California, USA: American Scientific Publishers, 2011. p. 513–532.

SOLER, M. A.G. *et al.* Surface passivation and characterization of cobalt-ferrite nanoparticles. **Surface Science**, [*s. l.*], v. 575, n. 1–2, p. 12–16, 2005.

SOLER, M. A.G.; PATERNO, L. G. Magnetic nanomaterials. *In*: NANOSTRUCTURES. [*S. l.*]: Elsevier Inc., 2017. p. 147–186.

SOLER, Maria A. G.; QU, Fanyao. Raman Spectroscopy of Iron Oxide Nanoparticles. *In*: RAMAN SPECTROSCOPY FOR NANOMATERIALS CHARACTERIZATION. Berlin, Heidelberg: Springer Berlin Heidelberg, 2012. p. 379–416. *E-book*.

SOUZA, Aryane Tofanello de**. Síntese e caracterização de nanopartículas magnéticas de óxido de ferro para aplicações biomédicas – um estudo citotóxico em linhagem celular de carcinoma cervical humano (células HeLa)**. 2011. 111 f. Dissertação (mestrado) - Universidade Estadual Paulista, Instituto de Biociências, Letras e Ciências Exatas, 2011.

SUN, Shouheng; ZENG, Hao. Size-Controlled Synthesis of Magnetite Nanoparticles.

Journal of the American Chemical Society, v. 124, n. 28, p. 8204–8205, 2002.

TEICHMANN, Alexa *et al.* Differential stripping: Determination of the amount of topically applied substances penetrated into the hair follicles. **Journal of Investigative Dermatology**, [*s. l.*], v. 125, n. 2, p. 264–269, 2005.

TELES, Paulo Alexandre Cardoso. **Desenvolvimento e otimização de modelos lipídicos para avaliação da permeação cutânea de fármacos**. 2023. Dissertação (Mestrado em Biofísica e Bionanossistemas) - Universidade do Minho, Braga, 2023.

USHIROBIRA, Camila Y. **Desenvolvimento de nanopartículas poliméricas contendo dutasterida para o tratamento da alopecia androgênica**. 2019. 1–53 f. Dissertação (Mestrado em Ciências Farmacêuticas) - Universidade de Brasília, Brasília, 2019.

USHIROBIRA, Camila Y *et al.* Dutasteride nanocapsules for hair follicle targeting : Effect of chitosan-coating and physical stimulus. **International Journal of Biological Macromolecules**, [*s. l.*], v. 151, p. 56–61, 2020.

VIALI, Wesley R. et al. Investigation of the molecular surface coating on the stability of insulating magnetic oils. **Journal of Physical Chemistry C**, v. 114, n. 1, p. 179–188, 2010.

VIALI, Wesley Renato. **Síntese e Caracterização de nanopartículas de maghemita revestidas com ácido oléico para obtenção de fluidos magnéticos a base de óleos isolantes**. 2009. 100 f. Dissertação (Mestrado em Educação em Química) - Universidade Federal de Goiás, Goiânia, 2009.

VIEIRA, Sara Patrícia Pais. **Promoção da Absorção Cutânea de Fármacos: Estado da Arte**. 2013. Dissertação (Mestrado em Ciências Farmacêuticas) - Universidade Fernando Pessoa, Porto, 2013.

VIRATCHAIBOOTT, Nitinon *et al.* Release of 5-FU loaded pectin/Fe3O4 from porous PBSA matrix under magnetic and electric fields. **Journal of Alloys and Compounds**, [*s. l.*], v. 906, p. 164239, 2022.

YAN-LEI SU *et al.* Study of Salt Effects on the Micellization of PEO−PPO−PEO Block

Copolymer in Aqueous Solution by FTIR Spectroscopy. **Langmuir**, [*s. l.*], v. 18, n. 3, p. 865–871, 2002.

ZHANG, Ling-kun *et al.* Bacterial cellulose based composites enhanced transdermal drug targeting for breast cancer treatment. **Chemical Engineering Journal**, [*s. l.*], v. 370, n. March, p. 749–759, 2019.

ZHAO, Hong *et al.* Synergic enhancing-effect of DEET and dodecylamine on the skin permeation of testosterone from a matrix-type transdermal delivery system Transdermal delivery system of testosterone Hong Zhao et al. **Drug Delivery**, [*s. l.*], v. 16, n. 5, p. 249–253, 2009.

ZHAO, Hong *et al.* The effects of pressure-sensitive adhesives and solubilizers on the skin permeation of testosterone from a matrix-type transdermal delivery system. **Drug Development and Industrial Pharmacy**, [*s. l.*], v. 28, n. 9, p. 1125–1131, 2002.

ZOABI, Amani; TOUITOU, Elka; MARGULIS, Katherine. Recent Advances in Nanomaterials for Dermal and Transdermal Applications. **Colloids Interfaces**, [*s. l.*], v. 5, n. 18, 2021.

ANEXOS

A1. Artigo publicado dentro do contexto desta dissertação

International Journal of Pharmaceutics 587 (2020) 119709

Contents lists available at ScienceDirect

International Journal of Pharmaceutics

journal homepage: www.elsevier.com/locate/ijpharm

Novel iron oxide nanocarriers loading finasteride or dutasteride: Enhanced skin penetration for topical treatment of alopecia

Luana A.F. Afiune[a,b], Camila Y. Ushirobira[a], Débora P.P. Barbosa[b], Paulo E.N. de Souza[c], Maria I.G. Leles[d], Marcilio Cunha-Filho[a], Guilherme M. Gelfuso[a], Maria A.G. Soler[b], Tais Gratieri[a,*]

[a] *Laboratory of Food, Drugs, and Cosmetics (LTMAC), School of Health Sciences, University of Brasília, 70910-900 Brasilia, DF, Brazil*
[b] *Nanofilms and Nano Devices Laboratory, Institute of Physics, University of Brasília, 70910-900 Brasília, DF, Brazil*
[c] *Laboratory of Electron Paramagnetic Resonance, Institute of Physics, University of Brasília, 70910-900 Brasilia, DF, Brazil*
[d] *Institute of Chemistry, Federal University of Goias, 74690-900 Goiânia, GO, Brazil*

ARTICLE INFO

Keywords:
Alopecia
Dutasteride
Finasteride
Hair follicles
Metallic nanoparticles
Skin penetration

ABSTRACT

In the present study, iron oxide nanoparticles, in the form of maghemite core coated with lauric acid (ION), were synthesized and loaded with finasteride (FIN) or dutasteride (DUT) as a novel drug delivery system for the topical treatment of alopecia. Additionally, developed formulations (FIN-ION and DUT-ION) were completely elaborated with components involved in the follicle metabolism, i.e., lauric acid, which acts as a 5α-reductase inhibitor, and iron which deficiency has been related to hair loss aggravation. Stability assessment conducted over the course of 90 days showed they are highly stable, with pH 7.4, constant EE% (> 99%), and practically unchanged particle size and zeta potential. Besides drug distribution, the actual number of iron oxide nanoparticles, through a newly developed method using ferromagnetic resonance, was determined in each skin layer following permeation experiments. Despite the same donor concentration of colloids, nanoparticle distribution in the skin varied according to the loaded molecule. While DUT did not interfere with the nanoparticle natural tendency to accumulate within the hair follicle shafts, FIN presence hampered nanosystem interaction with the skin. Still, both formulations provided a higher skin drug penetration, compared to each respective control solution. Additionally, iron nanocarriers present a desirable visual characteristic, as the dark color aspect might instantly help disguise scarce hair follicle areas. These findings suggest the nanoformulations are highly promising for alopecia therapies.

1. Introduction

Androgenic alopecia is a multifactorial and polygenetic hair loss disorder, in which androgen levels in the scalp is one of the primary triggers to follicular miniaturization and subsequent hair loss (Gupta et al., 2019; Sadick et al., 2017). Therefore, a target for its treatment is the enzyme 5α-reductase, responsible for the intracellular testosterone conversion to dihydrotestosterone, the preferred ligand for androgen receptor transactivation (Azzouni et al., 2012; Sadick et al., 2017). Two from the three 5α-reductase isozymes that are expressed in human tissues are the preferential target of commercialized inhibitors. These are type I – manifested mainly in the skin and in the outer sheath of the hair follicle root and sebaceous glands – and type II – expressed mostly in the prostate, but is also found in the inner epithelial root sheath of hair follicles and skin (Azzouni et al., 2012). Finasteride (FIN) is a potent (mean inhibitory concentration [IC_{50}], 69 nmol L^{-1}) competitive 5α-reductase type II inhibitor, but inhibits less effectively 5α-reductase type I (IC_{50} 360 nmol L^{-1}) (Tian et al., 1994). In comparison, dutasteride (DUT) is more potent and inhibits both types I and II 5α-reductase (IC_{50} of 7 and 6 nmol L^{-1}, respectively) (Clark et al., 2004), therefore showing positive results on alopecia treatment at lower doses than FIN (Shanshanwal and Dhurat, 2017; Tian et al., 1994; Zhou et al., 2019). The problem is, because of their mechanism of action, a decrease in the serum levels of dihydrotestosterone produce various side effects

---

Abbreviations: FIN, finasteride; FIN-ION, iron oxide nanoparticles functionalized with lauric acid and loaded with finasteride; FIN-SOL, finasteride in solution; ION, colloidal iron oxide nanoparticles functionalized with lauric acid; DUT, dutasteride; DUT-ION, iron oxide nanoparticles coated with lauric acid and loaded with dutasteride; DUT-SOL, dutasteride in solution; FMR, ferromagnetic resonance

* Corresponding author at: Campus Universitário Darcy Ribeiro, s/n. 70910-900, Asa Norte, Brasília, DF, Brazil.
E-mail address: tgratieri@gmail.com (T. Gratieri).

https://doi.org/10.1016/j.ijpharm.2020.119709
Received 20 May 2020; Received in revised form 8 July 2020; Accepted 27 July 2020

when these drugs are orally administered, such as impotence, decreased libido, ejaculation disorders, gynecomastia, dizziness, headache, and fatigue (Rosen et al., 2019; Tsai et al., 2018; Zhou et al., 2019).

The alternative for the oral administration is the topical cutaneous drug delivery, which is especially auspicious for drugs with clinical usage limitations resultant of systemic side effects. More specifically, the topical application of nanosystems could improve therapy outcome, considering the site of action of 5α-reductase inhibitors in the treatment of alopecia to be within the hair follicle region, and the natural tendency of nanoparticles to accumulate into the skin appendageal structures (Angelo et al., 2020; Radtke et al., 2017). Moreover, depending on the excipients used and drug-loaded properties, controlled drug delivery can be achieved (Matos et al., 2015), prolonging the administration's intervals and consequently improving patients compliance.

Not inadvertently, several nanosystems have been proposed for the topical delivery of FIN, such as liposomes (Lee et al., 2011; Tabbakhian et al., 2006), niosomes (Tabbakhian et al., 2006), ethosomes (Rao et al., 2015; Rao et al., 2008; Wilson et al., 2018), polymersomes (Caon et al., 2014), and liquid crystalline nanoparticles (Madheswaran et al., 2015; Madheswaran et al., 2013; Madheswaran et al., 2014; Madheswaran et al., 2017). Still, a problematic factor in many of these studies is the use of permeation enhancers within the formulation (Madheswaran et al., 2014) or coating the nanosystem (Caon et al., 2014; Madheswaran et al., 2017), that, not only enhance local drug concentrations retained in the skin but also enhance drug delivery through the skin (Caon et al., 2014; Lee et al., 2011; Madheswaran et al., 2017; Rao et al., 2008) ultimately facilitating its entry into the systemic circulation. Such transdermal drug flux diminishes the targeting potential of the nanosystem (Wilson et al., 2018) and can lead to unwanted systemic effects. Another limitation of all of these studies cited, with only one exception (Tabbakhian et al., 2006), was that cumulated drug amounts within the hair follicles were not assessed.

Although much less studied than FIN, DUT has also been topically delivered from nanosystems, including lipid-core nanocapsules (Ushirobira, 2020), nanolipid carriers (Noor et al., 2017), and liquid crystalline nanoparticles (Madheswaran et al., 2015; Madheswaran et al., 2017). Some of these studies have also observed a transdermal DUT flux (Madheswaran et al., 2015; Madheswaran et al., 2017), but, admitting some of these systems might indeed be promising drug carriers, all these formulations cited are still in the proof-of-concept phase. Excipients safety, formulation stability, and final sensorial presentation are crucial aspects yet of being solved for an actual clinical application.

To address these issues, colloidal iron oxide nanoparticles (ION), mainly maghemite (γ-Fe_2O_3), and magnetite (Fe_3O_4), are strong candidates as nanocarriers due to their unique properties such as superparamagnetism, biocompatibility, and very controllable surface chemistry (Soler and Paterno, 2017). Further, the easy up-scaling and cost-effective chemical routes allowing excellent size control, size distribution, shape, and stability, make them attractive for diagnostic tools or to deliver therapeutic agents to specifically targeted sites in a controlled manner, as well as other applications (Alcantara et al., 2013; Israel et al., 2020; Letti et al., 2017; Luque-Michel et al., 2019; Rivera et al., 2019). Since they were already investigated for several medical purposes, their safety profiles are already well-established (Musazzi et al., 2017; de Freitas et al., 2008; Pradhan et al., 2007; Pöttler et al., 2015).

The ION-based systems comprise an iron oxide nanoparticle core, few nanometers in diameter, with a functionalized surface that promotes long term colloidal stability and enables the anchoring/binding of the drug (Mamani et al., 2013). Among the surface-coatings used nowadays, lauric acid has been successfully employed in the surface functionalization of ION-based materials enabling its dispersion in the same pH and ionic strength as of physiological media (da Silva et al., 2018).

Moreover, ION nanocolloids display a dark color aspect bringing the advantage of an instant optical effect of filling the scalp, helping to disguise scarce hair follicle areas. Also, the own iron constituting the nanoparticles could be a useful mineral source for the hair follicle. Although the relationship between alopecia and iron deficiency is still controversial (Dhaher et al., 2018), a description of iron-dependent genes in the hair follicle bulge region can be found in the literature (St Pierre et al., 2010).

In the present study, FIN or DUT was anchored in an ION-based nanocarrier comprising nanosized maghemite, surface functionalized with lauric acid, as a proposed formulation for the topical treatment of androgenic alopecia. Lauric acid was chosen as a surface-coating excipient, considering it also inhibits types I and II of 5α-reductase (Raynaud et al., 2002). Hence, the here envisioned drug delivery system is completely constituted by active molecules related to follicles' metabolism. To our knowledge, this is the first study to investigate the use of ION-systems for the treatment of a hair-follicle related disorder. Along with proposing an innovative FIN and DUT delivery system, this paper aims to examine the actual nanoparticle distribution within the skin layers, including the hair follicle shafts. Typically, drug-loaded nanoparticles are topically applied, and nanoparticle distribution is indirectly assessed by evaluating the drug penetration profile only, extracting the drug from different skin layers (Matos et al., 2015). In some cases, microscopy images of fluorescently-marked nanosystems are obtained (Angelo et al., 2020), generating qualitative or indirect quantitative data (when pixel counting methods are employed) (Gratieri et al., 2010). Here, utilizing ION superparamagnetic property, the actual number of ION, and the amount of iron permeated in each skin layer were estimated through a newly developed method using ferromagnetic resonance (FMR).

2. Material and methods

2.1. Material

FIN and DUT (purity > 98%) were purchased from Purifarma (Anapolis, Brazil). Iron (II) chloride tetrahydrate ($FeCl_2{\cdot}4H_2O$), iron (III) chloride hexahydrate ($FeCl_3{\cdot}4H_2O$), sodium hydroxide (NaOH), hydrochloric acid (HCl), perchloric acid ($HClO_4$), potassium bromide (KBr) and lauric acid were purchased from Sigma Aldrich Corporate (St. Louis, Missouri, USA). Cellulose membranes for dialysis were purchased from InLab (São Paulo, Brazil). Sterile syringe filters with a pore size of 0.45 µm were purchased from Analitica (São Paulo, Brazil). Solvents used for extraction and chromatographic analysis were all of HPLC grade. All procedures were performed using ultra purified water (Millipore, Illkirch-Graffenstaden, France). Skin from porcine ears was obtained from a local abattoir (Sabugy Agroindustria e Comércio de Alimentos LTDA, Brazil), and frozen at −20 °C up to 1 month before the use. The whole skin was removed from the outer region of the ear, separated from its underlying layer, and used "full-thickness" to guarantee the intactness of the hair follicles. Final skin thickness used was approximately 1 mm. Hence, the skin contained part of the dermis.

2.2. Synthesis of iron oxide nanoparticles

ION nanocarriers were synthesized by coprecipitating Fe^{2+} and Fe^{3+} in an alkaline medium following a protocol reported in the literature with minor modifications (Viali et al., 2010).

Initially, a solution of $FeCl_2{\cdot}4H_2O$ (0.020 mol) and $FeCl_3{\cdot}4H_2O$ (0.043 mol) was slowly added to 125 mL of NaOH (1.5 mol L^{-1}) under mechanical stirring (2000 rpm) at room temperature (25 °C). The as precipitated, nanosized magnetite (solid black) was repeatedly washed with deionized water, and dispersed in perchloric acid solution at pH 3.5, producing a stable ionic magnetic fluid. This colloidal dispersion was used for further oxidation by bubbling O_2 gas (3 h, at 80 °C, under constant stirring) to obtain nanosized maghemite particles (γ–Fe_2O_3). After cooling, maghemite was isolated by centrifugation, washed several times with aqueous solution, and coated with lauric acid.

Nanoparticle surface functionalization was performed as previously reported (da Silva et al., 2018), with modifications. Freshly oxidized nanoparticles were suspended in 500 mL of deionized water, and pH was adjusted to 8 with a NaOH solution and heated to 60 °C. Under continuous stirring, pure lauric acid (2.5 g) was slowly added to the suspension and stirred for 30 min, originating the first coating layer. After that, an additional 1.5 g of lauric acid was added, and the suspension was stirred for 1 h (70 °C, pH 8), forming the second coating layer enabling the nanoparticles to be dispersed in the aqueous medium. This dispersion was then dialyzed against deionized water for three days to remove the free lauric acid. The resulting dispersion was centrifuged to remove agglomerates and dialyzed for three days. Lastly, pH was adjusted to 7.3, and the nanocolloidal sample comprising lauric acid coated maghemite, bearing negative charge due to lauric acid adsorption, was named ION, and employed as a platform for drug incorporation. An aliquot of the ION nanocolloid sample was lyophilized for 6 h in a SpeedVac Concentrator (SPD121P, with refrigerated vapor trap, RVT400, Savant) to produce a solid sample. Dynamic light scattering and electrophoretic mobility measurements were performed to confirm the presence of lauric acid at the nanoparticle's surface. Transmission electron microscopy (TEM) micrographs of the maghemite nanoparticles were recorded in order to access the average particle size (D_m) and standard diameter deviation (σ).

2.3. Drug incorporation

FIN and DUT formulations were prepared by drug incorporation in the ION nanocolloids using an orbital shaker (Kline, GT-201BDU model, São Paulo, Brazil). Previously, each drug (12.5 mg of FIN and 6.25 mg of DUT) was solubilized in 3 drops of methanol in a volumetric flask (50 mL), and the volume was completed with ION. The flasks were kept under stirring for 24 h generating the formulations, namely FIN-ION and DUT-ION at the final concentrations of 250 and 125 μg mL^{-1}, respectively. Aliquots of FIN-ION and DUT-ION nanocolloid samples were lyophilized following the same protocol as mentioned for the ION sample (Section 2.1), producing powder samples.

2.4. Formulations characterization

2.4.1. Infrared spectroscopy

Infrared spectroscopy was used to investigate drug loading. Solid samples were dispersed in KBr, and the infrared spectra were obtained in the spectrometer Vertex 70 (Bruker Corporation, USA) in transmission mode ranging from 4000 to 400 cm^{-1} with eight scans and resolution of 4 cm^{-1}.

2.4.2. Thermogravimetric analysis

Thermogravimetric analyses (TG) were performed using the equipment TG/SDTA 822 (Mettler Toledo, Switzerland). Samples (5–6 mg) placed in platinum pans were analyzed under nitrogen atmosphere at a flow of 50 mL min^{-1} from room temperature up to 1,000 °C using a heating rate of 10 °C min^{-1}. Data were evaluated based on the mass loss curves and its first derivative (DTG). This equipment provides measurements with an uncertainty lower than 0.5%.

2.4.3. Hydrodynamic size distribution and zeta potential

Hydrodynamic size and size distribution were determined by dynamic light scattering (DLS), while the zeta (ζ) potential was obtained by electrophoretic measurements, Zetasizer Nano ZS (Malvern Instruments, Worcestershire, United Kingdom). These analyses were performed with a 4 mW He–Ne laser operating at a wavelength of 633 nm and a scattering angle of 90°_ at 25°_C. Analysis of colloidal samples by DLS provided the hydrodynamic diameter of dispersed nanoparticles and the polydispersity index (PDI). Formulation samples for DLS and ζ potential measurements were diluted (1:10 v/v) at pH 7.4, and 1 mL was used for both analyses. Measurements were performed three times, and mean values were taken.

2.4.4. Encapsulation efficiency and drug recovery

The encapsulation efficiency of drugs (EE%) was determined in two steps. For the total quantification of FIN or DUT in the colloidal dispersion formulation, samples of 100 μL were diluted in methanol (1:10 v/v), filtered, and quantified using the HPLC method described in Section 2.6. For the determination of free drug in the colloidal dispersion medium (FD), nanoparticles were forcedly decantated using a magnet, and the supernatant was collected and quantified. The concentration of encapsulated drug in nanoparticles was determined by the difference between the amount of total drug in the formulation (TD) and the amount of free drug in the medium (FD). EE% and drug recovery (DR%) were calculated as follows:

$$EE\% = [(TD - FD)/TD] \times 100$$

$$DR\% = [(TD - FD)/\text{amount of drug added}] \times 100$$

2.4.5. Physicochemical stability

Physicochemical stability studies of the formulations FIN-ION, DUT-ION and control nanocolloid ION, were conducted during 90 days on samples stored at temperatures of 4 °C ± 2.0 and 25 °C ± 2.0. Hydrodynamic size, PDI, zeta potential, pH, and EE% were monitored at 0, 7, 15, 30, 60, and 90 days.

2.5. In vitro drug release

Determination of FIN and DUT release from nanoparticles was performed by adding 1 mL of each formulation (FIN-ION and DUT-ION) in a volumetric flask containing 24 mL of a medium composed by 60% Water, 0.5% Tween 80, and 40% ethylene glycol under stirring (600 rpm) at 32 ± 2.0 °C. Preliminary studies showed FIN, and DUT solubility in this medium was respectively 255.1 ± 3. 6 and 125.9 ± 1.1 μg mL^{-1}, sufficient for attaining Sink conditions. Particles were decanted with a magnet at 0, 1, 2, 4, 6, 8, 10, 12, 24, 30, 36, 48, 72, and 96 h, when samples of 1 mL were removed and replaced with fresh medium. Drug assay was performed, as described in Section 2.7. Determination of FIN and DUT dissolution profile were also determined as controls by adding, respectively 250 and 125 μg of each drug to the dissolution medium. At the same pre-determined intervals 1 mL of sample was removed and quantified.

2.6. In vitro skin permeation

Preliminary permeation experiments were performed using modified Franz-type diffusion cells (diffusion area = 5.7 cm^2) mounted with full-thickness porcine's ear skin. The receptor compartment was filled with 75 mL of 0.5% SDS aqueous solution, while 2 mL of test samples (FIN-ION and DUT-ION) were placed in the donor compartment in contact with the stratum corneum for 24 h. As these preliminary experiments showed neither FIN nor DUT was found in the receptor compartment, the modified Saarbruecken method, which does not have a receptor compartment (Angelo et al., 2016), was used for further permeation experiments of FIN-ION and DUT-ION.

As control samples, solutions of FIN (250 μg mL^{-1}) and DUT (125 μg mL^{-1}) solubilized in 60% water: 0.5% Tween 80: 40% ethylene glycol was prepared and labeled FIN-SOL, DUT-SOL, respectively. The diffusion area remained 5.72 cm^2. After 12 h and 24 h, FIN or DUT was extracted from the skin layers separated by differential tape-stripping technique (Matos et al., 2015; Pereira et al., 2017). Briefly, the skin was removed from the diffusion cell and placed onto a flat surface with the stratum corneum facing up. The skin was cleaned with a water-soaked gause pad and tape-stripped 15 times, using Scotch book tapes. A drop of cyanoacrylate superglue was applied to the stripped skin area and covered with a further tape-strip using light pressure. After total polymerization of the glue (~5 min), tape-strip was removed and the skin surface biopsy containing follicular casts obtained, from which drugs were extracted with methanol and quantified. Finally, reminiscent skin was cut into small pieces and placed in plastic tube along with 3 mL of methanol under magnetic stirring for 3 h. The resulting suspensions were filtered on 0.22 µm filters and quantified by HPLC. FIN and DUT recovery efficiency from the stratum corneum, follicular material, and remaining skin had been previously determined with values higher than 97%, as described in Section 2.7.

A second series of *in vitro* skin permeation experiments using the modified Saarbruecken method were performed placing the developed formulations (FIN-ION and DUT-ION) in the donor compartment, but instead of determining the drug distribution, the quantity iron oxide nanoparticles and iron permeated in each skin layer were evaluated through FMR. A blank formulation (ION colloid) was used as control. The permeated amounts of formulations and the blank were expressed as a percentage of the amount administered in the donor compartment. FMR experiments were performed in an EMX Plus spectrometer (Bruker, Germany), equipped with an X-band (9 GHz) standard sensitivity cavity (Bruker ER4102ST, Germany), using 100 kHz modulation frequency, 10 gauss of modulation amplitude and 2 mW microwave power.

For the analysis, a central area of 0.1215 cm^2 from either the tapes containing the stratum corneum or hair follicles or from the remaining skin was selected. These rectangular fragments of the tapes containing stratum corneum or hair follicles or the rectangular fragment of the own remaining layer were inserted into 1 mL syringes, which were filled with 600 µL of distilled water and frozen in liquid nitrogen before the injection into the Quartz Finger Dewar holder – Noxygen (Germany) for the analysis through FMR.

The calibration curve for ION concentration was obtained by fitting the FMR data as a function of the concentration of diluted samples of ION, specially prepared from an initial sample whose Fe concentration was determined by Atomic Absorption Spectrometry $-$ 6.85 µg mL^{-1}, the average mass of an ION (1.16×10^{-18} g), its volume (2.39×10^{-19} cm^3), and considering the approximately spherical format, the average diameter (D_{TEM}) obtained in the histogram of the TEM (7.55 nm) and the density of maghemite (4.87 g cm^{-3}). The linearity for ION was $r = 0.999$; $y = 1.74 \times 10^{-10} \times -0.08694$ over a concentration range between 1.69×10^{9} and 1.69×10^{11} ION mL^{-1}.

2.7. Drug assay

FIN was quantified following a reversed-phase HPLC method with UV detection at 210 nm (model LC-20AD, Shimadzu, Kyoto, Japan). A C_{18} column (Shimadzu, 4.6 mm × 15 cm) was used. The mobile phase consisted of acetonitrile: phosphoric acid 0.01 mol L^{-1} (40:60 v/v) in a flow rate of 1 mL min^{-1} at 40 °C using an injection volume of 20 µL.

DUT was also quantified following a reversed-phase HPLC method using the same apparatus with detection at 280 nm (Ushirobira et al., 2020). The mobile phase consisted of acetonitrile: phosphoric acid 0.01 mol L^{-1} (62:38 v/v), at a flow rate of 0.8 mL min^{-1} at 40 °C, and injection volume of 20 µL.

Both methods were validated following the International Conference on Harmonization (ICH) guidelines and were selective and linear ($r^2 = 0.999$; $y = 20938x - 338.61$ and $r^2 = 0.999$; $y = 8000.9x - 157.9$ for FIN and DUT, respectively), both over a drug concentration range of 0.5–15 µg mL^{-1}. Intra- and inter-day precision and accuracy of the methods showed a coefficient of variation of less than 5% for both drugs. For FIN, the quantification and detection limits were 0.13 µg mL^{-1} and 0.04 µg mL^{-1}, respectively. For DUT, these limits were 0.23 µg mL^{-1} and 0.09 µg mL^{-1}, respectively.

2.8. Statistical analyses

The results were expressed as mean ± standard deviation (SD). Significant differences between data set were obtained by analysis of variance (two-way ANOVA), followed by Tukey's multiple comparison test to compare more than two experimental groups and unpaired Student's T-test for comparison of two experimental groups. The significance level was set at $p < 0.05$.

3. Results and discussion

3.1. Synthesis and characterization of drug-loaded nanoparticles

Dynamic light scattering and electrophoretic mobility measurements were performed at each step of the synthesis process. Initially, the nanocolloid formed by bare maghemite nanoparticles exhibiting positive charges on the surface was produced, ascribed to protonation of surface iron oxyhydroxy groups (Bacri et al, 1990). This suspension in aqueous medium (pH 3.5, at 25 °C) displayed zeta potential of 43 mV and hydrodynamic diameter of 107,2 ± 0,8 nm, with a PDI of 0,22 ± 0,03. After nanoparticle functionalization, these measurements confirm the presence of lauric acid at the nanoparticle's surface, providing mean hydrodynamic diameter (~123 nm) and high negative zeta potential (around −36 mV). TEM micrographs of the maghemite nanoparticles were recorded in order to access the average particle size (D_m) and standard diameter deviation (σ). Vertical bars in Fig. 1 represents the particle size histogram obtained from the TEM micrographs, whereas the solid line results from the curve-fitting of the data using the log-normal distribution function (Popplewell and Sakhnini, 1995). Values of the average particle diameter (D_m) and standard diameter deviation (σ), obtained from the fitting of the data presented in Fig. 1 were 7.55 ± 0.07 nm and 0.27 ± 0.01, respectively. The inset of Fig. 1 shows a typical TEM micrograph of the ION sample, recorded in a JEM-1011 (JEOL, Japan) microscope operated at 80 keV. Raman spectrum obtained from the powder ION sample provided in Supplementary material as Fig. SM1 confirms the maghemite phase, displaying characteristic vibration modes at 344, 501, and 695 cm^{-1} (Soler and Fanyao, 2012).

Drug incorporation in formulations was investigated through thermogravimetric and FT-IR measurements. Thermogravimetric analysis showed two significant mass losses of ION sample below 400 °C, which might correspond to the lauric acid decomposition of the molecules physiosorbed and chemosorbed onto the nanoparticle surface, depicting percentage loss of mass (Δm) of 20.3% and DTG at 231.5 and 349.5 °C, as observed in Fig. 2. The presence of two decomposition steps suggests a double coating layer of lauric acid. It was also observed that one of the

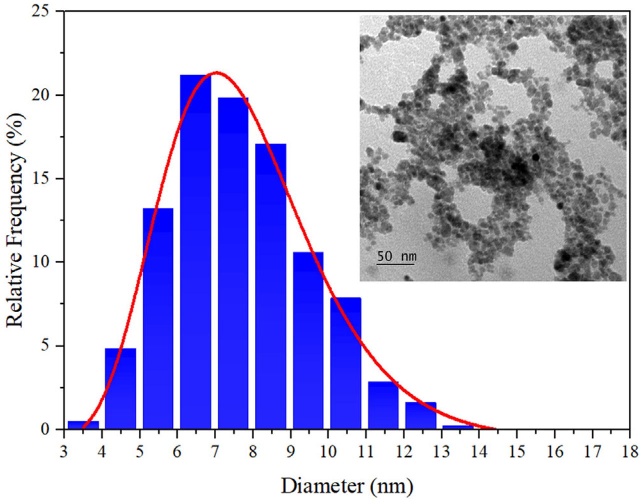

Fig. 1. Particle size histogram of the ION sample. The inset is a typical TEM micrograph of the sample. Solid lines in the inset represent the best curves fitting using a log-normal distribution function.

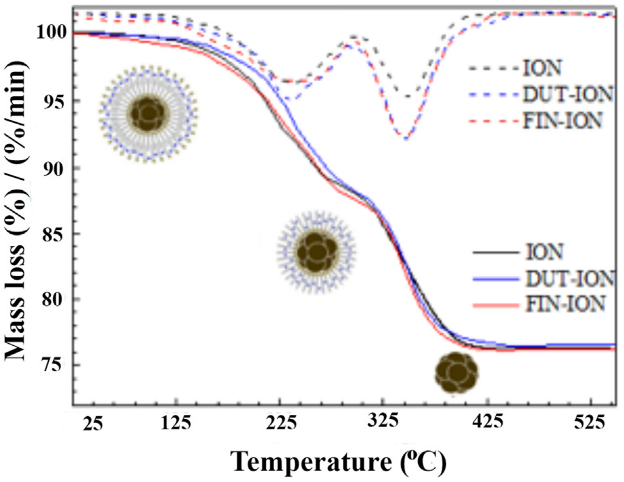

Fig. 2. TG/DTG curves for the samples (ION, FIN-ION, and DUT-ION) performed under a nitrogen atmosphere, together with a schematic illustration of the particle transformation.

mass losses occurs at almost the same temperature of decomposition of pure lauric acid displayed by the TG/DTG curve provided as Supplementary material as Fig. SM2 (A), (B), and Table SM1, which most likely corresponds to the decomposition of the physiosorbed molecules, due to its weaker interaction with the nanoparticle core. Accordingly, such two significant mass losses were also observed in FIN-ION and DUT-ION samples, in which an additional mass loss occurred at 349.5 °C, referring to the decomposition of the drugs, with the total Δm of 24.1 and 25.1%, respectively. These findings may suggest that both drugs decompose with the chemosorbed molecules of lauric acid, in a slightly lower decomposition temperature than the pure drugs (Fig. SM2 (A), (B) and Table SM1). This shift of the decomposition temperature was also observed when analyzing the TGA curves of a mixture of LA-FIN and LA-DUT (Fig. SM2 (A), (B) and Table SM1), 1:1 ratio, which could also indicate that the drugs are associated with the LA bilayer.

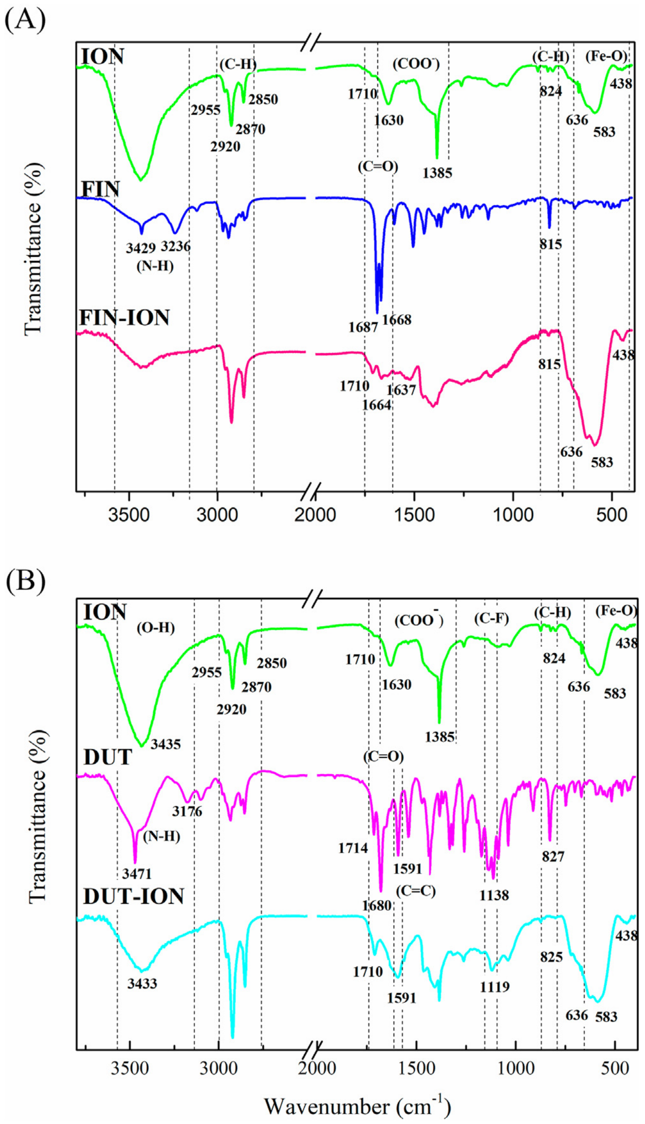

Fig. 3. FT-IR of neat FIN, ION, and FIN-ION (A) and neat DUT, ION, and DUT-ION (B) samples. Spectra were normalized to enhance visual inspection.

The drug incorporation is also denoted analyzing the presence of characteristic FIN and DUT bands in their formulation FT-IR spectra (Fig. 3(A) and (B)). Comparing the carboxyl group peak (C═O) characteristics depicted for control FIN and formulation FIN-ION, it is observed a widening of the carboxyl group peak (C═O) and its displacement to a lower wavenumber from 1687 and 1668 cm^{-1} to 1664 and 1637 cm^{-1} respectively (Fig. 3A). Similarly, in Fig. 3b, the carboxyl group peaks (C═O) of DUT and DUT-ION change from 1714 to 1710 cm^{-1} and 1680 to a broad band between 1680 and 1591 cm^{-1}, respectively. These spectra changes in lipid such as lauric acid are associated with the inclusion of hydrophobic drugs or molecules. They are directly proportional to the strengthening of the hydrogen bond with oxygen in the lipid carboxylic group (Biruss et al., 2007; Dies et al., 2015; Kim et al., 2014). It is likely that the FIN and DUT, in addition to strengthening the hydrogen bonds between the C═O groups of the LA molecules, will also make inner hydrogen bonds. Intermolecular hydrophobic interactions also can occur between FIN and DUT molecules and the LA bilayer, providing better, anchoring of FIN and DUT at the double layer of LA at the nanoparticle' surface. Additionally, FT-IR spectra reinforce the presence of the maghemite phase and its functionalization with lauric acid. In both spectra (FIN-ION and DUT-ION, Fig. 3A and B respectively), the characteristic bands of maghemite core, such as stretching vibrations of Fe-O at 636, 583, and 438 cm^{-1}, and also lauric acid bands are observed. Namely, the asymmetric (ν_aC–H) and symmetric (ν_sC–H) stretching vibrations of C–H from CH_3 groups of fatty acid coating are observed at 2955 and 2870 cm^{-1}, respectively, as well as the symmetric ν_a(C–H) and ν_s(C–H) stretching vibrations related to CH_2 groups at 2920 and 2850 cm^{-1}, respectively, and the C═O stretching vibration at 1710 cm^{-1}, characteristic of carboxylic acids, possibly related to protonated LA physiosorbed molecules (Soler et al., 2007; da Silva et al., 2018). Also, it was observed in the ION sample FT-IR spectrum a broad band between 1680 and 1585 cm^{-1} and a peak at 1385 cm^{-1}, corresponding to the asymmetric (ν_aCOO$^-$) and symmetric (ν_sCOO$^-$) stretching vibrations of the carboxylate head of the deprotonated lauric acid. The wavenumber separation, Δν, between the ν_a (COO$^-$) and ν_s (COO$^-$) IR bands can be used to predict the coordination between the carboxylate head and the metallic Fe atom. In this study, it was obtained a difference (Δν) between 200 and 295 cm^{-1}, which suggests a monodentate coordination (Deacon and Phillips, 1980; Nakamoto, 1986). The broadness of the band around 1680 and 1585 cm^{-1} may have been caused by the presence of adsorbed water molecules on the nanoparticle surface, considering that the asymmetric OH_2 stretching mode occurs in this same region, around 1630 cm^{-1} (Soler et al., 2007). FT-IR peaks (Fig. 3A and B) of ION, FIN, ION-FIN, DT, ION-DT samples with their respective assignments are listed in Table 1.

3.2. Stability studies

Formulations showed to be stable for up to 90 days of storage

(Table 2). Prepared samples (day 1) presented a hydrodynamic size and polydispersity index (PDI) equal to 122.63 ± 0.75 nm and 0.19 ± 0.01 for ION sample; 116.37 ± 0.46 nm and 0.18 ± 0.01 for FIN-ION, and 117.70 ± 0.10 nm and 0.19 ± 0.01 for DUT-ION, respectively. The pH of all formulations was maintained at approximately 7.4. All formulations showed a slow tendency of hydrodynamic diameter increase with significative difference only when comparing values obtained in the first and the last day of storage ($p > 0.05$). Still, formulations and control sample preserved their monodispersity and electrical characteristics, with unchanged PDI and zeta potential ($p < 0.0001$). A monomodal dispersion was obtained, as indicated by the low PDI for all samples (~0.18). As observed in the FT-IR and TG analysis, the drug loading on the coating layers, contributed to the very high EE% and DR% (> 99%) for both FIN-ION and DUT-ION formulations. Moreover, drug incorporation did not affect the zeta potential, as for instance, for the day 1, as listed in Table 1, −35.53 ± 0.66 mV before drug loading (ION) and −34.40 ± 0.26 and −36.77 ± 0.49 mV after FIN and DUT incorporation, respectively. Remarkably after 90 days of storage, drug expulsion was not observed, and EE% remained > 99%.

Table 1

Selected FT-IR peaks Fig. 3(A) and (B) of ION, FIN, ION-FIN, DUT, ION-DUT samples with their respective assignments.

Bands	ION	FIN	ION-FIN	DUT	ION-DUT
ν(O–H)	3435	–	3433	–	3433
ν(N–H) amida	–	3429	–	3471	–
ν(N–H) lactama	–	3234	–	3176	–
νa(C–H) CH_3	2955	2968	2955	2977	2955
νs(C–H) CH_3	2870	2866	2870	2873	2870
ν_a(C–H) CH_2	2920	2937	2920	2914	2920
ν_s(C–H) CH_2	2850	2846	2850	2854	2850
ν(C=O) carboxylic acid	1710	–	1710	–	1710
ν(C=O) amida	–	1685	1664	1714	1710
ν(C=O) lactama	–	1666	1637	1680	1680–1591
ν_a(COO^-)	1624	–	–	–	–
ν(C=C)	–	–	–	1591	1591
ν_s(COO^-)	1431	–	–	–	–
ν(C–F)	–	–	–	1138	1119
δ(C–H)	824	815	815	827	825
ν(Fe–O)	636, 583, 438	–	636, 583, 438	–	636, 583, 438

Table 2

Hydrodynamic diameter, polydispersity index, zeta potential, pH, and encapsulation efficiency (EE%) of ION, FIN-ION, and DUT-ION. Measurements were conducted on samples stored at room temperature (25 °C ± 2 °C), or at 4 °C ± 2 °C, after 1, 3, 5, 7, 15, 30, 60 and 90 days of preparation.

	ION		FIN-ION		DUT-ION	
Day 1	**4 ± 2 °C**	**25° ± 2 °C**	**4 ± 2 °C**	**25° ± 2 °C**	**4 ± 2 °C**	**25° ± 2 °C**
Particle size (nm)	124.40 ± 0.70	122.63 ± 0.75	116.83 ± 0.83	116.37 ± 0.46	118.27 ± 0.70	117.70 ± 0.10
PDI	0.190 ± 0.001	0.192 ± 0.006	0.180 ± 0.001	0.182 ± 0.008	0.176 ± 0.008	0.185 ± 0.006
Zeta potential (mV)	−35.57 ± 0.31	−35.53 ± 0.67	−34.23 ± 0.15	−34.40 ± 0.26	−35.80 ± 0.53	−36.77 ± 0.49
pH	7.42 ± 0.09	7.43 ± 0.09	7.42 ± 0.03	7.47 ± 0.02	7.48 ± 0.03	7.48 ± 0.02
EE (%)	–	–	99.50 ± 0.05	99.59 ± 0.04	99.92 ± 0.01	99.93 ± 0.01
Day 3	**4 ± 2 °C**	**25° ± 2 °C**	**4 ± 2 °C**	**25° ± 2 °C**	**4 ± 2 °C**	**25° ± 2 °C**
Particle size (nm)	125.63 ± 0.64	123.60 ± 0.92	117.67 ± 0.35	117.63 ± 0.21	120.33 ± 1.42	117.87 ± 0.58
PDI	0.196 ± 0.011	0.192 ± 0.004	0.186 ± 0.009	0.177 ± 0.002	0.174 ± 0.007	0.184 ± 0.006
Zeta potential (mV)	−35.80 ± 0.20	−35.83 ± 0.25	−36.30 ± 1.13	−35.80 ± 0.30	−35.83 ± 0.80	−35.80 ± 0.50
pH	7.41 ± 0.04	7.48 ± 0.07	7.43 ± 0.04	7.48 ± 0.02	7.41 ± 0.01	7.41 ± 0.02
EE (%)	–	–	99.75 ± 0.02	99.60 ± 0.03	99.83 ± 0.05	99.78 ± 0.07
Day 7	**4 ± 2 °C**	**25° ± 2 °C**	**4 ± 2 °C**	**25° ± 2 °C**	**4 ± 2 °C**	**25° ± 2 °C**
Particle size (nm)	126.43 ± 0.12	125.40 ± 0.44	119.13 ± 1.27	117.37 ± 0.86	120.90 ± 0.44	119.20 ± 0.44
PDI	0.194 ± 0.011	0.195 ± 0.006	0.187 ± 0.006	0.177 ± 0.001	0.175 ± 0.005	0.192 ± 0.002
Zeta potential (mV)	−35.20 ± 0.17	−35.60 ± 1.01	−34.57 ± 0.47	−37.25 ± 0.21	−35.30 ± 0.36	−36.30 ± 0.42
pH	7.39 ± 0.03	7.44 ± 0.06	7.41 ± 0.02	7.40 ± 0.02	7.47 ± 0.04	7.53 ± 0.09
EE (%)	–	–	99.65 ± 0.03	99.47 ± 0.03	99.78 ± 0.01	99.76 ± 0.01
Day 15	**4 ± 2 °C**	**25° ± 2 °C**	**4 ± 2 °C**	**25° ± 2 °C**	**4 ± 2 °C**	**25° ± 2 °C**
Particle size (nm)	129.47 ± 0.21	123.40 ± 2.83	120.37 ± 0.40	112.37 ± 3.04	121.20 ± 0.66	119.03 ± 1.66
PDI	0.188 ± 0.004	0.200 ± 0.008	0.183 ± 0.006	0.191 ± 0.002	0.184 ± 0.010	0.193 ± 0.009
Zeta potential (mV)	−35.37 ± 0.45	−35.33 ± 1.01	−34.40 ± 0.30	−35.03 ± 0.75	−34.50 ± 0.66	−35.13 ± 1.17
pH	7.44 ± 0.09	7.45 ± 0.03	7.48 ± 0.03	7.43 ± 0.11	7.45 ± 0.10	7.22 ± 0.06
EE (%)	–	–	99.71 ± 0.01	99.41 ± 0.02	99.83 ± 0.03	99.76 ± 0.01
Day 30	**4 ± 2 °C**	**25° ± 2 °C**	**4 ± 2 °C**	**25° ± 2 °C**	**4 ± 2 °C**	**25° ± 2 °C**
Particle size (nm)	133.03 ± 1.36	129.70 ± 0.96	123.00 ± 1.57	121.30 ± 1.95	127.33 ± 2.05	121.87 ± 1.15
PDI	0.200 ± 0.001	0.193 ± 0.001	0.186 ± 0.008	0.189 ± 0.005	0.176 ± 0.003	0.175 ± 0.007
Zeta potential (mV)	−35.17 ± 0.40	−36.47 ± 0.84	−34.10 ± 0.14	−36.05 ± 0.49	−35.07 ± 0.75	−36.27 ± 0.06
pH	7.47 ± 0.02	7.46 ± 0.10	7.40 ± 0.05	7.34 ± 0.12	7.44 ± 0.07	7.43 ± 0.29
EE (%)	–	–	99.08 ± 0.01	99.15 ± 0.03	99.80 ± 0.01	99.77 ± 0.01
Day 60	**4 ± 2 °C**	**25° ± 2 °C**	**4 ± 2 °C**	**25° ± 2 °C**	**4 ± 2 °C**	**25° ± 2 °C**
Particle size (nm)	141.47 ± 2.40	130.97 ± 0.83	125.97 ± 1.05	120.25 ± 0.64	141.47 ± 2.40	130.97 ± 0.83
PDI	0.204 ± 0.003	0.203 ± 0.004	0.196 ± 0.007	0.189 ± 0.002	0.177 ± 0.001	0.176 ± 0.002
Zeta potential (mV)	−35.97 ± 0.12	−35.53 ± 0.66	–33.77 ± 0.75	−35.33 ± 0.25	−35.80 ± 0.57	–33.95 ± 1.34
pH	7.47 ± 0.09	7.46 ± 0.10	7.40 ± 0.05	7.34 ± 0.10	7.41 ± 0.10	7.43 ± 0.29
EE (%)	–	–	99.27 ± 0.02	99.22 ± 0.03	99.84 ± 0.06	99.72 ± 0.01
Day 90	**4 ± 2 °C**	**25° ± 2 °C**	**4 ± 2 °C**	**25° ± 2 °C**	**4 ± 2 °C**	**25° ± 2 °C**
Particle size (nm)	142.60 ± 1.73	131.87 ± 2.15	126.20 ± 1.18	120.47 ± 1.65	129.57 ± 1.64	125.43 ± 0.38
PDI	0.190 ± 0.008	0.199 ± 0.004	0.193 ± 0.003	0.171 ± 0.001	0.183 ± 0.006	0.177 ± 0.004
Zeta potential (mV)	−35.67 ± 0.47	−36.47 ± 0.38	−34.77 ± 0.37	−35.80 ± 0.40	−36.53 ± 0.35	−36.73 ± 0.69
pH	7.34 ± 0.06	7.34 ± 0.14	7.40 ± 0.04	7.22 ± 0.01	7.47 ± 0.23	7.44 ± 0.34
EE (%)	–	–	99.30 ± 0.06	99.34 ± 0.05	99.78 ± 0.02	99.82 ± 0.02

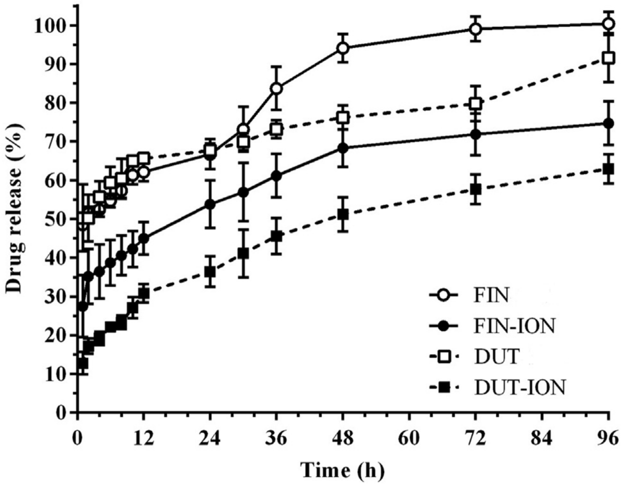

Fig. 4. Release profiles of FIN from FIN-ION and DUT from DUT-ION. FIN and DUT represent the dissolution profile of each drug, assessed as controls (n = 5).

3.3. Drug release studies

Samples of FIN-ION and DUT-ION were submitted to a drug release assay for 96 h and Fin and DUT dissolutions profiles were assessed for comparison. Dissolution profiles of each drug show that already in the first hour, 48.5 ± 0.9% of FIN and 50.3 ± 8.6% of DUT are solubilized in the medium, highlighting the significant sustained release for both drugs achieved with the nanoencapsulation (Fig. 4). FIN-ION reached a drug release of about 50% after 24 h of experiment, while DUT-ION released 50% of the drug after only 48 h, which could be explained by the higher lipophilicity of DUT (low aqueous solubility 0.908 mg.L^{-1}, Log P = 5.09) in comparison to FIN (Log P = 3.03).

3.4. Cutaneous penetration studies

Cutaneous penetration studies were performed for either 12 or 24 h from the developed nanosystems dispersed in aqueous solution. Such aqueous solution would already be a good topical dosage form, as it is easy to be administered, spread and would not hinder particle accumulation within the hair follicle. However, to avoid the liquid from running off some polymer could be added as a thickener agent in a final commercial formulation. Nonetheless, immediately after the penetration experiment and skin removal, a "hair filling" appearance could be clearly noted in treated skin (Fig. 5B), compared with the non-treated one (Fig. 5A). We believe such coloring may be desirable for individuals with dark-colored hair and would promptly help to disguise scarce hair follicle areas. Such appearance though, is expected to disappear upon a simple hair washing (Lewinski et al., 2017).

After skin removal from the penetration experiments, nanoparticles and drug distribution were determined in each skin layer, namely stratum corneum, hair follicles, and remaining skin. Fig. 6 depicts nanoparticles' distribution from formulations containing 6.85 µg mL^{-1} of iron, corresponding to 8.47 × 10^{12} ION mL^{-1}. Blank nanocolloid (ION) was used as a control.

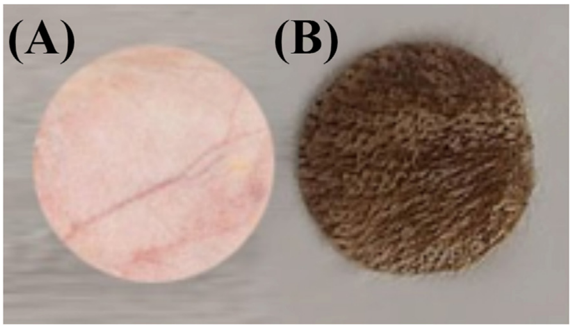

Fig. 5. Porcine skin pieces untreated (A) and after 24 h of penetration experiment of ION (B). Images represent a real size picture.

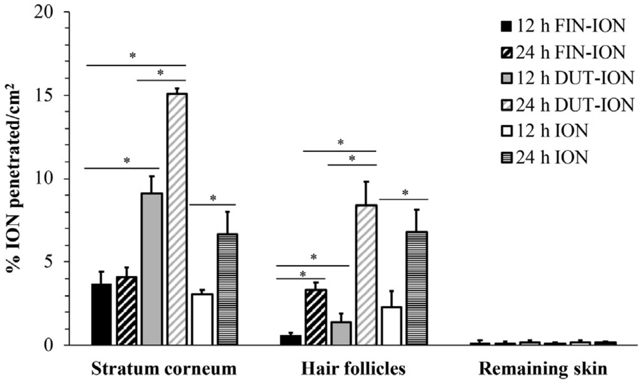

Fig. 6. Iron oxide nanoparticles (ION) distribution in the skin after 12 and 24 h of penetration studies performed with FIN loaded nanosystems (FIN-ION), DUT loaded nanosystems (DUT-ION), and blank iron nanoparticles (ION). Asterisks indicate a significant difference between the nanoformulations (n = 5, $^{*}p < 0.05$).

Fig. 7 depicts drug distribution from formulations containing

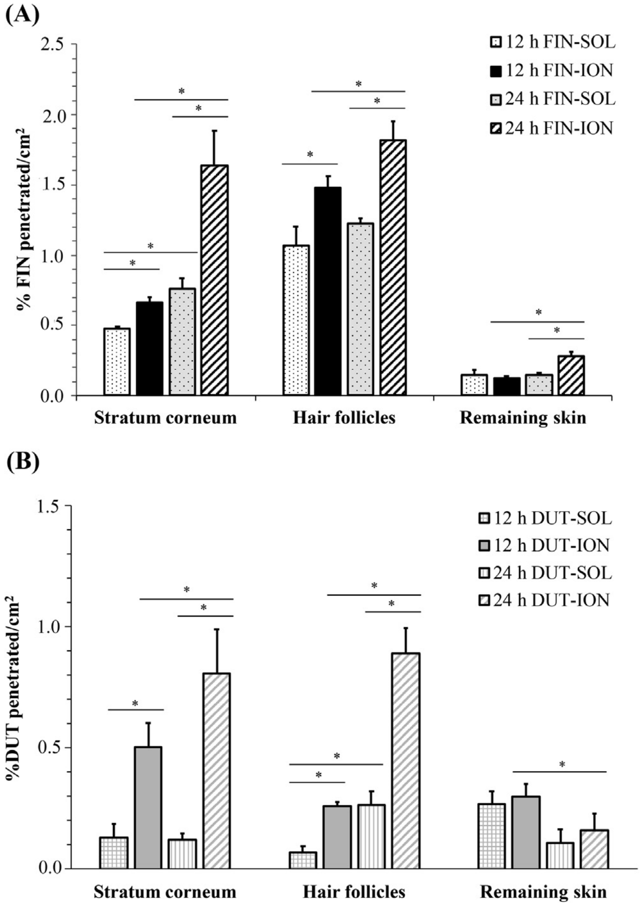

Fig. 7. Drug distribution in the stratum corneum, hair follicle, and remaining skin from (a) FIN loaded nanoparticles (FIN-ION) and FIN solution (FIN-SOL) and (b) DUT loaded nanoparticles (DUT-ION) and DUT solution (DUT-SOL), after 12 and 24 h of permeation experiments. Asterisks indicate a significant difference between controls and their correspondent nanoformulations (n = 5, $^{*}p < 0.05$).

250 μg mL^{-1} of FIN or 125 μg mL^{-1} of DUT (FIN-ION and DUT ION). Drug solutions at these same concentrations were used as controls. Penetrated amounts of FIN, DUT, and ION were expressed as a percentage of the amount administered in the donor compartment.

Surprisingly, even though the same number of ION was applied in the donor compartment in all permeation experiments, nanoparticles distribution in the skin varied according to the loaded molecule. Independently from the duration of the experiment, more nanoparticles (~the double) were retained in the stratum corneum when the nanosystems were loaded with DUT (9.10 ± 1.03%.cm^{-2}), in comparison to FIN loaded nanosystems (3.70 ± 0.79%.cm^{-2}) and blank nanosystems (3.07 ± 0.27%.cm^{-2}). The higher DUT lipophilicity and slower release from the nanoparticles might have increased whole nanosystem (ION agglomerate + coating material + loaded drug) interaction with the lipid lamellae filling the intercellular space between the corneocytes in the stratum corneum (Haque and Talukder, 2018).

Still, this higher lipophilicity did not interfere on the nanoparticle natural tendency to accumulate within the hair follicle shafts, as there was no difference ($p > 0.05$) in the iron oxide amount in this layer when compared to the blank formulation, independently from the experiment duration (1.41 ± 0.47 and 2.3 ± 0.8%.cm^{-2} from DUT-ION and ION, respectively, for 12 h and 8.39 ± 1.45 and 6.76 ± 1.35%.cm^{-2} from DUT-ION and ION, respectively, for 24 h).

FIN presence, otherwise, seemed to hamper nanosystem interaction with the skin. At more extensive permeation experiments, the number of nanoparticles retained in the stratum corneum was actually lower in comparison with blank nanoparticles ($p < 0.05$). Stratum corneum lamellae consist of ceramides, cholesterol, cholesterol esters, cholesterol sulfate, and free fatty acids (Haque and Talukder, 2018). Lauric acid, coating the nanosystems, as being a saturated fatty acid with a 12-carbon atom chain (Log P = 4.6), presents a strong interaction with this layer (Lee et al., 1994). Such strong interaction explains the ION accumulation after 24 h compared to the shorter permeation experiment. Diversely, when FIN-ION was applied, the FIN release might have disassembled the ION structure. A possible explanation is with drug release, at least the outermost lauric acid layer preferably interacted with the skin than with the nanosystem, switching ION surface characteristics, and exposing the more polar molecule groups. Therefore, after FIN release, polar nanoparticles were much likely left “behind” to further interact with the skin, which simply did not happen.

Nevertheless, more importantly, deposition into hair follicles was significantly impaired when FIN was loaded. Compared to blank nanosystems, approximately only one fourth of the nanoparticles were deposited in this layer after 12 h of treatment when nanosystems were loaded with FIN (0.58 ± 0.22 and 2.30 ± 0.81%.cm^{-2}, respectively). This accumulation difference dropped to half after 24 h (3.35 ± 0.43 and 6.76 ± 1.35%.cm^{-2}, respectively), as more FIN-ION continued to penetrate.

Nevertheless, results showed, even with the more prolonged exposure, the number of nanoparticles actually reaching the remaining skin was meager (~0.15%.cm^{-2}) and not different from the amount observed after 12 h ($p > 0.05$), independently from the drug-loaded, which can be perceived as the safety of this topical administration.

Drug amounts in the remaining skin were only significantly higher after 24 h application of FIN-ION compared to respective drug solution control (Fig. 7). Since permeation is increased from FIN-ION and the drug is released, free FIN molecules continue to diffuse and permeate. Even so, such increased retention can be considered minimal as less than 0.5% of the drug dose per square centimeter of the remaining skin was found after 24 h. Besides, as already mentioned, preliminary experiments did not detect FIN in the receptor solution when the FIN-ION permeation experiment was performed in Franz diffusion cells. In this aspect, FIN-ION distinguishes from previously reported nanosystems, which presented a transdermal flux of this drug (Caon et al., 2014; Lee et al., 2011; Madheswaran et al., 2017; Rao et al., 2008). When a liquid crystalline nanoparticle dispersion equivalent to the same 500 μg of FIN used in FIN-ION experiments was applied on porcine skin for 24 h, a drug flux in the order of 0.010 μg $cm^{-2}h^{-1}$ was observed (Madheswaran et al., 2017). Chitosan coating even enhanced such flux in 1.6-fold. However, drug retained amounts in the skin (epidermis + dermis) were the same (~20 μg mL^{-1}) (Madheswaran et al., 2017), like those found from FIN-ION, as discussed following.

Nonetheless, DUT-ION application on skin also did not lead to drug penetration in the receptor compartment when Franz diffusion cells were used, and more meaningful, despite increasing DUT distribution in the stratum corneum and within the hair follicles, did not further increase DUT penetration in the remaining skin compared to the control solution. Because of the controlled drug release, topical administration of this molecule, when loaded in the ION nanoparticles, might favor a local targeting effect, and as despite being more potent, might lead to less systemic adverse reactions. A similar “epidermal targeting” effect has been previously observed for nanostructured lipid carriers loaded with clobetasol (Silva et al., 2016). Clobetasol is also a potent molecule but has comparable lipophilicity than the one of FIN (Log P = 3.0). The critical aspect for restraining the drug molecules to more superficial skin layers was the controlled release achieved with the nanoencapsulation rather than the own molecule characteristics (Angelo et al., 2020; Silva et al., 2016). In fact, similar adverse effects for FIN and DUT following topical applications have been observed (Zhou et al., 2019). Therefore, even if the nanosystem enhances drug penetration, as long as the controlled release is accomplished, clinical studies may adjust the dosage so that a local therapeutic concentration is achieved without systemic exposure.

Indeed, for both drugs, skin penetration from the nanosystems was higher compared to each respective control solution. After 24 h of the penetration experiment FIN-ION lead to almost double of the FIN amount in the skin compared to control solution (18.64 ± 0.69 and 10.65 ± 0.38 μg.cm^{-2}, corresponding to 3.73 ± 0.14 and 2.13 ± 0.08%.cm^{-2}), while DUT-ION lead to almost 4-times the amount of DUT in the skin compared to control solution (4.66 ± 0.45 and 1.24 ± 0.27 μg.cm^{-2}, corresponding to 1.86 ± 0.18 and 0.50 ± 0.11%.cm^{-2}). Therefore, when each drug penetration is compared to its respective control, DUT-ION was twice more effective than FIN-ION (4-fold *versus* 2-fold increase, respectively), which makes sense considering that more ION penetrated the skin when loaded with DUT ($3.99 \pm 0.32 \times 10^{12}$ ION.cm^{-2}) than when loaded with FIN ($1.28 \pm 0.19 \times 10^{12}$ ION.cm^{-2}). But more importantly, the nanosystem's efficiency can be established by the drug increase within the hair follicles, as it is the target for treating alopecia. DUT-ION provided a 3.4-fold drug increase in the hair follicles compared to the control solution (2.23 ± 0.26 and 0.66 ± 0.14 μg.cm^{-2}, corresponding to 0.89 ± 0.11 and 0.27 ± 0.06%.cm^{-2}), while FIN-ION increase was of approximately only 1.5-fold (9.08 ± 0.67 and 6.11 ± 0.20 μg.cm^{-2}, corresponding to 1.82 ± 0.14 and 1.23 ± 0.04%.cm^{-2}). As previously discussed, FIN loading hampered nanoparticle deposition within the hair follicles' shafts. Nonetheless, FIN amounts achieved were comparable to those found in the only study in the literature that assessed the FIN accumulation within the pilosebaceous units. Accordingly, Tabbakhian et al. reported ~2%.cm^2 of the applied drug dosage was retained in the hair follicles of hamster skin (Tabbakhian et al., 2006).

Hence, this better efficiency of DUT-ION in increasing DUT skin penetration compared to the control solution does not make the FIN-ION formulation less attractive for alopecia therapy.

4. Conclusion

Developed nanocarriers comprising lauric acid coated maghemite loaded with FIN or DUT are promising formulations for the topical treatment of alopecia, especially because they are completely constituted by active molecules related to the follicle metabolism. Besides, both nanosystems provided a higher skin drug penetration, consisting in a formulation that is easily prepared with an inexpensive synthesis protocol, allowing higher yield, and facility for scaling up rendering highly stable formulations, for at least 90 days. Noticeably, formulations present desirable visual characteristics, as the dark color aspect may instantly help disguise scarce hair follicle areas. Further clinical studies are necessary for establishing treatment protocols.

CRediT authorship contribution statement

Luana A.F. Afiune: Investigation, Methodology, Formal analysis, Writing - original draft. **Camila Y. Ushirobira:** Investigation, Methodology. **Débora P.P. Barbosa:** Investigation, Methodology, Formal analysis. **Paulo E.N. de Souza:** Investigation, Methodology, Formal analysis. **Maria I.G. Leles:** Investigation, Methodology, Formal analysis. **Marcilio Cunha-Filho:** Conceptualization, Resources, Writing - review & editing, Supervision. **Guilherme M. Gelfuso:** Conceptualization, Writing - review & editing. **Maria A.G. Soler:** Conceptualization, Resources, Project administration, Formal analysis, Resources, Writing - review & editing, Supervision. **Tais Gratieri:** Conceptualization, Resources, Project administration, Formal analysis, Resources, Writing - review & editing, Supervision.

Declaration of Competing Interest

The authors declare that they have no known competing financial interests or personal relationships that could have appeared to influence the work reported in this paper.

Acknowledgments

The authors acknowledge the Brazilian funding agencies FAP-DF (Fundação de Apoio à Pesquisa do Distrito Federal, Grant numbers 00193-00001252/2019-18, and 193.001.358/2016), CNPq (Conselho Nacional de Desenvolvimento Científico e Tecnológico, Grant number 424152/2016-9), CAPES (Coordenação de Aperfeiçoamento de Pessoal de Nível Superior) and University of Brasilia (Edital DPI/UnB 04/2019) for financial support. The authors would also like to thank "Sabugy Agroindustria e Comercio de Alimentos" for gently providing the porcine ears.

Appendix A. Supplementary data

Supplementary data to this article can be found online at https://doi.org/10.1016/j.ijpharm.2020.119709.

References

Alcantara, G.B., Paterno, L.G., Fonseca, F.J., Pereira-da-Silva, M.A., Morais, P.C., Soler, M.A.G., 2013. Dielectric properties of cobalt ferrite nanoparticles in ultrathin nanocomposite films. Phys. Chem. Chem. Phys. 15, 19853–19861.

Angelo, T., Barbalho, G.N., Gelfuso, G.M., Gratieri, T., 2016. Minoxidil topical treatment may be more efficient if applied on damp scalp in comparison with dry scalp. Dermatol. Ther. 29, 330–333.

Angelo, T., El-Sayed, N., Jurisic, M., Koenneke, A., Gelfuso, G.M., Cunha-Filho, M., Taveira, S.F., Lemor, R., Schneider, M., Gratieri, T., 2020. Effect of physical stimuli on hair follicle deposition of clobetasol-loaded Lipid Nanocarriers. Sci. Rep. 10, 176.

Azzouni, F., Godoy, A., Li, Y., Mohler, J., 2012. The 5 alpha-reductase isozyme family: a review of basic biology and their role in human diseases. Adv. Urol. 2012, 530121.

Bacri, J.-C., Perzynski, R., Salin, D., 1990. Ionic ferrofluids: a crossing of chemistry and physics. J. Magn. Magn. Mater. 85, 27–32.

Biruss, B., Dietl, R., Valenta, C., 2007. The influence of selected steroid hormones on the physicochemical behaviour of DPPC liposomes. Chem. Phys. Lipids 148, 84–90.

Ushirobira, Camila Y., L.A.F.A., Pereira, Maira N., Cunha-Filho, Marcilio, Gelfuso, Guilherme M., Gratieri, Tais, 2020. Dutasteride nanocapsules for hair follicle targeting: Effect of chitosan-coating and physical stimulus. Int. J. Biol. Macromol.

Caon, T., Porto, L.C., Granada, A., Tagliari, M.P., Silva, M.A.S., Simoes, C.M.O., Borsali, R., Soldi, V., 2014. Chitosan-decorated polystyrene-b-poly(acrylic acid) polymersomes as novel carriers for topical delivery of finasteride. Eur. J. Pharm. Sci. 52, 165–172.

Clark, R.V., Hermann, D.J., Cunningham, G.R., Wilson, T.H., Morrill, B.B., Hobbs, S., 2004. Marked suppression of dihydrotestosterone in men with benign prostatic hyperplasia by dutasteride, a dual 5 alpha-reductase inhibitor. J. Clin. Endocr. Metab. 89, 2179–2184.

da Silva, M.O., Carneiro, M.L.B., Siqueira, J.L.N., Bao, S.N., de Souza, A.R., 2018. Development of a promising antitumor compound based on rhodium(II) succinate associated with iron oxide nanoparticles coated with lauric acid/albumin hybrid: synthesis, colloidal stability and cytotoxic effect in breast carcinoma cells. J. Nanosci. Nanotechnol. 18, 3832–3843.

Deacon, G.B., Phillips, R.J., 1980. Relationships between the carbon-oxygen stretching frequencies of carboxylate complexes and the type of carboxylate coordination. Coord. Chem. Rev. 33, 227–250.

de Freitas, E.R.L., Soares, P.R.O., Santos, R.P., Santos, R.L., Silva, J.R., Porfirio, E.P., Bao, S.N., Lima, E.C.O., Morais, P.C., Guilo, L.A., 2008. In vitro biological activities of anionic y-Fe2O3 nanoparticles on human melanoma cells. J. Nanosci. Nanotechnol. 8, 2385–2391.

Dhaher, S.A., Yacoub, A.A., Jacob, A.A., 2018. Estimation of zinc and iron levels in the serum and hair of women with androgenetic alopecia: case-control study. Indian J. Dermatol. 63, 369–374.

Dies, H., Cheung, B., Tang, J., Rheinstadter, M.C., 2015. The organization of melatonin in lipid membranes. Biochim. Biophys. Acta 1848, 1032–1040.

Gratieri, T., Schaefer, U.F., Jing, L.H., Gao, M.Y., Kostka, K.H., Lopez, R.F.V., Schneider, M., 2010. Penetration of quantum dot particles through human skin. J. Biomed. Nanotechnol. 6, 586–595.

Gupta, A.K., Mays, R.R., Versteeg, S.G., Shear, N.H., Piguet, V., Piraccini, B.M., 2019. Efficacy of off-label topical treatments for the management of androgenetic alopecia: a review. Clin. Drug Invest. 39, 233–239.

Haque, T., Talukder, M.M.U., 2018. Chemical enhancer: a simplistic way to modulate barrier function of the stratum corneum. Adv. Pharm. Bull. 8, 169–179.

Israel, L.L., Galstyan, A., Holler, E., Ljubimova, J.Y., 2020. Magnetic iron oxide nanoparticles for imaging, targeting and treatment of primary and metastatic tumors of the brain. J. Control. Release 320, 45–62.

Kim, N.A., Choi du, H., Lim, J.Y., Kim, K.H., Lim, D.G., Lee, E., Park, E.S., Jeong, S.H., 2014. Investigation of polymeric excipients for dutasteride solid dispersion and its physicochemical characterization. Arch. Pharm. Res. 37, 214–224.

Lee, C.K., Uchida, T., Kitagawa, K., Yagi, A., Kim, N.S., Goto, S., 1994. Relationship between lipophilicity and skin permeability of various drugs from an ethanol/water/lauric acid system. Biol. Pharm. Bull. 17, 1421–1424.

Lee, S.I., Nagayya-Sriraman, S.K., Shanmugam, S., Baskaran, R., Yong, C.S., Yoon, S.K., Choi, H.G., Yoo, B.K., 2011. Effect of charge carrier lipid on skin penetration, retention, and hair growth of topically applied finasteride-containing liposomes. Biomol. Ther. 19, 231–236.

Letti, C.J., Costa, K.A.G., Gross, M.A., Paterno, L.G., Pereira-da-Silva, M.A., Morais, P.C., Soler, M.A.G., 2017. Synthesis, morphology and electrochemical applications of iron oxide based nanocomposites. Adv. Nano Res. 5, 215–230.

Lewinski, N.A., Berthet, A., Maurizi, L., Eisenbeis, A., Hopf, N.B., 2017. Effectiveness of hand washing on the removal of iron oxide nanoparticles from human skin ex vivo. J. Occup. Environ. Hyg. 14, D115–D119.

Luque-Michel, E., Sebastian, V., Larrea, A., Marquina, C., Blanco-Prieto, M.J., 2019. Co-encapsulation of superparamagnetic nanoparticles and doxorubicin in PLGA nanocarriers: development, characterization and in vitro antitumor efficacy in glioma cells. Eur. J. Pharm. Biopharm. 145, 65–75.

Madheswaran, T., Baskaran, R., Sundaramoorthy, P., Yoo, B.K., 2015. Enhanced skin permeation of 5 alpha-reductase inhibitors entrapped into surface-modified liquid crystalline nanoparticles. Arch. Pharm. Res. 38, 534–542.

Madheswaran, T., Baskaran, R., Thapa, R.K., Rhyu, J.Y., Choi, H.Y., Kim, J.O., Yong, C.S., Yoo, B.K., 2013. Design and in vitro evaluation of finasteride-loaded liquid crystalline nanoparticles for topical delivery. AAPS Pharmscitech. 14, 45–52.

Madheswaran, T., Baskaran, R., Yong, C.S., Yoo, B.K., 2014. Enhanced topical delivery of finasteride using glyceryl monooleate-based liquid crystalline nanoparticles stabilized by cremophor surfactants. AAPS Pharmscitech. 15, 44–51.

Madheswaran, T., Baskaran, R., Yoo, B.K., Kesharwani, P., 2017. In vitro and in vivo skin distribution of 5 alpha-reductase inhibitors loaded into liquid crystalline nanoparticles. J Pharm. Sci.-US 106, 3385–3394.

Mamani, J.B., Costa, A.J., Cornejo, D.R., Vieira, E.D., Gamarra, L.F., 2013. Synthesis and characterization of magnetite nanoparticles coated with lauric acid. Mater. Charact. 81, 28–36.

Matos, B.N., Reis, T.A., Gratieri, T., Gelfuso, G.M., 2015. Chitosan nanoparticles for targeting and sustaining minoxidil sulphate delivery to hair follicles. Int. J. Biol. Macromol. 75, 225–229.

Musazzi, U.M., Santini, B., Selmin, F., Marini, V., Corsi, F., Allevi, R., Ferretti, A.M., Prosperi, D., Cilurzo, F., Colombo, M., Minghetti, P., 2017. Impact of semi-solid formulations on skin penetration of iron oxide nanoparticles. J. Nanobiotechnol. 15.

Nakamoto, K., 1986. Infrared and Raman Spectra of Inorganic and Coordination Compounds. John Wiley & Sons, New York.

Noor, N.M., Sheikh, K., Somavarapu, S., Taylor, K.M.G., 2017. Preparation and characterization of dutasteride-loaded nanostructured lipid carriers coated with stearic acid-chitosan oligomer for topical delivery. Eur. J. Pharm. Biopharm. 117, 372–384.

Pereira, M.N., Schulte, H.L., Duarte, N., Lima, E.M., Sa-Barreto, L.L., Gratieri, T., Gelfuso, G.M., Cunha-Filho, M.S.S., 2017. Solid effervescent formulations as new approach for topical minoxidil delivery. Eur. J. Pharm. Sci. 96, 411–419.

Popplewell, J., Sakhnini, L., 1995. The dependence of the physical and magnetic-properties of magnetic fluids on particle-size. J. Magn. Magn. Mater. 149, 72–78.

Pöttler, M., Staicu, A., Zaloga, J., Unterweger, H., Weigel, B., Schreiber, E., Hofmann, S., Wiest, I., Jeschke, U., Alexiou, C., Janko, C., 2015. Genotoxicity of superparamagnetic iron oxide nanoparticles in granulosa cells. Int. J. Mol. Sci. 16, 26280–26290.

Pradhan, P., Giri, J., Banerjee, R., Bellare, J., Bahadur, D., 2007. Cellular interactions of lauric acid and dextran-coated magnetite nanoparticles. J. Magn. Magn. Mater. 311, 282–287.

Radtke, M., Patzelt, A., Knorr, F., Lademann, J., Netz, R.R., 2017. Ratchet effect for nanoparticle transport in hair follicles. Eur. J. Pharm. Biopharm. 116, 125–130.

Rao, Y.F., Zheng, F.Y., Liang, X.G., Wang, H.Y., Zhang, J., Lu, X.Y., 2015. Penetration profile and human cadaver skin distribution of finasteride from vesicular nanocarriers. Drug Deliv. 22, 1003–1009.

Rao, Y.F., Zheng, F.Y., Zhang, X.G., Gao, J.Q., Liang, W.Q., 2008. In vitro percutaneous permeation and skin accumulation of finasteride using vesicular ethosomal carriers. AAPS Pharmscitech. 9, 860–865.

Raynaud, J.P., Cousse, H., Martin, P.M., 2002. Inhibition of type 1 and type 2 5 alpha-reductase activity by free fatty acids, active ingredients of permixon((R)). J. Steroid Biochem. 82, 233–239.

Rivera, L.M.R., Paterno, L.G., Chaves, N.L., Gregurec, D., Bao, S.N., Moya, S.E., Jain, M., Azevedo, R.B., Morais, P.C., Soler, M.A.G., 2019. Biocompatible superparamagnetic carriers of chondroitin sulfate. Mater. Res. Express 6.

Rosen, R.C., Roehrborn, C.G., Manyak, M.J., Palacios-Moreno, J.M., Wilson, T.H., Lulic, Z., Giuliano, F., 2019. Evaluation of the impact of dutasteride/tamsulosin combination therapy on libido in sexually active men with lower urinary tract symptoms (LUTS) secondary to benign prostatic hyperplasia (BPH): a post hoc analysis of a prospective randomised placebo-controlled study. Int. J. Clin. Pract. 73.

Sadick, N.S., Callender, V.D., Kircik, L.H., Kogan, S., 2017. New insight into the pathophysiology of hair loss trigger a paradigm shift in the treatment approach. J. Drugs Dermatol. 16, 5–10.

Shanshanwal, S.J.S., Dhurat, R.S., 2017. Superiority of dutasteride over finasteride in hair regrowth and reversal of miniaturization in men with androgenetic alopecia: a randomized controlled open-label, evaluator-blinded study. Indian J. Dermatol. Vet. 83, 47–54.

Silva, L.A., Andrade, L.M., de Sa, F.A., Marreto, R.N., Lima, E.M., Gratieri, T., Taveira, S.F., 2016. Clobetasol-loaded nanostructured lipid carriers for epidermal targeting. J. Pharm. Pharmacol. 68, 742–750.

Soler, M.A.G., Alcantara, G.B., Soares, F.Q., Viali, W.R., Sartoratto, P.C., Fernandez, J.R.L., da Silva, S.W., Garg, V.K., Oliveira, A.C., Morais, P.C., 2007. Study of molecular surface coating on the stability of maghemite nanoparticles. Surf. Sci. 601, 3921–3925.

Soler, M.A.G., Fanyao, Q., 2012. Raman spectroscopy of iron oxide nanoparticles. In: Kumar, C.S.S.R. (Ed.), Raman Spectroscopy of Nanomaterials Characterization. Springer, Berlin.

Soler, M.A.G., Paterno, L.G., 2017. Magnetic Nanomaterials, in: F. Leite, M.F., O.N. Oliveira Jr. (Ed.), Nanostructures. Elsevier Oxford, United Kingdom.

St Pierre, S.A., Vercellotti, G.M., Donovan, J.C., Hordinsky, M.K., 2010. Iron deficiency and diffuse nonscarring scalp alopecia in women: more pieces to the puzzle. J. Am. Acad. Dermatol. 63, 1070–1076.

Tabbakhian, M., Tavakoli, N., Jaafari, M.R., Daneshamouz, S., 2006. Enhancement of follicular delivery of finasteride by liposomes and niosomes – 1. In vitro permeation and in vivo deposition studies using hamster flank and ear models. Int. J. Pharmaceut. 323, 1–10.

Tian, G.C., Stuart, J.D., Moss, M.L., Domanico, P.L., Bramson, H.N., Patel, I.R., Kadwell, S.H., Overton, L.K., Kost, T.A., Mook, R.A., Frye, S.V., Batchelor, K.W., Wiseman, J.S., 1994. 17-Alpha-(N-tert-butylcarbamoyl)-4-aza-5-alpha-androstan-1-en-3-one is an active-site-directed slow time-dependent inhibitor of human steroid 5-alpha-reductase-1. Biochemistry-US 33, 2291–2296.

Tsai, T.F., Choi, G.S., Kim, B.J., Kim, M.B., Ng, C.F., Kochhar, P., Jasper, S., Brotherton, B., Orban, B., Lulic, Z., 2018. Prospective randomized study of sexual function in men taking dutasteride for the treatment of androgenetic alopecia. J. Dermatol. 45, 799–804.

Viali, W.R., Alcantara, G.B., Sartoratto, P.P.C., Soler, M.A.G., Mosiniewicz-Szablewska, E., Andrzejewski, B., Morais, P.C., 2010. Investigation of the molecular surface coating on the stability of insulating magnetic oils. J. Phys. Chem. C 114, 179–188.

Wilson, V., Siram, K., Rajendran, S., Sankar, V., 2018. Development and evaluation of finasteride loaded ethosomes for targeting to the pilosebaceous unit. Artif. Cell Nanomed. B 46, 1892–1901.

Zhou, Z.B., Song, S.Q., Gao, Z.L., Wu, J.T., Ma, J.J., Cui, Y.S., 2019. The efficacy and safety of dutasteride compared with finasteride in treating men with androgenetic alopecia: a systematic review and meta-analysis. Clin. Interv. Aging 14, 399–406.

A2. Artigos publicados fora do contexto desta dissertação

polymers

MDPI

Article

UV-Accelerated Synthesis of Gold Nanoparticle–Pluronic Nanocomposites for X-ray Computed Tomography Contrast Enhancement

Deizilene S. B. Gomes [1,2], Leonardo G. Paterno [3], Aline B. S. Santos [1], Debora P. P. Barbosa [1], Beatriz M. Holtz [4], Maysa R. Souza [4], Rafaianne Q. Moraes-Souza [4], Aisel V. Garay [5], Laise R. de Andrade [6], Patricia P. C. Sartoratto [7], Damien Mertz [8], Gustavo T. Volpato [4], Sonia M. Freitas [5] and Maria A. G. Soler [1,*]

[1] Universidade de Brasilia, Instituto de Física, Laboratório de Nanofilmes e Nano Dispositivos, Brasilia-DF 70910-900, Brazil
[2] Instituto Federal de Educação, Ciencia e Tecnologia de Rondonia, Ji-Parana-RO 76900-730, Brazil
[3] Universidade de Brasilia, Instituto de Quimica, Laboratorio de Pesquisa em Polimeros e Nanomateriais, Brasilia-DF 70910-900, Brazil
[4] Federal University of Mato Grosso, Institute of Biological and Health Sciences, Laboratory of System Physiology and Reproductive Toxicology, Barra do Garças-MT 78605-091, Brazil
[5] Universidade de Brasilia, Instituto de Ciências Biológicas, Departamento de Biologia Celular, Laboratório de Biofisica Molecular, Brasilia-DF 70910-900, Brazil
[6] Universidade de Brasilia, Instituto de Ciências Biologicas, Brasilia-DF 70910-900, Brazil
[7] Universidade Federal de Goias, Instituto de Quimica, Goiania-GO 74690-900, Brazil
[8] Institut de Physique et Chimie des Materiaux de Strasbourg (IPCMS), UMR-7504 CNRS-Universite de Strasbourg, 23 rue du Loess, BP 34, CEDEX 02, 67034 Strasbourg, France
* Correspondence: soler@unb.br

Abstract: Eco-friendly chemical methods using FDA-approved Pluronic F127 (PLU) block copolymer have garnered much attention for simultaneously forming and stabilizing Au nanoparticles (AuNPs). Given the remarkable properties of AuNPs for usage in various fields, especially in biomedicine, we performed a systematic study to synthesize AuNP-PLU nanocomposites under optimized conditions using UV irradiation for accelerating the reaction. The use of UV irradiation at 254 nm resulted in several advantages over the control method conducted under ambient light (control). The AuNP-PLU-UV nanocomposite was produced six times faster, lasting 10 min, and exhibited lower size dispersion than the control. A set of experimental techniques was applied to determine the structure and morphology of the produced nanocomposites as affected by the UV irradiation. The MTT assay was conducted to estimate IC50 values of AuNP-PLU-UV in NIH 3T3 mouse embryonic fibroblasts, and the results suggest that the sample is more compatible with cells than control samples. Afterward, in vivo maternal and fetal toxicity assays were performed in rats to evaluate the effect of AuNP-PLU-UV formulation during pregnancy. Under the tested conditions, the treatment was found to be safe for the mother and fetus. As a proof of concept or application, the synthesized Au:PLU were tested as contrast agents with an X-ray computed tomography scan (X-ray CT).

Keywords: gold nanoparticle; Pluronic F127; nanocomposites; UV accelerated synthesis; X-ray computed tomography; cytotoxicity; maternal and fetal toxicity assays

check for updates

Citation: Gomes, D.S.B.; Paterno, L.G.; Santos, A.B.S.; Barbosa, D.P.P.; Holtz, B.M.; Souza, M.R.; Moraes-Souza, R.Q.; Garay, A.V.; de Andrade, L.R.; Sartoratto, P.P.C.; et al. UV-Accelerated Synthesis of Gold Nanoparticle–Pluronic Nanocomposites for X-ray Computed Tomography Contrast Enhancement. *Polymers* **2023**, *15*, 2163. https://doi.org/10.3390/polym15092163

Academic Editor: Marinos Pitsikalis

Received: 1 March 2023
Revised: 1 April 2023
Accepted: 5 April 2023
Published: 1 May 2023

1. Introduction

Gold nanoparticles (AuNPs) display unique physicochemical properties, mainly related to the localized surface plasmon resonance (LSPR) phenomenon and following applications [1,2]. For multiple purposes, they are engineered into highly stable colloidal suspensions, and using different surface functionalization procedures, they show biocompatibility and colloidal stability in physiological conditions and in vivo assays [3,4]. Consequently, this nanomaterial has recently found meaningful applications in cell imaging and therapeutic processes in addition to different types of optoelectronic devices such as biosensors, solar cells, and surface-enhanced Raman spectroscopy, as well as in photocatalysis [5–12]. In the biomedical field, AuNPs have been used in electrochemical dopamine sensors [13] and intensified in early diagnosis of Parkinson's disease [14]. New approaches to the fabrication of sensing platforms have been proposed, for instance, combining plasmonically active waveguides with microfluidics [15] or using single plasmonic nanoparticles as ultrasensitive sensors [16]. Concerning therapeutic uses, studies suggested AuNP systems for the controlled delivery of anticancer agents, resulting in enhanced antitumor activity with negligible toxicity to major organs [17]. Despite this, there is a need to thoroughly investigate the potential toxicological effects of AuNPs during pregnancy, particularly given their ability to cross the placental barrier and enter fetal circulation [18,19]. Studies have suggested that the size, shape, surface charge, and surface coating of gold nanoparticles can impact their toxicity, and it is likely that the same factors will influence their potential effects during pregnancy [19]. In addition, the route of administration may also be an important consideration, as the risks associated with intravenous administration may differ from those associated with topical or oral administration. Thereby, it is necessary to know all their possible toxicological effects [20] in order to harness all the advantages offered by this nanomaterial when delivering therapeutic formulations.

Regarding the light–matter interaction, the LSPR phenomenon in metal nanoparticles (NPs) is based on the resonance condition achieved between the frequencies for the collective oscillation of conduction band electrons in the NPs and the incident electromagnetic radiation. In the resonance condition, the wavelength of incident light is about ten times greater than the size of the NPs when the maximum LSPR extinction is reached. The resulting and very active LSPR band leads to unique scattering and absorption spectra for the NPs. In terms of NP structure, the resonance frequency depends on their size, shape, aggregation extent, surface chemistry, dielectric properties of the surrounding medium, and the level of interparticle interactions.

Among synthetic/engineering methods for producing AuNP with tailored characteristics, chemical methods have been dominant so far, enabling the production of a variety of nanostructures in sizeable amounts [21–23]. In addition, new approaches have been developed such as the novel high-throughput (HTP) synthetic platform for AuNPs, consisting of an HTP centrifugal microfluidic device and a portable automatic workstation. [24], sodium glutamate and sodium dodecyl sulfate as reducing and stabilizing agents [25], using the block copolymer template approach [26], and continuous in-flight synthesis [27]. Eco-friendly approaches have also been explored, for example, using natural extracts [28], biocompatible polymers [29], or light of different wavelengths [30] as reducing agents.

A particular type of chemical synthesis, which is the subject of the present contribution, is that performed at room temperature by simply mixing aqueous chloroauric acid ($HAuCl_4$) and FDA (Food and Drug Administration)-approved block copolymers displaying a triblock PEO–PPO–PEO structure PEO: poly(ethylene oxide); PPO: poly(propylene oxide). Commercially available under the name Pluronic, one of its several grades, F-127 was used in this study These copolymers are water soluble and work simultaneously as reducing and stabilizer agents [29]. The main advantage of such a method is that colloidal stabilization is achieved simultaneously with NP formation and no other reducing agent is required. The dynamics of the redox reactions and the size and size distribution of the produced AuNPs are influenced by the Au:copolymer stoichiometry and the copolymer molecular weight/architecture. Indeed, these variables can be adjusted to produce AuNPs with controlled size and distribution. Isothermal calorimetry titration performed in a subsequent study revealed that during the formation of F127:Au nanocomposites, at a very low F127:Au molar ratio (below 0.05), the association between tetrachloroaurate anion ($AuCl_4^-$) and F127 is the prevailing event (exothermic process). However, at a larger F127:Au (0.05 to 0.12), particle growth becomes dominant when the Au^0 nuclei and poly(propylene oxide) block interact by entropic hydrophobic forces [31]. In parallel, cyclic voltammetry indicated that complete reduction of Au^{3+} occurs only above the critical micellar concentration (cmc)

(~0.2–0.8 wt%) of F127 [31]. Another study suggested that the size and polydispersity of these AuNPs depend almost exclusively on the copolymer concentration [32].

A recent detailed study on the formation of AuNPs as a result of the reduction of chloroauric acid with Pluronic block copolymers [33] demonstrated that in the course of this reaction, the copolymer chains undergo oxidation, although the oxidation of the polymer does not go all the way down to carboxylic acids. Analysis of the soluble products suggested that the copolymer undergoes partial degradation, preferentially at the PPO sites, with cleavage of the C–O bonds. Although the purified AuNPs contained organic components (13%, m/m), no PPO groups were observed in them, suggesting that PPO chains or intact Pluronic molecules are not adsorbed on the particle surface. Interestingly, the analysis of soluble products revealed the presence of the CH_3 group of PPO. The product analysis also indicated the presence of newly formed OH groups both in the purified AuNPs and in the soluble products. The reaction involves the formation of free radicals and hydroperoxides, which depends on the oxygen concentration. The purified nanoparticles contain organic components but can be fully separated from the excess of the copolymer. Various reaction parameters such as pH, temperature, sodium chloride addition, and the concentration of the reactants affect the rate of the reaction and the yield and morphology of the resulting AuNPs [33]. A further step to optimize this synthesis process would be the implementation of UV irradiation to accelerate the synthesis and to control shape and physicochemical properties of the produced NPs [34–38]. The UV irradiation generates a photoexcited species ($[AuCl_4]^{-*}$) that undergoes successive disproportionation and reduction reactions leading to the formation of metallic gold atoms and the initial formation of gold nanoparticles [37]. This reduction process is faster than that promoted by the block copolymer alone, which mainly functions as a template for the formation of the nanoparticles. As a result of these different reaction dynamics, better control of the size distribution of the nanoparticles can be achieved.

Aiming at optimizing this eco-friendly, one-step synthesis method, by simply mixing aqueous chloroauric acid ($HAuCl_4$) and PLU, here we report a systematic study involving the synthesis of Au:PLU nanocomposites assisted with UV irradiation. We found that the most important benefits of using UV irradiation 254 nm/16 W were that an Au:PLU nanocomposite of a specific formulation is produced about six times faster and with lower size dispersion than that made under ambient light. Those are great advantages since they offer a more cost-effective way to fabricate AuNPs with tailored properties to enable their use in different fields, especially in the biomedical field. A set of experimental techniques (UV-vis, Fourier Transform Infrared (FTIR) spectroscopies, thermogravimetry (TGA), transmission electron microscopy (TEM), measurement of the sedimentation coefficient using analytical ultracentrifugation (SV-AUC), and cyclic voltammetry) was performed to determine the structure and morphology of the nanocomposites as affected by UV irradiation. Then, the biological properties of the Au:PLU nanocomposites were assessed using in vitro cytotoxicity and in vivo maternal and fetal toxicity assays in rats. As a proof of concept or application, the Au:PLU synthesized in the absence/presence of UV irradiation were tested as contrast agents in an X-ray computed tomography scan (X-ray CT).

2. Materials and Methods

2.1. Materials

Pluronic block copolymer F-127 (PLU, MW 12,600 g/mol), chloroauric acid trihydrate ($HAuCl_4.3H_2O$) 99%, and dimethyl sulfoxide (DMSO) were purchased from Sigma–Aldrich (St. Louis, MO, USA). Analytical grade HCl 36%, HNO_3 65%, and KCl 99% were purchased from Vetec, Duque de Caxias-RJ, Brazil. All chemicals were used as received. All experimental procedures, including solution preparations and glassware cleaning, were performed with ultra-pure water (resistivity: 18 MΩ/cm) supplied by a Millipore Milli-Q water purification system. UV-assisted synthesis of AuNP-PLU nanocomposites was carried out in borosilicate beakers (5 mL), previously cleaned with aqua regia solution (HCl/HNO_3, 3:1, v/v) and rinsed properly with ultrapure water.

2.2. UV-Assisted Synthesis of AuNP-PLU Colloidal Nanocomposites

Precursor aqueous solutions of $HAuCl_4$ and PLU were prepared at room temperature with magnetic stirring. Colloidal AuNP-PLU were synthesized following the standard protocol as reported in [31] using gentle hand mixing of PLU and $HAuCl_4$ aqueous solutions at proper compositions (10:1 v/v) and then leaving them to rest. Additionally, part of the reaction mixture was submitted to UV irradiation (254 nm, 16 W, 25 °C) inside a lab-made chamber as reported elsewhere [37]. Two sets of AuNP-PLU samples were prepared, with either fixed or varied concentrations of $HAuCl_4$ and PLU, as described in Table 1. In group 1, samples were prepared with a fixed 2 mmol L^{-1} $HAuCl_4$ concentration and PLU concentrations (X) varied between 0.1 and 10 mmol L^{-1}. Samples labeled "UV" denote the reaction performed under UV 254 nm irradiation. This range of PLU concentrations comprises values below and above its critical micellar concentration (CMC), which is 0.6 mmol L^{-1} [39]. In group 2, the PLU concentration was kept fixed at 2.0 mmol L^{-1} to ensure the micellar structure, whereas the $HAuCl_4$ concentration (Y) was varied between 1.0 and 4.0 mmol L^{-1}, resulting in samples labeled YUV:AuNP-PLU. Control samples were prepared in the same way but under ambient light. The UV-assisted syntheses were carried out for different periods of time, up to 50 min, while the control sample was carried out for up to 300 min. Nonetheless, the reaction reached completion at about 10 min for most of the AuNP-PLU compositions, when it could be detected a color change in the reaction mixture from yellow to pink (Figure 1A). The UV-vis spectra precursors and control samples can be found in Supplementary Figure S1. After syntheses, the samples were transferred to common Eppendorf tubes (2 mL) and centrifuged (Mikro 22R, HETTICH Zentrifugen, Tuttlingen, Germany) at 12,000 rpm for 120 min at 10 °C to remove the excess PLU. In order to conduct Raman characterization and thermogravimetric analysis (TGA), solid samples of AuNP-PLU were obtained using extensive centrifugation and lyophilization as previously described [31] The obtained powder sample was labeled s-AuNP-PLU:XUV.

Table 1. Labeling of samples resulting from mixtures of aqueous solutions of precursors.

Samples	**Concentration (mmol L^{-1})**	
	PLU (*X*)	**$HAuCl_4$ (*Y*)**
AuNP-PLU:0.1UV	0.1	2.0
AuNP-PLU:0.3UV	0.3	
AuNP-PLU:0.5UV	0.5	
AuNP-PLU:1.0UV	1.0	
AuNP-PLU:2.0UV	2.0	
AuNP-PLU:4.0UV	4.0	
AuNP-PLU:6.0UV	6.0	
AuNP-PLU:8.0UV	8.0	
AuNP-PLU:10.0UV	10.0	
1.0UV:AuNP-PLU	2.0	1.0
3.0UV:AuNP-PLU		3.0
4.0UV:AuNP-PLU		4.0

2.3. Structural and Morphological Characterizations

Ambient light and UV-assisted syntheses were continuously monitored, ex situ, using UV-vis spectroscopy in the range of 185–900 nm, at 0.1 nm resolution, and a scan rate of 600 nm/min (0.1 s integration by 1 nm) the spectrophotometer (Shimadzu UV 2600, Shimadzu Europe, Duisburg, Germany) and quartz cuvette of 1.0 cm optical path. UV-vis spectra were recorded at different time intervals until the absorbance of the LSPR band reached a plateau. FTIR spectra were registered using the attenuated total reflectance (ATR) method (Novertex 70, Bruker Corporation, Billerica, MA, USA), with a spectral resolution of 4 cm^{-1} and 1 scan/min for 27 min. An aliquot of 10 µL of the colloidal suspensions AuNP-PLU:2.0UV, AuNP-PLU:2.0 (used as control), or plain PLU solution was dropped onto the ATR crystal and left to dry. Afterward, successive spectra were recorded, monitoring the water's hydroxyl stretching band (ν O–H), in order to confirm the sample was dried before registering representative spectra of samples.

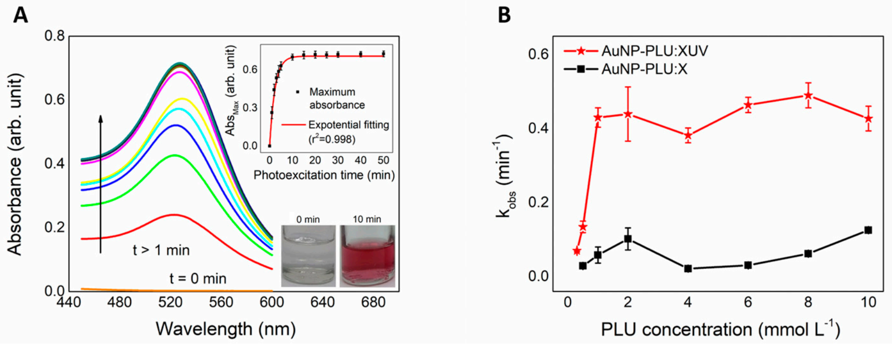

Figure 1. (**A**) UV-vis spectra obtained from monitoring the AuNP-PLU:2.0UV formation from the precursor mixture (HAuCl4 + PLU) at t = 0 and after 10 min. The formation of the AuNP-PLU:2.0UV nanocomposite is observed after 10 min. The lower and upper insets show digital snapshots of the reaction mixture at t = 0 min and t = 10 min and changes in the maximum absorption for AuNP-PLU:2.0UV of the plasmonic band during the photoexcitation time, respectively. (**B**) The observed rate constant of AuNP-PLU:2.0UV and AuNP-PLU:2.0 by the PLU concentration used in the synthesis process, as indicated.

Thermogravimetric analysis (TGA) curves were registered with a DTG60H (Shimadzu Corporation, Kyoto, Japan) system from 25 to 600 °C with a heating rate of 10 °C/min in a N_2 atmosphere with a flux rate of 30 mL/min in an aluminum sample holder. This equipment provides measurements with an uncertainty of 0.5%/weight.

The morphology of the AuNP-PLU samples was observed using transmission electron microscopy (TEM) carried out with a JEOL 2100 microscope. The mean diameter (DTEM) and polydispersity index (σ) were determined from size histograms fitted with a log-normal distribution function. The diameters of approximately 1000 particles, measured with the aid of the Image J software in different TEM images, were used to build the histograms. In addition, the hydrodynamic diameter and zeta potential of colloidal samples were determined using dynamic light scattering and electrophoresis mobility, respectively, measured with a Zetasizer Nano ZS Malvern Instruments, UK. The analyses were performed at a scattering angle of 173° at 25 °C using a 4 mW He-Ne laser operating at 632.8 nm.

Cyclic voltammetry (CV) was used to estimate the amount of Au^{+3} ions that were not reduced during synthesis and thus qualitatively evaluate the efficiency of chemical/photochemical reduction. Voltammograms were recorded with a Metrohm potentiostat/galvanostat model Autolab PGSTAT 204 in a three-electrode configuration cell (Ag/AgCl reference electrode with saturated KCl, Pt wire as the counter electrode, and an indium-doped tin oxide (ITO) slide—0.60 cm^2 active area—as the working electrode). The electrochemical cell was filled with the $HAuCl_4$-PLU mixtures or AuNP-PLU samples containing KCl (0.1 mol L^{-1}) as the supporting electrolyte. Experiments were carried out at 25 °C at 50 mV/s after purging the electrochemical cell with N_2 for 5 min.

The particles produced using UV irradiation (AuNP-PLU:2.0UV) and using ambient light (AuNP-PLU:2.0) were investigated with sedimentation velocity analytical ultracentrifugation (SV-AUC) using a Proteome-Lab XL-A analytical ultracentrifuge equipped with a 4-hole titanium An-60 Ti rotor, cells with 12 mm path length, a double channel centerpiece, and quartz windows (Beckman Coulter, Brea, CA, USA). The assay was carried out at 2500 rpm at 20 °C in a vacuum system. Absorbance was measured at two wavelengths (260 and 530 nm) at scanning intervals for each sample reading of 2 min with 0.007 cm radial resolution. PLU absorbs at 260 nm, whereas AuNP-PLU absorbs at 530 nm. The collected radial scans were analyzed using the size distribution analysis ls-g(s) model with the SEDFIT v14.7 software using a resolution of 400, a sedimentation coefficient analysis interval of 0–10,000, and a confidence level of 0.951. The c(s) was calculated using the appropriate correction for the viscosity and density of water at 20 °C (S20,w) with the SEDFIT software.

2.4. Cell Viability Test

2.4.1. Cell Culture

NIH-3T3 mouse embryonic fibroblast cells (ATCC® CRL-1658TM) were cultured in Dulbecco's Modified Eagle Medium (DMEM, Gibco® Life Technologies, Ltd., Carlsbad, CA, USA) supplemented with 10% (*v*/*v*) fetal bovine serum (Gibco® Invitrogen™, Waltham, MA, USA) and antibiotics (100 IU mL^{-1} penicillin and 100 µg mL^{-1} streptomycin-Sigma-Aldrich) at 37 °C in a 5% CO_2 incubator.

2.4.2. In Vitro Cytotoxicity Assay

The NIH-3T3 cells were seeded at a density of 5 × 103 cells per well in 96-well plates. After 24 h of incubation, 200 µL of the culture medium containing AuNP-PLU:2.0UV (0.22 to 3.4 µM AuNP; 0.03–0.41 mM PLU) were added to the wells for 15 min or 24 h. Following 15 min exposure, cells were rinsed twice with phosphate buffer saline (PBS pH 7.4), and then the culture conditions were reestablished for 24 h. The potential cytotoxic effect was determined using a (4,5-dimethylthiazol-2-yl)-2,5-diphenyltetrazolium bromide (MTT) (Waltham, MA, USA) assay. Cells were incubated with MTT solution (5 mg mL^{-1}) for 2 h, and the colorimetric product, formazan crystals, was solubilized in DMSO. The absorbance values were measured with a spectrophotometer (Molecular Devices SpectraMax M2®, Silicon Valley, CA, USA) at 595 nm. The raw data were normalized to the control data (cells treated with culture medium containing PBS, PBS replaced AuNP-PLU:2.0UV). The IC50 value (half-maximal inhibitory concentration) was calculated using a nonlinear regression dose–response analysis with AuNP concentration in logarithm. Results were expressed as mean ± standard deviation (SD) of triplicate determinations from three independent experiments (n = 9/concentration). The AuNP-PLU:2.0 (0.05 to 0.86 µM AuNP; 0.03–0.48 mM PLU) and PLU solutions were tested under the same conditions for comparison purposes.

2.5. In Vivo Maternal and Fetal Toxicity of AuNP-PLU:2.0UV in Rats

Adult female (180–200 g) and male (220–240 g) Wistar rats were maintained in cages for three rats with autoclaved wood chips under standard laboratory conditions (23 ± 2 °C, humidity 50 ± 10%, 12 h light/dark cycle), with pelleted food and tap water provided ad libitum. The local Experimental Ethical Committee for Animal Research approved procedures and animal handling protocols used in this study (Protocol Number: 23108.022668/2019-23).

After two weeks of acclimation in the vivarium of the Laboratory of System Physiology and Reproductive Toxicology, Federal University of Mato Grosso (UFMT), all female rats were mated overnight with male rats. Gestational day zero (D0) was recorded and assigned the following morning when spermatozoa were found in the vagina smear [40]. The pregnant rats were randomly distributed using computer random numbers into two experimental groups (n = 12 animals/group): Control = pregnant rats treated with water and Treated = pregnant rats treated with AuNP-PLU:2.0UV. The rats were treated with AuNP-PLU:2.0UV or vehicle (water) in the morning with the intragastric route (gavage) during pregnancy (from gestational day 0 to 21). The dosage selection of AuNP-PLU (137.5 µg/kg) was made according to the previously reported dose [4], which in humans is equivalent to 22 µg/kg based on the body surface area (BSA) [41].

On days 0, 7, 14, and 21 of pregnancy (at 9 a.m.), the maternal body weights, food, and water consumption were determined. On day 21 of pregnancy, the rats were anesthetized using sodium pentobarbital (Thiopentax®-120 mg/kg). Then, they were submitted to laparotomy for exposure to uterine horns. The gravid uterus was, withdrawn, weighed, and dissected. The percentage of embryonic loss before and after implantation was calculated [42]. Fetuses and placentas were weighed. Fetuses were then classified by body weight [43] and evaluated to determine the presence of external anomalies. After external analysis, half of the fetuses were fixed in Bouin's fluid, and serial sections were prepared as described by Wilson [44] for visceral examination. The remaining fetuses were prepared for an examination of skeletons using the staining procedure of Staples and Schnell [45]. In addition to the skeletal analyses, counting of ossification sites was performed to determine the degree of fetal development [46,47].

The Student's t-test was performed to evaluate mean values, whereas the Fisher Exact test was conducted to compare percentages. $p < 0.05$ was applied and considered as the limit of statistical significance.

2.6. X-ray Computed Tomography Scan

CT images were performed at the Laboratório de Caracterização Tecnológica, Escola Politécnica, Universidade de São Paulo-SP, Brazil. Liquid samples containing the synthesized nanocomposites were stored in Eppendorf and analyzed in batches containing 6 samples using the 3D X-ray microscope: Zeiss Xradia Versa XRM-510 equipment, for beam energies of 80, 100, 120, and 140 KV. The attenuation coefficients of air and deionized water were used for calibration. The AuNP-PLU:2.0UV with Au of 1.23 mg/mL sample was compared with Optiray@320_1 (Liebel-Flarsheim Company LLC, Raleigh, NC, USA (EUA) containing I at the same concentration (I = 1.23 mg/mL) and AuNP-PLU: 2.0 containing a Au concentration of 1.09 mg/mL was compared with Optiray@320_2 with I at the same concentration (I = 1.09 mg/mL).

3. Results and Discussion

3.1. Effect of the UV Light on the Features of Synthesized AuNP-PLU

3.1.1. Kinetics of UV-Assisted Synthesis of AuNP-PLU

The formation of the AuNP-PLU NC under UV light was monitored using UV-vis spectroscopy with the evolution of the typical LSPR band of AuNPs. An overview of the formation of AuNP-PLU:2.0UV, chosen as the reference sample, is provided in Figure 1. In Figure 1A, the UV-vis spectra recorded at different time intervals display the LSPR band typical of AuNPs from the very beginning of the reaction. The LSPR band is centered at 526 nm for t = 10 min. The inset in Figure 1A shows digital snapshots of the reaction mixture at t = 0 min and t = 10 min. After 10 min of reaction, the typical pink color of AuNPs is clearly seen. Otherwise, for the reaction carried out under ambient light, the formation of AuNPs is visually detected solely after 60 min (as observed in ref. [32], where the LSPR band is centered at 536 nm), thus indicating that UV irradiation accelerates the reaction and the LSPR band of AuNP-PLU:2.0UV is blue-shifted in comparison to the sample AuNP-PLU:2.0. Indeed, Supplementary Figure S2 displays isotherms for the formation of AuNP-PLU under ambient light (AuNP-PLU:2.0) (data from ref. [32]) and UV irradiation (AuNP-PLU:2.0UV). Although both isotherms show an asymptotic behavior, it is noted that the reaction is much faster in the presence of UV irradiation, which reaches equilibrium in about 10 min, in contrast to the reaction carried out under ambient light, which reaches equilibrium in about 60 min. Experimental data were further fitted with a first-order kinetics model as expressed by Equation (1):

$$Abs_{max} = Abs_{\infty}\left(1 - exp^{-k_{obs}t}\right) \tag{1}$$

In Equation (1), Abs_{max} is the maximum LSPR absorbance (in arbitrary units) in the reaction time t (expressed in min), Abs_{∞} is the absorbance of the LSPR band at an infinite time of reaction (in arbitrary units), k_{obs} is the observed rate constant (in min^{-1}), and t is the reaction time (in min). As shown in Figure 1B, k_{obs} becomes independent of the PLU concentration as the cmc condition is reached for both reaction conditions (ambient light and UV irradiated). Nonetheless, k_{obs} is about four times larger under UV irradiation.

3.1.2. Evaluation of the Yield of AuNP-PLU-UV Production

Cyclic voltammetry (CV) was used to further investigate the effect of the UV irradiation by measuring the amount Au^{+3} ions left over during reduction by PLU. This experiment was conducted with the sample AuNP-PLU:0.1UV, which was produced with the lowest PLU concentration, as well as with the sample 4.0UV:AuNP-PLU, which was produced with the largest $HAuCl_4$ concentration. In addition, the experiment also used the sample AuNP-PLU:0.5, which was prepared under ambient light with the smallest PLU concentration, but sufficient to produce sizeable amounts of AuNPs. As shown in Figure 2A, the voltammogram (green curve) of the plain HAuCl4 solution clearly shows the Au^0/Au^{3+} redox pair at +1.0 V and +0.56 V, respectively, plus the cathodic wave for Au^{1+}/Au^0 at –0.2 V. The voltammogram of plain PLU shows a subtle anodic event at +0.11 V. Indeed, this is sufficient to reduce Au^{3+} to Au^0, which occurs at a much higher potential, as discussed in a previous contribution [32]. On the other hand, these electrochemical signals almost disappear in the voltammograms of the nanocomposites as a result of the Au^{3+} reduction. Nonetheless, the sample AuNP-PLU:0.5 still has a considerable residual amount of Au^{3+} (about 7 wt%), whereas in AuNP-PLU:0.1UV, the nanocomposite produced under UV irradiation, this amount is only 0.3 wt%, even though this sample was produced using a 5-fold lower PLU concentration. It is worth noting that the sample 4.0UV:AuNP:PLU, which was produced in a less favorable composition with an excess of $HAuCl_4$, presented only 1.5 wt% of unreduced gold ions. These observations are corroborated further by the UV-vis spectra of these samples, as shown in Figure 2B. In particular, the absorption of $AuCl_4^-$ species at 220 nm is only detectable in the spectra of the plain $HAuCl_4$ solution and AuNP:PLU:0.5, which were not submitted to UV irradiation. In summary, the implementation of UV irradiation not only accelerated the reaction performed under ambient light but also increased its yield, even at a very low PLU concentration (AuNP-PLU:0.1UV).

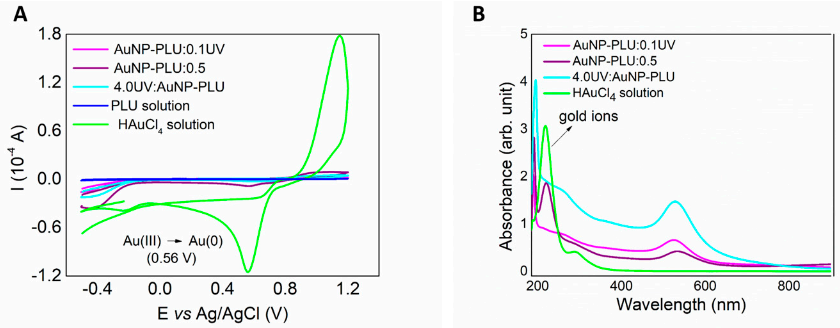

Figure 2. Cyclic voltammograms of the HAuCl4 solution at a concentration of 2.0 mmol L^{-1}, and the AuNP-PLU:0.1UV (lowest PLU concentration), 4.0UV:AuNP-PLU NCs, and AuNP-PLU:0.5 control sample, as indicated. (**B**) UV-vis spectra of the same samples displayed in (**A**), as indicated.

The percentual of PLU in the nanocomposites was estimated using TGA curves, shown in Supplementary Figure S3. The TGA curves of the plain PLU, AuNP-PLU:2.0UV, and AuNP-PLU:2.0 are very similar showing a single mass loss event around 400 °C, which is regarded as the degradation of PLU. According to the derivative TGA, however, the degradation of PLU occurs slightly below this temperature in the nanocomposites as a result of the oxidation of PLU by Au^{3+}. The estimated concentration of PLU in AuNP-PLU:2.0UV and AuNP-PLU:2.0 is approximately 20 mg/mL (1.58 mmol L^{-1}) and 24 mg/mL (1.90 mmol L^{-1}), respectively. In addition, the atomic absorption analysis performed on AuNP-PLU:2.0UV and AuNP-PLU:2.0 samples gives a gold concentration of 3.12 mmol L^{-1} and 2.77 mmol L^{-1}, respectively. These results corroborate those achieved by cyclic voltammetry, which also suggested that the UV-assisted synthesis process has a higher yield than that conducted under ambient light in the same compositional conditions.

3.1.3. Morphology of AuNP-PLU

The morphology of the nanocomposite and the mean size of the AuNP cores were evaluated using TEM. Typical TEM micrographs of the AuNP-PLU:2.0UV and AuNP-PLU:2.0 samples are provided in Figures 3A and 3B, respectively. Both samples are composed mainly of spheric-like nanoparticles. The high-resolution micrographs shown in the inset also reveal a high crystalline appearance with regularly spaced crystallographic planes. The interplanar distance in each sample was assessed using ImageJ software as follows: 2.36 Å (AuNP:PLU:2.0) and 2.37 Å (AuNP:PLU:2.0UV). These values are comparable to that provided by the Joint Committee on Powder Diffraction Standards-crystallographic plugs for the fcc structure of gold, which corresponds to the {111} family planes.

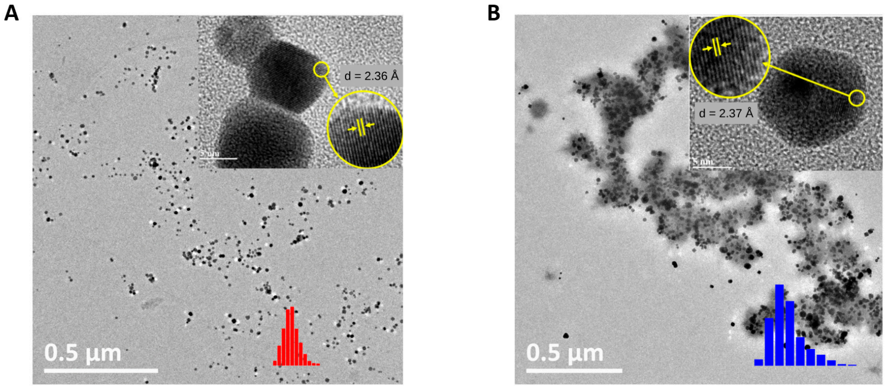

Figure 3. TEM micrographs of the AuNP-PLU:2.0UV sample (**A**) and of the AuNP-PLU:2.0 control (**B**) both with a scale bar of 0.5 µm and 5 nm in the respective insets. The upper insets depict a crystalline plane {111} of gold nanoparticles; the lower insets (red and blue) show the nanoparticle diameter histograms as vertical bars, as indicated. Data of (**B**) were reproduced with permission [31]. Copyright 2018, Elsevier B. V.

Particle size histograms were built with sizes measured in TEM micrographs and fitted with a log-normal distribution function give the following diameter (D_{TEM}) and standard diameter deviation (σ) attained from nanoparticle diameter histogram (vertical bars) fitted with a log-normal distribution function, as displayed in Supplementary Figure S4. The results were 12.2 ± 0.2 ($\sigma = 0.2 \pm 0.02$) and 18.5 ± 0.2 nm ($\sigma = 0.3 \pm 0.27$) for AuNp-PLU:2.0UV and AuNP-PLU:2.0 [31], respectively. It is noticeable that AuNPs prepared with UV irradiation are smaller with a standard diameter deviation lower than the control AuNp-PLU:2.0. These findings show an improvement in the morphology of AuNPs produced under UV irradiation. Furthermore, a thin polymeric coating around the UV-synthesized AuNPs is seen in the TEM images (Figure 3A), while AuNPs control samples are enfolded by the polymer (Figure 3B). Although the estimated concentration of PLU in AuNP-PLU:2.0UV is only 20% less than in AuNP-PLU:2.0, it is intriguing that only a thin PLU coating was seen in the micrographs of the former. This observation may be associated with the higher yield of AuNPs when using UV light, but it could also be related to a more extensive degradation/oxidation of PLU under UV light. These findings suggest an improvement in the morphology of AuNPs produced under UV irradiation.

The concentration of AuNPs present in the NCs was estimated considering the data of the mean diameter D_{TEMt} and the gold concentration obtained with atomic absorption measurements. The values found were 13.6 and 3.4 µmol L^{-1} for the AuNP-PLU-2.0UV and AuNP-PLU:2.0 samples, respectively. Considering those values as the amount of PLU being adsorbed by AuNPs, the molar ratios given by the amount of PLU by AuNPs [PLU/AuNPs] for AuNP-PLU:2.0UV and AuNP-PLU:2.0 are 116 and 559, respectively. These results indicate that the amount of PLU by AuNP in the control sample is approximately 4-fold greater than that in AuNP-PLU:2.0UV, which agrees with the TEM micrograph shown in Figure 3B.

According to the scattered intensity distribution data obtained with DLS measurements (Supplementary Figure S5), the average hydrodynamic diameter of AuNP-PLU:2.0UV and AuNPPLU:2.0 is 37.2 ± 2.2 nm and 50.2 ± 0.4 nm, respectively, with a PDI of 0.2. These findings indicated that the incidence of UV irradiation not only accelerates the reaction, but it also decreases the size of the AuNP cores and the hydrodynamic size produced by nanocomposites.

The size distribution of the NCs produced with UV-assisted synthesis and the control using environment light was further analyzed using the apparent sedimentation coefficient distribution (ls-g*(s)) in an SV-AUC assay, as described in the experimental section. This approach is used without any knowledge of the partial specific volumes of the sedimentation species, according to those previously described. Figure 4 displays the results for AuNP-PLU:2.0UV and AuNP-PLU:2.0.

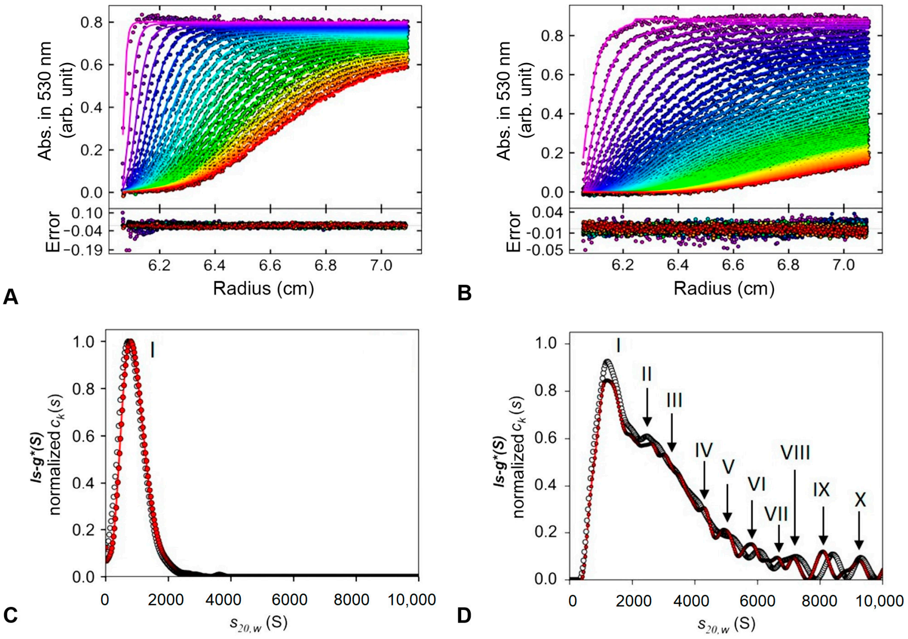

Figure 4. Sedimentation velocity analytical ultracentrifugation assay. Typical raw sedimentation profiles of absorbance at 530 nm versus cell radius for the particles present in the NCs are shown in (**A**,**B**). Residual plot produced using SEDFIT v14.7 software showing the fitting goodness. The lower panels show the apparent distributions of the sedimentation coefficient Is−g* (S) at 260 nm (black) and 530 nm (red) obtained for AuNP-PLU:2.0UV (**C**) and control AuNP-PLU:2.0 (**D**). The peaks correspond to different populations of nanoparticles and are indicated with Roman numerals.

When AuNP-PLU:2.0UV (Figure 4A) is subjected to a high-field centrifuge, uniform sedimentation of the particles is observed with an exponential curve behavior that reaches a concentration plateau (abs. ∼0.8). The best fit of the curve in Figure 4A was attained with a mathematical model based on the Lamm, which describes the spatial and temporal behavior of the concentration considering the sedimentation by mass transport by diffusion [48]. Using the ls-g*(s) procedure, fair RMS deviation values (<0.007) were obtained for both data sets. In the case of ls-g*(s) sedimentation profiles at 530 nm for photoexcited AuNP-PLU:2.0UV, a single peak (Figure 4C) with sedimentation coefficient S20,w of 947.10S was observed, indicating a homogeneous population of nanoparticles (Figure 4D and Table 2).

Table 2. Sedimentation parameters of the nanoparticles.

Synthesis Methods	Distribution at 530 nm			Distribution at 260 nm		
	ls-g* (S) Peaks	S20,w	Percentage Ratio (%)	ls-g* (S) Peaks	S20,w	Percentage Ratio (%)
Environment light (Control)	I	1451.17	43.21	I	1418.534	44.17
	II	2613.09	13.30	II	3555.02	43.80
	III	3477.32	20.04	III	6118.22	2.71
	IV	4403.81	5.24	IV	7145.20	3.26
	V	5030.07	4.98	V	8441.53	2.02
	VI	5811.97	3.67	VI	9364.58	1.69
	VII	6343.14	0.85			
	VIII	6681.68	1.44			
	IX	7198.76	1.44			
	X	8125.44	2.16			
photoexcited synthesis (UV)	I	947.10	99.36	I	857.78	99.15

However, for AuNP-PLU:2.0, which was produced under ambient light (Figure 4B), faster sedimentation is observed, which may be associated with the presence of larger particles. Similar to our previous report [31], the ls-g*(s) sedimentation distribution profiles at 260 nm and 530 nm for this NC showed the highest and broadest peak with smaller and less abundant ones, probably formed by heterogeneous particle populations according to the distribution analyses.

The main particle population measured at 530 nm corresponds to peak I (43.2%) with a sedimentation coefficient S20,w of 1451.17S, while the next two populations that contribute significantly are those related to peak II (13.3%) and III (20.04%) with 2613.09S and 3477.32S, respectively (Figure 4D and Table 2). Other peaks with less than 5% in the distribution analyzed are also detected, suggesting a small content of other particle sizes. A control experiment performed with plain PLU showed that the same conditions of ultracentrifugation are unable to sediment the polymer during the experimentation time. The similarity between the ls-g*(S) distribution versus S20,w at 260 and 530 nm of the samples suggests that all particles detected are formed by complexes of gold and polymer. The absence of polymeric aggregates without gold in its structure indicates that the presence of gold or UV irradiation, by itself, does not induce spontaneous aggregation of the polymer.

The SV-AUC results are in agreement with those found using transmission electron microscopy (TEM), presented in Figure 3, where the sample synthesized with UV photoexcitation (AuNP-PLU:2.0UV) presented a narrower size distribution. Indeed, the TEM and SV-AUC characterizations show that implementation of UV irradiation improves the reaction by producing samples with a more controlled size and size distribution.

3.1.4. The Role of UV Light and PLU on the Formation of AuNP-PLU

The results of the UV-vis and FTIR-ATR analyses presented in Figures 1 and 5 showed that the PLU and $HAuCl_4$ solutions do not show spectral variations when exposed to UV radiation. Thus, the formation of AuNP-PLU is surely related to the effect of irradiation in the reaction mixture (PLU + $HAuCl_4$).

The structural features of nanocomposites were evaluated further using ATR FTIR and Raman spectroscopies. As shown in Figure 5, the ATR-FTIR spectrum of plain PLU after being submitted to UV irradiation for 10 min does not show any signs of additional oxidation or any conformational change, remaining identical to that not exposed to UV [31]. On the other hand, the spectrum of AuNP-PLU:2.0UV contains an additional broad band between 1700 and 1750 cm^{-1}, which is ascribed to the C=O stretching in aldehydes, ketones, or carboxylic acids, thus confirming the oxidation of the polymer when irradiated in the presence of $AuCl_4^-$ ions. In addition, the ν(C-O-C) band is shifted to higher wavenumbers (1100 to 1110 cm^{-1}). This shift could be related to the presence of a lower amount of PLU, as observed in the TGA analysis of AuNP-PLU:2.0UV, or changes in PLU molecular weight due to more extensive polymer degradation and oxidation in the UV light method.

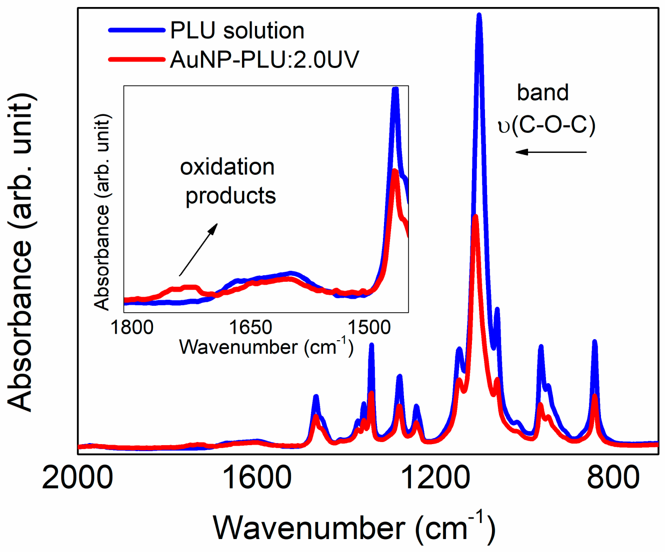

Figure 5. ATR FTIR spectra obtained for aqueous solutions of F127 at a concentration of 2.0 mmol L^{-1} and the AuNP-PLU:2.0UV sample after 10 min of photoexcitation. Inset: enlarged view of the region close to 1700 cm^{-1}.

It is known that the thermal reduction of $AuCl_4^-$ in the presence of an aqueous solution of various organic molecules creates AuNPs by the nucleation and growth processes [49]. Usually, the first step is the association of anionic Au^{3+} complexes with the organic molecules, followed by a multiple-step redox reaction that results in Au^0 nuclei and oxidized organic molecules. In these cases, the size of AuNPs depends strongly on the rate of reduction of the Au^{3+} species; an increase in the rate of the redox reaction creates a large number of Au^0 nuclei and decreases the number of oxidized gold species in the solution. The consequence is a more uniform growth of small AuNPs. The mechanism of AuNP formation under UV irradiation of a reaction mixture containing $HAuCl_4$ and citric acid seems to be similar to the respective thermal mechanism, with the photoexcited citrate–$AuCl_3^-$ complex being responsible for the speeding up the formation of Au^0 nuclei [49].

It is well established that when trivalent gold ions $AuCl_4^-$ are irradiated with UV-light, the reduction occurs in successive steps: (i) reduction into the unstable bivalent state Au^{2+}; (ii) disproportionation of Au^{2+} into Au^{3+} and Au^{1+}; and (iii) reduction of accumulated Au^{1+} ions to Au^0 [35]. It is worthwhile to note that Au^{1+} is not easily reduced as long as Au^{3+} ions are present in high amounts, and it does not disproportionate because the reduction potential Au^{1+}/Au^0 is considerably negative (−1.4 V). Mallick et al. propose that photolysis of H_2O (UV source dependent) generates both H and OH radicals that can react with organic molecules producing strong reducing molecular radicals, which are able to reduce Au^{1+} to Au^0 [36]. Thus, it can be concluded that the presence of organic radicals is very likely to accelerate the formation of Au^0 nuclei. In this regard, Sokolsky-Papkov and Kabanov studied the formation of AuNPs from $HAuCl_4$ in the presence of Pluronic F127, and they found a strong relation between the presence of oxygen reactive species (i.e., superoxide, hydroxyl radicals, hydrogen peroxide), which were formed by the decomposition of the hydroperoxides initially present in Pluronic, and the characteristics of AuNPs [34]. Simply stated, as the amount of oxygen-reactive species increases, the size and polydispersity of AuNPs reduce. Further, they concluded that Pluronic undergoes oxidation/degradation with the formation of lower molecular mass alcohols. Although this detailed study was performed without UV irradiation, it is reasonable to consider that these oxygen-reactive species play an important role in the formation of AuNPs from

$HAuCl_4$/PLU mixtures under UV light, and it may explain a great part of our results regarding reaction time, size, morphology, yield, and polydispersity of AuNps.

3.2. In Vitro Cytotoxicity Assay

Figure 6 shows the effect of concentration and exposure time of AuNP-PLU:2.0UV and AuNP-PLU:2.0 on the viability of NIH-3T3 cells. In the short term (15 min), the largest concentrations of AuNP-PLU:2.0UV and AuNP-PLU:2.0 caused a slight reduction in viability compared to controls, less than 20%. However, after 24 h of incubation, AuNP-PLU:2.0UV (at 1.7 µM) and 3.4 µM AuNP reduced respectively, about 62 and 90% of NIH-3T3 cells viability, compared to control group. Additionally, for the same dose (0.86 µM), AuNP-PLU:2.0UV was significantly less toxic (reduction of 26%) than AuNP-PLU:2.0 (reduction of 92%). The IC50 value estimated for AuNP-PLU:2.0UV was 1.29 µM (R^2 = 0.7453), whereas the value for AuNP-PLU:2.0 was 0.32 µM (R^2 = 0.7495). Cells treated only with PLU showed viability greater than 80% (Supplementary Figure S6).

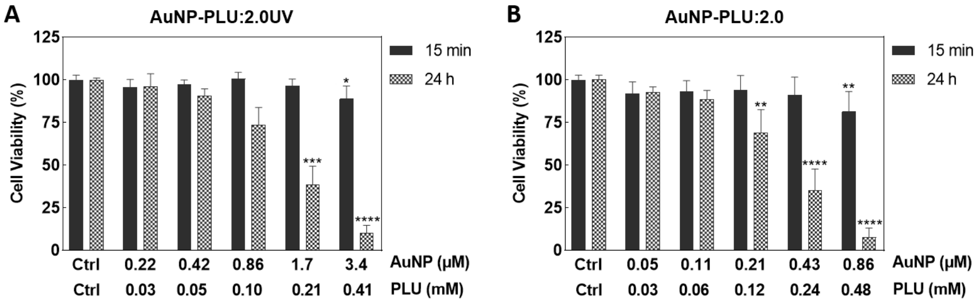

Figure 6. Effect of AuNP-PLU:2.0UV or AuNP-PLU:2.0 on viability of the NIH-3T3 cells determined using an MTT assay. Cells were incubated with AuNP-PLU:2.0UV (**A**) or AuNP-PLU:2.0 (**B**) for 15 min or 24 h. AuNP concentrations ranged from 0.22 to 3.4 µM in the AuNP-PLU:2.0UV sample and 0.05 to 0.86 µM in the AuNP-PLU:2.0 sample. Data are presented as mean ± standard deviation (SD) from three independent experiments. Differences among groups were determined using the Kruskal–Wallis test and Dunn's multiple comparison post hoc test. Asterisks indicate significant differences compared to the respective control group: * $p < 0.05$, ** $p < 0.01$, *** $p < 0.001$, **** $p < 0.0001$.

According to these findings, AuNP-PLU:2.0UV nanocomposites are potential candidates for use as biocompatible carriers of drug and/or contrast agents. In general, information about the toxicity of NPs, particularly in vulnerable populations such as pregnant women and their fetuses, has lagged behind the development of new applications. AuNPs can cross the placental barrier and directly damage fetal tissues and/or interfere with proper placental development and function, creating a hostile gestational environment for fetal growth and development [50]. There is evidence that 3–4 nm AuNPs cross the human placental barrier in limited amounts and accumulate in the placental, depending on their size and surface modification [51]. To support the safety-by-design concept within nanotechnology research, we seek to understand if AuNP-PLU:2.0UV impacts maternal–fetal health using a model of pregnant rats.

3.3. In Vivo Maternal and Fetal Toxicity in Rats

While there may not be many studies specifically evaluating the maternal toxicity or teratogenicity of AuNPs during pregnancy, there is some evidence suggesting that these particles could have harmful effects [52–54]. Therefore, the toxicological effects of AuNPs for both mother and fetus were evaluated. Table 3 shows the maternal toxicological parameters, and no differences were noted among the groups in maternal weight, gravid uterus weight, food and water consumption, relative organ weight, and biochemical parameters. In an animal laboratory, factors such as body weight and water and feed consumption, as well as organ weight, are considered important parameters in the assessment of the systemic toxicity of a substance [55]. In addition, increased AST and ALT concentrations in blood are used as biochemical markers of hepatic tissue damage, and urea and creatinine are used to evaluate renal function [43]. Our data showed no differences in these parameters between groups, thus suggesting that treatment performed with AuNP-PLU:UV should not impart maternal toxicity.

Table 3. Maternal toxicological parameters of rats treated with water (Control) or AuNP-PLU:2.0UV (Treated) during the pregnancy.

	Groups	
	Control (n = 12)	**Treated (n = 12)**
Weight gain in pregnancy (g)		
1st week	19.75 ± 5.96	20.42 ± 7.95
2nd week	22.75 ± 10.60	20.75 ± 4.90
3rd week	79.67 ± 15.76	79.67 ± 15.76
Total body weight gain—WG	121.1 ± 12.2	115.3 ± 19.0
Gravid uterus weight—GUW (g)	72.5 ± 19.3	79.4 ± 12.1
BWG minus GUW (g)	44.27 ± 14.96	38.34 ± 10.65
Daily food consumption (g)	20.32 ± 2.11	21.39 ± 2.60
Daily water intake (mL)	55.55 ± 6.96	56.48 ± 12.64
Relative organ weight (g/100g)		
Heart	0.31 ± 0.03	0.31 ± 0.03
Liver	3.94 ± 0.41	3.98 ± 0.31
Spleen	0.22 ± 0.06	0.20 ± 0.02
Kidneys	0.55 ± 0.04	0.55 ± 0.03
	Biochemical serum parameters	
ALT (U/L)	41.41 ± 10.61	39.50 ± 8.79
AST (U/L)	145.82 ± 32.42	127.98 ± 42.13
Urea (mg/dL)	45.43 ± 8.69	49.80 ± 7.70
Creatinine (mg/dL)	0.62 ± 0.16	0.58 ± 0.12

Data shown as mean ± standard deviation (SD). $p > 0.05$ compared with the Control group (Student's *t*-test).

For the success of pregnancy, it is essential that, during the implantation period, the physiological and molecular processes are coordinated, involving close interactions between the uterus and the blastocyst [56]. The pre- and post-implantation loss rates did not differ statistically among the groups (Figure 7).

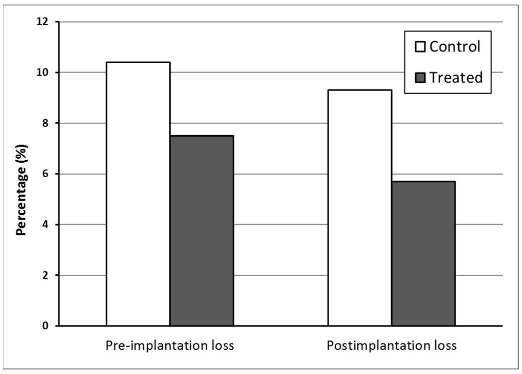

Figure 7. Percentage of losses of embryos before and after implantation at the term of pregnancy (DP21) for rats treated with water (Control) or AuNP (Treated) during pregnancy. $p > 0.05$ compared with the Control group (Fisher's Exact test).

During pregnancy, exposure to toxic agents may lead to different effects ranging from functional or morphological changes, developmental delay, and anomalies to lethality in fetuses [57]. Figure 8 shows fetal and placental development. The rats that received AuNP presented a decrease in placenta weight and skeletal anomalies rate and an increase in normal (without anomalies) fetuses rate. Although the AuNP-PLU:UV treatment decreased placental weight, this modification did not affect fetal development, which showed unchanged fetal weight, weight classification, and ossification sites.

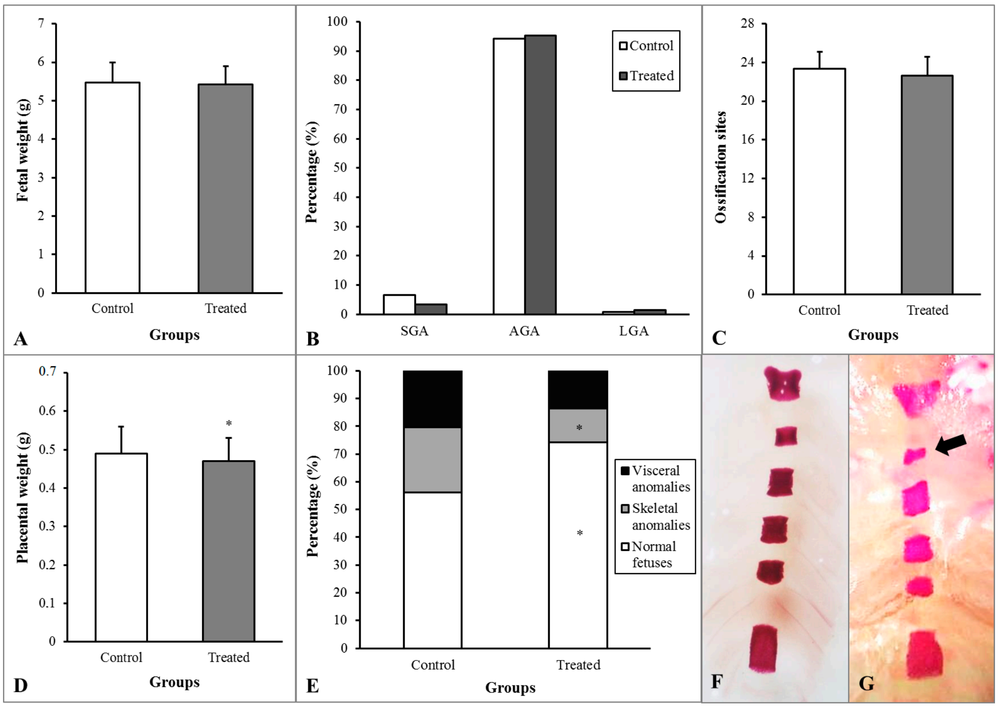

Figure 8. Fetal and placental development of rats treated with water (Control) or AuNP (Treated) during pregnancy. (**A**)—Fetal weight. (**B**)—Percentages of fetuses classified as small (SGA), adequate (AGA), or large (LGA) for gestational age. (**C**)—Ossification sites of fetuses. (**D**)—Placenta weight. (**E**)—Percentage of anomalies. (**F**)—Image of normal sternebra of rat fetuses. (**G**)—Incomplete ossification of sternebra (arrow). * $p < 0.05$ compared with the Control group (A,C,D—Student's *t*-test; B,F—Fisher's Exact test).

3.4. X-ray CT Scanner

X-ray computed tomography (CT) is an imaging technique used to uncover the interior features of a patient body in a three-dimensional view. The CT image stems from attenuation of the X-ray intensity by the body parts, in such a way that denser parts will attenuate more than softer ones. CT images can be produced from plain organs, but better resolution is only achieved using contrast agents, such as iodine and gadolinium. Indeed, greater atomic number elements will attenuate the incoming X-ray more [58].

Figure 9A shows CT images of AuNP-PLU: 2.0UV with Au of 1.23 mg/mL, compared with Optiray@320_1 containing I at the same concentration (I = 1.23 mg/mL), and AuNP-PLU: 2.0 containing Au concentration of 1.09 mg/mL, compared with Optiray@320_2 with I at the same concentration (I = 1.09 mg/mL) attained for beam energies of 80, 100, 120, and 140 KV. Figure 9B displays variations in the CT number with the beam energy for the commercial iodine contained contrast Optiray@320 and photochemically made Au-PLU:2.0UV. To compare, samples of both contrast agents were tested at the same concentration (expressed in mmol L^{-1} of iodine or gold). Data from AuNP-PLU:2.0UV containing a Au concentration of 1.23 mg/mL was compared with data from Optiray@320_1 with an I concentration of 1.23 mg/mL. Similarly, AuNP-PLU: 2.0 with a Au concentration of 1.09 mg/mL was compared with an Optiray@320_2 sample with an I concentration of 1.09 mg/mL.

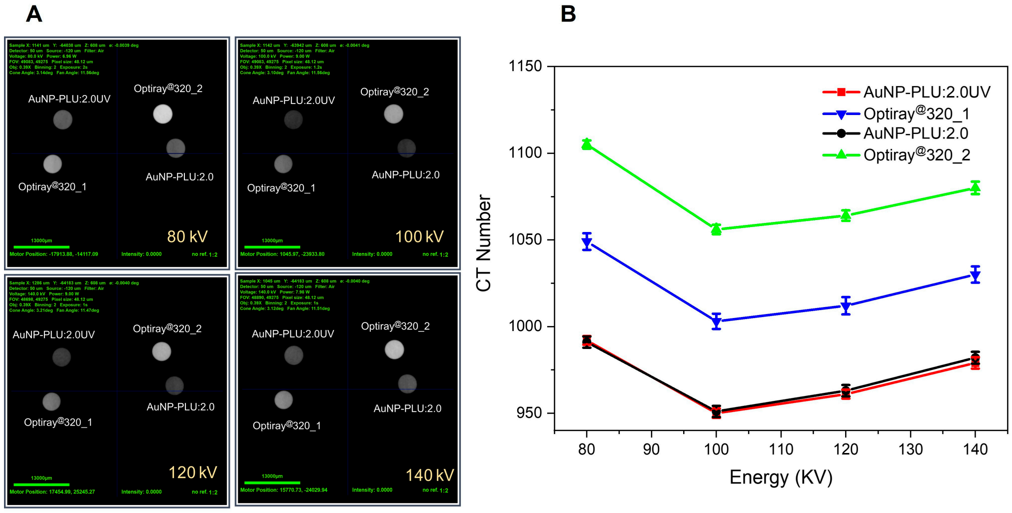

Figure 9. (**A**) CT images of AuNP-PLU:2.0UV with Au of 1.23 mg/mL compared with Optiray@320_1 containing I at the same concentration (I = 1.23 mg/mL), and AuNP-PLU:2.0 containing a Au concentration of 1.09 mg/mL compared with Optiray@320_2 with I at the same concentration (I = 1.09 mg/mL) attained for beam energies of 80, 100, 120, and 140 KV. (**B**) CT number attained for the same samples displayed in (**A**) as a function of beam energy.

As shown in Figure 9B, the Au-PLU samples provide CT contrast comparable to iodine for a same beam energy. Likewise, the CT number achieved with both agents is similar and decreases more or less linearly with the beam energy, as shown in Figure 9B. Furthermore, it is observed that the nanocomposite AuNP-PLU:2.0UV shows a closer CT number to its iodine control (Optiray@320_1) than the AuNP-PLU:2.0 when compared with Optiray@320_2. It is noteworthy that despite its established use, iodine as a contrast agent can promote unwanted side effects, ranging from a simple skin allergy to more acute effects including vascular permeation and renal toxicity [59]. Indeed, many patients cannot use iodine at all when submitted to CT procedures. Gadolinium is an alternative, although it provides lower contrast at comparable doses [60]. Recently, AuNPs were tested for this task and showed even better attenuation ability than iodine allied to longer circulation time, which enables for more accurate observation of vessels and tissues [61]. Furthermore, they can be designed with biocompatible and non-toxic surface coatings, which mitigate eventual side effects during administration [62]. Considering that the proposed photochemical method uses light instead of a reducing agent and that PLU is recognized for its biocompatibility and negligible toxicity, the present Au-PLU:2.0UV is a potential contrast agent for CT.

4. Conclusions

In this study we employed an UV-assisted synthesis protocol to produce biocompatible colloidal nanocomposites, comprising gold nanoparticles (AuNPs) and Pluronic F127 (PLU). Under optimized conditions, the proposed synthesis process produces AuNP-PLU nanocomposites at much faster rates (at least six times) than the process conducted under ambient light. Moreover, the synthesized nanoparticles display a controlled shape, narrower size distribution, and lower levels of PLU. Cytotoxicity assays demonstrate that the AuNP-PLU produced under UV irradiation is significantly less toxic than that produced under ambient light. In vivo maternal and fetal toxicity assays in rats reveal this nanocomposite is safe for both mother and fetus. As a proof of concept, we tested the nanocomposite as a contrast agent in X-ray computed tomography scans and found that it performs similarly to the commercially available iodine contrast agent Optiray@320. This is a promising feature, suggesting that AuNP-PLU synthesized under UV irradiation has high potential as a biocompatible nanocarrier and contrast agent.

Supplementary Materials: The following supporting information can be downloaded at: https://www.mdpi.com/article/10.3390/polym15092163/s1, Figure S1: The UV-vis spectra precursors and control samples title; Figure S2: Changes in the maximum absorption of the plasmonic band during the reaction time title; Figure S3: The nanocomposites thermogravimetric analysis title; Figure S4: Nanoparticle diameter histogram title; Figure S5: Scattered light intensity distribution profiles as a function of the hydrodynamic diametertitle; Figure S6: Effect of PLU on viability of the NIH-3T3 cells determined by MTT assay title.

Author Contributions: Conceptualization, M.A.G.S., L.G.P. and G.T.V.; methodology, D.S.B.G., R.Q.M.-S., D.M. and M.R.S.; software, A.V.G. and D.P.P.B.; validation, D.S.B.G., R.Q.M.-S. and B.M.H.; formal analysis, D.P.P.B. and A.B.S.S.; investigation, S.M.F., D.M., P.P.C.S., L.R.d.A. and A.V.G.; writing—original draft preparation, D.S.B.G. and R.Q.M.-S.; writing—review and editing, M.A.G.S., L.G.P., G.T.V., L.R.d.A., A.V.G., D.M. and P.P.C.S.; visualization, D.P.P.B.; supervision, M.A.G.S.; project administration, M.A.G.S.; funding acquisition, M.A.G.S., S.M.F., L.G.P. and G.T.V. All authors have read and agreed to the published version of the manuscript.

Funding: The financial support from the Brazilian agencies MCT-CNPq (Process 424152/2016-9), FINEP, FAP-DF, FINATEC and CAPES is gratefully acknowledged. Support from the FP7-PEOPLE-HIGRAPHEN project (612704) is also acknowledged. M.A.G.S. thanks the Universidade de Brasilia (Edital DPI/DPG 02/2021) for financial support. D.S.B.G. thanks FAPERO (process n. 07/2014-015).

Institutional Review Board Statement: The Protocol Nº 23108.022668/2019-23, related to the Project entitled "Effects of Treatment with Gold, Iron and Polymeric Nananoparticles on the Pregnancy of Rats", is in agreement with the Ethical Principles for Animal Research established by the National Council for Control of Animal Experimentation (CONCEA). This Project was approved by the Committee on Ethics in the Use of Animals of Araguaia (Federal University of Mato Grosso—UFMT/Campus of Araguaia) in reunion at 04/05/2019.

Data Availability Statement: Not applicable.

Acknowledgments: The authors thank MSc P. R. Teixeira for performing the cyclic voltammetry experiments.

Conflicts of Interest: The authors declare no conflict of interest.

References

1. Wei, X.Z.; Mulvaney, P. Chapter 3—Optical Properties of Strongly Coupled Plasmonic Nanoparticle Clusters. In *Modern Plasmonics*; Maradudin, A., Sambles, J.R., William, L.B., Eds.; Elsevier: Amsterdam, The Netherlands, 2014; Volume 4, pp. 75–108.
2. Csaki, A.; Thiele, M.; Jacqueline Jatschka, J.; Dathe, A.; Zopf, D.; Stranik, O.; Fritzsche, W. Plasmonic nanoparticle synthesis and bioconjugation for bioanalytical sensing. *Eng. Life Sci.* **2015**, *15*, 266–275. [CrossRef]
3. Pallotta, A.; Boudier, A.; Creusot, B.; Brun, E.; Sicard-Roselli, C.; Bazzi, R.; Roux, S.; Clarot, I. Quality control of gold nanoparticles as pharmaceutical ingredients. *Int. J. Pharm.* **2019**, *569*, 118583. [CrossRef] [PubMed]
4. Zhang, X.-D.; Wu, H.-Y.; Wu, D.; Wang, Y.-W.; Chang, J.H.; Zhai, Z.-B.; Meng, A.-M.; Liu, P.-X.; Zhang, L.-A.; Fan, F.-Y. Toxicologic effects of gold nanoparticles in vivo by different administration routes. *Int. J. Nanomed.* **2010**, *5*, 771–781. [CrossRef] [PubMed]
5. Kaur, A.; Shimoni, O.; Wallach, M. Novel screening test for celiac disease using peptide functionalised gold nanoparticles. *World J. Gastroenterol.* **2018**, *24*, 5379–5390. [CrossRef]
6. Martínez Porcel, J.E.; Churio, M.S.; Moya, S.E.; Arce, V.B.; Martire, D.O. Plasmonic silica-gold core-shell nanoparticles: Interaction with organic dyes for light-induced applications. *J. Photochem. Photobiol. A Chem.* **2022**, *431*, 114016. [CrossRef]
7. Liu, J.; Shen, Y.; Guangxian, W.; Xiang, Y.; Guo, Y.; Sun, X.; Liu, Y. Highly-sensitive electrochemiluminescence biosensor for detection of inosine monophosphate in meat based on graphdiyne/AuNPs/luminol nanocomposites. *Food Sci. Hum. Wellness* **2023**, *12*, 1149–1156. [CrossRef]
8. Vieira, F.M.; Gabriela Calisto, C.M.; Izumi, C. Construction of SERS substrates by gold nanoparticles assembly on polymeric matrices. *Appl. Surf. Sci.* **2023**, *612*, 155818. [CrossRef]
9. Tao, Z.; Feng, J.; Yang, F.; Zhang, L.; Shen, H.; Cheng, Q.; Liu, L. Plasmon-enhanced photocatalysis using gold nanoparticles encapsulated in nanoscale molybdenum oxide shell. *Nanotechnology* **2023**, *34*, 155604. [CrossRef]
10. Hainfeld, J.F.; Slatkin, D.N.; Focella, T.M.; Smilowitz, H.M. Gold nanoparticles: A new X-ray contrast agent. *Br. J. Radiol.* **2006**, *79*, 248–253. [CrossRef]
11. Silvestri, A.; Zambelli, V.; Ferretti, A.M.; Salerno, D.; Bellani, G.; Polito, L. Design of functionalized gold nanoparticle probes for computed tomography imaging. *Contrast Media Mol. Imaging* **2016**, *11*, 405–414. [CrossRef]

12. Tu, N.V.; Anh, N.N.; Hau, T.V.; Hao, N.V.; Huyen, N.T.; Thang, B.H.; Minh, P.N.; Chuc, N.V.; Fukata, N.; Trinh, P.V. Improving the efficiency of n-Si/PEDOT:PSS hybrid solar cells by incorporating AuNP-decorated graphene oxide as a nanoadditive for conductive polymers. *RSC Adv.* **2022**, *12*, 27625–27632. [PubMed]
13. Rizalputri, L.N.; Anshori, I.; Handayani, M.; Gumilar, G.; Septiani, N.L.W.; Hartati, Y.W.; Annas, M.S.; Purwidyantri, A.; Prabowo, B.A.; Brian Yuliarto, B. Facile and controllable synthesis of monodisperse gold nanoparticle bipyramid for electrochemical dopamine sensor. *Nanotechnology* **2023**, *35*, 55502. [CrossRef] [PubMed]
14. Sun, K.; Xia, N.; Zhao, L.; Liu, K.; Hou, W.; Liu, L. Aptasensors for the selective detection of alpha-synuclein oligomer by colorimetry, surface plasmon resonance and electrochemical impedance spectroscopy. *Sens. Actuators B Chem.* **2017**, *245*, 87–94. [CrossRef]
15. Doherty, B.; Csáki, A.; Thiele, M.; Zeisberger, M.; Schwuchow, A.; Kobelke, J.; Fritzsche, W.; Schmidt, M.A. Nanoparticle functionalised smallcore suspended-core fibre—A novel platform for efficient sensing. *Biomed. Opt. Express* **2017**, *8*, 790–799. [CrossRef] [PubMed]
16. Xie, T.; Jing, C.; Long, Y.-T. Single plasmonic nanoparticles as ultrasensitive sensors. *Analyst* **2017**, *142*, 409–420. [CrossRef]
17. Zhenga, K.; Zhoua, D.; Wud, L.; Lia, J.; Zhaoa, B.; Zhange, S.; Heb, R.; Xiaof, L.; Zoyae, I.; Yub, L.; et al. Gold-nanoparticle-based multistage drug delivery system for antitumor therapy. *Drug Deliv.* **2022**, *29*, 3186–3196. [CrossRef]
18. Irvin-Choy, N.S.; Nelson, K.M.; Dang, M.N.; Gleghorn, J.P.; Day, E.S. Gold nanoparticle biodistribution in pregnant mice following intravenous administration varies with gestational age. *Nanomedicine* **2021**, *36*, 102412. [CrossRef] [PubMed]
19. Yang, H.; Du, L.; Tian, X.; Fan, Z.; Sun, C.; Liu, Y.; Keelan, J.A.; Nie, G. Effects of nanoparticle size and gestational age on maternal biodistribution and toxicity of gold nanoparticles in pregnant mice. *Toxicol Lett.* **2014**, *230*, 10–18. [CrossRef]
20. Semmler-Behnke, M.; Lipka, J.; Wenk, A.; Hirn, S.; Schaffler, M.; Tian, F.; Schmid, G.; Oberdörster, G.; Kreyling, W.G. Size dependent translocation and fetal accumulation of gold nanoparticles from maternal blood in the rat. *Part Fibre Toxicol.* **2014**, *11*, 33. [CrossRef]
21. Alexandridis, P. Gold Nanoparticle Synthesis, Morphology Control, and Stabilization Facilitated by Functional Polymers. *Chem. Eng. Technol.* **2011**, *34*, 15–28. [CrossRef]
22. Alexandridis, P.; Tsianou, M. Block copolymer-directed metal nanoparticle morphogenesis and organization. *Eur. Polym. J.* **2011**, *47*, 569–583. [CrossRef]
23. Saha, K.; Agasti, S.S.; Kim, C.; Li, X.; Rotello, V.M. Gold Nanoparticles in Chemical and Biological Sensing. *Chem. Rev.* **2012**, *112*, 2739–2779. [CrossRef]
24. Nguyen, H.V.; Nguyen, H.V.; Phan, V.M.; Park, B.J.; Seo, T.S. Serially diluting centrifugal microfluidics for high-throughput gold nanoparticle synthesis using an automated and portable workstation. *Chem. Eng. J.* **2023**, *452*, 139044. [CrossRef]
25. Cabrera, G.F.S.; Balbin, M.M.; Eugenio, P.J.G.; Zapanta, C.S.; Monserate, J.J.; Salazar, J.R.; Mingala, C.N. Green synthesis of gold nanoparticles reduced and stabilized by sodium glutamate and sodium dodecyl sulfate. *Biochem. Biophys. Res. Commun.* **2017**, *484*, 774–780. [CrossRef] [PubMed]
26. Shajkumar, A.; Nandan, B.; Sanwaria, S.; Albrecht, V.; Libera, M.; Lee, M.-H.; Auffermann, G.; Stamm, M.; Horechyy, A. Silica-supported Au@hollow-SiO_2 particles with outstanding catalytic activity prepared via block copolymer template approach. *J. Colloid Interface Sci.* **2017**, *491*, 246–254. [CrossRef]
27. Maguire, P.; Rutherford, D.; Macias-Montero, M.; Mahony, C.; Kelsey, C.; Tweedie, M.; Pérez-Martin, F.; McQuaid, H.; Diver, D.; Mariotti, D. Continuous In-Flight Synthesis for On-Demand Delivery of Ligand-Free Colloidal Gold Nanoparticles. *Nano Lett.* **2017**, *17*, 1336–1343. [CrossRef]
28. Patil, M.P.; Kim, G.-D. Eco-friendly approach for nanoparticles synthesis and mechanism behind antibacterial activity of silver and anticancer activity of gold nanoparticles. *Appl. Microbiol. Biotechnol.* **2017**, *101*, 79–92. [CrossRef]
29. Sakai, T.; Alexandridis, P. Single-Step Synthesis and Stabilization of Metal Nanoparticles in Aqueous Pluronic Block Copolymer Solutions at Ambient Temperature. *Langmuir* **2004**, *20*, 8426–8430. [CrossRef]
30. Grzelczak, M.; Liz-Marzan, L.M. The relevance of light in the formation of colloidal metal nanoparticles. *Chem. Soc. Rev.* **2014**, *43*, 2089–2097. [CrossRef]
31. Gomes, D.S.; Paterno, L.G.; Santos, A.B.; Garay, A.V.; Mertz, D.; Freitas, S.M.; Soler, M.A. New insights on the formation of gold nanoparticles and Pluronic nanocomposites: Kinetics and thermodynamics parameters. *J. Mol. Liq.* **2018**, *268*, 181–189. [CrossRef]
32. Santos, D.C.; de Souza, V.C.; Vasconcelos, D.A.; Andrade, G.R.S.; Gimenez, I.F.; Teixeira, Z. Triblock copolymer-mediated synthesis of catalytically active gold nanostructures. *J. Nanopart. Res.* **2018**, *20*, 105. [CrossRef]
33. Sokolsky-Papkov, M.; Kabanov, A. Synthesis of Well-Defined Gold Nanoparticles Using Pluronic: The Role of Radicals and Surfactants in Nanoparticles Formation. *Polymers* **2019**, *11*, 1553. [CrossRef] [PubMed]
34. Pal, A. Photoinitiated gold sol generation in aqueous Triton X-100 and its analytical application for spectrophotometric determination of gold. *Talanta* **1998**, *46*, 583–587. [CrossRef] [PubMed]
35. Mandal, M.; Ghosh, S.K.; Kundu, S.; Esumi, K.; Pal, T. UV Photoactivation for Size and Shape Controlled Synthesis and Coalescence of Gold Nanoparticles in Micelles. *Langmuir* **2002**, *18*, 7792–7797. [CrossRef]
36. Shang, Y.; Min, C.; Hu, J.; Wang, T.; Liu, H.; Hu, Y. Synthesis of gold nanoparticles by reduction of $HAuCl_4$ under UV irradiation. *Solid State Sci.* **2013**, *15*, 17–23. [CrossRef]
37. Teixeira, P.R.; Santos, M.S.; Silva, A.L.G.; Báo, S.N.; Azevedo, R.B.; Sales, M.J.A.; Paterno, L.G. Photochemically-assisted synthesis of non-toxic and biocompatible gold nanoparticles. *Colloid Surf. B-Biointerfaces* **2016**, *148*, 317–323. [CrossRef]

38. Mallick, K.; Wang, Z.; Pal, T. Seed-mediated successive growth of gold particles accomplished by UV irradiation: A photochemical approach for size-controlled synthesis. *J. Photochem. Photobiol. A-Chem.* **2001**, *140*, 75–80. [CrossRef]
39. Alexandridis, P.; Holzwarth, J.F.; Hatton, T.A. Micellization of Poly(ethylene oxide)-Poly(propylene oxide)-Poly(ethylene oxide) Triblock Copolymers in Aqueous Solutions: Thermodynamics of Copolymer Association. *Macromolecules* **1994**, *27*, 2414–2425. [CrossRef]
40. Soares, T.S.; Moraes-Souza, R.Q.; Carneiro, T.B.; Araujo-Silva, V.C.; Schavinski, A.Z.; Gratão, T.B.; Damasceno, D.C.; Volpato, G.T. Maternal-fetal outcomes of exercise applied in rats with mild hyperglycemia after embryonic implantation. *Birth Defects Res.* **2021**, *113*, 287–298. [CrossRef]
41. Reagan-Shaw, S.; Nihal, M.; Ahmad, N. Dose translation from animal to human studies revisited. *FASEB J.* **2008**, *22*, 659–661. [CrossRef]
42. Gallego, F.Q.; Sinzato, Y.K.; Miranda, C.A.; Iessi, I.L.; Dallaqua, B.; Volpato, G.T.; Scarano, W.R.; SanMartín, S.; Damasceno, D.C. Pancreatic islet response to diabetes during pregnancy in rats. *Life Sci.* **2018**, *214*, 1–10. [CrossRef] [PubMed]
43. Paula, V.G.; Cruz, L.L.; Sene, L.B.; Gratão, T.B.; Soares, T.S.; Moraes-Souza, R.Q.; Damasceno, D.C.; Volpato, G.T. Maternal-fetal repercussions of *Phyllanthus niruri* L. treatment during rat pregnancy. *J. Ethnopharmacol.* **2020**, *254*, 112728. [CrossRef] [PubMed]
44. Wilson, J.G. Methods for administering agents and detecting malformations in experimental animal. In *Teratology: Principles and Techniques*; Wilson, J.C., Warkany, J., Eds.; University of Chicago Press: Chicago, IL, USA, 1965; pp. 47–74.
45. Staples, R.E.; Schnell, V.L. Refinements in rapid clearing technique in the KOH-alizarin red S method for fetal bone. *Stain Technol.* **1964**, *39*, 61–63.
46. Aliverti, V.; Bonanomi, L.; Giavini, E.; Leone, V.G.; Mariani, L. The extent of fetal ossification as an index of delayed development in teratogenic studies on the rat. *Teratology* **1979**, *20*, 237–242. [CrossRef] [PubMed]
47. Moraes-Souza, R.Q.; Reinaque, A.P.; Soares, T.S.; Silva, A.L.T.; Giunchetti, R.C.; Takano, M.A.S.; Akamatsu, M.A.; Kubrusly, F.S.; Lúcio-Macarini, F.; Raw, I.; et al. Safety evaluation of a vaccine: Effect in maternal reproductive outcome and fetal anomaly frequency in rats using a leishmanial vaccine as a model. *PLoS ONE* **2017**, *12*, e0172525. [CrossRef] [PubMed]
48. Correia, J.J.; Stafford, W.F. Sedimentation Velocity: A Classical Perspective. In *Methods in Enzymology*; Cole, J.L., Ed.; Academic Press: Cambridge, MA, USA, 2015; Volume 562, pp. 49–80.
49. Shiraishi, Y.; Tanaka, H.; Sakamoto, H.; Ichikawa, S.; Takayuki, H. Photoreductive synthesis of monodispersed Au nanoparticles with citric acid as reductant and surface stabilizing reagent. *RSC Adv.* **2017**, *7*, 6187–6192. [CrossRef]
50. Dugershaw, B.B.; Aengenheister, L.; Hansen, S.S.K.; Hougaard, K.H.; Buerki-Thurnherr, T. Recent insights on indirect mechanisms in developmental toxicity of nanomaterials. *Part. Fibre Toxicol.* **2020**, *17*, 31. [CrossRef] [PubMed]
51. Aengenheister, L.; Dietrich, D.; Sadeghpour, A.; Manser, P.; Diener, L.; Wichser, A.; Karst, U.; Peter Wick, P.; Buerki-Thurnherr, T. Gold nanoparticle distribution in advanced in vitro and ex vivo human placental barrier models. *J Nanobiotechnol.* **2018**, *16*, 79. [CrossRef]
52. Yamashita, K.; Yoshioka, Y.; Higashisaka, K.; Mimura, K.; Morishita, Y.; Nozaki, M. Silica and titanium dioxide nanoparticles cause pregnancy complications in mice. *Nat. Nanotechnol.* **2011**, *6*, 321–328. [CrossRef]
53. Hong, F.; Zhou, Y.; Zhao, X.; Sheng, L.; Wang, L. Maternal exposure to nanosized titanium dioxide suppresses embryonic development in mice. *Int. J. Nanomed.* **2017**, *12*, 6197–6204. [CrossRef]
54. Mohamadzadeh, N.; Zirak Javanmard, M.; Karimipour, M.; Farjah, G. Developmental toxicity of the neural tube induced by titanium dioxide nanoparticles in mouse embryos. *Avicenna J. Med. Biotechnol.* **2021**, *13*, 74–80. [CrossRef]
55. Leal-Silva, T.; Souza, M.R.; Cruz, L.L.; Moraes-Souza, R.Q.; Paula, V.G.; Soares, T.S.; Dela Justina, V.; Giachini, F.R.; Daasceno, D.C.; Américo, M.F.; et al. Toxicological effects of the Morinda citrifolia L. fruit extract on maternal reproduction and fetal development in rats. *Drug Chem. Toxicol.* **2023**, *46*, 609–615. [CrossRef] [PubMed]
56. Cha, J.; Sun, X.; Dey, S.K. Mechanisms of implantation: Strategies for successful pregnancy. *Nat. Med.* **2012**, *18*, 1754–1767. [CrossRef] [PubMed]
57. Moraes-Souza, R.Q.; Soares, T.S.; Carmo, N.O.; Damasceno, D.C.; Campos, K.E.; Volpato, G.T. Adverse effects of Croton urucurana B. exposure during rat pregnancy. *J. Ethnopharmacol.* **2017**, *199*, 328–333. [CrossRef]
58. Withers, P.J.; Bouman, C.; Carmignato, S.; Cnudde, V.; Grimaldi, D.; Hagen, C.K.; Maire, E.; Manley, M.; Du Plessis, A.; Stock, S.R. X-ray computed tomography. *Nat. Rev. Methods Prim.* **2021**, *1*, 18. [CrossRef]
59. Andreucci, M.; Solomon, R.; Tasanarong, A. Side effects of radiographic contrast media: Pathogenesis, risk factors, and prevention. *BioMed Res Int.* **2014**, *2014*, 741018. [CrossRef] [PubMed]
60. Bongers, M.N.; Schabel, C.; Krauss, B.; Claussen, C.D.; Nikolaou, K.; Thomas, C. Potential of gadolinium as contrast material in second generation dual energy computed tomography—An ex vivo phantom study. *Clin. Imaging* **2017**, *43*, 74–79. [CrossRef]
61. Mesbahi, A.; Famouri, F.; Ahar, M.; Ghaffari, M.; Ghavami, S. A study on the imaging characteristics of Gold nanoparticles as a contrast agent in X-ray computed tomography. *Pol. J. Med. Phys. Eng.* **2017**, *23*, 9–14. [CrossRef]
62. Santos-Martinez, M.J.; Rahme, K.; Corbalan, J.J.; Faulkner, C.; Holmes, J.D.; Tajber, L.; Medina, C.; Radomski, M.W. Pegylation Increases Platelet Biocompatibility of Gold Nanoparticles. *J. Biomed. Nanotechnol.* **2014**, *10*, 1004–1015. [CrossRef]

nanomaterials

Article

Phosphate Capture Enhancement Using Designed Iron Oxide-Based Nanostructures

Paula Duenas Ramirez [1], Chaedong Lee [2], Rebecca Fedderwitz [3], Antonia R. Clavijo [4], Débora P. P. Barbosa [4], Maxime Julliot [1], Joana Vaz-Ramos [1,5], Dominique Begin [5], Stéphane Le Calvé [5], Ariane Zaloszyc [5], Philippe Choquet [6], Maria A. G. Soler [4], Damien Mertz [1], Peter Kofinas [3], Yuanzhe Piao [2,7] and Sylvie Begin-Colin [1,*]

[1] Institut de Physique et Chimie des Matériaux de Strasbourg, UMR 7504, University of Strasbourg, CNRS, 67034 Strasbourg, France
[2] Graduate School of Convergence Science and Technology, Seoul National University, 145 Gwanggyo-ro, Yeongtong-gu, Suwon-Si 16229, Gyeonggi-do, Republic of Korea
[3] Department of Chemical and Biomolecular Engineering, University of Maryland, 4418 Stadium Dr., College Park, MD 20740, USA
[4] Institute of Physics, University of Brasilia, Brasilia 70910900, Brazil
[5] Institut de Chimie et Procédés pour l'Energie, l'Environnement et la Santé (ICPEES), UMR-7515 CNRS-Université de Strasbourg, 25 rue Becquerel, 67087 Strasbourg, France
[6] Laboratoire des Sciences de l'Ingénieur, de l'Informatique et de l'Imagerie (ICube) —CNRS/University of Strasbourg, UMR 7357 Preclinical Imaging Lab, Imaging Dpt, Hôpitaux Universitaires de Strasbourg, 67098 Strasbourg, France
[7] Advanced Institutes of Convergence Technology, 145 Gwanggyo-ro, Yeongtong-gu, Suwon-si 16229, Gyeonggi-do, Republic of Korea
* Correspondence: sylvie.begin@ipcms.unistra.fr or sylvie.begin@unistra.fr; Tel.: +33-388-107-192

Abstract: Phosphates in high concentrations are harmful pollutants for the environment, and new and cheap solutions are currently needed for phosphate removal from polluted liquid media. Iron oxide nanoparticles show a promising capacity for removing phosphates from polluted media and can be easily separated from polluted media under an external magnetic field. However, they have to display a high surface area allowing high removal pollutant capacity while preserving their magnetic properties. In that context, the reproducible synthesis of magnetic iron oxide raspberry-shaped nanostructures (RSNs) by a modified polyol solvothermal method has been optimized, and the conditions to dope the latter with cobalt, zinc, and aluminum to improve the phosphate adsorption have been determined. These RSNs consist of oriented aggregates of iron oxide nanocrystals, providing a very high saturation magnetization and a superparamagnetic behavior that favor colloidal stability. Finally, the adsorption of phosphates as a function of pH, time, and phosphate concentration has been studied. The undoped and especially aluminum-doped RSNs were demonstrated to be very effective phosphate adsorbents, and they can be extracted from the media by applying a magnet.

Keywords: iron oxide nanoclusters; iron precursor effect; aluminium; zinc and cobalt doping; phosphate adsorption studies

check for updates

Citation: Ramirez, P.D.; Lee, C.; Fedderwitz, R.; Clavijo, A.R.; Barbosa, D.P.P.; Julliot, M.; Vaz-Ramos, J.; Begin, D.; Le Calvé, S.; Zaloszyc, A.; et al. Phosphate Capture Enhancement Using Designed Iron Oxide-Based Nanostructures. *Nanomaterials* **2023**, *13*, 587. https://doi.org/10.3390/nano13030587

Academic Editor: Antonino Gulino

Received: 23 December 2022
Revised: 20 January 2023
Accepted: 21 January 2023
Published: 1 February 2023

1. Introduction

Phosphates released into the environment come from agricultural (fertilizers) and industrial sources, from human excreta, and from phosphate-based detergents or washing powder. In Western Europe, point-source phosphate pollution is estimated at 3.5 grams per capita per day: 1.2 grams from human excreta, and the rest mainly from detergents. Moreover, 0.5 to 2.5% of phosphorus used in fertilizers is washed away from cultivated soils by rain and drainage water [1]. Phosphates are the main cause of eutrophication and dystrophication in France and worldwide. Although they are not toxic in themselves for animal and plant life, they are harmful to the environment when present in high concentrations:

they become real fertilizers for aquatic environments, which they help enrich excessively in organic matter. For instance, the algae growth induced by phosphorus makes waters less attractive for swimming and other aquatic recreation and degrades the conditions that fish, bugs, wildlife, and desired plants need to grow. In addition to these pollution problems, phosphorus remains a scarce resource, and world reserves of phosphates are limited [2]. A shortage of phosphate fertilizers would have significant consequences for world food production. It is therefore urgent to find solutions for phosphorus recovery.

Iron oxide nanoparticles have been widely developed to remove phosphates from polluted media [3–6] and appear to be very suitable compounds to enhance the phosphate removal from polluted media due to the high affinity of phosphate for iron. In addition, iron oxide nanoparticles may be recycled. Indeed, an earlier study using iron oxide nanoparticles of 40 nm demonstrated that it was possible to recycle iron oxide nanoparticles by adjusting pH, and the performance was maintained after several cycles [7]. The effective recycling implies that the nanoparticles can be easily separated from polluted media by an external magnetic field. For such magnetic extraction, the nanoparticles have to display a high saturation magnetization, but at the nanoscale, the saturation magnetization of iron oxide nanoparticles is strongly decreased due to spin canting and defect effects [8–10]. At the same time, the nanoparticles have to display a high surface area that would allow high removal pollutant capacity. Therefore, a balance between high saturation magnetization and high surface specific area has to be found. Iron oxide raspberry-shaped nanostructures (RSNs), which consist of oriented aggregates/nanoclusters of iron oxide nanograins, possess very high saturation magnetization close to that of the bulk magnetite phase (85 emu/g), which makes them easy to recover from liquid media with a magnet. In addition, these nanostructures are synthesized by a modified polyol-solvothermal process, which allows for the production of large amounts of powder [11].

Table 1. Influence of the substituents on magnetite adsorption capacity towards phosphates in aqueous media.

Substituents	Adsorption Capacity of Magnetite ($mg \cdot g^{-1}$)	Adsorption Capacity of Doped Magnetite ($mg \cdot g^{-1}$)	Increase in the Adsorption Capacity (%)	Ref.
Aluminum	1.21	5.96	492	[4]
Zinc-aluminum	/	21.8	/	[12]
Magnesium-aluminum	/	20.0	/	
Nickel-aluminum	/	17.4	/	
Silica-lanthanum oxide	11.02	27.8	252	[13]
Aluminum-doped ferrite	/	43.9	/	[14]
Cobalt ferrite and magnetite	1.16	1.05	/	[15]
Fe-Cu binary oxide		35.2	/	[16]
Fe_3O_4@C@ZrO_2	5.2	13.99	/	[17]
Fe-Zr binary oxide	5	13.65	/	
	3.2	21.3	/	

Furthermore, it was demonstrated that doping of iron oxide is also a promising approach to improve phosphate uptake [4,13–18]. Table 1 presents some studies on how the doping of spinel iron oxide nanoparticles may increase the phosphate adsorption capacity. However, the many missing data points in the literature on the adsorption capacity of undoped spinel iron oxide make it difficult to estimate the increase in adsorption capacity. In addition, the homogeneous doping of iron oxide nanostructures synthesized by a polyol-solvothermal approach remains a chlenge. Nevertheless, among doping elements, aluminum appears promising and was thus selected to dope RSNs to enhance phosphate removal [4,12].

In this work, the reproducibility of the synthesis of raspberry-shaped iron oxide nanostructures (RSNs) described by Gerber et al. [11] was first studied, followed by the doping of RSNs by zinc, cobalt, and aluminum. We demonstrated the strong impact of starting iron chloride precursors and of the mixing and reaction times on the nanostructure characteristics (diameter, nanograin size, doping efficiency). Then, the phosphate uptake of RSNs and aluminum-doped RSNs in water was compared. Figure 1 summarizes the different studies on the RSN and the performed experiments on the RSNs and aluminum-doped RSNs (Al-RSNs) for phosphate removal.

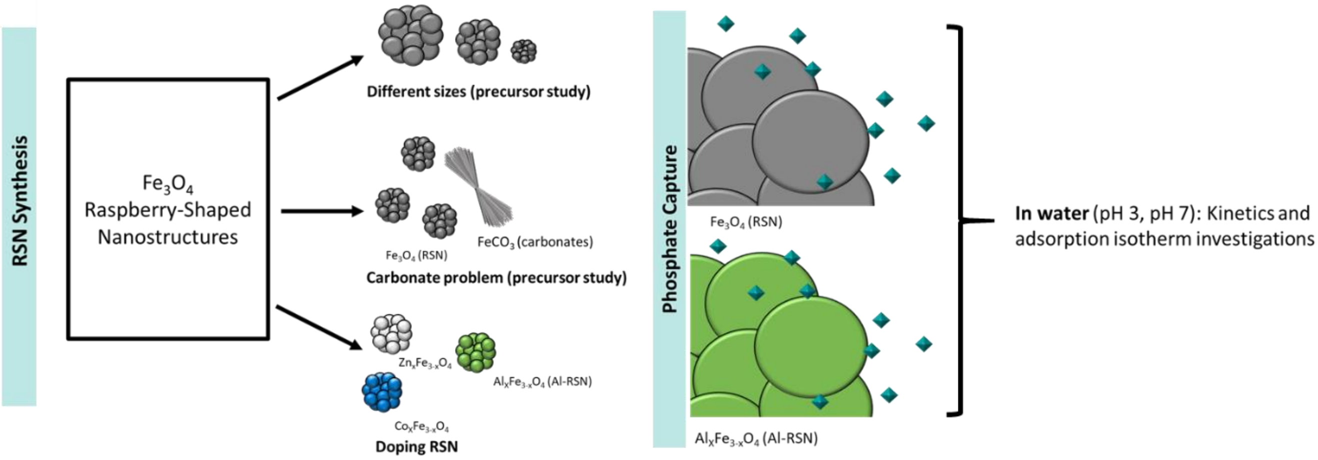

Figure 1. General concept schematizing the different performed investigations on the synthesis of the raspberry-shaped nanostructures and on the evaluation of the RSN and the Al-RSN materials for phosphate removal.

2. Materials and Methods

2.1. Materials

Iron(III) chloride hexahydrate (CAS: 10025-77-1), urea 99.3+% (CAS: 57-13-6), ethylene glycol 99% (CAS: 107-21-1), trisodium citrate dihydrate 99% (CAS: 6132-04-3), ammonium molybdate 99% (CAS 13106-76-8), zinc(II) chloride 98% (CAS 7646 85 7), and cobalt(II) chloride hexahydrate 98% (CAS 7791-13-1) were supplied by Alfa Aesar. Succinic acid (CAS: 110-15-6), ammonium hydroxide solution 25% (CAS: 1336-21-6), and nickel(II) chloride 98% (CAS 7718-54-9) were provided by Sigma-Aldrich, and cetyltrimethylammonium bromide 99% (CTAB) (CAS: 57-09-0) by Roth. Deionized water was used for all experiments.

2.2. Synthesis Conditions of Iron Oxide Based RSNs

Magnetite $Fe_{3-x}O_4$ RSN synthesis. In a typical synthesis, $FeCl_3{\cdot}6H_2O$ (1.626 g), succinic acid (0.24 g), and urea (3.6 g) were completely dissolved in ethylene glycol (EG) (60 mL) by vigorous mechanical mixing (700 rpm) (for 2 hours up to overnight) and sonication (3 times 20 minutes, changing the water of the ultrasound bath) (Figure 2). The solution was carefully sealed in a Teflon-lined stainless steel autoclave (75 mL capacity) and slowly heated at 200 °C at a heating rate of 1.5 °C/min. The temperature was kept at 200 °C for several hours (between 5 and 10.5 h). The autoclave was then cooled down to room temperature outside of the oven for 3 hours. The black sediment was separated from the supernatant by magnetic decantation. In the first trial, it was washed three times with ethanol and three times with deionized water to eliminate organic and inorganic impurities. This washing step has been improved here and will be discussed later.

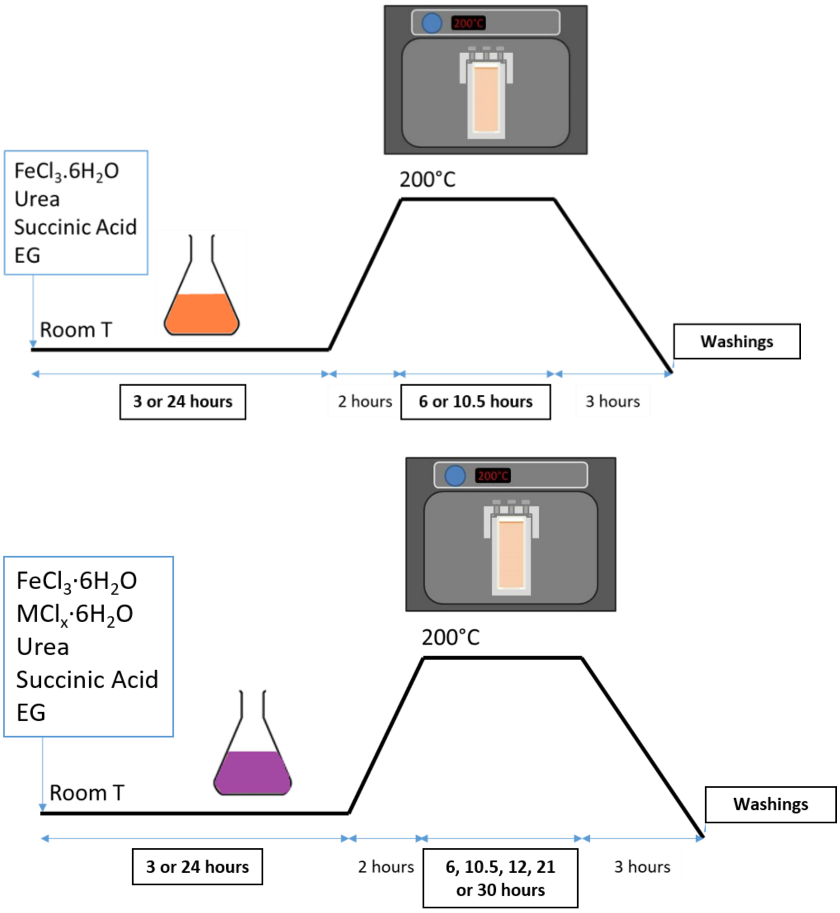

Figure 2. Synthesis conditions of RSNs (top) and of doped RSNs (down). EG: ethylene glycol.

Systematically, before each synthesis experiment, the glasses and Teflon containers were cleaned with an acidic solution (HCl, 6 M) for at least one hour and then washed with deionized water and ethanol.

The optimized parameters were the following: reactants dissolution step by adjusting the mixing time (3 h, 8 h or overnight, 24 h), the reaction time (6 or 10.5 h), the autoclave size, the cooling protocol of the autoclave (inside or outside the oven).

Doped RSNs. The same protocol as for the iron oxide RSNs was kept (Figure 2). Zinc chloride ($ZnCl_2{\cdot}6H_2O$) was used as the precursor for zinc, cobalt, chloride hexahydrate ($CoCl_2{\cdot}6H_2O$) for cobalt, and aluminum chloride hexahydrate ($AlCl_3{\cdot}6H_2O$) for aluminum. The synthesis of doped nanostructures by applying the same synthesis protocol as for undoped iron oxide RSNs has not been successful. We have therefore investigated this doping step by carrying out the synthesis by substituting cobalt to iron in different 1:X ratios (X = 1, 2, 3, 4, 7, 9—depending on the synthesis). The total concentration of metal cations was kept at 0.1 $mol{\cdot}L^{-1}$.

The synthesis conditions for each doping element are given below.

Zinc-doped RSNs. Mixing time of 3 h and reaction time of 12 h. A long reaction time is needed to ensure the dispersion of the Zn inside the structure. Indeed, a study by Nguyen et al. [19] reported on the formation, at first, of a Zn shell around the RSNs, with Zn gradually diffusing when increasing the reaction time.

Cobalt-doped RSNs. Mixing time of 3 h or overnight, and a reaction time of 10.5, 21, or 30 h. The two different mixing times evidenced the importance of a good dissolution of $CoCl_2{\cdot}6H_2O$ in the reaction mixture.

Aluminum-doped RSNs. Due to the similarities between Fe^{3+} and Al^{3+} cations (same valence, similar ionic sizes, same hydration), we kept a mixing time of 3 h and a reaction time of 10.5 h.

Washings of RSNs. After their synthesis, the RSNs were separated from the supernatant by magnetic decantation and dispersed in a mixture of 50/50 ethanol and warm acetone (60 °C). The suspension was ultrasonicated for 5 min, then magnetically decanted to remove the supernatant. Different washing treatments were tested, but traces of reactants (especially EG) always remained at the RSN surface. To remove the most of EG traces, the RSNs were washed 9–10 times.

2.3. Phosphate Adsorption Experiments

2.3.1. Preparation of Phosphates Solutions

Orthophosphoric acid was used as a phosphate source. A first solution at 309.9 P-mg/L was freshly prepared by introducing 68.4 µL of orthophosphoric acid (85%) in 100 ml of Milli-Q water. The solution was adjusted using a 2 M NaOH aqueous solution to precisely set pH 7. Other phosphate solutions were prepared by diluting this solution.

2.3.2. Adsorption Experiments

The RSN suspension was added to a solution containing phosphate at a known concentration. After magnetic mixing for different times for the kinetics study and for 24 h for the adsorption study, the RSNs were separated by magnetic decantation and washed with water. Finally, the phosphate remaining in supernatants was analyzed by UV–vis spectrophotometry using the "blue of *molybdene*" *method* described below.

The blue of molybdenum method. This method was already performed by Daou et al. [20] in order to quantify the amount of phosphates in supernatants. This method is effective and allows quantifying very low concentrations of phosphates in water. It consists in generating a phosphate complex, which can be quantified using UV spectroscopy.

$$7\ H_2PO_4^- + 12\ (NH_4)6Mo_7O_{24} + 72\ H^+ \rightarrow 7\ (NH_4)H_2PO_4(MoO_3)_{12} + 65\ NH_4^+ + 36\ H_2O \quad (1)$$

$$(NH_4)H_2PO_4(MoO_3)_{12} + 6\ Sn^{2+} \rightarrow \text{'Blue of Molybdenum'} + 6\ Sn_4^+ \quad (2)$$

Preparation: 2.5 g of ammonium molybdate ($(NH_4)_6Mo_7O_{24}$) was dispersed into 17.5 mL of pure water. In parallel, 28 mL of sulfonic acid (H_2SO_4, Carlo Erba) was dispersed in 40 mL of ddH_2O. Both solutions were then mixed and diluted up to 100 mL with ddH_2O to obtain the first reagent.

The second reagent was prepared as follows: 0.5 g of tin chloride dihydrate ($SnCl_2{\cdot}2H_2O$) was dispersed in 50 mL of 85% glycerol. Both reagents were kept in glass containers and wrapped with aluminum paper to avoid premature degradation from light exposure.

Five hundred microliters of the molybdenum reagent and 500 µL of the tin reagent were mixed with the appropriate amount of the phosphate solution and filled up to 10 mL with ddH_2O.

Nota Bene: These experiments have to be carried out under specific conditions: (i) the temperature must be between 20 and 25 °C to ensure the complex formation; (ii) to ensure that no traces of phosphates remain on the glasses, all required glasses are cleaned before each measurement with NaOH 2 M [20]; (iii) the blue of molybdenum complex is not stable with time, requiring a rapid measurement of absorption, typically after 10 min of mixing. Indeed, at the end of the mixing step, the complex is stable for only 15 min.

The reference mixture (obtained without phosphate) also undergoes a form of degradation. Therefore, the reference has to be repeated for each measurement. Regarding the measurement uncertainties, the complexation reaction itself does not always occur at the same reaction rate, leading to different values for a fixed concentration. The precision of the 10 min timing can also generate additional uncertainty.

Kinetics of phosphate adsorption as a function of time. For these experiments, a known amount of RSNs was dispersed in a phosphate solution with a given concentration, and the amount of remaining phosphate in the supernatant was analyzed at different times. Experimentally, 20 mg of RSNs was dispersed in 20 mL of a phosphate solution (50 P-mg·L^{-1} at pH 7). The mixture was stirred on a rotating wheel for 30 min up to 24 h.

Isotherm of adsorption experiments. Twenty milligrams of RSNs was dispersed in 20 mL of phosphate solution at different concentrations. The experiments were performed in water at pH 3 and 7. The range of investigated phosphate concentrations was 3.1–154.9 P-mg·L^{-1}. The mixtures were stirred on a rotating wheel for 24 h.

In the first approach, we considered the S, L, H, and C isotherm models to understand the interactions between phosphates and iron oxide. Then, different kinetics models were used to characterize more precisely the phosphate adsorption kinetics: the Langmuir, Freundlich, and Redlich–Peterson models.

2.4. Characterization Techniques

Thermal gravimetric analysis (TGA) measurements were performed with a TA Instruments DSCQ1000 instrument (New Castle, DE, USA) operated at a scanning rate of 5 °C min^{-1} on heating and cooling.

The NPs were characterized by transmission electron microscopy (TEM) with a JEOL 2100 microscope (Tokyo, Japan) operating at 200 kV (point resolution: 0.18 nm).

The X-ray diffraction (XRD) pattern was collected at room temperature with a Bruker D8 Advance diffractometer equipped with a monochromatic copper radiation source ($K\alpha$ = 0.154056 nm) and a Lynx-Eye detector in the 25–65°(2θ) range with a scan step of 0.03°. High-purity silicon powder (a = 0.543082 nm) was systematically used as an internal standard. Profile matching refinements were performed through the Fullprof program [21] using Le Bail's method [22] with the modified Thompson–Cox–Hasting (TCH) pseudo-Voigt profile function.

Standard infrared spectra were recorded between 4000 and 400 cm^{-1} with a Fourier transform infrared (FTIR) spectrometer, (Spectrum 100, Perkin Elmer, Waltham, MA, USA). Samples were gently ground and diluted in non-absorbent KBr matrices.

Magnetic measurements were performed using a superconducting quantum interference device (SQUID) magnetometer (Quantum Design MPMS-XL 5, San Diego, CA, USA). Magnetization curves as a function of a magnetic field (M(H) curves) were measured at 300 K. Magnetization saturation (M_S) was measured from hysteresis recorded at 300 K and was determined after removing the mass of organic ligands according to TGA experiments.

BET nitrogen (N_2) adsorption/desorption isotherms. To characterize the surface specific area of the RSNs, adsorption and desorption of nitrogen isotherms were measured on an ASAP 2420 V instrument with around 100 mg of RSNs. The Brunauer–Emmett–Teller (BET) method was used to calculate the surface area.

3. Results

3.1. Optimization of the Synthesis of Iron Oxide Nanostructures

3.1.1. Reproducibility of RSN Synthesis

The protocol of Gerber et al. [11] was first reproduced using the same reactants (iron precursor flask: Alfa-Aesar 2 (AA2)) and under the same conditions (Table S1). The so-synthesized RSNs were characterized with SEM and TEM, FTIR spectroscopy, X-ray diffraction, and magnetic measurements. These characterizations are detailed in the SI and summarized in Table S1. The structural and magnetic characterizations (Figure S1) confirmed an oriented aggregation of nanograins, but the RSN diameter and nanograin sizes were observed to be different from the study of Gerber et al. [11]. Indeed, using the same reactants and synthesis conditions, the mean diameter of RSNs is smaller (245 vs. 157 nm) when the mean grain size is higher (25 vs. 30 nm). For both RSN samples, the grain size is higher than the crystallite size deduced from the XRD pattern. Gerber et al. [23] attributed such a mismatch between both sizes to the presence of defects or dislocations resulting from the formation mechanism of the oriented aggregates (coalescence of grains, recrystallization processes). The lattice parameter is similar and agrees with the presence of mostly magnetite. Its slightly higher value than the bulk magnetite phase value may be explained by the presence of defects and strains induced by the oriented aggregation. The saturation magnetization ($M_{S,\ 300K}$) value is also lower (78 [23] vs. 70 emu·g^{-1} (this study)) and may be explained by the difference in sizes leading to a slightly higher oxidation of the magnetite phase in RSNs. Indeed, Gerber et al. observed similar results in RSNs, with larger nanograins displaying lower interfaces, which normally contribute to preventing nanograins from oxidation.

To conclude, the reactants and experimental conditions were the same, and the only parameter was their "aging" (two years). An impact of the precursor nature on the synthesis of RSNs was at first suspected. Indeed, the iron precursor flask was stored in the laboratory without particular precautions and an effect of the aging of the iron precursor was also suspected. In order to investigate a possible effect of the iron chloride precursor, the RSN synthesis was performed using different $FeCl_3{\cdot}6H_2O$ precursors provided by different companies or stocked at different times in the laboratory.

3.1.2. Effect of the Commercial Nature of Hexahydrate Iron Chloride(III) Precursor

In the following experiments, the sole difference was the brand and batch of hexahydrate iron chloride(III), the other used reactants and the experimental conditions were the same. The previous synthesis was performed with the reactant Alfa Aesar-2 (AA2). The characteristics of RSNs obtained using different types of iron precursor are given in Table 2.

Table 2. Mean crystallite size (deduced from XRD patterns) and mean diameter and nanograin size of RSNs as a function of the used iron precursor and representative SEM images of the synthesis.

Brand and Lot	Sigma-1	Alfa Aesar-1	Alfa-Aesar-2	Acros Organics-1
RSN size (nm)	291 ± 52	296 ± 35	157 ± 42	~100
TEM nanograin size (nm)	38 ± 7	26 ± 6	30 ± 6	27 ± 9
XRD crystallite size (nm)	32.4	19.9	20.2	25.4
TEM image (scale bar = 1 µm)	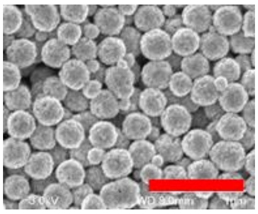	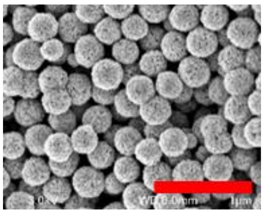	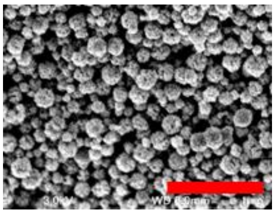	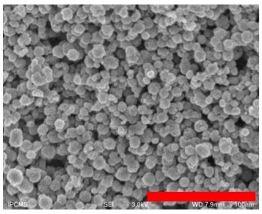

SEM images show that all experiments gave nanoclusters with an aggregated and spherical morphology, but RSNs have different mean sizes of nanoclusters, nanograins, and crystallites. The nanograin sizes determined from TEM images are always larger than the crystallite sizes. A correlation with the used iron chloride precursor is evident. Several hypotheses may explain such a discrepancy; our first hypothesis is the hydrolysis of iron chloride, as the latter is well known to be very sensitive to hydrolysis [24,25]. The iron precursors would display different hydration rates as a function of the aging time. Several groups also reported on the effect of water in polyol synthesis [26,27] and more precisely, in the nanocluster formation. Cao et al. [28,29] controlled the particle size and size distribution by adjusting the amount of water. They pointed out that the coordination of water molecules with iron ions is stronger than that of EG with iron. They observed a modification of the morphology with water: when water is added, the size of grains increases, and that of nanoclusters decreases. However, a direct link cannot be confirmed because these authors also increased the concentration of iron in their initial solution, and several groups have already confirmed a link between iron concentration and morphology [28].

Another problem encountered in these experiments was the random formation of iron carbonates within the final product (see details in SI: iron carbonate formation). The iron carbonate particles (siderite) with their characteristic brush morphology [30] were observed in the SEM images (Figure S2). As they are not identified by X-ray diffraction (except for one sample), these iron carbonates should represent less than 5 weight % of the sample (the necessary percentage to be detected by XRD). Iron carbonates are certainly formed out of CO_2 produced by the thermal decomposition of urea into CO_2 and ammonia [9]. Once formed, this $FeCO_3$ cannot be decomposed further because of its stability over a wide range of temperatures. Similar carbonate formation was reported by Li et al. [31], who observed the intermediate formation of cobalt carbonates, $CoCO_3$, which decompose to form cobalt ferrite at very high temperatures (>800 °C). It is worth noting that if a new (unaged) iron chloride precursor was used in the synthesis, no carbonates were detected. Therefore, the potential hydration of the reactant could be linked to the carbonates' formation.

Thus, the above results could be explained by an aging effect resulting in the gradual hydration of different iron precursors. All iron chlorides were characterized to check if the iron chlorides were hydrolyzed or polluted by other substances. XRD, TGA, element analyses, and iron quantification experiments were performed and are detailed in the SI.

First, the color of the four iron precursors is different (Figure S3). Sigma 1 has a bright yellow color; Alfa Aesar-1 is darker and presents a brown-orange color rather than yellow; Alfa Aesar 2 is visually more similar to Sigma, and Acros Organics (AO1) is opaquer. The morphology of powders is also different: Sigma 1 and Alfa Aesar 2 (AA2) are less compact than Alfa Aesar 1 (AA1) and Acros Organics. The iron amount has also been determined by relaxometry measurements (Table 3). All commercial batches of iron chloride(III) hexahydrate contain less iron than expected. However, there is no strong correlation between the amount of iron and the mean RSN diameter (Table 3). The lower iron content is suggested to be due to a higher water content or hydrolysis rate of the iron precursors.

Table 3. Fe/Cl and Fe/O atomic ratios determined by SEM-EDS and amount of iron in the different iron precursors determined by relaxometry measurements.

Iron Precursor	**Sigma 1**	**Alfa Aesar 1**	**Alfa Aesar 2**	**Acros Organics 1**
RSN diameter (nm)	291 ± 52	296 ± 35	157 ± 42	100 ± 50
Iron amount determined by relaxometry measurements				
Expected iron weight (mg)	1	1	1	1
Measured iron weight (mg)	0.89	0.93	0.94	0.93
SEM-EDS analysis: Theoretical Fe/Cl = 0.33 and Fe/O = 0.17				
Fe/Cl	0.35	0.36	0.38	0.44
Fe/O $FeCl_x \cdot yH_2O$	0.33 $FeCl_{2.86} \cdot 3H_2O$	0.30 $FeCl_{2.78} \cdot 3.3H_2O$	0.38 $FeCl_{2.63} \cdot 2.6H_2O$	0.37 $FeCl_{2.27} \cdot 2.7H_2O$

SEM images of the four reactants (Figure S4) showed the same morphology: a rough but uniform surface without grains or sheets. The associated EDS elementary analysis (Figure S4) showed, in addition to iron, chlorine, and oxygen, the presence of traces of some elements (aluminum and silicium), which do not seem to impact the RSN synthesis (see details in SI). Fe/Cl and Fe/O ratios have been extracted from these analyses (Table 3, Figure S4, Fe and Cl from $FeCl_3$, and Fe and O from H_2O). In theory, the atomic ratios for Fe/Cl of 0.33 and Fe/O of 0.165 are expected. The mean diameter of RSNs decreases with the increase in both ratios, showing the impact of these elements in the synthesis. The analysis of these results, detailed in SI, led us to conclude that a hydrolysis of iron chloride [24] has certainly occurred. However, as the iron precursors are in the form of big particles (SEM images in Figure S4), one might expect that the particles consist of a core of $FeCl_3 \cdot 6\ H_2O$ with a hydrolyzed layer at the surface.

The hydrolysis of the precursors may be calculated (Table S3), and the hydrolyzed species given in Table S3 are similar to those observed during the synthesis of the iron stearate precursor from iron chlorides: $Fe(OH)_{2.6}(H_2O)_{3.4}$ [25]. Some differences are observed, suggesting a higher hydrolysis of Sigma and AA1 by comparison with other iron chlorides. However, these hydrolysis reactions do not allow explaining the observed ratios and are obtained by putting iron chlorides in direct contact with water, which is not the case here. A partial hydration may explain the decrease in the Fe/Cl ratio but not that of the Fe/O ratio, which in all cases remains in the range of 0.30–0.38. In fact, the O/Fe ratio is very close to 3 without a large amount of water and it suggests the formation of either $Fe(OH)_x(H_2O)_y$ with a lower amount of water than a hydrolysis in water and even quite no water or $Fe(OH)_xCl_y$ type compounds. The formation of iron oxychlorides cannot be excluded, nor can the beginning of the olation reaction lead to oxo-hydroxides such as FeOOH. The main problem is that there are numerous papers on the hydrolysis of iron chlorides in water but not on the aging of iron chlorides in powder form [24,25]. The AA2 and AO1 iron chloride samples are likely more "hydrolyzed", which could explain the lower diameter of RSNs synthesized from these.

The different iron precursors have been characterized by XRD, FTIR spectroscopy, and TGA (Figure S6). XRD patterns (Figure S6A) show only the XRD peak characteristic of $FeCl_3 \cdot 6H_2O$ (PDR 00-033-0645), but FTIR spectra (Figure S6B) confirm the contamination of the precursors with silicon and the surface hydrolysis of the iron chlorides with a different hydrolysis rate. TGA experiments (Figure S6C) were performed to try to quantify the amount of water, but, if the water quantification remains difficult, TGA curves were shown to exhibit different characteristics (see SI on TGA experiments).

3.1.3. Discussion on the Synthesis of RSNs

To conclude on the effect of the commercial origin of iron precursors: different commercial batches of $FeCl_3 \cdot 6H_2O$ led to RSNs with different mean diameters and nanograin sizes. The different characterizations performed showed that they are all hydrated and that a hydrolysis of some precursors cannot be excluded. This hydration/hydrolysis is certainly responsible for the different observed results. In an agglomerate of reactant particles, a gradual modification of the composition should be observed: from the initial iron chloride (in the center) to a more hydrated form at the surface. In agreement with the reported results on the effect of water on the RSN diameter [26], the hydration of the iron chloride precursor leads to a smaller diameter of RSNs. The variation of the nanograin size is not easy to explain, but it should also depend on the hydration rate.

In the RSN formation mechanism reported in [11] and Figure S7, the coprecipitation of iron oxide nanoparticles occurs first due to ammonia resulting from urea decomposition, and then there is a heterogeneous nucleation and growth induced by the decomposition of an intermediate iron precursor resulting from the reaction of remaining iron chloride with EG. We may hypothesize that the different hydration rates of commercial precursors would affect these different steps. The hydration may favor the coprecipitation step leading to a higher amount of RSNs resulting from coprecipitation and there is thus not enough intermediate precursor to induce a heterogeneous nucleation. The intermediate precursor contributes only to the growth of the first-formed RSNs, which would explain their smaller diameter and also the different observed nanograin sizes. Further experiments would be needed to confirm these hypotheses.

Besides these observed differences in RSN diameter and nanograin sizes, we have evidenced another drawback of the iron precursors' hydration, which is the formation of iron carbonates. This hydration affects their dissolution in ethylene glycol. Indeed, the effect of mixing time allowing to dissolve the reactants has been studied: with an "old" iron chloride flask, a mixing of the reaction mixture for overnight allowed avoiding the formation of carbonates. With "new" and "well stored" iron chlorides, overnight mixing was not necessary. This confirms another impact of the hydration rate of iron precursors.

Therefore, to obtain reproducible results, it is mandatory to store the flask in optimal conditions: under a vacuum atmosphere to avoid humidity and at a controlled temperature (maximum suggested temperature: 35 °C). RSN syntheses were then realized with a "new" $FeCl_3 \cdot 6H_2O$ precursor, stored under the previous conditions, and renewed every six months.

3.2. Optimization of the RSN Synthesis

A typical RSN synthesis (3 h of mix and 10.5 h of reaction) with the new iron precursor leads to the expected raspberry-shaped morphology (Figure S8A) with oriented aggregates of nanograins (Figure S8B). These nanoclusters, whose characterizations are detailed in SI, have a diameter of around 296 ± 35 nm with nanograins of ca. 25 nm, and a magnetite composition. Magnetic measurements confirmed their superparamagnetic behavior (no hysteresis) and led to a saturation magnetization value of ca. 90 $emu \cdot g^{-1}$, a value close to that of bulk magnetite (92 $emu \cdot g^{-1}$) [32]. These results are compared with those of Gerber et al. [23] and with previous results with the aged precursor in Table 4. The diameter and nanograin size are higher and would confirm the impact of the hydration of the precursor. The higher nanograin size leads to a composition as close to that of magnetite as expected and thus to a higher saturation magnetization [8,33].

Table 4. Comparison of the RSNs synthesized with different iron precursors.

	Gerber et al. (Sample RSN25)	**First RSNs (AA2 Precursor)**	**New RSNs (New Precursor)**
Size of RSN (nm)	245 ± 12	157 ± 42	296 ± 35
TEM nanograin size (nm)	25 ± 3	30 ± 6	38 ± 10
XRD crystallite size (nm)	15.5 ± 0.2	20.2 ± 0.3	30 ± 0.2
Lattice parameter (Å)	8.39 ± 0.01	8.39 ± 0.01	8.40 ± 0.01
Saturation magnetization (emu g^{-1})	78	70	90

As the objective is to synthesize RSNs with the highest specific surface area in order to capture as much phosphate as possible, different synthesis parameters have been tuned: the mixing times to dissolve reactants (3 h and overnight) and the reaction times (6 and 10.5 h).

Effect of mixing time and reaction time. SEM images confirmed the formation of aggregates of nanoparticles, and the characterization results are given in Table 5. The values of the lattice parameter confirm a magnetite composition for all samples. For experiments B, C, and D, nanoclusters of around 300 nm are obtained when, in synthesis A, RSN diameters are around 266 nm. In experiments A and B, with 3 hours of mixing and different reaction times, there is a strong correlation between the reaction time and the RSN size and grain size. This result agrees with the observations of Gerber et al., that longer reaction time produced the bigger RSNs with higher grain size [11]. Therefore, it explains the increase in the crystallite size with the reaction time, whatever the mixing time.

However, considering experiments C and D with different reaction times and conducted with a similar but longer mixing time (overnight), one may notice that RSNs have almost the same size and only the crystallite size has increased. This suggests that the overnight mixing led to RSNs, which reached their maximal diameter after 6 h of reaction while 10.5 h of reaction time is needed when the reactants' mixing time is only 3 h.

The effect of the dissolution time (mixing time) of reactants is also visible by comparing experiments A and C, and B and D. After 6 h hours of reaction, the mixing time of 3 h (A) leads to smaller RSNs compared to that of 24 h (C). By contrast, 3 h of mixing and 10.5 h of reaction lead to similar RSN sizes as 24 h of dissolution and 6 h of reaction, but the grain size is higher. Therefore, the longer the mixing time the faster the reaction. These experiments show that the dissolution of the reactants is a very important step and affects the reaction kinetics and thus the characteristics of RSNs.

Table 5. RSN synthesis of experiments A, B, C, and D with 3 or 24 h of mixing and 6 or 10.5 h of reaction time at the highest reaction temperature (standard deviation for lattice parameter: ±0.01).

Experimental Conditions	A 3h Mixing, 6h Plateau	B 3 h Mixing, 10.5 h Plateau	C Overnight Mixing, 6 h Plateau	D Overnight Mixing, 10.5 h Plateau
SEM image (scale bar: 100 nm)	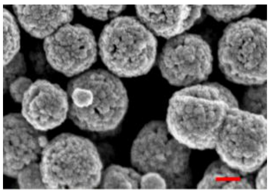	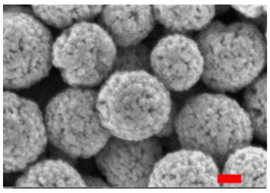	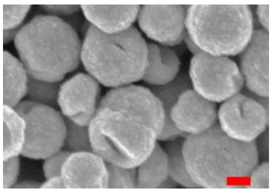	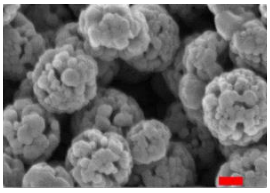
RSN size (nm)	~266	~317	~320	~310
Nanograin size (nm)	24 ± 5	29 ± 8	36 ± 12	43 ± 10
Lattice parameter (Å)	8.41	8.39	8.40	8.40
Specific surface area (m^2 g^{-1})	24.2	27	18.9	17.8

Finally, Brunauer–Emmett–Teller (BET) measurements showed the specific surface area in the range of 17 and 30 $m^2 \cdot g^{-1}$. As expected, the RSNs with the smaller nanograin sizes display the highest values.

Therefore, the conditions leading to RSNs with the highest surface specific area are: 3 hours of mixing and 10.5 hours when the temperature plateau is reached (200 °C).

3.3. Synthesis of Doped Iron Oxide Nanostructures

The doping conditions have been optimized by taking care to preserve the raspberry morphology, to be able to remove the particles with a magnet and to obtain a high specific surface area.

3.3.1. Doping of RSNs with Zinc (Zn-RSNs)

Zinc doping is interesting for modulating saturation magnetization. In the doped ferrite, zinc mostly occupies the tetrahedral sites in the spinel structure, and M_S would increase if x in $Zn_xFe_{2-x}O_4$ increases [34]. Nevertheless, after a given x, the measured magnetization decreases. Indeed, zinc ferrite ($ZnFe_2O_4$) has a spinel structure, and the absence of Fe^{3+} in Td sites (occupied by Zn) results in a weak antiferromagnetic material within Fe^{3+} and Fe^{2+} at Oh sites [35].

Preliminary experiments suggested that the zinc diffusion inside iron oxide in the RSNs would be longer, and thus the reaction time has been increased from 10.5 to 12 h and different iron/zinc ratios have been tested. In all cases, the SEM images (Figure 3(A.1–A.3)) confirm the formation of clusters of NPs with a partial conservation of the raspberry morphology. All ratios produced nanoclusters of similar size (300 ± 103 nm, 280 ± 86 nm, and 272 ± 46 nm, respectively). However, the 1.2:1 and 2:1 syntheses led to a larger particle size distribution. EDS analysis further showed a very low (<1%) amount of zinc for these syntheses.

In order to enhance the zinc doping, the initial ratio of Fe-Zn was increased to 9:1. SEM images confirmed the RSN morphology, and EDS analysis showed an increase in the zinc amount (3%) even if it is always lower than expected. XRD patterns showed only the characteristic XRD peaks of a spinel phase but no modification of the lattice parameter (respectively: 8.391; 8.391 and 8.388 Å) confirming the low Zn doping. The calculated crystallite size was 32.6 nm for the last sample, this value corresponds to the grain size of the previous magnetite RSNs. The low amount of zinc in the doped RSNs confirmed the reported difficulty in doping magnetite RSNs with zinc [19].

From these experiments and reported results, we conclude that the difficulty is the complete dissolution of the zinc chloride precursor. In future experiments, other zinc precursors will be tested, as well as varying the mixing time.

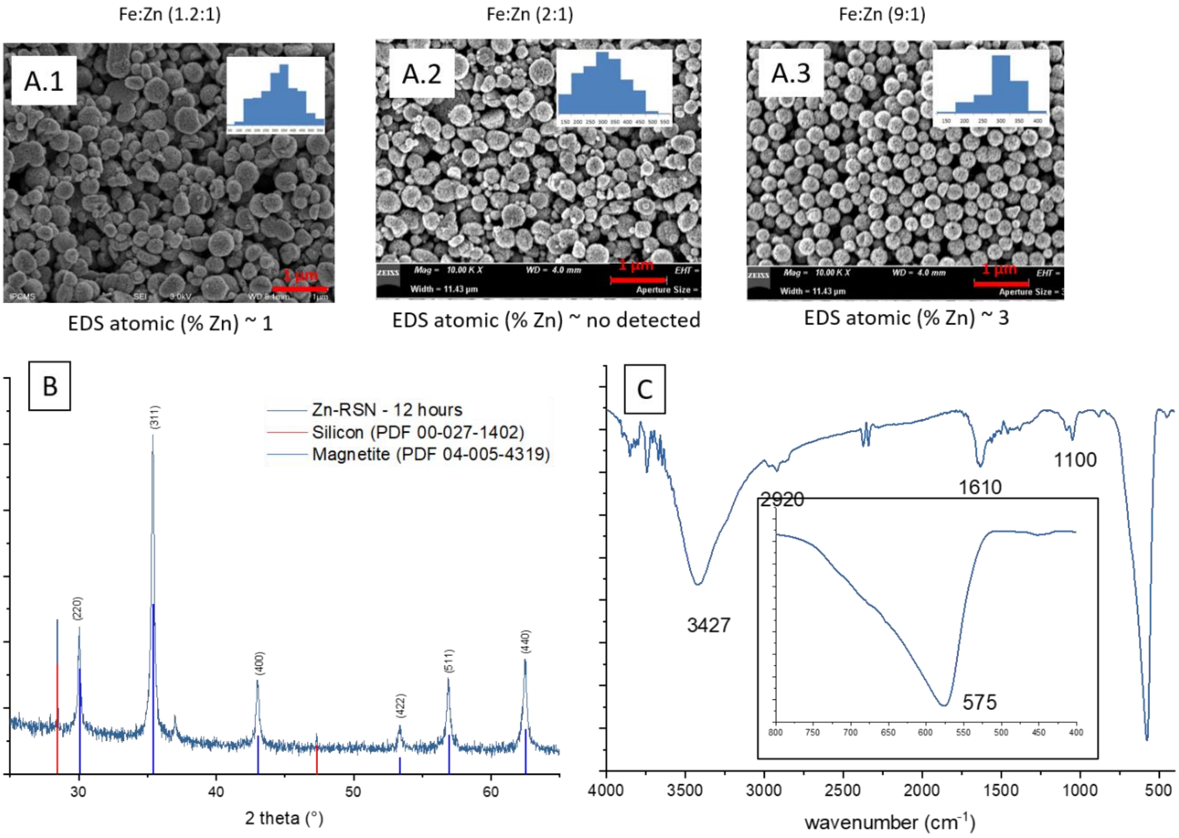

EDS atomic (% Zn) ~ 1

EDS atomic (% Zn) ~ no detected

EDS atomic (% Zn) ~ 3

Figure 3. (**A.1**–**A.3**) SEM images of all zinc-doped RSNs (inner image: size distribution); (**B**) XRD pattern; (**C**) IR spectrum of zinc-doped RSNs (9:1) (mixing time: 3 h; reaction time 12 h) (inner image: zoom on the Fe–O band characteristic of slightly oxidized magnetite).

3.3.2. Doping of RSNs with Cobalt (Co-RSNs)

The ferrite $CoFe_2O_4$ drew attention because, in its bulk state, it is a well-known hard magnetic material with a high coercivity (H_C), a high Curie temperature (520 °C), a moderate saturation magnetization (80 $emu \cdot g^{-1}$) and a high anisotropy constant (2.65×10^6–5.1×10^6 $erg \cdot cm^{-3}$). Stoichiometric $CoFe_2O_4$ NPs would present a higher saturation magnetization due to the presence of Co^{2+} ions in the octahedral sites of the spinel structure: $[(Fe^{3+})_{Td}(Co^{2+}Fe^{3+})_{Oh}](O^{2-})_4$ [36]. However, at the nanosize, Co^{2+} atoms are observed to replace also some Fe^{3+} atoms in tetrahedral sites leading to an inverse spinel structure: $(Co_xFe_{1-x})_{Td}[Co_{1-x}Fe_{1+x}]_{Oh}O_4$, where x depends on the synthesis conditions [37].

Following the previous protocol (3 h of mixing), the RSN synthesis has been performed with two different Fe:Co ratios. For a Fe:Co ratio of 1:1, RSNs with a mean size of 292 ± 76 nm (Figure 4(A1)) are observed, but the size distribution is quite broad. With the Fe:Co ratio 2:1 (Figure 4(A2)), the RSN size distribution is narrower and the diameter smaller: 224 ± 26 nm. Some of the RSNs are hollow, and at the top of the SEM image, metal carbonate particles are identified. This carbonate formation is random and linked to the reactant dissolution step. Even if the SEM-EDS analysis showed a higher Co doping amount than with zinc (from 7 to 12 atomic %), the presence of carbonates affects this value. To avoid carbonate formation, the mixing time and the reaction time of 21 and 30 h have been increased to favor the reactants' dissolution in the reaction media. SEM images (Figure 4B) showed RSNs with a close mean diameter: 287 ± 25 nm for 10.5 h, 262 ± 25 nm for 21 h, and 267 ± 22 nm for 30 h). However, for the synthesis for 10.5 h, nanograins appear smaller and the surface is less rough than the others. EDS analysis shows a decrease in the cobalt amount (7–7.5 %) (no carbonate was detected). From the three experiments, the reaction time appears to have no effect on the cobalt doping amount.

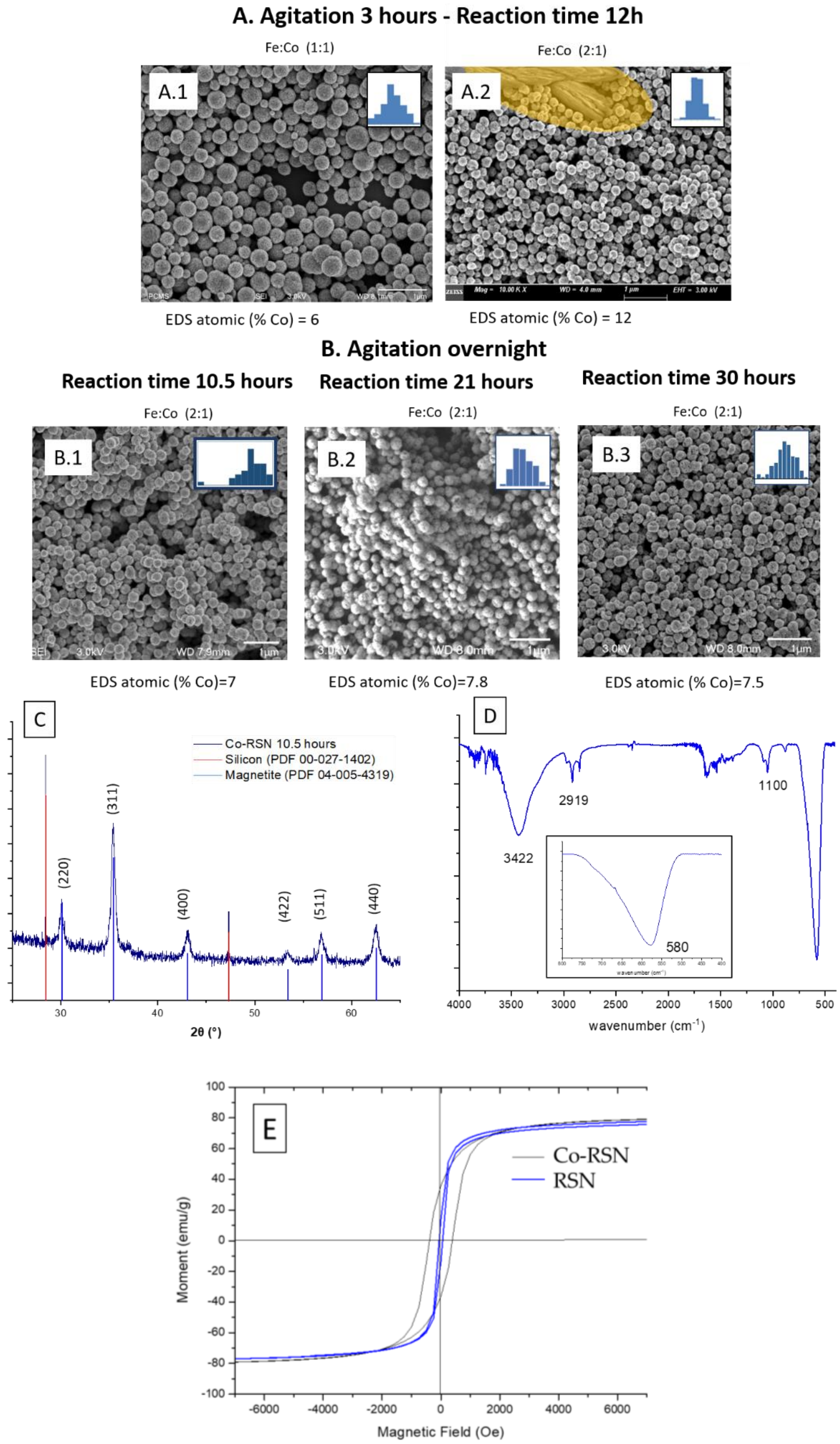

Figure 4. SEM images of cobalt-doped RSNs. (**A**) Experiments with 3 h mixing (golden shading in A2 shows the carbonate particles and inner images = SEM size distribution). (**B**) Experiments with overnight mixing. (**C**) XRD pattern. (**D**) FTIR spectrum (inner image = zoom on Fe–O bands showing one band at 580 cm^{-1} characteristic of the magnetite phase). (**E**) Magnetization curves of the undoped and cobalt-doped (B.1) RSN at 300 K.

Figure 4C displays the XRD pattern of the last sample (stirred overnight and 10.5 h of reaction time); those of other samples are very similar and not presented here. The XRD peaks are related to a spinel structure (maghemite, magnetite) without the presence of another phase (same observation for the sample containing carbonates). The lattice parameter was calculated to be 8.41 Å, a slightly higher value than that of bulk magnetite; this increase can be related to the insertion of cobalt in the structure. The crystallite sizes are: 17, 27.8, and 36 nm for Co-RSNs with reaction times of 10.5, 21, and 30 h, respectively. The IR spectrum confirms the presence of the magnetite phase (inner image in Figure 4D) and the presence of EG traces. SQUID measurement at 300 K of the sample B.1 (with the smallest nanograin size) led to a saturation magnetization of 83.5 emu·g^{-1} for $Co_xFe_{3-x}O_4$ vs. 83.8 emu·g^{-1} for similar magnetite RSNs. As for other cobalt-doped iron oxide NPs, a hysteresis curve was observed, confirming the cobalt doping with a coercivity value of 400 Oe (Figure 4E).

3.3.3. Doping of RSNs with Aluminum (Al-RSNs)

Aluminum has been shown to be a suitable doping element to enhance phosphate removal. However, aluminum is a non-magnetic element, and Al substitution decreases Ms because, unlike Zn, Al^{3+} substitutes for Fe^{3+}, not Fe^{2+}. So, to keep the possibility of "magnetic decantation", the magnetite RSNs should be doped with a small amount of aluminum. The doping of magnetite nanostructures with aluminum should be easier than with Zn and Co because the ionic radius of Al and Fe^{3+} is quite close and their valence is the same (+3). For the doping process, a reaction time of 10.5 hours and a mixing time of 3 hours were tested, as well as three Fe:Al ratios. SEM images (Figure 5) show nanostructures with the morphology of undoped RSNs, but a broad size distribution is noticed with a mean diameter of 269 ± 45 nm for the last sample. EDS analyses confirm the success of the aluminum doping, with quite high doping amounts increasing with the amount of introduced Al.

However, during the washing step, samples with an iron quantity in the Fe:Al ratio of 2 to 7 were difficult to decant magnetically. To facilitate this step, samples were centrifuged. However, it confirms that aluminum doping modifies the magnetic properties (in particular, saturation magnetization). The only sample that could be magnetically decanted was the last one (Fe:Al 10:1). Thus, this sample, called Al-RSNs, was characterized and then used for phosphate removal experiments.

XRD patterns (Figure 5B) confirm the preservation of the iron oxide spinel structure without the presence of other phases. The XRD peaks are broader for RSNs, with high Al content suggesting a loss of crystallinity or smaller crystallite sizes. The lattice parameter, 8.389 Å, is lower than that observed usually with undoped RSNs but would confirm the aluminum insertion in the spinel structure. The crystallite size is calculated to be 19.5 nm (Figure 5(A5)), suggesting that the Al doping leads to a smaller crystallite size. The highest surface specific area measured for this sample (40 m^2/g) confirmed the smallest nanograin size of Al-RSNs compared to undoped RSNs. The magnetization curve at 300 K is characteristic of superparamagnetic behavior, and the saturation magnetization (Figure 5D), 64 emu·g^{-1} for $Al_xFe_{3-x}O_4$, is lower than that of undoped RSNs, confirming the doping of magnetite by Al and previously reported results of other groups [15,38,39].

3.4. Phosphate Removal Using Undoped and Al-Doped Iron Oxide Nanostructures

RSNs, used for these experiments, have a mean diameter of 319 nm and a mean nanograin size of 29 nm (surface specific area = 27 m^2 g^{-1}). RSNs doped with 10% of Al have a mean diameter of 269 nm, a mean nanograin size of 19.5 nm, and a surface specific area of 40 m^2·g^{-1}.

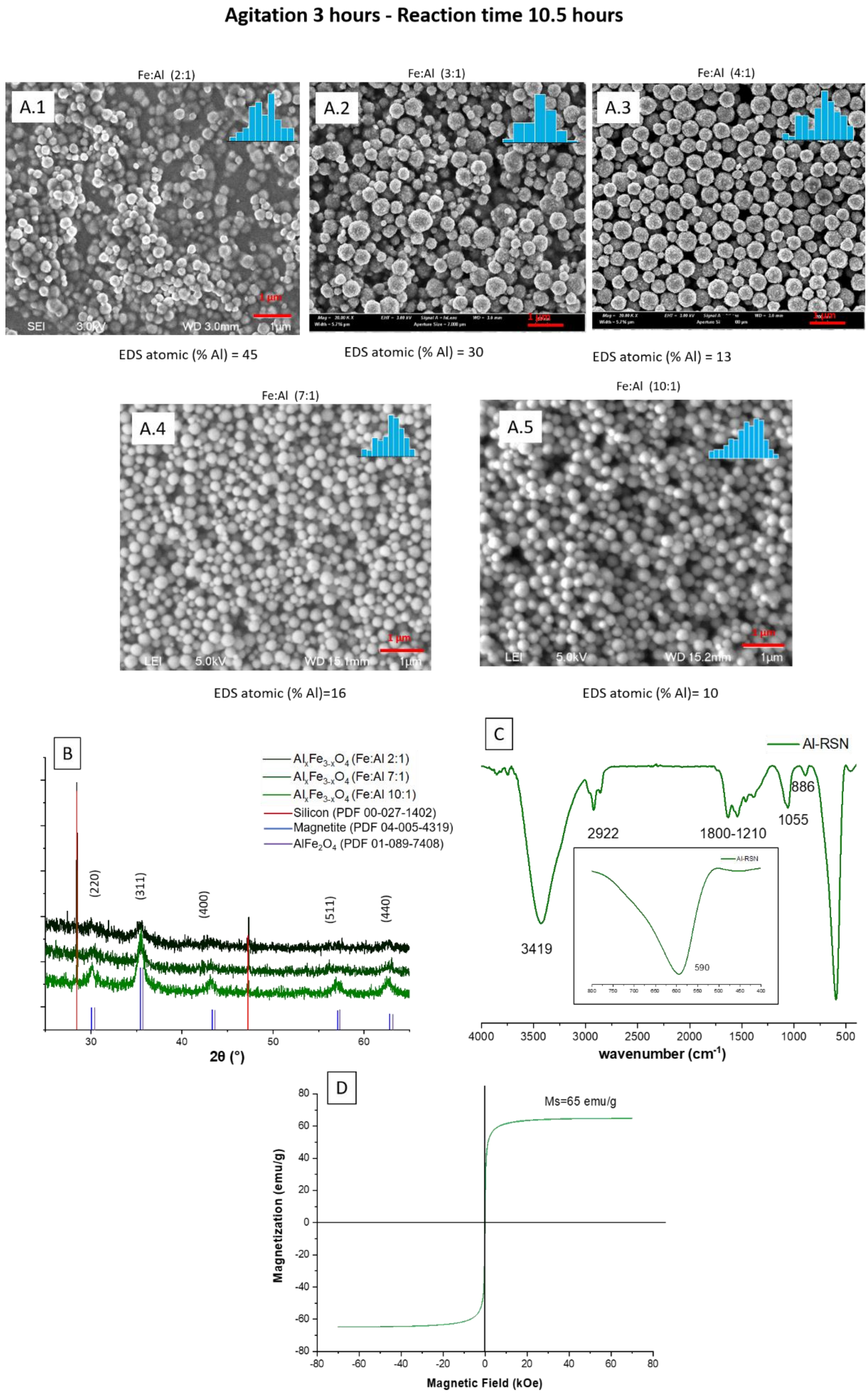

Figure 5. (**A.1**–**A.5**) SEM images of Al-RSNs (inner image: size distribution); (**B**) XRD pattern as a function of the Fe:Al ratio; (**C**) FTIR spectra (inner image: zoom of Fe–O band characteristic of a slightly oxidized magnetite phase); (**D**) magnetization curve of Al-RSNs at 300 K.

To ensure a high adsorption of phosphate at the surface of iron oxide nanostructures, it is important to favor electrostatic interactions between phosphate and the iron oxide surface. The isoelectric point (IEP) of RSNs is about 5.6, as depicted in Figure S9, and is slightly shifted by comparison with the reported IEP of iron oxide, usually in the range 6–7 [40].

This is certainly due to the washing process, which does not completely remove all reactants (especially ethylene glycol) from the RSN surface. For phosphates, an increase in pH leads to a change in the main species in the solution from H_3PO_4 to PO_4^{3-} (Figure S9). Thus, the suitable electrostatic interactions between deprotonated phosphates and iron oxide surfaces are for pH < 5.5. Thus, optimal adsorption conditions would be around pH 3, as the phosphates are deprotonated (negatively charged) and the iron oxide surface is positively charged. However, in water depollution conditions, the pH is often around 7. At this pH, the solution contains phosphates in $H_2PO_4^-$ and HPO_4^{2-} form when the surface of RSNs is slightly positively charged. At such a pH, the adsorption maximum is expected to be much lower than at pH 3.

The zeta potential curve of Al-RSNs as a function of pH in Figure S9 shows clearly that the insertion of aluminum into the spinel iron oxide structure induces a shift of the ZP curve towards higher pH. The value of the isoelectric point is shifted from 5.6 to 7.2, and therefore, at pH 7, the electrostatic interactions would be stronger, and the phosphate capture should be favored.

3.4.1. Phosphate Removal from Undoped and Al-Doped RSN Solutions as a Function of Time

In the first experiment, RSNs were put in contact with phosphate solutions at various times. Figure 6 shows that the maximum adsorption is reached after one hour for RSNs and 3 h for Al-RSNs. Then, the curve tends to reach a saturation plateau. Some adsorption results with Fe- and Al-Fe-based materials are given in Tables S4 and S5. In other studies of Al-Fe-based materials (Table S5), the maximum adsorption is reached after 5 h [15,38,40–42]. So, at first sight, the Al-RSNs synthesized in the present work would ensure a faster phosphate caption.

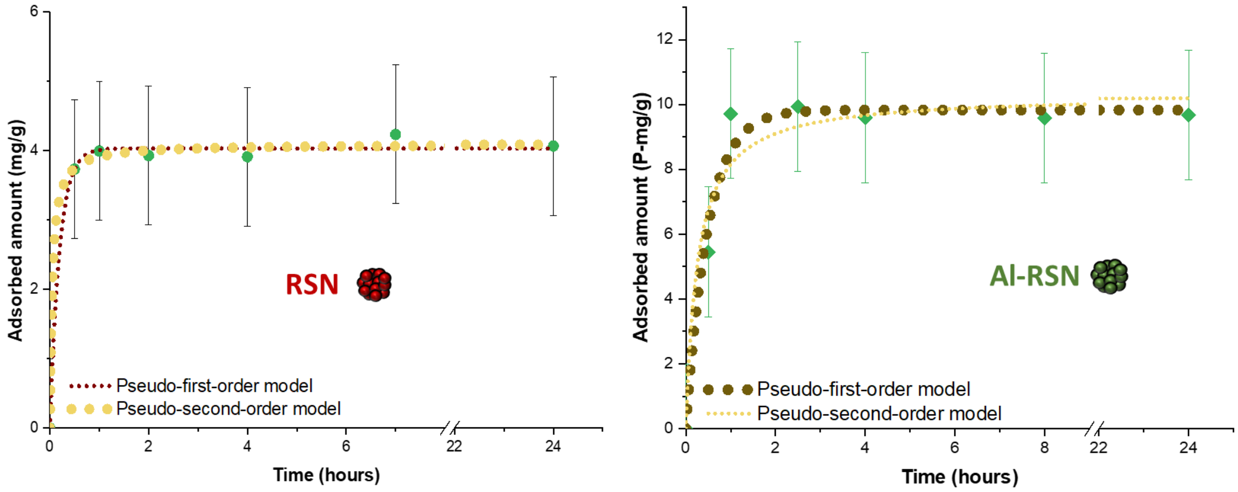

Figure 6. Adsorbed amount of phosphate by RSNs (left) and Al-RSNs (right) in a phosphate solution (50 P-mg·L^{-1}) at pH 7 for different durations.

For most other iron oxide-based nanomaterials (Table S4), the maximum phosphate caption is reached after 5 to 15 h. The only nanomaterial that shows a caption time similar to ours is the iron hydroxide eggshell of Mezenner et al. [43]. These authors observed a maximum adsorption after 3 hours. From these results, we may conclude that the iron oxide RSNs without Al adsorb the phosphates at the fastest rate.

The adsorption curves have been fitted with two kinetic equations. In Figure 6, we can observe that, for RSNs, both models seem to fit quite well the experimental data and give similar kinetics parameter values (Table 6). The R^2 value of the pseudo-second-order model is the highest and closest to 1. This model suggests that chemical sorption is the rate-determining parameter [44–46]. More precisely, the pseudo-second-order model describes the adsorption in two steps. The first step is a rapid adsorption on the surface of the adsorbent with abundant vacant adsorption sites. The second step is a slower diffusion to finish the saturation of adsorbent sites [47]. This would be in agreement with a quick adsorption of phosphate on iron sites and then the diffusion of phosphates to fill the remaining sites. It is difficult to compare our results with published results because the adsorption is strongly dependent on the initial concentration, the amount of adsorbent introduced, and the temperature. To remove phosphates from water, different iron oxide-based materials have been designed (Table S4): for example, iron oxide-impregnated strong base anion exchange resin [48], a hybrid fibrous exchanger containing hydrated ferric oxide nanoparticles [49], or a hybrid anion exchanger containing triethylamine functional groups and hydrated Fe(III) oxide nanoparticles [50]. Our results are compared with studies performed on iron oxide (nano)materials (Table S4). In Table S4, most of the data also fit better with the pseudo-second-order model. The comparison of our RSNs to the other iron-based materials shows that the k_2 value is the highest (5.28 h^{-1}), which confirms that our RSNs can adsorb phosphates faster.

Table 6. Kinetic parameters for pseudo-first-order and pseudo-second-order models for RSNs and Al-RSNs.

	Pseudo-First-Order			**Pseudo-Second-Order**		
	q_e **(P-mg·g^{-1})**	K_1 **(h^{-1})**	**R^2**	q_e **(P-mg·g^{-1})**	K_2 **(g·P-mg^{-1}·h^{-1})**	**R^2**
RSN	4.0 ± 0.1	5.17 ± 0.84	0.951	4.1 ± 0.1	5.28 ± 2.18	0.996
Al-RSN	9.8 ± 0.3	2.04 ± 0.35	0.974	10.3 ± 0.6	0.37 ± 0.18	0.942

For Al-RSNs, both models seem to fit the data quite well, but the pseudo-first-order model fits the experimental data better. Such a model suggests a diffusion-controlled process. Few works have been published on phosphate capture by iron oxide doped with aluminum nanoparticles, and the main results are summarized in Table S5. The results in Table S5 show that most kinetics results are fitted with the pseudo-second-order model.

To conclude, experimental results showed a maximum adsorption of phosphate after 2 hours with RSNs and 3 hours with Al-RSNs, which can be considered a "fast adsorption".

3.4.2. Phosphate Removal from RSN and Al-RSN Solutions as a Function of the Initial Phosphate Concentration

The adsorption curves as a function of pH and phosphate concentrations are given in Figure 7. As expected, and in agreement with already reported results, the adsorption is more efficient at pH 3 than at pH 7 due to more favorable electrostatic interactions. This trend was also reported by several groups with different materials: magnetite [7], goethite [51], aluminum oxide hydroxide [52], or MnO_2 [53].

If we compare the phosphatation behavior of RSNs and Al-RSNs (Figure 7A,B), the capture of phosphates with Al-RSNs appears slower, and the plateau is reached for an initial phosphate concentration higher than 60–70 P-mg·L^{-1} whereas for RSNs, it was reached at 50 P-mg·L^{-1}. For pH 3, the maximum adsorption amount of Al-RSNs is 15.5 P-mg·g^{-1}, and at pH 7, the value is about 10 P-mg·g^{-1}. These values are higher than those with RSNs, in agreement with the higher surface specific area of Al-RSNs.

Concerning these isotherms, curves are of the «L» type. Such an "L" isotherm confirms the strong affinity of phosphate for iron oxide surfaces and a progressive saturation of the surface when the concentration increases. These curves, obtained in water at pH 3 and 7, were fitted with three different equilibrium models. The fitting curves and the adsorption parameters are presented in Figure S10 and one may observe that these models do not allow for fitting well the experimental curves. Nevertheless, one may notice that the Langmuir model seems to be the most suitable model. This model suggests that the adsorption sites do not interact between them and that their energies are equivalent. More experimental data are needed in the curves to conclude the most suitable model and also to consider parameters resulting from the fitting.

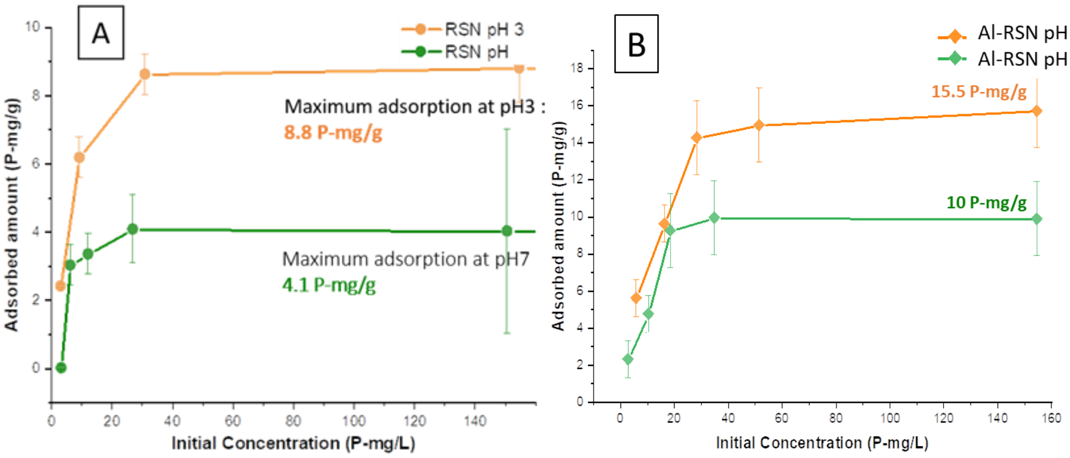

Figure 7. Adsorbed amount of phosphate in different media for 24 h by (**A**) RSNs and (**B**) Al-RSNs. In orange, in water at pH 3; in green, in water at pH 7.

To compare our results with the reported adsorption studies listed in Table S5, we have to be careful again, as this adsorption strongly depends on the experimental conditions: media, temperature, initial amount of adsorbent, and concentration of phosphates. The conditions and adsorption results are summarized in Table S6 for RSNs and Table S7 for Al-RSNs. In Table S6 for RSNs, the models that fit better are the Langmuir and Freundlich ones. It confirms the fitting of the previous RSN isotherm curve in water with the Langmuir model. The smaller adsorbed amount of phosphates with RSNs than with the other iron materials may be explained by their lower surface specific area. In Table S7 for Al-RSNs, the model that better fits the curve is the Langmuir one. It confirms that the Al-RSN isotherm curve in water could be fitted with this model. This model suggests that the adsorption sites do not interact among themselves and that their energies are equivalent.

3.4.3. Adsorption Amount

The maximum adsorption of RSNs at pH 3 was calculated to be 8.8 P-mg·g^{-1}. At physiological pH in water, the maximum adsorbed value drops to 4.1 P-mg·g^{-1}. At pH 7, the maximum adsorption value for Al-RSNs is 10 P-mg·g^{-1}, at pH 3, it rises to 15.5 P-mg·g^{-1}. Both values are significantly larger than for RSNs (4.1 P-mg·g^{-1} and 8.8 P-mg·g^{-1}), but the surface specific area of Al-RSNs is also higher. Thus, one reason for Al doping is to increase the surface specific area, allowing a higher phosphatation capture per g of material. One may notice that the maximum adsorption values obtained with Al-RSNs are quite high compared to those reported in the literature (Table S5) except for the studies of Xu et al. [15].

Our adsorption amounts were compared to those of Daou et al. [7], who have used nanoparticles with a close surface specific area (30 m^2·g^{-1}) and similar experimental conditions (room T, t = 24 h, adsorbent: 1 g·L^{-1}, pH 3 and pH 7). The adsorption amounts with RSNs and Al-RSNs are higher than those reported by Daou et al.: at pH 3, they measured 5.2 P-mg·g^{-1} (3.26 P-molecule·nm^{-2}) and at pH 7, 1.5 P-mg·g^{-1} (1.02 P-molecule·nm^{-2}). Therefore, RSNs and even Al-RSNs allow a higher adsorption of phosphates on their surfaces than iron oxide NPs. It could be explained by a different phosphate complex (i.e., monodentate, bidentate), the formation of a second phosphate layer, or a more favorable nanostructuration of RSN (higher curvature of grains or stronger adsorption at interfaces).

4. Conclusions

This study investigated the use of iron oxide nanostructures as an adsorbent to improve phosphate removal for water depollution. The synthesis of iron oxide and aluminum-doped ferrite raspberry-shaped nanostructures (RSNs and Al-RSNs) was optimized using a solvothermal–polyol method. The impact of synthesis parameters such as the nature of the iron precursor, the reaction time, and the mixing/solubilization step has been demonstrated. Then, the phosphate removal properties of these nanostructures were tested by studying their adsorption capacity and kinetics. The RSNs showed great affinity for phosphate, with a maximum adsorption capacity of 4.1 P-mg/g at pH 7 and 8.8 P-mg/g at pH 3. The Al-RSNs allowed a higher enhancement of adsorption capacity, with 10 P-mg/g at pH 7 and 15.5 P-mg/g at pH 3. The Al doping of RSNs shifted the IEP of RSNs and allows thus favorable electrostatic interactions. In addition, the surface specific area of Al-RSNs was higher. In addition, it was demonstrated that the phosphate maximum absorption was reached in less than 3 h for both undoped and Al-doped RSNs. These overall results showed that such nanostructures are promising for phosphate removal in water depollution.

Supplementary Materials: The following supporting information can be downloaded at: https://www.mdpi.com/article/10.3390/nano13030587/s1, Figure S1: (A) SEM, (B) TEM and (C) HRTEM images of RSN. (D) FITR spectrum of RSN with in insert (D1) Zoom of FTIR spectrum in the range 800–400 cm^{-1} corresponding to Fe–O bands characteristic here of a slightly oxidized magnetite. (E) XRD pattern and (F) Magnetization curves of RSN at 300 K; Table S1. Comparison of the characteristics of RSN of Gerber et al. [23] and the RSN of this work; Figure S2: SEM images corresponding to the synthesis of RSN without (A) and with (B) iron carbonates (brushes). XRD pattern of both RSN batches; Figure S3: Images of the four flasks containing the different iron precursors: A. Sigma 1, B. Alfa Aesar 1, C. Alfa Aesar 2, and D. Acros Organics 1; Table S2: Amount of iron in the different iron precursors determined by relaxometry measurements; Figure S4: SEM images and EDX graphs corresponding to the iron precursors. Table summarizing the atomic ratio of Fe/Cl and Fe/O; Figure S5: (Left) crystal structure of $FeCl_3 \cdot 6H_2O$ and (right) asymmetric unit. Iron is represented in brown, water in red and chlorine in green [54]. Table S3: $pH_{measured}$, $h_{calculated}$ and main species for the different iron precursors at 0.1 M (in theory); Figure S6: A. XRD patterns under air, B. FTIR spectra and C.TGA curves under air (5 °C/min) of the different iron precursors; Figure S7: Reminder: Reaction steps of the synthesis of magnetite RSN [11]; Figure S8: (A) SEM, (B) TEM and (C1) HRTEM images of RSN; (C2) SAED pattern; (D) XRD pattern. (E) FT-IR and (F) Magnetization curve at 300 K.; Figure S9: Zeta potential curve of RSN vs. pH and phosphate species as a function of pH (top) and Zeta Potential curves of RSN (in violet) and Al-RSN (in pink) as a function of pH (down). Table S4: Kinetics results of different iron-based materials; Table S5: Kinetics results of different aluminum-iron oxide materials; Figure S10: Fitting results of the isotherm adsorption curves for RSN (A,B) and Al-RSN (C,D) (Ce = equilibrium concentration). In red, the Langmuir model, in blue the Freundlich model and in green, the Redlich-Peterson model. Tables summarizes the parameter values corresponding to this fitting; Table S6: Adsorption isotherm results for different iron oxide-based materials; Table S7: Adsorption isotherm results of different aluminum doped ferrite materials. References [4–8,11,14,23,24,28,32,33,54–67] are cited in the Supplementary Materials.

Author Contributions: Methodology: P.D.R.; investigation: P.D.R., C.L., R.F., A.R.C., M.J. and J.V.-R.; formal analysis: P.D.R. and S.L.C.; writing original draft: P.D.R.; methodology: C.L. and D.P.P.B.; visualization: M.J., A.Z. and M.A.G.S.; formal analysis: J.V.-R.; resources: D.B. and D.M.; conceptualization: S.L.C., P.C., Y.P. and S.B.-C.; funding acquisition: M.A.G.S., P.K. and Y.P.; supervision: D.M. and S.B.-C.; validation: D.M., P.K. and S.B.-C.; project administration: S.B.-C.; writing–review & editing: S.B.-C. All authors have read and agreed to the published version of the manuscript.

Funding: This research was supported by the Asian Office of Aerospace Research and Development, Grants # FA2386-15-1-4112, # FA2386-18-1-4120. The Region Alsace, France, and the Asian Office of Aerospace Research and Development are gratefully acknowledged for the doctoral fellowship to Paula Duenas Ramirez. The authors acknowledge financial support from the Marie Curie project "Hierarchical functionalization and assembly of graphene for multiple device fabrication" (HiGRAPHEN) (Grant ref: 612704) and the PHC STAR 2020 PROJECT N° 43583PG.

Data Availability Statement: The data that support the findings of this study are available in the supplementary material of this article. The data are also available on request from the corresponding author. The data are not publicly available because the authors want to keep priority for conference presentations.

Acknowledgments: The scanning and transmission electronic microscopies and XRD platforms of the IPCMS including Cédric Leuvrey and Marc Lenertz are acknowledged for technical supports.

Conflicts of Interest: The authors declare that they have no known competing financial interest or personal relationship that could have appeared to influence the work reported in this paper.

References

1. Smil, V. P HOSPHORUS IN THE ENVIRONMENT: Natural Flows and Human Interferences. *Annu. Rev. Energy. Environ.* **2000**, *25*, 53–88. [CrossRef]
2. Alewell, C.; Ringeval, B.; Ballabio, C.; Robinson, D.A.; Panagos, P.; Borrelli, P. Global Phosphorus Shortage Will Be Aggravated by Soil Erosion. *Nat. Commun.* **2020**, *11*, 4546. [CrossRef] [PubMed]
3. Li, M.; Liu, J.; Xu, Y.; Qian, G. Phosphate Adsorption on Metal Oxides and Metal Hydroxides: A Comparative Review. *Environ. Rev.* **2016**, *24*, 319–332. [CrossRef]
4. Li, M.; Liu, H.; Chen, T.; Wei, L.; Wang, C.; Hu, W.; Wang, H. The Transformation of α-(Al, Fe)OOH in Natural Fire: Effect of Al Substitution Amount on Fixation of Phosphate. *Chem. Geol.* **2019**, *524*, 368–382. [CrossRef]
5. Shahid, M.K.; Kim, Y.; Choi, Y.-G. Magnetite Synthesis Using Iron Oxide Waste and Its Application for Phosphate Adsorption with Column and Batch Reactors. *Chem. Eng. Res. Des.* **2019**, *148*, 169–179. [CrossRef]
6. Lalley, J.; Han, C.; Li, X.; Dionysiou, D.D.; Nadagouda, M.N. Phosphate Adsorption Using Modified Iron Oxide-Based Sorbents in Lake Water: Kinetics, Equilibrium, and Column Tests. *Chem. Eng. J.* **2016**, *284*, 1386–1396. [CrossRef]
7. Daou, T.J.; Begin-Colin, S.; Grenèche, J.M.; Thomas, F.; Derory, A.; Bernhardt, P.; Legaré, P.; Pourroy, G. Phosphate Adsorption Properties of Magnetite-Based Nanoparticles. *Chem. Mater.* **2007**, *19*, 4494–4505. [CrossRef]
8. Baaziz, W.; Pichon, B.P.; Fleutot, S.; Liu, Y.; Lefevre, C.; Greneche, J.-M.; Toumi, M.; Mhiri, T.; Begin-Colin, S. Magnetic Iron Oxide Nanoparticles: Reproducible Tuning of the Size and Nanosized-Dependent Composition, Defects, and Spin Canting. *J. Phys. Chem. C* **2014**, *118*, 3795–3810. [CrossRef]
9. Demortière, A.; Panissod, P.; Pichon, B.P.; Pourroy, G.; Guillon, D.; Donnio, B.; Bégin-Colin, S. Size-Dependent Properties of Magnetic Iron Oxide Nanocrystals. *Nanoscale* **2011**, *3*, 225–232. [CrossRef]
10. Vichery, C.; Maurin, I.; Bonville, P.; Boilot, J.-P.; Gacoin, T. Influence of Protected Annealing on the Magnetic Properties of γ-Fe_2O_3 Nanoparticles. *J. Phys. Chem. C* **2012**, *116*, 16311–16318. [CrossRef]
11. Gerber, O.; Pichon, B.P.; Ihiawakrim, D.; Florea, I.; Moldovan, S.; Ersen, O.; Begin, D.; Grenèche, J.-M.; Lemonnier, S.; Barraud, E.; et al. Synthesis Engineering of Iron Oxide Raspberry-Shaped Nanostructures. *Nanoscale* **2016**, *9*, 305–313. [CrossRef]
12. Yan, L.; Yang, K.; Shan, R.; Yan, T.; Wei, J.; Yu, S.; Yu, H.; Du, B. Kinetic, Isotherm and Thermodynamic Investigations of Phosphate Adsorption onto Core–Shell Fe_3O_4@LDHs Composites with Easy Magnetic Separation Assistance. *J. Colloid Interface Sci.* **2015**, *448*, 508–516. [CrossRef] [PubMed]
13. Lai, L.; Xie, Q.; Chi, L.; Gu, W.; Wu, D. Adsorption of Phosphate from Water by Easily Separable Fe_3O_4@SiO_2 Core/Shell Magnetic Nanoparticles Functionalized with Hydrous Lanthanum Oxide. *J. Colloid Interface Sci.* **2016**, *465*, 76–82. [CrossRef] [PubMed]
14. Xu, J.; Luu, L.; Tang, Y. Phosphate Removal Using Aluminum-Doped Magnetic Nanoparticles. *Desalination Water Treat.* **2017**, *58*, 238–249. [CrossRef]
15. Cepan, C.; Segneanu, A.-E.; Grad, O.; Mihailescu, M.; Cepan, M.; Grozescu, I. Assessment of the Different Type of Materials Used for Removing Phosphorus from Wastewater. *Materials* **2021**, *14*, 4371. [CrossRef]
16. Li, G.; Gao, S.; Zhang, G.; Zhang, X. Enhanced Adsorption of Phosphate from Aqueous Solution by Nanostructured Iron(III)–Copper(II) Binary Oxides. *Chem. Eng. J.* **2014**, *235*, 124–131. [CrossRef]
17. Zhang, C.; Li, Y.; Wang, F.; Yu, Z.; Wei, J.; Yang, Z.; Ma, C.; Li, Z.; Xu, Z.; Zeng, G. Performance of Magnetic Zirconium-Iron Oxide Nanoparticle in the Removal of Phosphate from Aqueous Solution. *Appl. Surf. Sci.* **2017**, *396*, 1783–1792. [CrossRef]
18. Su, Y.; Yang, W.; Sun, W.; Li, Q.; Shang, J.K. Synthesis of Mesoporous Cerium–Zirconium Binary Oxide Nanoadsorbents by a Solvothermal Process and Their Effective Adsorption of Phosphate from Water. *Chem. Eng. J.* **2015**, *268*, 270–279. [CrossRef]
19. Nguyen, X.S.; Zhang, G.; Yang, X. Mesocrystalline Zn-Doped Fe_3O_4 Hollow Submicrospheres: Formation Mechanism and Enhanced Photo-Fenton Catalytic Performance. *ACS Appl. Mater. Interfaces* **2017**, *9*, 8900–8909. [CrossRef]
20. Daou, T.J. Synthèse et Fonctionnalisation de Nanoparticules d'oxydes de Fer Magnétiques. Ph.D. Thesis, University of Strasbourg, Strasbourg, France, 2007.
21. Rodríguez-Carvajal, J. Recent Advances in Magnetic Structure Determination by Neutron Powder Diffraction. *Phys. B Condens. Matter* **1993**, *192*, 55–69. [CrossRef]
22. Le Bail, A.; Duroy, H.; Fourquet, J.L. Ab Initio Structure Determination of $LiSbWO_6$ by X Ray Powder Diffraction. *Mater. Res. Bull.* **1988**, *23*, 447–452. [CrossRef]

23. Gerber, O.; Pichon, B.P.; Ulhaq, C.; Grenèche, J.-M.; Lefevre, C.; Florea, I.; Ersen, O.; Begin, D.; Lemonnier, S.; Barraud, E.; et al. Low Oxidation State and Enhanced Magnetic Properties Induced by Raspberry Shaped Nanostructures of Iron Oxide. *J. Phys. Chem. C* **2015**, *119*, 24665–24673. [CrossRef]
24. Jolivet, J.-P.; Henry, M. *De la solution à l'oxyde-Condensation des cations en solution aqueuse. Chimie de surface des oxyde*; EDP Sciences: Les Ulis, France, 1994; ISBN 978-2-7598-0292-0.
25. Perton, F.; Cotin, G.; Kiefer, C.; Strub, J.-M.; Cianferani, S.; Greneche, J.-M.; Parizel, N.; Heinrich, B.; Pichon, B.; Mertz, D.; et al. Iron Stearate Structures: An Original Tool for Nanoparticles Design. *Inorg. Chem.* **2021**, *60*, 12445–12456. [CrossRef]
26. Ammar, S.; Helfen, A.; Jouini, N.; Fiévet, F.; Rosenman, I.; Villain, F.; Molinié, P.; Danot, M. Magnetic Properties of Ultrafine Cobalt Ferrite Particles Synthesized by Hydrolysis in a Polyol MediumBasis of a Presentation given at Materials Discussion No. 3, 26–29 September, 2000, University of Cambridge, UK. *J. Mater. Chem.* **2001**, *11*, 186–192. [CrossRef]
27. Feldmann, C.; Jungk, H.-O. Polyol-Mediated Preparation of Nanoscale Oxide Particles. *Angew. Chem. Int. Ed.* **2001**, *40*, 359–362. [CrossRef]
28. Cao, S.-W.; Zhu, Y.-J.; Chang, J. Fe_3O_4 Polyhedral Nanoparticles with a High Magnetization Synthesized in Mixed Solvent Ethylene Glycol–Water System. *New J. Chem.* **2008**, *32*, 1526–1530. [CrossRef]
29. Yu, D.; Sun, X.; Zou, J.; Wang, Z.; Wang, F.; Tang, K. Oriented Assembly of Fe_3O_4 Nanoparticles into Monodisperse Hollow Single-Crystal Microspheres. *J. Phys. Chem. B* **2006**, *110*, 21667–21671. [CrossRef]
30. Ueda, M.; Ikeda, A. *Effect of Microstructure and Cr Content in Steel on CO_2 Corrosion*; NACE: Houston, TX, USA, 1996.
31. Li, W.; Qiao, X.; Zheng, Q.; Zhang, T. One-Step Synthesis of MFe_2O_4 (M=Fe, Co) Hollow Spheres by Template-Free Solvothermal Method. *J. Alloys Compd.* **2011**, *509*, 6206–6211. [CrossRef]
32. Kingery, W.D.; Uhlmann, D.R.; Bowen, H.K. *Introduction to Ceramics*, 2nd ed.; Wiley: New York, NY, USA, 1976; ISBN 978-0-471-47860-7.
33. Daou, T.J.; Pourroy, G.; Bégin-Colin, S.; Grenèche, J.M.; Ulhaq-Bouillet, C.; Legaré, P.; Bernhardt, P.; Leuvrey, C.; Rogez, G. Hydrothermal Synthesis of Monodisperse Magnetite Nanoparticles. *Chem. Mater.* **2006**, *18*, 4399–4404. [CrossRef]
34. Kavas, H.; Baykal, A.; Toprak, M.S.; Köseoğlu, Y.; Sertkol, M.; Aktaş, B. Cation Distribution and Magnetic Properties of Zn Doped $NiFe_2O_4$ Nanoparticles Synthesized by PEG-Assisted Hydrothermal Route. *J. Alloys Compd.* **2009**, *479*, 49–55. [CrossRef]
35. Kremenović, A.; Antić, B.; Vulić, P.; Blanuša, J.; Tomic, A. $ZnFe_2O_4$ Antiferromagnetic Structure Redetermination. *J. Magn. Magn. Mater.* **2017**, *426*, 264–266. [CrossRef]
36. Baaziz, W. Synthèse et Caractérisation Des Nanoparticules Spinelles et Coeur-Coquille à Base d'oxyde de Fer et de Cobalt. Ph.D. Thesis, University of Strasbourg, Strasbourg, France, 2011.
37. Amiri, S.; Shokrollahi, H. The Role of Cobalt Ferrite Magnetic Nanoparticles in Medical Science. *Mater. Sci. Eng. C* **2013**, *33*, 1–8. [CrossRef]
38. Aghazadeh, M.; Karimzadeh, I.; Reza Ganjali, M.; Malekinezhad, A. Al3+ Doped Fe_3O_4 Nanoparticles: A Novel Preparation Method, Structural, Magnetic and Electrochemical Characterizations. *Int. J. Electrochem. Sci.* **2017**, *12*, 8033–8044. [CrossRef]
39. Ehsani, M.H.; Esmaeili, S.; Aghazadeh, M.; Kameli, P.; Tehrani, F.S.; Karimzadeh, I. An Investigation on the Impact of Al Doping on the Structural and Magnetic Properties of Fe_3O_4 Nanoparticles. *Appl. Phys. A* **2019**, *125*, 280. [CrossRef]
40. Illés, E.; Tombácz, E. The Effect of Humic Acid Adsorption on PH-Dependent Surface Charging and Aggregation of Magnetite Nanoparticles. *JCIS* **2006**, *295*, 115–123. [CrossRef] [PubMed]
41. Li, L.; Stanforth, R. Distinguishing Adsorption and Surface Precipitation of Phosphate on Goethite (α-FeOOH). *JCIS* **2000**, *230*, 12–21. [CrossRef]
42. de Sousa, A.F.; Braga, T.P.; Gomes, E.C.C.; Valentini, A.; Longhinotti, E. Adsorption of Phosphate Using Mesoporous Spheres Containing Iron and Aluminum Oxide. *Chem. Eng. J.* **2012**, *210*, 143–149. [CrossRef]
43. Mezenner, N.Y.; Bensmaili, A. Kinetics and Thermodynamic Study of Phosphate Adsorption on Iron Hydroxide-Eggshell Waste. *Chem. Eng. J.* **2009**, *147*, 87–96. [CrossRef]
44. Netzahuatl-Muñoz, A.R.; Cristiani-Urbina, M.D.C.; Cristiani-Urbina, E. Chromium Biosorption from Cr(VI) Aqueous Solutions by Cupressus Lusitanica Bark: Kinetics, Equilibrium and Thermodynamic Studies. *PLoS ONE* **2015**, *10*, e0137086. [CrossRef] [PubMed]
45. Febrianto, J.; Kosasih, A.N.; Sunarso, J.; Ju, Y.-H.; Indraswati, N.; Ismadji, S. Equilibrium and Kinetic Studies in Adsorption of Heavy Metals Using Biosorbent: A Summary of Recent Studies. *J. Hazard. Mater.* **2009**, *162*, 616–645. [CrossRef]
46. Azimvand, J.; Didehban, K.; Mirshokraie, S. Safranin-O Removal from Aqueous Solutions Using Lignin Nanoparticle-g-Polyacrylic Acid Adsorbent: Synthesis, Properties, and Application. *Adsorpt. Sci. Technol.* **2018**, *36*, 1422–1440. [CrossRef]
47. Long, F.; Gong, J.-L.; Zeng, G.-M.; Chen, L.; Wang, X.-Y.; Deng, J.-H.; Niu, Q.-Y.; Zhang, H.-Y.; Zhang, X.-R. Removal of Phosphate from Aqueous Solution by Magnetic Fe–Zr Binary Oxide. *Chem. Eng. J.* **2011**, *171*, 448–455. [CrossRef]
48. Nur, T.; Johir, M.A.H.; Loganathan, P.; Nguyen, T.; Vigneswaran, S.; Kandasamy, J. Phosphate Removal from Water Using an Iron Oxide Impregnated Strong Base Anion Exchange Resin. *J. Ind. Eng. Chem.* **2014**, *20*, 1301–1307. [CrossRef]
49. You, X.; Farran, A.; Guaya, D.; Valderrama, C.; Soldatov, V.; Cortina, J.L. Phosphate Removal from Aqueous Solutions Using a Hybrid Fibrous Exchanger Containing Hydrated Ferric Oxide Nanoparticles. *J. Environ. Chem. Eng.* **2016**, *4*, 388–397. [CrossRef]
50. Wiriyathamcharoen, S.; Sarkar, S.; Jiemvarangkul, P.; Nguyen, T.T.; Klysubun, W.; Padungthon, S. Synthesis Optimization of Hybrid Anion Exchanger Containing Triethylamine Functional Groups and Hydrated Fe(III) Oxide Nanoparticles for Simultaneous Nitrate and Phosphate Removal. *Chem. Eng. J.* **2020**, *381*, 122671. [CrossRef]

51. Hawke, D.; Carpenter, P.D.; Hunter, K.A. Competitive Adsorption of Phosphate on Goethite in Marine Electrolytes. *Environ. Sci. Technol.* **1989**, *23*, 187–191. [CrossRef]
52. Tanada, S.; Kabayama, M.; Kawasaki, N.; Sakiyama, T.; Nakamura, T.; Araki, M.; Tamura, T. Removal of Phosphate by Aluminum Oxide Hydroxide. *J. Colloid Interface Sci.* **2003**, *257*, 135–140. [CrossRef]
53. Yao, W.; Millero, F.J. Adsorption of Phosphate on Manganese Dioxide in Seawater. *Environ. Sci. Technol.* **1996**, *30*, 536–541. [CrossRef]
54. Louvain, N.; Fakhry, A.; Bonnet, P.; El-Ghozzi, M.; Guérin, K.; Sougrati, M.-T.; Jumas, J.-C.; Willmann, P. One-Shot versus Stepwise Gas–Solid Synthesis of Iron Trifluoride: Investigation of Pure Molecular F_2 Fluorination of Chloride Precursors. *CrystEngComm* **2013**, *15*, 3664–3671. [CrossRef]
55. Nakamoto, K. *Infrared and Raman Spectra of Inorganic and Coordination Compounds*, 4th ed.; John Willey and Sons: New York, NY, USA, 1986.
56. Lind, M.D. Crystal Structure of Ferric Chloride Hexahydrate. *J. Chem. Phys.* **1967**, *47*, 990–993. [CrossRef]
57. Perton, F. Architecture de Nanoparticules Hybrides Pour Une Imagerie et/Ou Thérapie. Multimodales. Thesis, University of Strasbourg, Strasbourg, France, 2019. Available online: https://www.theses.fr/en/257283293 (accessed on 20 December 2022).
58. Tartaj, P.; Morales, M.P.; Veintemillas-Verdaguer, S.; González-Carreño, T.; Serna, C.J. The Preparation of Magnetic Nanoparticles for Applications in Biomedicine. *J. Phys. D Appl. Phys.* **2003**, *36*, R182–R197. [CrossRef]
59. Guzman, A.; Zuazo, I.; Feller, A.; Olindo, R.; Sievers, C.; Lercher, J.A. On the Formation of the Acid Sites in Lanthanum Exchanged X Zeolites Used for Isobutane/Cis-2-Butene Alkylation. *Microporous Mesoporous Mater.* **2005**, *83*, 309–318. [CrossRef]
60. Yassin, F.A.; El Kady, F.Y.; Ahmed, H.S.; Mohamed, L.K.; Shaban, S.A.; Elfadaly, A.K. Highly Effective Ionic Liquids for Biodiesel Production from Waste Vegetable Oils. *Egypt. J. Pet.* **2015**, *24*, 103–111. [CrossRef]
61. Capeletti, L.B.; Zimnoch, J.H. Fourier Transform Infrared and Raman Characterization of Silica-Based Materials. *Appl. Mol. Spectrosc. Curr. Res. Chem. Biol. Sci.* **2016**, *32*, 137–144. [CrossRef]
62. Scardera, G.; Puzzer, T.; Conibeer, G.; Green, M.A. Fourier Transform Infrared Spectroscopy of Annealed Silicon-Rich Silicon Nitride Thin Films. *J. Appl. Phys.* **2008**, *104*, 104310. [CrossRef]
63. Müller, M.; Villalba, J.C.; Anaissi, F.J. Thermal Decomposition (TG-DTA) of Iron Salts [$FeCl_3 \cdot 6H_2O$] and [$Fe(NO_3)_3 \cdot 9H_2O$] with Morphologic and Chemical Analysis of Final Product. *Semin. Ciências Exatas Tecnológicas* **2014**, *35*, 9–14. [CrossRef]
64. Yoon, S.-Y.; Lee, C.-G.; Park, J.-A.; Kim, J.-H.; Kim, S.-B.; Lee, S.-H.; Choi, J.-W. Kinetic, Equilibrium and Thermodynamic Studies for Phosphate Adsorption to Magnetic Iron Oxide Nanoparticles. *Chem. Eng. J.* **2014**, *236*, 341–347. [CrossRef]
65. Zeng, L.; Li, X.; Liu, J. Adsorptive Removal of Phosphate from Aqueous Solutions Using Iron Oxide Tailings. *Water Res.* **2004**, *38*, 1318–1326. [CrossRef]
66. Cao, D.; Jin, X.; Gan, L.; Wang, T.; Chen, Z. Removal of Phosphate Using Iron Oxide Nanoparticles Synthesized by Eucalyptus Leaf Extract in the Presence of CTAB Surfactant. *Chemosphere* **2016**, *159*, 23–31. [CrossRef]
67. Ajmal, Z.; Muhmood, A.; Usman, M.; Kizito, S.; Lu, J.; Dong, R.; Wu, S. Phosphate Removal from Aqueous Solution Using Iron Oxides: Adsorption, Desorption and Regeneration Characteristics. *J. Colloid Interface Sci.* **2018**, *528*, 145–155. [CrossRef]